# INVESTIGATION OF MOLECULAR AND SEGMENTAL MOTIONS IN POLYMERS USING SOLID-STATE NMR AND DEVELOPMENT OF NEW EXPERIMENTS USING SYMMETRY BASED PULSE SEQUENCES

**BY**
**ELDHO K. MATHAI**

**AUGUST 2014**

# INVESTIGATION OF MOLECULAR AND SEGMENTAL MOTIONS IN POLYMERS USING SOLID-STATE NMR AND DEVELOPMENT OF NEW EXPERIMENTS USING SYMMETRY BASED PULSE SEQUENCES

THESIS SUBMITTED TO THE

**UNIVERSITY OF PUNE**

FOR THE DEGREE OF

**DOCTOR OF PHILOSOPHY**

IN

**CHEMISTRY**

**By**

**ELDHO K. MATHAI**

**Central NMR Facility**

**Physical Chemistry Division**

**CSIR-National Chemical Laboratory**

**Pune - 411008**

**India**

**August 2014**

# CERTIFICATE

Certified that the work incorporated in the thesis entitled **"Investigation of molecular and segmental motions in polymers using Solid-State NMR and development of new experiments using symmetry based pulse sequences"**, submitted by **Mr. Eldho K. Mathai** for the Degree of **Doctor of Philosophy** was carried out by the candidate under our supervision in Central NMR Facility, Physical Chemistry Division, National Chemical Laboratory, Pune, India. Materials obtained from other sources have been duly acknowledged in the thesis.

| | | |
|---|---|---|
| Date :Pune | **Dr. T. G. Ajithkumar** | **Dr. P. R. Rajamohanan** |
| Place : | (Research Co-Guide) | (Research Guide) |
| | Central NMR Facility | Central NMR Facility |
| | Division of Physical Chemistry | Division of Physical Chemistry |
| | NCL, Pune-8 | NCL, Pune-8 |

# DECLARATION

I hereby declare that the thesis entitled **"Investigation of molecular and segmental motions in polymers using Solid-State NMR and development of new experiments using symmetry based pulse sequences"**, submitted for the Degree of **Doctor of Philosophy in Chemistry** to the University of Pune, has not been submitted by me to any other university or institution. This work has been carried out at Central NMR Facility, Physical Chemistry Division, National Chemical Laboratory, Pune under the supervision of Dr. T. G. Ajithkumar (Research co-guide) and Dr. P. R. Rajamohanan (Research guide).

Place:Pune
Date:

**Eldho K. Mathai**
(Research student)
Central NMR Facility
Division of Physical Chemistry
NCL, Pune-8

*Dedicated to my family and Teachers*

# Acknowledgement

*Undeniably, this thesis would remain incomplete without acknowledging the immense support of all the important people who helped me to realize my aspirations. It has been a journey that prepared and encouraged me to envisage further avenues. To start with... first and foremost I owe to my deepest gratitude to Almighty God, who always provided me with direction, courage and strength to pursue my dreams.*

*Certainly, I feel enormously indebted to my* ***parents*** *who held me up always in testing times. They are the best gift from God that I shall forever revere. Their unwavering support, love and confidence over me always gave me courage to overcome every stumbling block. All the lessons that I've learnt from them would always within me to remain humble and diligent.*

*I owe my deep gratitude to my research Guide* ***Dr. P. R. Rajamohanan****, who helped and guided me greatly in carrying out NMR studies. His most respectable aspect is the willingness to helping at any time and every instance, which I value greatly. It is my privilege to express my gratitude to my research co-guide* ***Dr. T.G. Ajitthkumar*** *for introducing me to the fascinating area, Physics of solid-state NMR and Polymer dynamics and pursue a Ph.D. His suitable suggestions, comments, timely reviews guided me during the testing time of my Ph.D. and thesis writing. I'm deeply thankful to him for giving me complete freedom in research, which I enjoyed profoundly. My sincere thanks to him for his timely helps and supports both scientifically and personally, on all occasion during my research period.*

*I am grateful to* ***Dr. Ashish Lele*** *and* ***Dr. Neelima Bulakh*** *for their timely advices and support in the polymer projects PLA and PSF, which was major part of my Ph.D. work. I am grateful to* ***Dr. Guruswamy Kumaraswamy*** *for his help in the POM project, and giving me useful suggestions. I would like to thank* ***Prof. Dr. Detlef Reichert*** *(Martin Luther University, Halle), for providing an opportunity to visit University of Halle as part of a DST-DAAD exchange programme an carrying out some of the preliminary CODEX experiments in PLA, which I value throughout my Ph.D. Special thanks to* ***Dr. Bhaskar Idige*** *and* ***Dr. Subhangi Idige*** *for providing the lab facility for preparing SC POM, for useful suggestions about the polymer crystallization and for providing different information about poly lactic acid during the thesis writing. I also must thank* ***Dr. S. Ganapathy****,* ***Dr. Sapna Ravindranathan, Sathe*** *sir and* ***Phalgune*** *madam for their encouraging words and support.*

*In solid-state NMR the technical support is very important. I am grateful to* ***P.M. Suryavamshi*** *who sorted out the problems which I have faced during the work in Central NMR Facility, especially repairing and troubleshooting the probes. It would have been very difficult to complete my Ph.D. without his continuous help. I am also grateful to* ***K.D. Deshpande, P.K. Mane*** *and* ***Umesh Kamatkar*** *for their full technical support in the facility. Special thanks to* ***Sachin Kate****, Application Engineer, Bruker for his technical and software support and for timely suggestions and help.*

*I would like to thanks* ***Dr. S. Mahesh*** *(IISER, Pune),* ***Prof. Dr. P.K. Madhu*** *(TIFR, Mumbai),* ***Prof. Dr. Neils Chr. Neilsen*** *(University of Arhus),* ***Dr. Nishiyamma*** *(JEOL Japan) for their valuable suggestions and support. I am profoundly grateful to my teacher* ***Prof. Dr. Dilip D. Dhawale****, who provided me the basics of practical research and helped me to pursue a career in research. I want to thank my late teacher* ***Dr. CV Ashokan*** *for his wonderful teachings in organic chemistry and gave me a chance to work under him as a project assistant.*

*I am also thankful to* ***Dr. Sourav Pal****, Director and* ***Dr. S. Sivaram*** *former Director and* ***Dr. Anil Kumar****, Head of the Physical Chemistry Division for providing the infrastructure to work in this prestigious research institute. I am also thankful to the* ***CSIR****, India for my research fellowship. I am profoundly grateful to all my teachers, who guided me immensely to envisage a career in research. My heartfelt gratitude to* ***Dr. K.A. Ajithkumar,*** *SS College, Kalady for providing timely advices and encouragements.*

*The best part of one's life is made of people and the moments that you are deeply moved with. This is sure a huge list as there are great number of beautiful people, whom I've closely known and shared every feeling freely with, and gained priceless guidance, incessant love and care. I owe a lot of such moments to all my closest seniors especially* ***Dr. Ajish Kumar K.S., Dr. K.L.M. Manoj*** *who stayed with me, supported and guided during my difficult moments. Thanks to all my colleagues* ***Ganesh F. Jogdand, Bindhu Baby, Anjali K., Cornelius Franz, Christiane Huckal, Poorvi Purohith, Biyas Posha, Athira K, Anjali Krishna, Dr. Vinod Chandran, Dr. Deepak Nand, Dr. Harindranath K., Ralph Anto, Sumesh Raman, Renny Mathews, Dr. E. Viswanath, Dr. Padma Prasad, Dr. Soumya Singha Roy, Abhishek Sukla*** *for lovely times in the lab. I would also like to thank my friends and seniors* ***E.***

***Venugopal, Suresh K.K., Alson Mart, Rajesh T., Anumon V., Sharath K., Manu M.S., Dr. Swaroop S., Shantil M., Renjith Kumar P.V., Dr. Shijo K. Cherian, Shoy George, Vijaydas N., Dr. Roshna V., Anish Lazar, Govind Raj, Kiran J.N., Sunil S., Vysakh, Dr. Leon Prasanth, Dr. Prasnth M., Dr. Krishnaraj, Dr. Prinson P. Samuel, Dr. Prasanth P., Lenin R., Dr. Edwin G, Manoj Sharma, Kshirodra, Chandan Choudhary, Jino John, Madhu chettan*** *for their valuable support.*

*Finally, I would like to thank all those who have contributed to the successful realization of this dissertation as well as expressing my apology to those I could not mention personally.*

*May the almighty God richly help all of you.*

***Eldho K. Mathai***

# CONTENTS

# ABBREVIATIONS

| | |
|---|---|
| *AFM* | *Atomic Force Microscopy* |
| *AHT* | *Average Hamiltonion theory* |
| *BPA* | *Bisphenol A polycarbonates* |
| *CODEX* | *Center Band Only Detection of Exchange* |
| *CSA* | *Chemical Shift Anisotropy* |
| *CRAMPS* | *Combined Rotation And Multiple Pulse Sequences* |
| *DDMAS* | *Dipolar Decoupled Magic Angle Spinning* |
| *DSC* | *Differential Scanning Calorimeter* |
| *CW* | *Continuous Wave* |
| *COSY* | *Correlation Spectroscopy* |
| *CP* | *Cross Polarization* |
| *DRSE* | *Dipolar Rotational Spin-Echo experiments* |
| *DMA* | *Dynamic Mechanical Analyzer* |
| *DES* | *Di Electric Spectroscopy* |
| *DIPSHIFT* | *Dipolar Chemical Shift correlation* |
| *DMS* | *Dimethylsulfone* |
| *EFG* | *Electric Field Gradient* |
| *FCC* | *Folded Chain Crystal* |
| *FID* | *Free Induction Decay* |
| *FSLG* | *Frequency Switched Lee-Goldberg* |
| *FT* | *Fourier Transform* |
| *HSQC* | *Heteronuclear Single Quantum Correlation* |
| *HMQC* | *Heteronuclear Multiple Quantum Correlation* |
| *HMBC* | *Heteronuclear Multiple Bond Correlation* |
| *KWW* | *Kolhrash's William Watt function* |
| *LF* | *Lab Frame* |

| | |
|---|---|
| *MAS* | *Magic angle spinning* |
| *MC* | *Melt Crystal* |
| *MF* | *Molecular Frame* |
| *NS* | *Neutron Scattering* |
| *NOESY* | *Nuclear Overhauser Effect SpectroscopY* |
| *ODESSA* | *One-Dimensional Exchange Spectroscopy by Sideband Alteration* |
| *PESU* | *Polyethersulfone (trade name VERADEL)* |
| *PSU* | *Polysulfone (trade name UDEL)* |
| *PPSU* | *Polyphenylsulfone (trade name RADEL)* |
| *PAF* | *Principle Axis Frame* |
| *PMLG* | *Phase-Modulated Lee-Goldberg* |
| *PISEMA* | *Polarization Inversion Spin Exchange at Magic Angle* |
| *POM* | *Polyoxymethylene* |
| *PSF* | *Polysulfone* |
| *PDLLA* | *Poly D-L Lactic Acid* |
| *PLA* | *Poly Lactic Acid* |
| *PDLA* | *Poly D Lactic Acid* |
| *PLLA* | *Poly L Lactic Acid* |
| *REDOR* | *Rotational Echo Double Resonance* |
| *RF* | *Rotor Frame* |
| *ROESY* | *Rotating frame nuclear Overhauser Effect Spectroscopy* |
| *RRR* | *Rotary Resonance Recoupling* |
| *SC* | *Solution Crystal* |
| *SLF* | *Separated Local Field* |
| *SAXS* | *Small Angle X-ray Scattering* |
| *SPINAL* | *Small Phase INcremental ALteration* |
| *SSNMR* | *Solid-State NMR* |
| *SSS dig ram* | *Space-Spin Selection Diagrams* |

| | |
|---|---|
| *SF* | *Scaling Factor* |
| *SUPER* | *Separation of Undistorted Powder pattern by Effortless Recoupling* |
| *TMBPA-PC* | *Tetra methyl bisphenol A poly carbonate* |
| *tr-ODESSA* | *Time Reverse One-Dimensional Exchange Spectroscopy by Sideband Alteration* |
| *TSR* | *Thermally Stimulated Recovery* |
| *TPPM* | *Two Pulse Phase Modulation* |
| *TOCSY* | *Total Correlation Spectroscopy* |
| *TOSS* | *Total Suppression of Spinning Side band* |
| *WAHUHA* | *Waugh Huber Haeberlen* |
| *XiX* | *X-inverse-X* |
| $\delta_{iso}$ | *Isotropic chemical shift* |
| $\delta_{aniso}$ | *Chemical shift anisotropy* |
| $\eta$ | *Asymmetry parameter* |
| *DD* | *Direct dipole-dipole interaction* |
| *J* | *Scalar coupling* |
| $T_1$ | *Spin lattice relaxation time* |
| $T_2$ | *Spin spin relaxation time* |
| $T_g$ | *Glass transition temperature* |
| $T_{1\rho}$ | *rotating frame spin lattice relaxation time* |
| $\tau_m$ | *Mixing times* |
| $\tau_z$ | *z-filter time* |
| $\tau_c$ | *Correlation time* |

# Synopsis

**Preamble:** In this thesis, different ranges of motions in three polymers have been studied using advanced solid-state NMR techniques. The symmetry based sequences have been explored for modifying the solid-state NMR experiment CODEX, which is used to study dynamics in polymers. A brief content of all the chapters in this thesis is given below.

**Chapter 1: Introduction to NMR of Polymers**

Specific application of a polymer depends on its mechanical property and the mechanical property of the polymer is a function of many factors such as chemical structure, morphology, molecular and segmental motions of polymer chains. In the first part of this PhD project, functional group and segmental motion in three polymers, polyoxymethylene (POM), polysulfones (PSF) and poly D-L lacticacid (PDLLA) are studied using advanced solid-state NMR experiments such as center band only detection of exchange (CODEX) and polarization inversion spin exchange at magic angle (PISEMA). In the second part of the project, new experiments using symmetry based sequences have been developed, which are proposed to be used as an alternative to the CODEX experiment.

At the molecular level, all polymers have motions such as vibration, rotation, chemical exchange, segmental reorientation etc. NMR is a powerful technique that can monitor these motions. The time-scales that can be probed by NMR are shown in the figure S1.

Motions in polymers can be measured using different solid-state NMR techniques such as deuterium NMR, 2D exchange NMR, line shape analysis, relaxation measurements, SLF-PISEMA, and CODEX experiments. Deuterium NMR is a very efficient method for the investigation of dynamics in polymers. However, this requires deuterated polymer samples which are usually difficult to prepare. One of the main aims of this project was to investigate molecular motions in polymers that can be obtained readily without any special synthetic procedure like deuterium ($^{2}H$) or $^{13}C$ labeling. $^{13}C$ exchange experiment provides information about the geometry and time-scale of motion but has the disadvantage that it is a static or quasi static experiment and require tremendous amount of experimental time. Line shape analysis

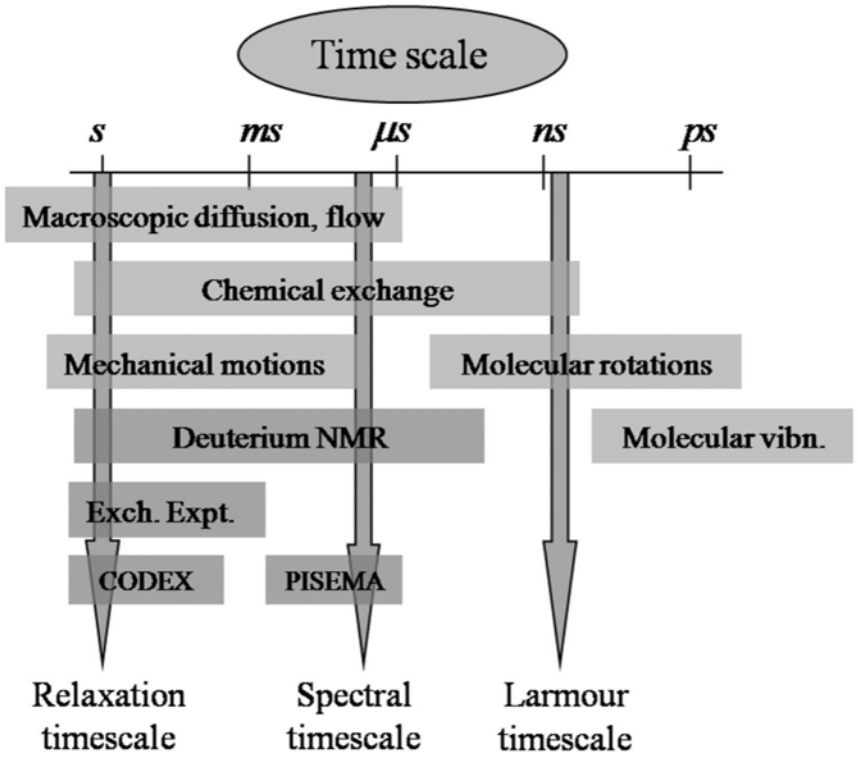


*Figure S1: Different range of motions which can be probed by NMR[1]*

and relaxation experiments also have difficulties because the extraction of dynamics from them is not straight forward. Our aim is to use solid-state NMR techniques that can be applied on naturally abundant $^{13}C$ nuclei and has reasonable experimental times. The separated local field - PISEMA (SLF-PISEMA) and CODEX are experiments which can be performed on naturally abundant $^{13}C$ nuclei in a reasonable experiment time and they have been chosen for our studies on polymers. CODEX experiment have been used for the detecting motions in the range of 0.1 Hz to 1000 Hz and PISEMA experiment was used for the measurement of motion in the range of 100s of kHz.

**Chapter 2: Crystalline motions and morphology of POM**

POM is a high performance engineering polymer which is semicrystalline. Melt crystallized sample of POM melts at 175$^{o}$C, while the stiffness of the material deteriorate around 100$^{o}$C. Therefore, the material has limited applications near and above this temperature. POM forms helical structures that pack into crystals during its formation. Kentgens *et al.* measured the slow crystalline motion in melt crystallized (MC) POM at around 100$^{o}$C using two dimensional exchange experiments [2]. Hagmeyr *et al.* have also reported similar crystalline motions in MC POM around

100°C [3]. Based on these results, they concluded that torsional motions of crystalline chains are responsible for softening in POM, at 100°C. They have determined the activation energy of crystalline motions as 80 kJ /mol. However, in a recent study on melt crystallized and solution crystallized (SC) POM, Guru *et al.* showed that solution crystallized POM does not show softening and therefore concluded that lamellar melting is responsible for the softening in MC POM [4]. In this study, a detailed investigation on melt crystallized and solution crystallized POM was carried out using SSNMR to measure the crystalline motions and to understand the morphology of POM and thereby understand the reasons for softening in the melt crystallized sample at 100°C. CODEX experiments were carried out from 23°C to the softening temperature 100°C to extract the correlation time ($\tau_c$) and calculated the activation energies ($E_a$) using Arrhenius plots. Activation energy of 77.9 and 75.4 kJ/mol was observed in case of melt crystallized and solution crystallized sample respectively. The similarity of the activation energies of SC and MC POM indicates that even if crystalline motions are present, it is not responsible for the softening in melt crystallized POM. Figure S2 shows the activation energy plots of the melt crystallized and solution crystallized POM.

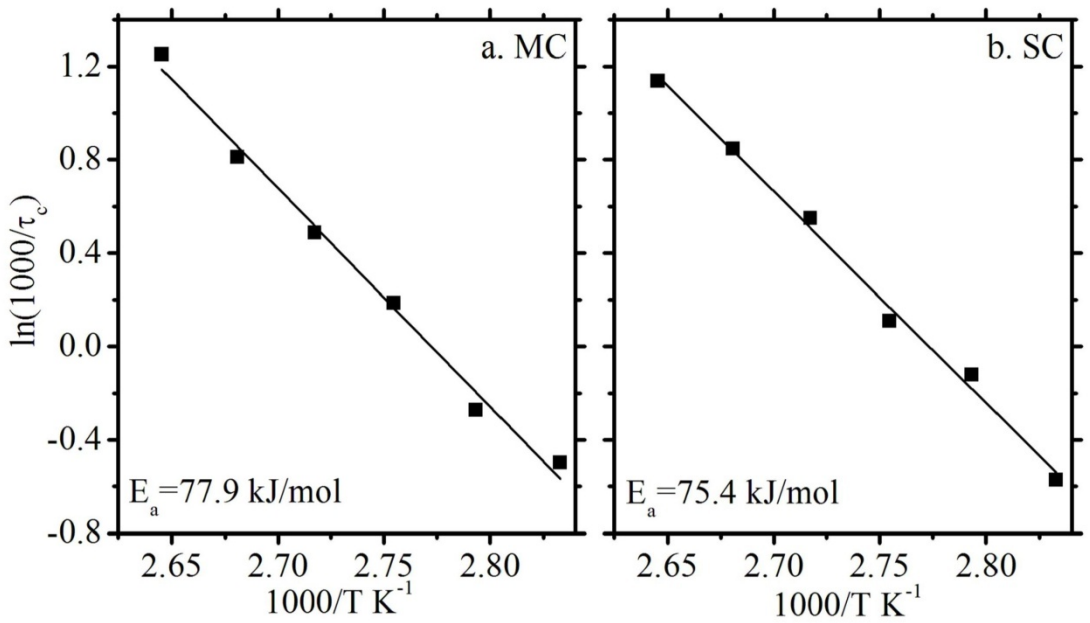


*Figure S2: Arrhenius plot of a). Melt crystallized (MC) and b). Solution crystallized (SC) POM near the softening point (97°C). In MC POM the activation energy of crystalline motion is 77.9 kJ/mol, while in SC POM the activation energy is 75.4 kJ/Mol.*

$T_1$ and $T_2$ filtered PISEMA experiments were carried out for understanding the nature of crystalline and amorphous phase respectively. $T_1$ filtered PISEMA on melt crystallized and solution crystal POM shows a constant dipolar coupling of 21.5 kHz at all temperatures, reiterating that the origin of softening is not from crystalline phase. The $T_2$ filtered PISEMA spectra on MC and SC POM are shown in figure S3 showing that the amorphous region of MC POM have smaller dipolar coupling compared to SC POM at each temperatures. Apart from that a distribution in heteronuclear dipolar coupling for the melt crystallized amorphous phase is observed, while this distribution is absent in the case of the solution crystallized amorphous region. This confirms that it is not the crystalline motion but the amorphous phase of the melt crystallized POM that plays the major role in softening.

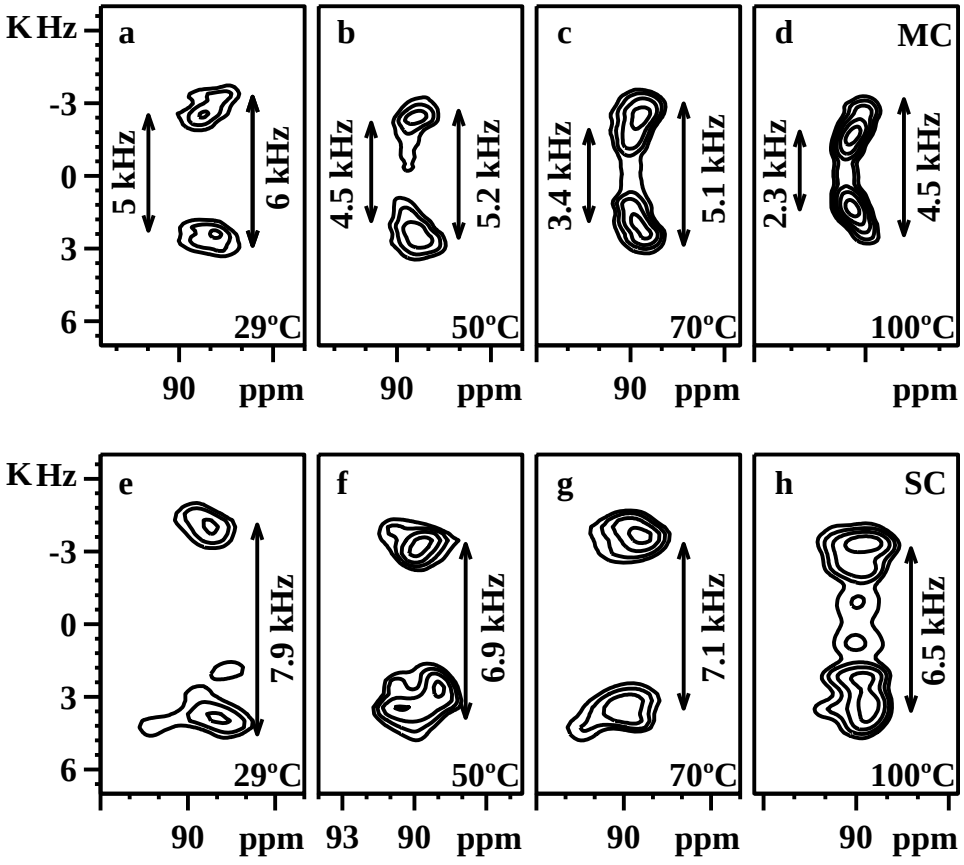


*Figure S3: $T_2$ filtered PISEMA spectra showing the amorphous region of the melt crystallized (top) and solution crystallized (down) POM at different temperatures.*

A CP based $T_1$ relaxation experiment was also carried out to monitor the difference in amorphous region. From both the relaxation measurements and $T_1$ filtered PISEMA experiments, it was observed that there is no separate phase which has mobility in between the amorphous and the crystalline phase (the rigid amorphous

phase) in melt crystallized POM. However, it is seen that the amorphous phase has a continuum of mobility from less mobile to highly mobile region. Figure S4 shows the relaxation time as a function of temperature which shows the nature of the amorphous and crystalline regions.

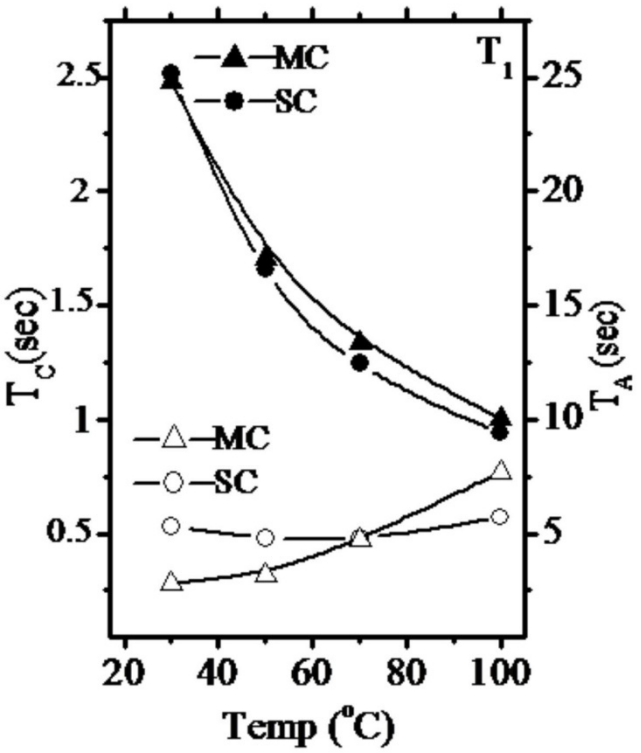


*Figure S4: $T_1$ relaxation times of amorphous and crystalline components of melt crystallized and solution crystallized POM at different temperatures.*

**Chapter 3: Phenyl group motions in Polysulfones**

PSF are high performance engineering thermoplastic amorphous polymers. It is used as flame retardants, in autoclave and in membrane materials due to its high resistance to physical and chemical forces. In this project, the molecular and segmental motions in three grades of polysulfones: polyethersulfone (PESU), polysulfone (PSU) and polyphenylsulfone (PPSU) were measured to obtain insights into the superior ductility of PPSU. The structures of PESU, PSU and PPSU are shown in figure S5.

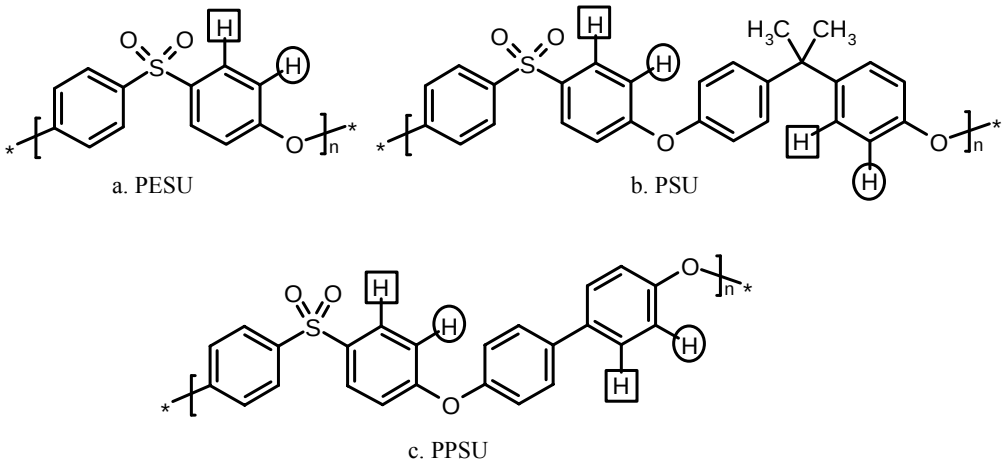


*Figure S5: Structures of a).PESU, b).PSU and c).PPSU.*

PISEMA experiments have been used to measure the phenyl group C-H dipolar coupling of these three polymers. Figure S6 shows the comparison of PISEMA spectra of PESU, PSU and PPSU for the C-H moiety near the ether linkages of the aromatic ring at 29°C, 60°C and 100°C. It is seen that in all the samples, the phenyl groups have regions with high mobility and low mobility, with dipolar coupling of 11.7 kHz and 21.5 kHz respectively. On comparison, it is seen that the PPSU has the least amount of the region with low mobility at 29°C. On heating, it is seen that the regions with low mobility in PPSU have almost disappeared at 60°C, while the regions with low mobility in PESU and PSU are still present. The disappearance of low mobility region at 60°C may be the reason for superior ductility of the PPSU grade in comparison to the PSU and PESU. The PISEMA spectra at 100°C show that the rigid part of all the three grades have almost vanished. The CH moiety near isopropyl/sulfone/biphenyl linkage also show similar behavior.

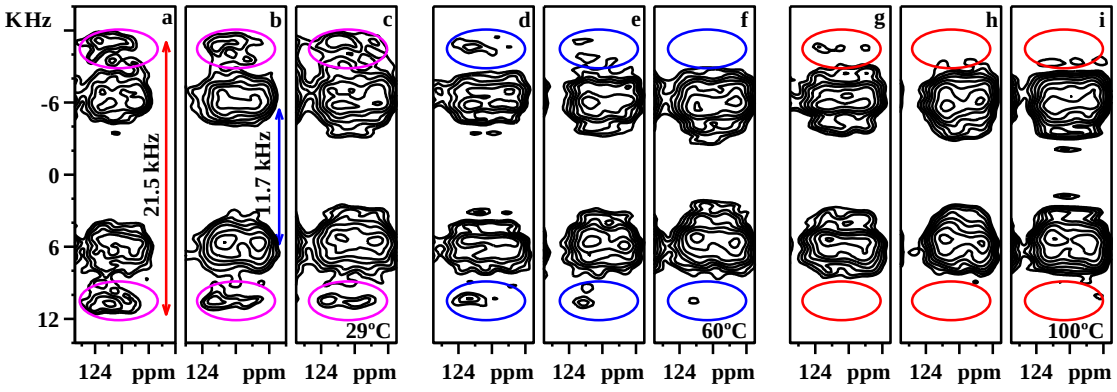


*Figure S6: PISEMA spectra of PESU (a,d,g), PSU(b,e,h), PPSU(c,f,i) at temperatures of 29, 60 and 100°C for CH carbons near to the ether linkage.*

From the PISEMA experiments it can be confirmed that all the three polymers PESU, PSU and PPSU have two dynamically different environments: rigid and mobile. Further experiments were carried out to investigate if there are regions with mobility in between mobile and rigid components. A combination of $^{13}C$ longitudinal relaxation ($T_1$) experiments and $^{13}C$ $T_1$ filtered PISEMA experiments were carried out on all the three polymers to answer this question. $T_1$ filtered PISEMA experiments along with longitudinal relaxation time experiments at 29°C confirms that there are three dynamically distinct regions in all the three grades of PSF, a mobile component with relaxation time of the order of 0.45 *sec*, an intermediate component with relaxation time of the order of 4.0 *sec* and a rigid component with relaxation times of the order of 25 *sec*. The PISEMA data obtained with different $T_1$ filter times of 0 *sec*, 2.5 *sec*, 5 *sec*, 10 *sec* and 15 *sec* for CH moiety near to ether linkage of PESU is shown in figure S7. A similar trend is seen in PSU and PPSU.

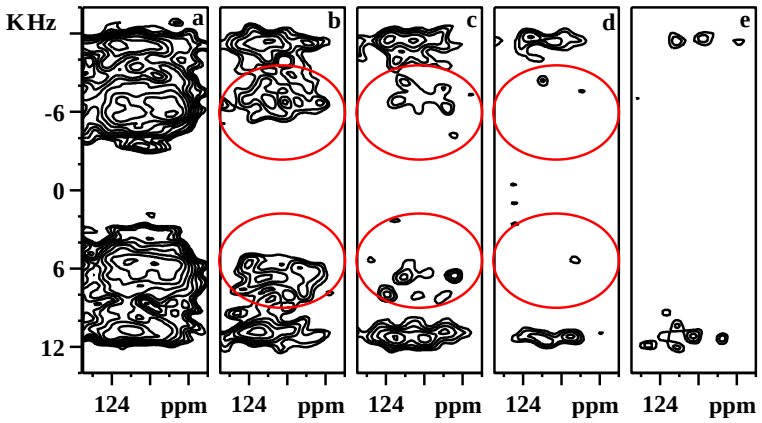


*Figure S7: $T_1$ filtered PISEMA spectra of PESU at 29°C with $T_1$ filters of a)0 sec, b)2.5 sec, c)5 sec, d)10 sec and e)15 sec. The mobile component with a dipolar coupling of 13.7 kHz present in the spectrum with a $T_1$ filter of 2.5 sec confirms the presence of intermediate component since mobile component with a $T_1$ filter of 0.45 sec is expected to vanish with a $T_1$ filter of 1.5 sec.*

CODEX experiments were carried out on these samples to detect the presence of slow motions. The results of the CODEX experiment at 26°C for carbon near the ether linkage is shown in the figure S8a and it is seen that all the three grades have slow motions of the order of few tens of seconds. Since the dephasing curve has not reached a plateau, extraction of correlation time is not possible. CODEX experiments were carried out at 100°C to probe which of the three components of the polymer contribute to the slow motions and the results for the PESU and PPSU are shown in

figure S8b. At 100°C also both the samples show CODEX dephasing similar to that at 26°C. At 100°C, in all the three polymers, the rigid component is absent which is already established from the PISEMA experiments. The frequency of motion of the mobile region is expected to be of the order of 100s of kHz and therefore will not contribute to the CODEX dephasing. Therefore, the dephasing which is seening in the CODEX experiment is from the intermediate component. At 100°C also the dephasing curve does not reach a plateau making the extraction of a correlation time impossible. The carbon near to the isopropyl/sulfone/biphenyl linkage also shows a similar trend.

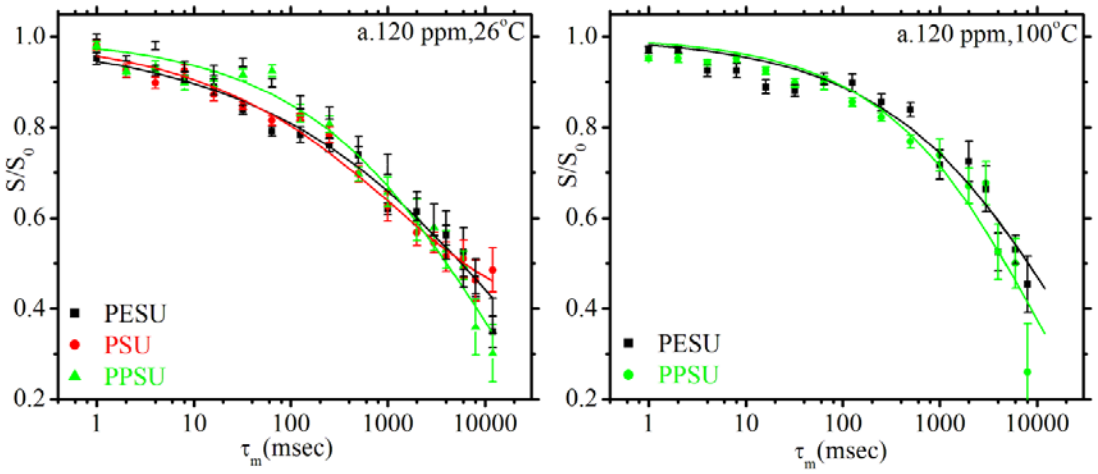


*Figure S8: The results of the CODEX experiments for CH moiety near the ether linkage of PESU, PSU and PPSU at a).26°C and b).100°C, show similar CODEX dephasing.*

**Chapter 4: Segmental motions in PLA at the $T_g$**

Most of the polymers which we encounter in our day-to-day life are made from petroleum based products. Once these polymers are discarded after use, they exist in nature for many years without degradation and are hazardous to our environment. A possible solution to this problem is to replace the petroleum based polymers with bio based polymers. Polylacticacid (PLA) is one of the popular bio-based polymer considered as potential replacement for petroleum based polymers. Slow segmental motions in poly D-L Lactic acid (PDLLA) were investigated at the glass transition temperature ($T_g$) as a function of thermal aging. The CODEX curve obtained for different thermally aged samples are shown in figure S9a. It is observed that segmental motions in PDLLA at $T_g$ decreases with sample aging and this is due to the increase in the crystallinity during aging. The correlation times of the polymer chain at different annealing times are shown in the figure S9b. The amount of

crystallinity (%) at different aging times estimated from Differential Scanning Calorimeter (DSC) is shown in figure S9c. A direct correlation between the degree of crystallization and the slowing down of the polymer chain motion is observed near the $T_g$.

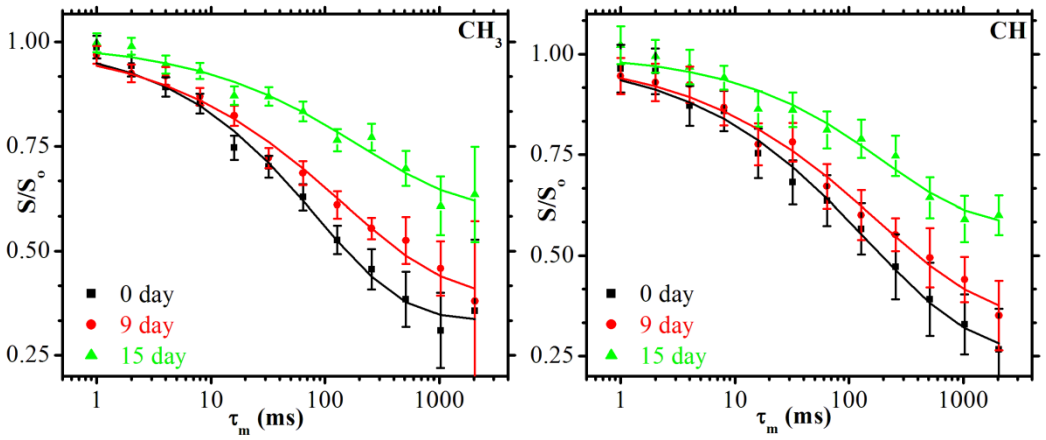


*Figure S9a: CODEX curves obtained at 60°C for $CH_3$ and CH group with different thermally aged samples. The CODEX curves indicate that slow motions with correlation times of the order of 100s of msec are present in the polymer. It is also to be noted that as the annealing time increases there is a slowing down in the chain motions which is indicated by the upward shift in the CODEX curve.*

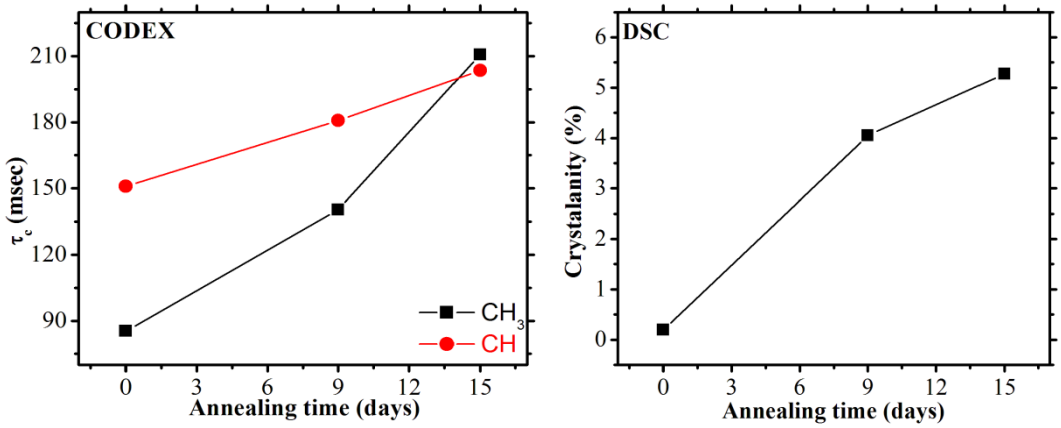


*Figure S9b: Comparison of the correlation time with annealing time. S9c: Comparison of crystallinity with annealing time. The data indicates, as the crystallinity increases, the correlation time increases ie. motions slows down.*

## Chapter 5: Modification of the CODEX experiment using symmetry sequences

The CODEX experiment gives information about slow chain dynamics in polymers and biomolecules. The most important component of the CODEX

experiment is the rotor synchronized 180° pulse trains which recouple the CSA. In this study, 180° pulse trains of the CODEX experiment have been replaced by the symmetry based CSA recoupling sequences $R10_1^3$, $R10_1^4$, $R18_2^5$, $R18_2^7$, $R18_4^5$, $R14_4^3$ and their performance are evaluated. The sequences are divided into two categories based on the component of CSA which is recoupled: $R10_1^4$, $R18_2^7$, $R18_4^5$, $R14_4^3$ sequences recouple the 1st order space component ($\sigma_1$) while $R10_1^3, R18_2^5$ sequences recouple the 2nd order component ($\sigma_2$).

Before implementing the R sequences into CODEX experiments, their recoupling efficiencies were evaluated using 2D experiments at spinning rates of 3 kHz and 10 kHz. The $R_{\pi\nu/N}R_{-\pi\nu/N}$ is the basic element used in an R sequence. Using SIMPSON simulations, it was shown that there are two modes of acquisition possible for the 2D experiment using R sequences: the $n$ and the $N/2$ modes. For the $n$ mode the $t_1$ was incremented in steps of the length $[R_{\pi\nu/N}R_{-\pi\nu/N}]_{N/2}$ while for $N/2$ mode the $t_1$ was incremented in steps of the length $R_{\pi\nu/N}R_{-\pi\nu/N}$. The recoupled CSA line shape from a $R18_2^7$ sequence simulated using SIMPSON is shown in figure S10a, shows the $N/2$ mode acquisition is similar to the $n$ mode acquisition. The advantage of the $N/2$ mode acquisition is that it has a resolution which is $N/2$ times higher than that of the $n$ mode acquisition. Therefore, all the 2D CSA recoupling experiments were carried out in the $N/2$ mode acquisition. All the sequences recouple the CSA at spinning speeds of 3 kHz and 10 kHz, except for the $\sigma_1$ sequence at 3 kHz, where the recoupling efficiency was not good. The recoupling efficiency was monitored by comparing the simulated and experimental spectra and by extracting the CSA parameters using the OPT package in SIMPSON. Figure S10b shows the experimental and the fitted spectra of a 2D CSA recoupling sequence using $R18_2^7$ at a spinning speed of 10 kHz. The CSA parameters obtained from fitting are very close to the expected values shows its recoupling efficiently.

The CODEX experiments using symmetry R sequences are called R-CSA CODEX experiments. The R-CSA CODEX $N\tau_r$ and $\tau_m$ dependence experiments have been carried out using different R sequences at spinning speeds of 3 and 10 kHz using $n$ and $N/2$ mode acquisition. The R-CSA CODEX $N\tau_r$ dephasing curves obtained using $\sigma_1$ recoupling sequences ($R10_1^4$, $R18_2^7$) at a spinning speed of 3 kHz

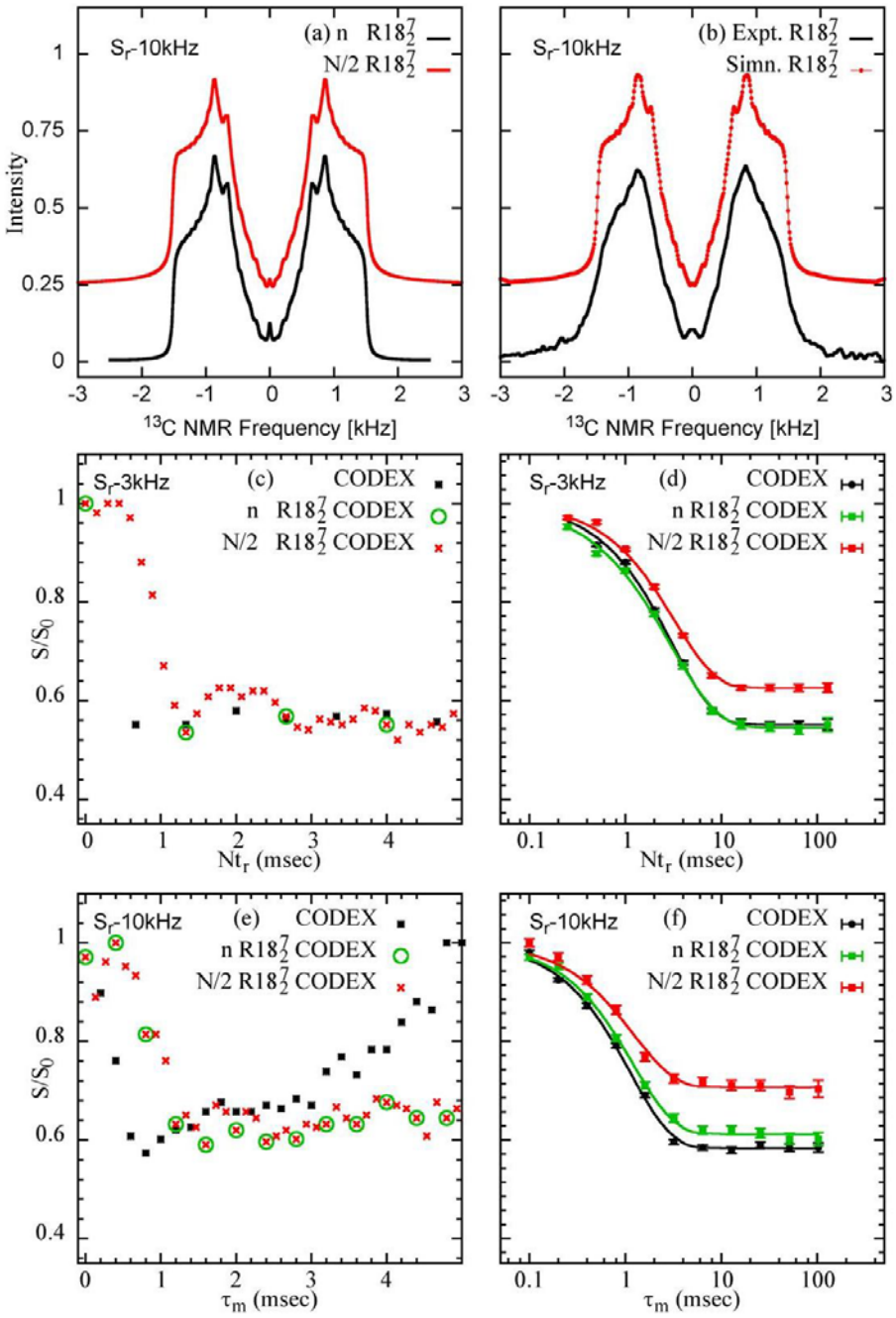


*Figure S10: The experimental and simulation results obtained for the R-sequence* $R18_2^7$*. CSA recoupling is demonstrated on the carbonyl environment of alanine while CODEX is demonstrated on DMS. a) Comparison of* $n$ *and* $N/2$ *mode acquisition using SIMPSON simulations at a spinning speed 10 kHz. b) Fitting of the experimental spectra with simulation using SIMPSON at 10 kHz. c). CODEX (black), R-CSA CODEX* $n$ *mode (green) and* $N/2$ *mode (red)* $N\tau_r$ *dependence experiment at 3 kHz spinning speed and corresponding d)* $\tau_m$ *dependence experiments e) CODEX (black), R-CSA CODEX* $n$ *mode (green) and* $N/2$ *mode (red)* $N\tau_r$ *dependence experiment at 10 kHz spinning speed and corresponding f).* $\tau_m$ *dependence experiment.*

in the $n$ mode matches with the CODEX $N\tau_r$ dephasing curves, while that using the $\sigma_2$ recoupling sequences ($R10_1^3, R18_2^5$), dephasing curves show large deviation or it oscillates around the plateau. For the R-CSA CODEX $N\tau_r$ dephasing curves obtained usng the $\sigma_2$ recoupling sequences in the $N/2$ mode also have large oscillations around plateau value while that using the $\sigma_1$ recoupling sequences the oscillations are less. The R-CSA CODEX mixing time ($\tau_m$) dependence experiments were carried out using the $N\tau_r$ value taken from the R-CSA CODEX $N\tau_r$ dependence experiments in the $n$ and $N/2$ mode. The $\tau_m$ curve obtained using $N\tau_r$ value acquired in the $n$ mode matches exactly with that from the CODEX experiment while from the $N/2$ mode show a deviation. However, the correlation times obtained from both modes are similar, irrespective of $N\tau_r$ at which dephasing reaches plateau or the intensity of dephasing $S/S_0$ at plateau.

The $N\tau_r$ dependence curve from the CODEX experiments at 10 kHz show an upward shift, which is due to the non-ideal nature of 180$^o$ pulses. Similar upward shift is seen in the $N\tau_r$ dependence curves from the R-CSA CODEX $N\tau_r$ dependence experiments using $\sigma_2$ recoupling sequences ($R10_1^3, R18_2^5$) while this is absent when $\sigma_1$ recoupling sequences ($R10_1^4$, $R18_2^7$, $R18_4^5$, $R14_4^3$) are used. The advantage of R-CSA CODEX sequence is that, ideal pulses are not needed for the CSA recoupling element and hence it is possible to implement these sequences at high spinning speeds. As seen in the case of the R-CSA CODEX experiments at 3 kHz, the correlation times obtained at 10 kHz from the $\tau_m$ dependence experiments are similar to the correlation time obtained from the CODEX $\tau_m$ dependence experiments at 10 kHz, irrespective of the $N\tau_r$ or the intensity of $S/S_0$ at the plateau.

# CHAPTER 1

# Introduction to Solid-state NMR of Polymers

Solid-state NMR is a powerful tool for the determination of dynamics in polymers at a microscopic level. Absorption of external impacts and mechanical stress on a polymer is determined by the segmental and/or cooperative mobility of the chains. Therefore, based on the information about the dynamics, NMR can give insights about the mechanical property of the material. Dynamic mechanical analysis (DMA), dielectric spectroscopy (DES), small angle x-ray scattering (SAXS) etc. gives information about the mechanical property at a macroscopic level but not at the microscopic level. NMR has a clear advantage over other techniques in terms of experiments available for measuring different ranges of motions and has access to different chemical sites which contributes to the dynamics. Neutron scattering (NS) is a complementary method to solid-state NMR. However, due the low availability of neutron sources, this technique is not widely used.

In solution-state NMR, the resonance peaks are very narrow due to the Brownian motion of molecules, and is therefore used for structural assignments. The resolution in solution-state NMR is because of the averaging of different anisotropic interactions such as chemical shift anisotropy, dipolar coupling, and quadrupolar coupling which are the probes for information about dynamics in solid polymeric materials. Therefore, solution-state NMR is not used for the characterization of chain dynamics in polymers. In solid-state NMR the Brownian motions are absent, results in an orientation dependent resonance peaks for the nucleus, hence produce broad powder patterns for each anisotropic interaction in polycrystalline samples. The overabundance of anisotropic interaction makes the analysis of solid-state NMR very difficult. Different experimental techniques have been developed in solid-state NMR for filtering out specific interactions from the pool of anisotropic interactions making the determination of different physical properties possible.

The basic difference between solution-state and solid-state NMR is anisotropic interaction which is present only in solid-state NMR. Even if solution-state and solid-

state NMR has evolved largely for the past 3 to 4 decades to different extent and directions, the basic principle behind both are the same. In this chapter the basic principles of NMR and the major developments that have happened in solid-state NMR of polymers are introduced. A brief history of NMR is presented followed by the basic principles of NMR and Solid-state NMR. The different techniques in solid-state NMR to obtain solution-state like spectrum and the major recoupling techniques in solid-state NMR are then discussed. An introduction to the solid-state NMR of polymers and the major NMR techniques used for measuring dynamics in polymers are then discussed.

## 1.1. Introduction to NMR

The first experimental detection of nuclear magnetic resonance signal was achieved by Bloch [5] and Purcell [6], independently in 1947. Since then NMR spectroscopy has continuously evolved and now stand as a pioneer technique for the characterization of structure and property in materials, from different research areas such as organic and inorganic chemistry, polymers, glasses, zeolites, catalysis, liquid crystals, peptides and proteins, quantum computing, medicine (MRI), etc.

The discovery of chemical shift in 1950s [7; 8] made NMR a powerful tool for characterization of molecular structure, where differences in the chemical environment of a nucleus gives distinct NMR spectrum. Another major discovery made during those times was the observation of splitting in the resonance peaks between $^{19}F$ and $^{31}P$ nucleus, in the solution-state NMR [9]. It was interpreted that the scalar spin-spin coupling was responsible for the splitting observed in the spectrum. The spin-spin coupling made NMR spectra very complicated during its initial observation, but later it was identified as a major tool for structural characterization in NMR spectroscopy. Therefore, chemical shift (CS) and spin-spin coupling ($J$) interactions are two indispensible tools for structural analysis in NMR spectroscopy.

In the early days of NMR, the data collection was very time consuming process due to the slow scanning rate that was employed and the technique is known as the continuous wave (CW) NMR. When Ernst and Anderson introduced the Fourier Transform technique for transforming the time domain signal into frequency domain signal in 1966 [10], it became a major milestone in the development of NMR spectroscopy. Introduction of Fourier transform spectrometer, super conducting

magnets and computer controlled pulse programming made NMR spectrum acquisition faster, easier and consistent. Another breakthrough in NMR was made by Ernst and group, when they introduced two dimensional experiments for structural characterization in 1976 [11]. The introduction of two dimensional experiments has provided NMR spectroscopy a window for the development of new n-dimensional experiments. The major advantages of Fourier Transform spectroscopy compared to the CW methods are its high resolution and low experimental time requirement.

The two dimensional (2D) spectroscopy has simplified the structural assignments of molecules in solution-state NMR. Correlation Spectroscopy (COSY) was one of the 2D experiment introduced in NMR, which uses two one dimensional experiments in perpendicular axes for structure assignments [12; 13]. A cross contour peak between two 1D peaks indicates the through bond proximity of corresponding nuclei in the molecule and hence used for structural assignments in COSY. Double quantum filtered COSY (DQF-COSY) technique which was introduced later has the advantage of observing the cross peaks with suppressed diagonal peaks and the spectrum becomes simple for analysis compared to the COSY experiment [14; 15]. Both these techniques give only two bond coupling information in the molecules. Total correlation spectroscopy (TOCSY) was introduced into solution-state NMR with the intention of obtaining 3, 4, 5 etc. bond coupling information and hence gave a full structural network information about the molecules [16]. Nuclear Overhauser effect spectroscopy (NOESY) and rotating frame nuclear Overhauser effect spectroscopy (ROESY) which were developed during that time gave the spatial proximity information between the nuclei and hence conformation analysis of molecules were made possible [17; 18]. Among this ROESY has advantage over NOESY in terms of molecule size which can be observed. ROESY is applicable to small, intermediate and large sized molecules, while NOSEY has a restriction towards intermediate size molecules which gives zero NOE. Introduction of heteronuclear techniques such as heteronuclear single quantum correlation (HSQC) [19], heteronuclear multiple quantum correlation (HMQC) [20] and heteronuclear multiple bond correlation (HMBC) [21] widened the scope of solution-state NMR for structural characterizations. HSQC and HMQC monitor single bond and HMBC uses 2 or 3 bond hetero nuclei correlation information. The 2D experiments mentioned

above along with the 1D experiment gives a complete picture about the molecular structure in solution-state NMR.

Introduction of density matrix and product operator formalism gave quantum mechanical understanding to different NMR experiments and simulation tools developed based on this gave theoretical understanding to different experiments before they were implemented into the spectrometer [22-24]. For structure characterization and secondary structure information several 3D experiments have been developed for peptides and proteins, while MRI has extended NMR spectroscopy into the field of medical science for diagnosis of disease, study of brain function etc. MRI is an area in NMR where expertise are pooled from different scientific fields such as physics, chemistry, biology, electronics and medicine.

Solid-state NMR has also grown along with solution-state NMR, where the main focus of the experiments was the measurement of properties in the solid phase. Presence of anisotropic interaction such as chemical shift anisotropy, dipole-dipole interaction and quadrupolar interaction make solid-state NMR spectrum very broad. Introduction of Magic angle spinning (MAS) by Andrew *et al.* in 1959, where the sample was spun at an angle of $54.74^{o}$ with respect to the external magnetic field narrowed the broadening caused by anisotropic interaction in solid-state NMR [25]. Using free induction decay (FID) and frequency domain spectrum, Lowe *et al.* in 1958 demonstrated a narrowing in the $^{19}F$ spectrum of powdered $CaF_2$ and Teflon, when the sample was spun at the magic angle [26; 27]. The magic angle spinning drastically improved the resolution of solid-state NMR spectra, but low sensitivity of the peaks remained as a major problem. Pines *et al.* in 1973 introduced the cross polarization (CP) technique into organic solids for sensitivity enhancement of rare $^{13}C$ nuclei by transferring magnetization from abundant $^{1}H$ nuclei [28]. The first CP experiment was on a static sample; hence resolution enhancement achieved by magic angle spinning was missed in the experiment. Schaefer and Stejskal in 1976 merged magic angle spinning with cross polarization and high power decoupling for sensitivity and resolution enhancement in solid-state $^{13}C$ spectrum of polysulfone polymers [29].

The introduction of magic angle spinning, cross polarization and high power decoupling gave high resolution to solid-state NMR spectra, but this resolution is

achieved by sacrificing different anisotropic interactions, which provide information about inter nuclear distance, bond angle, and molecular dynamics. Different recoupling techniques have been introduced in NMR which disturbs specifically the averaging of anisotropic interaction caused by magic angle spinning and high power decoupling. Rotary Resonance Recoupling (RRR) proposed by Oas *et al.* [30] and Rotational Echo Double Resonance (REDOR) proposed by Gullion *et al.* [31] are two early hetero-nuclear dipolar recoupling techniques that were introduced for obtaining bond distance information in solid-state NMR. In 1989, Tycko *et al*. introduced a 2D experiment with magic angle spinning for the reintroduction of undistorted CSA pattern in complex systems, where site specific CSA pattern separation became possible [32].

Internal spin interactions such as CSA and hetero-nuclear dipolar coupling give valuable information about the molecular structure and dynamics in systems such as polymers, and proteins. Hence development of new techniques which recouple these interactions efficiently and without distortion from static line shape pattern was a major challenge in solid-state NMR spectroscopy.

Towards the end of 1980s, Deuterium experiments and $^{13}C$ exchange experiments became the major techniques for the determination of segmental and functional group motions in polymers [3; 33-35]. The characteristic line shapes and ridges observed in these experiments give the geometry of the polymer chain dynamics. Isotope labeling on commercial polymer samples was a major limitation of Deuterium NMR experiments while relatively long experimental time required for exchange experiments was the drawback of $^{13}C$ based exchange experiments. Techniques such as total suppression of spinning sideband (TOSS) exchange [36], one-dimensional exchange spectroscopy by sideband alteration (ODESSA) [37], time reverse ODESSA (tr-ODESSA) [38], selectivity by destruction of magnetization-ODESSA (SELDOM-ODESSA) [39], and phase adjusted spinning side band time reversed ODESSA (PATROS) [40] are 1D experiments introduced later, which uses spinning side band intensity for obtaining information about the dynamics. However, for accurate information about the dynamics, a few spinning sidebands are required in the spectrum which is not achieved for systems with low CSA values. This was a major drawback of these sequences for determining dynamics in polymers with small chemical shift anisotropy. In the early 2000s, Center Band Only detection of

Exchange(CODEX), a one dimensional technique was introduced by Schmidt-Rohr and group for probing dynamics in polymers [41], where the measurement of dynamics is made possible by observing the central band intensity of the peak by varying the mixing time. The CODEX experiment uses chemical shift anisotropy (CSA) for probing the slow dynamic in polymers. In this thesis the CODEX experiment have been used for measuring slow segmental motions in three different polymers.

Schaefer *et al.* introduced the Dipolar Rotational Spin-Echo experiments (DRSE) for measuring hetero-nuclear dipolar coupling and used this for extracting information about dynamics in polymers [42; 43]. Mei Hong *et al.* demonstrated the Lee-Goldberg based Separated local Field Experiment (SLF) for the determination of hetero nuclear dipolar coupling with simultaneous suppression of homo-nuclear dipolar coupling interaction [44]. They applied this technique to polymers and proteins for extracting information about dynamics. An SLF Experiment called polarization inversion spin exchange at magic angle (PISEMA) was developed by Wu *et al.* for recoupling hetero-nuclear dipolar coupling in single crystals in 1994 [45]. This technique was extended to magic angle spinning samples by Dvinskikh *et al.* in 2003 [46]. In this thesis PISEMA experiment developed by Dvinskikh *et al.* has been used for obtaining information about the fast dynamics which are of the order of hundreds of kHz and for obtaining dynamic heterogeneity information in different polymers.

Malcolm Levitt introduced a general recoupling scheme called symmetry based pulse sequences for the reintroduction of internal spin interactions which are averaged during magic angle spinning [47-49]. There are several sequences that are possible which can reintroduce specific internal spin interactions making it fascinating for many applications. In the thesis, symmetry based CSA recoupling sequences have been used for the development of new CODEX experiments.

### 1.1.1. Basics of NMR

Nuclear magnetic resonance spectroscopy is made possible by the detection of nuclear spin magnetization, due to the transfer of nuclear spin from a higher energy state to lower energy state, where the initial non-equilibrium state is created by radio frequency irradiation on the spin system which is kept in an external magnetic field. A

detailed discussion on the principles of NMR are presented in monographs written by A. Abragam [50], R. R. Ernst *et al.* [22] and Malcolm H. Levitt [1].

All nuclei posses an intrinsic property called nuclear spin which is inherent to the atom. The spin of the nuclei is determined by the sum of proton and neutron spin quantum numbers. Nuclei that have nuclear spin greater than zero ($I$>0) is NMR active. Most of the nuclei in organic molecules such as $^{1}$H, $^{13}$C, $^{15}$N, $^{31}$P etc have spin quantum number ½ and are NMR active. Nuclei like $^{2}$H, $^{14}$N, $^{17}$O, $^{11}$B that have $I$>½ are called quadrupolar nuclei. Nuclei such as $^{12}$C, $^{16}$O, $^{56}$Fe etc. have nuclear spin $I$=0 and are therefore NMR inactive. The magnetic moment of the nuclei with nuclear spin $I$ is given by the expression

$$\mu = \gamma I \tag{1.1}$$

Where $\gamma$ is called the gyro magnetic ratio which is a constant for each nucleus. $^{1}$H has a $\gamma$ of 267.52*10$^{6}$ $rad\ s^{-1}T^{-1}$, while $^{13}$C has a γ of 67.28*10$^{6}$ $rad\ s^{-1}T^{-1}$, which is ¼$^{th}$ that of $^{1}$H. The $z$ component of the spin angular momentum is given by the equation

$$I_z = m\hbar \tag{1.2}$$

where $m$ is called the spin quantum number and takes values from $-I, -I+1, \ldots 0 \ldots, +I$ with a total of $(2I+1)$ states. In the absence of an external magnetic field, these energy levels are degenerate. Generally, the external magnetic field is considered to be applied along the $z$ axis of the Cartesian coordinate system and it is called the lab frame. In the presence of an external magnetic field $B_0$, the nuclei will try to align with the external field. The total energy of interaction between spin magnetic moment and external magnetic field is expressed by the equation

$$E = -\mu B_o = -m\hbar\gamma B_0 \tag{1.3}$$

In case of a spin ½ nuclei such as $^{1}$H and $^{13}$C, the energy levels split into two, the one with lower energy called $|\alpha\rangle$ state or (+½), where the spin align with the external magnetic field and the other with the higher energy is called the $|\beta\rangle$ state or (-½), where the spin is aligned opposite to the external magnetic field. The splitting of energy levels for spin ½ nuclei in the presence of external magnetic field is shown in the figure 1.1.

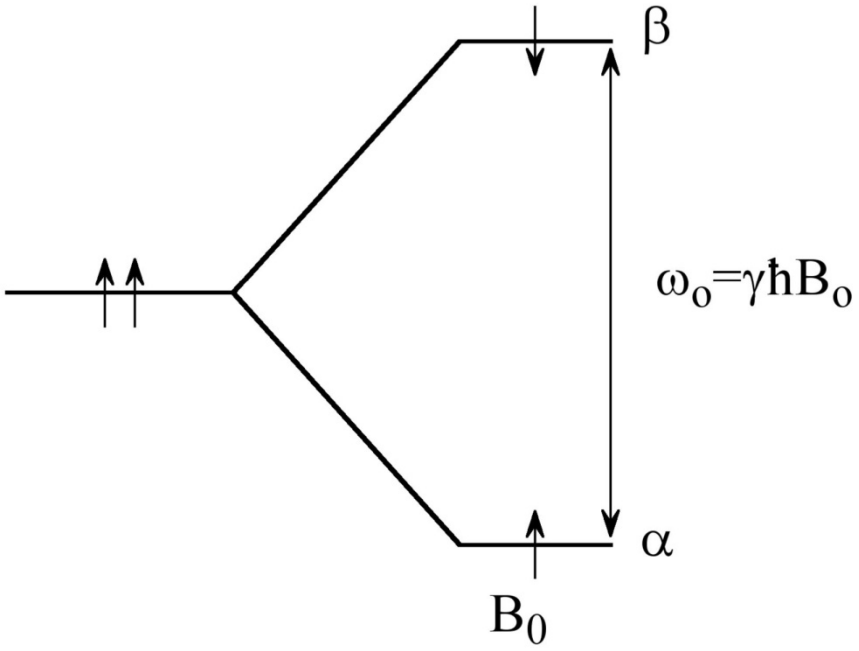


*Figure 1.1: Energy level diagram of a spin ½ nuclei in the presence of an external magnetic field, $B_0$. The energy level is split into two: $|\alpha\rangle$ and $|\beta\rangle$. The frequency of spin precession $\gamma\hbar B_o$ is equal to the energy gap between the spin levels.*

The energy of each level +½ and -½ is defined according to the above equation which is given by

$$E_{\pm 1/2} = \mp\frac{1}{2}\hbar\gamma B_0 \tag{1.4}$$

The spin with +½ spin quantum number is aligned with the external magnetic field, hence have a lower energy which is indicated by a negative value in the equation. It is opposite in the case of the spin with the spin quantum number -½. The energy difference between these two states is given by $\Delta E = \hbar\gamma B_0$. The nuclear spin precesses around the external magnetic field with a constant frequency called larmour frequency and the precession is called the larmour precession. The larmour precession frequency is given by $\omega_0 = -\gamma\hbar B_0$. The frequency of precession is determined by the gyromagnetic ratio, which is a constant for each nucleus, and the external magnetic field. From this equation it can be seen that nuclei with positive gyromagnetic ratio have a negative precession frequency while nuclei with negative gyromagnetic ratio have a positive precession frequency.

The state of the spin system in the presence of external magnetic field is called the thermal equilibrium state. When the spin system is at equilibrium, there is a

population difference between the upper and lower energy states and is expressed by the Boltzmann equation as

$$\frac{n_\beta}{n_\alpha} = \exp\left(-\frac{\Delta E}{KT}\right) \tag{1.5}$$

where $n_\alpha$ and $n_\beta$ are the number of spins in the $\alpha$ and $\beta$ states, $KT$ is the equilibrium thermal energy and $\Delta E$ is the energy of the precession $\omega_0$. The population difference between the two energy states is determined by three factors: external magnetic field, gyromagnetic ratio and the temperature. This population difference between the energy levels is manipulated for signal detection in NMR spectroscopy.

In the presence of the external magnetic field, the net magnetization generated in the longitudinal axis is very small compared to applied field and measuring this is impractical. Radio frequency (RF) pulses which are applied through the transverse plane are used to transform the longitudinal magnetization into the transverse plane for signal detection in NMR. After the application of the RF pulse, the magnetization relaxes back to the thermal equilibrium state through two relaxation processes: longitudinal relaxation (spin lattice relaxation [$T_1$]) and transverse relaxation (spin-spin relaxation [$T_2$]).

**Longitudinal relaxation ($T_1$):** After application of the RF pulse, the magnetization, in the $xy$ plane is in a coherent state, the state where all the spins are aligned in one direction. The spins in the coherent state goes back to the equilibrium state by the relaxation process called longitudinal relaxation. The longitudinal relaxation time is the time taken by the nuclear spin magnetization in the $xy$ plane to reach the direction of external magnetic field *ie.* time taken by the nuclear spins in the non-equilibrium state to reach the equilibrium state. The $T_1$ relaxation process is expressed by the Bloch equation

$$M(t) = M_{equ.}\left(1 - \exp\left(-\frac{t}{T_1}\right)\right) \tag{1.6}$$

where $M(t)$ is the magnetization at a time $t$ during free evolution, while $M_{equ.}$ is the equilibrium magnetization before the application of RF pulses.

**Transverse relaxation ($T_2$):** Transverse relaxation time is the time taken by coherent magnetization in the $xy$ plane to be completely decoherent. The Bloch equations for the Transverse relaxation are given by

$$M_y(t) = M_{equ.}\cos(\omega_0 t)\left(1 - \exp\left(-\frac{t}{T_2}\right)\right) \tag{1.7a}$$

$$M_x(t) = M_{equ.}\sin(\omega_0 t)\left(1 - \exp\left(-\frac{t}{T_2}\right)\right) \tag{1.7b}$$

The coherent NMR signal decay in the $xy$ plane though $T_2$ relaxation and the decay is named as free induction decay (FID). It is expressed by a complex function of sine and cosine function and is detected by coils which are placed in the $xy$ plane. The FID obtained in the time domain signal is converted into frequency domain by the process called Fourier Transformation (FT). Mathematically FT is expressed by the expression

$$S(\omega) = \int_{-\infty}^{+\infty} s(t)\exp(-i\omega t)\,dt \tag{1.8}$$

where $S(\omega)$ is the spectrum represented in the frequency domain while $s(t)$ is the spectrum in the time domain. The schematic representation of FT is shown in figure 1.2

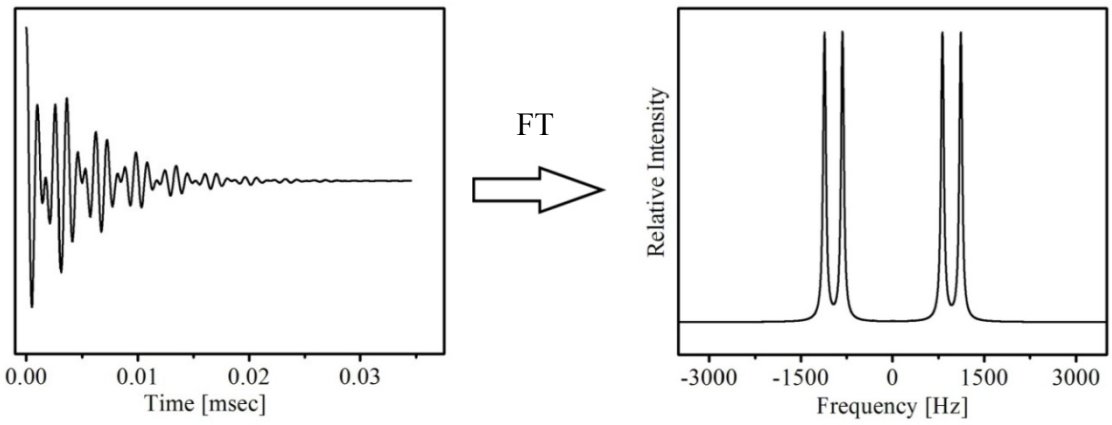


*Figure 1.2: The schematic representation of Fourier transform of time domain signal into frequency domain spectrum.*

As seen in the figure above, frequency domain spectrum discriminates different nuclei based on its resonance frequency (chemical environment and $J$-coupling), which is easy to analyze while in time domain spectra the FID is a sum of all the signals together, hence a distinction between chemical sites is difficult.

### 1.1.2. Solid-state NMR

The non-averaged anisotropic interactions in solid samples make the solid-state NMR spectrum very broad with poor resolution. But the anistotropic interactions in the solid-state NMR are rich in information about the system under study. Chemical shift anisotropy gives atomic orientation information in a molecule while dipolar coupling give both orientation and distance information. These anisotropic interactions are measured directly or indirectly using specialized pulse sequences and are used to determine information about structure, geometry and dynamics [51].

The interactions in NMR are divided into two, external spin interactions and internal spin interactions. In internal spin interactions, the nuclear spins are influenced by the magnetic field originated from the same or nearby molecules while in external spin interaction the spins are influenced by external sources. The total Hamiltonian of NMR interactions can be expressed as

$$H_{total} = H_{ext} + H_{int} \tag{1.9}$$

The external spin interactions is a sum of Zeeman and RF irradiation while internal spin interactions are the sum of chemical shift anisotropy, $J$-coupling, dipolar coupling, quadrupolar coupling etc.

$$H_{total} = H_0 + H_{rf} + H_{CS} + H_J + H_{DD} + H_Q \tag{1.10}$$

Among these, Zeeman interaction, RF irradiation, isotropic chemical shift and $J$-coupling are common to solution and solid-state NMR. The chemical shift anisotropy, the dipole-dipole interaction and the quadrupolar interaction are averaged to zero in the solution-state while in solid-state these interactions survive. Each of these interactions are explained below.

#### 1.1.2.1. Zeeman interaction and radio frequency field ($\mathbf{H_o}$ and $\mathbf{H_{RF}}$)

Zeeman interaction is the interaction of nuclear spin magnetic moment with the external magnetic field. The Hamiltonian of the Zeeman interaction is given by

$$H_0 = -\gamma\hbar B_0 I_z = \omega_0 I_z \tag{1.11}$$

where $\omega_0$ is the larmour frequency of the observing nuclei. This is the largest interaction in NMR. When an external RF field is applied to the spin system which is

present at the equilibrium Zeeman state, the total Hamiltonian is expressed by the equation

$$H = \omega I_z - \omega_1 (I_x \cos \omega t + I_y \sin \omega t) \quad (1.12a)$$

$$= \omega I_z - \omega_1 \exp(-i\omega t I_z/\hbar)\, I_x \exp(+i\omega t I_z/\hbar) \quad (1.12b)$$

where $\omega_1$ is the amplitude of the RF field, given by the expression $\omega_1 = -\gamma\hbar B_1$ and $\omega t$ is its phase. Quantum mechanically, the state of the spin system is obtained by the solution of the Schrodinger equation. The Schrodinger equation for a spin system under the influence of external magnetic field and RF pulse is given by the equation

$$i\hbar \frac{d}{dt}\Psi(t) = H(\mathrm{t})\Psi(t) \quad (1.13)$$

where $\Psi(t)$ represents the state of the spin which contain all the information about the system and $H(\mathrm{t})$ is the Hamiltonian which is given in equation 1.12, which is time dependent. Solving this Schrodinger equation is not easy because the Hamiltonian is time dependent and it become very complicated in the presence of external RF field. A mathematical technique has been introduced in NMR for removing the time dependence of the Hamiltonian, where the nuclear spin is viewed from a reference frame which precess at the larmour frequency with respect to the $z$-axis. This reference frame is called the rotating frame. The transformation of the wave function from the lab frame to the rotating frame is expressed mathematically by

$$\tilde{\Psi} = \mathrm{e}^{\mathrm{i}\omega \mathrm{t} \mathrm{I}_z/\hbar}\Psi(\mathrm{t}) \quad (1.14)$$

where $\tilde{\Psi}$ represents the wave function in the rotating frame. Inserting this into the time dependent Schrodinger equation (equation 1.13) and on rearranging, a time independent Schrodinger equation is generated which is expressed as

$$i\hbar \frac{d}{dt}\tilde{\Psi} = \tilde{H}\tilde{\Psi} \quad (1.15)$$

where, the Hamiltonian in the rotating frame is given by

$$\tilde{H} = \mathrm{e}^{\mathrm{i}\omega \mathrm{t} \mathrm{I}_z/\hbar}\, H(\mathrm{t})\mathrm{e}^{-\mathrm{i}\omega \mathrm{t} \mathrm{I}_z/\hbar} - \omega_0 \mathrm{I}_z \quad (1.16a)$$

$$\tilde{H} = -(\omega_o - \omega) I_z - \omega_1 I_x \quad (1.16b)$$

From equation (1.16) it can be seen that as $\omega$ reaches the larmour frequency ($\omega_o$), the first term of the equation vanishes and hence the spins start to precess about

$x$ axis with a frequency $\omega_1$. Therefore, the visualization of nuclear spin magnetization is easier in this frame.

In the actual NMR experiments, oscillating RF fields are used instead of rotating RF filed. The oscillating field has two components that rotate in opposite directions. Hence, the component which rotate in the same direction as the larmour frequency survive, while the component which rotate in the opposite direction with respect to the larmour frequency is neglected (equation 1.12).

### 1.1.2.2. Chemical Shift

In diamagnetic materials, the external magnetic field induces a circulation of electronic current around the nucleus. The circulation of electronic current generates a magnetic field around the nucleus which shields the nuclei from complete exposure to external magnetic field and this shielding is responsible for chemical shift. Nuclei having different chemical environment have different electronic environments and therefore different chemical shifts. As a result, chemical shift is used as a probe for molecular structure information in NMR. It has both isotropic and anisotropic components. In the Cartesian coordinate system, the chemical shift interaction can be represented by a 3 × 3 matrix. The Hamiltonian of the chemical shift interaction in an external magnetic field is give by the equation

$$H_{CS} = -\gamma\hbar * I.\delta.B^o \tag{1.17}$$
$$= -\gamma\hbar * (I_X \quad I_Y \quad I_Z).\begin{pmatrix}\delta_{XX} & \delta_{XY} & \delta_{XZ}\\ \delta_{YX} & \delta_{YY} & \delta_{YZ}\\ \delta_{ZX} & \delta_{ZY} & \delta_{ZZ}\end{pmatrix}.\begin{pmatrix}0\\0\\B_0\end{pmatrix}$$

where $\delta_{XZ}$ denotes the magnetic field induced in the x axis of nuclear spin interaction when the external magnetic field is applied along the Z axis and similarly for the other elements. In general, the CSA tensor is assumed to be symmetric and therefore $\delta_{XZ} = \delta_{ZX}$. The chemical shift tensor can be represented in a principle axis system, the reference system where non-diagonal elements vanishes and only diagonal elements survive. The orientation of the chemical shift tensor in the external magnetic field is shown in figure 1.3, where $\delta_{XX}$, $\delta_{YY}$ and $\delta_{ZZ}$ are the principle axis components of CSA tensor in the $X^{PAS}, Y^{PAS}, Z^{PAS}$ axis respectively.

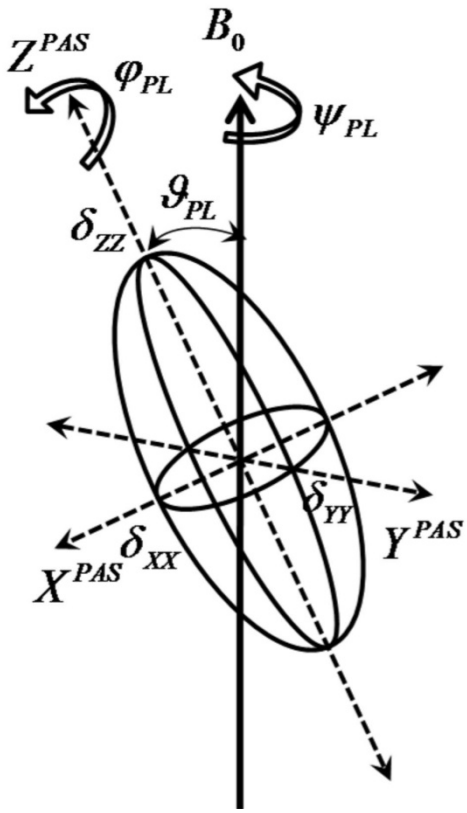


*Figure 1.3: The orientation of the chemical shift tensor in an external magnetic field, where $\delta_{XX}, \delta_{YY}$ and $\delta_{ZZ}$ are the principle axis components in $X^{PAS}, Y^{PAS}, Z^{PAS}$ axis respectively.*

The chemical shift tensor is represented by three parameters: isotropic chemical shift ($\delta_{iso}$), chemical shift anisotropy ($\delta_{aniso}$) and asymmetry parameter ($\eta$) and each of these parameters is defined as

$$\delta_{iso} = \frac{1}{3}(\delta_{XX} + \delta_{YY} + \delta_{ZZ}) \tag{1.18a}$$

$$\delta_{aniso} = \delta_{ZZ} - \delta_{iso} \tag{1.18b}$$

$$\eta = \frac{\delta_{YY} - \delta_{XX}}{\delta_{ZZ} - \delta_{iso}} \tag{1.18c}$$

By general convention, the principle values of the chemical shift tensor follow the order $|\delta_{ZZ} - \delta_{iso}| \geq |\delta_{XX} - \delta_{iso}| \geq |\delta_{YY} - \delta_{iso}|$. The mean of the principle value of the chemical shift tensor is known as the isotropic chemical shift. In solution-state NMR, due to the tumbling motion of molecules, the chemical shift anisotropy gets averaged out and only isotropic part of chemical shift interaction survives. Since the tumbling motions are absent in the solid-state, the anisotropic interaction survives and broad CSA patterns are seen in the NMR spectra. The difference between the

isotropic chemical shift and farthest principle axis value from isotropic value is called the chemical shift anisotropy ($\delta_{aniso}$). The ratio of the difference between $\delta_{YY}$, $\delta_{XX}$ and chemical shift anisotropy is called the asymmetry parameter ($\eta$). The value of ($\eta$) is defined in the range $0 \leq \eta \leq 1$. The value of $\eta$ determines the symmetry of the chemical shift tensor. For $\eta = 0$, the chemical shift tensor have cylindrical symmetry with respect to the axis $Z^{PAS}$ and for $\eta = 1$, the chemical shift tensor is completely unsymmetric.

In the principle axis frame, the CSA tensor is diagonal. But since the NMR measurements are carried out in the laboratory frame, the chemical shift tensor should be transformed from the principle axis frame to the laboratory frame. This frame inter conversion is done by Euler angles rotation defined by a combination of three angles ($\varphi_{PL}, \vartheta_{PL}, \psi_{PL}$), which is shown in figure 1.3. Among these, $\psi_{PL}$ is the angle of rotation of the CSA tensor with respect to the external magnetic field. Chemical shift Hamiltonian does not have any influence on the rotation of CSA tensor with respect to external magnetic field. Hence the angle $\psi_{PL}$ can be dropped from expression of the CSA Hamiltonian. The chemical shift Hamiltonian for a CSA tensor with respect to the laboratory frame is given by equation

$$H_{CS} = -\gamma\hbar(0 \quad 0 \quad I_z).R(\varphi,\vartheta).\begin{pmatrix}\delta_{XX} & 0 & 0\\ 0 & \delta_{YY} & 0\\ 0 & 0 & \delta_{ZZ}\end{pmatrix}.R(\varphi,\vartheta)^{-1}.\begin{pmatrix}0\\0\\B_0\end{pmatrix} \tag{1.19a}$$

$$= -\gamma\hbar I_z B_0(\delta_{XX}\, cos^2\varphi\, sin^2\vartheta + \delta_{YY}\, sin^2\varphi\, .sin^2\vartheta + \delta_{ZZ}\, cos^2\vartheta) \tag{1.19b}$$

$$= -\gamma\hbar I_z B_0(\delta_{iso} + \frac{1}{2}\delta_{aniso}[(3cos^2\vartheta - 1) + \eta\, sin^2\vartheta.cos2\varphi] \tag{1.19c}$$

$$= \omega(\varphi,\vartheta)I_z \tag{1.19d}$$

where the Euler angle rotation matrix which converts the CSA tensor from principle axis frame to lab frame is given by

$$R(\varphi,\vartheta) = \begin{pmatrix}cos\varphi.cos\vartheta & cos\varphi.sin\varphi & -sin\vartheta\\ -sin\varphi & cos\varphi & 0\\ cos\varphi.sin\vartheta & sin\varphi.sin\vartheta & cos\vartheta\end{pmatrix} \tag{1.20}$$

Different frames used in solid-state NMR for the transformation of internal spin interaction from the principle axis frame to the lab frame are explained in section 1.3.1. Equation 1.19c gives the Hamiltonian of the CSA tensor which is oriented in one particular angle with respect to the external magnetic field. In polycrystalline samples, there are millions of different orientations with respect to external magnetic

field and a powder average is needed to get the CSA line shape. The powder pattern of a poly crystalline sample is obtained by evaluation of equation 1.19c, by calculating the frequency for different $\varphi$ and $\vartheta$ over a sphere and then convoluting it with a line shape function. This is expressed mathematically by the equation

$$S(\omega) = \int_0^{2\pi} \int_0^{\pi} g[\omega - \omega(\varphi, \vartheta)].sin\vartheta.d\vartheta.d\varphi \tag{1.21}$$

where $\omega(\varphi, \vartheta)$ is the resonance frequency of spin defined by the equations 1.19c/1.19d and $g$ denotes the line shape function. Integration of the above equation gives the CSA line shape according to the CSA parameters used. The static CSA line shape for nuclei with $\eta = 0, 0.5, 1$ with positive $\delta_{aniso}$ is shown in figure 1.4.

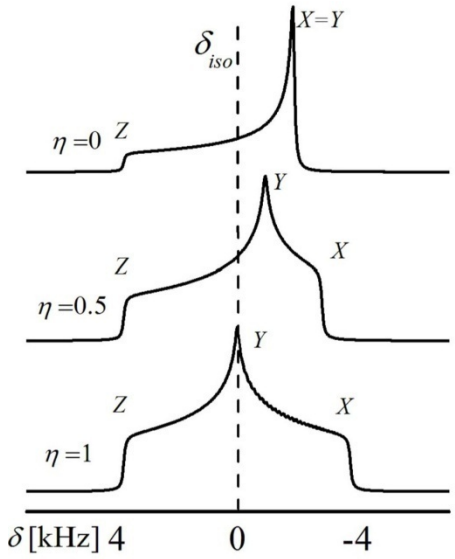


*Figure 1.4: The static CSA line shapes of a spin ½ nuclei in a powder sample with* $\eta = 0, 0.5, 1$. *The isotropic chemical shift is indicated by dashed line. All the CSA line shapes are simulated with a positive* $\delta_{aniso}$ *value.*

### 1.1.2.3. Direct dipole-dipole interaction

Direct dipole-dipole interaction is a through space interaction of two nuclei which are spatially close to each other. The strength of the dipolar coupling is determined by the magnetic moment of the nuclei, the inter nuclear distance and orientation of inter nuclear vector with respect to the external magnetic field. In solids the Brownian motions are absent and the anisotropic part of the dipolar coupling is observed as broad resonance peaks. The Hamiltonian of the dipole-dipole interaction between two magnetic dipoles is expressed by

$$\widehat{H}_{DD} = -\frac{\mu_0}{4\pi}\gamma_I\gamma_S\hbar\left(\frac{\hat{I}.\hat{S}}{r^3} - 3\frac{(\hat{I}.\hat{r})(\hat{S}.\hat{r})}{r^5}\right) \tag{1.22}$$

where $\gamma_I$ and $\gamma_S$ represents the gyromagnetic ratio of two interacting nuclei. The equation shows that the dipolar interaction is independent of the external magnetic field ($B_0$). It can be expressed in spherical polar coordinates using the transformation equations $x = rsin\vartheta.cos\varphi,\ y = rsin\vartheta.sin\varphi,\ z = rcos\vartheta$ and scalar product expansion. The polar angles that transform dipolar coupling to external magnetic field is represented in the figure 1.5

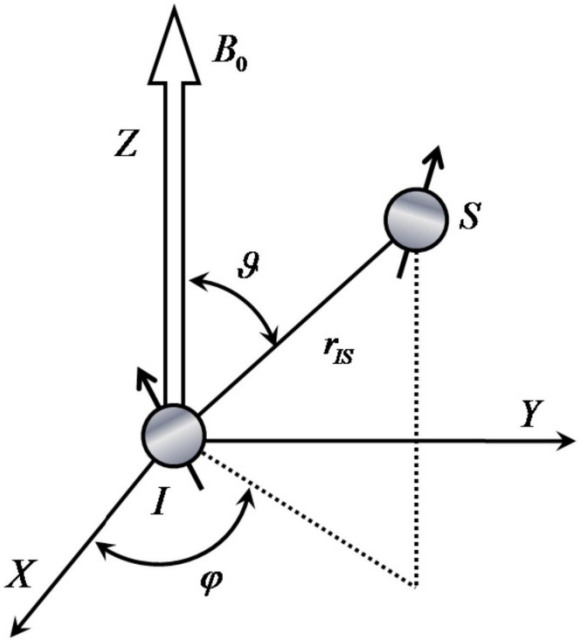


*Figure 1.5: The orientation of a dipole with respect to the external field.*

Substituting the transformation equations for polar coordinates into equation 1.22 and on rearranging, the Hamiltonian becomes

$$\begin{aligned}\widehat{H}_{DD} = -\frac{\mu_0\hbar}{4\pi}.\frac{\gamma_I\gamma_S}{r^3}[&\left(\hat{I}_z\hat{S}_z(3\,cos^2\vartheta - 1\right)\\ &-\tfrac{1}{4}\left(\hat{I}_+\hat{S}_- + \hat{I}_-\hat{S}_+\right)(3\,cos^2\vartheta - 1)\\ &+\frac{3}{2}\left(\hat{I}_Z\hat{S}_+ + \hat{I}_+\hat{S}_Z\right)\left(sin\vartheta.cos\vartheta.e^{-i\varphi}\right)\\ &+\frac{3}{2}\left(\hat{I}_Z\hat{S}_- + \hat{I}_-\hat{S}_Z\right)\left(sin\vartheta.cos\vartheta.e^{+i\varphi}\right)\\ &+\frac{3}{4}\left(\hat{I}_+\hat{S}_+\right)sin^2\vartheta.e^{-2i\varphi}\\ &+\tfrac{3}{4}\left(\hat{I}_-\hat{S}_-\right)sin^2\vartheta.e^{+2i\varphi}]\end{aligned} \tag{1.23}$$

where $\hat{I}_+, \hat{S}_+$ is the raising operators and $\hat{I}_-$, $\hat{S}_-$the lowering operators. The dipolar coupling constant of the interaction is expressed by the equation

$$d = -\frac{\mu_0 \hbar}{4\pi} \cdot \frac{\gamma_I \gamma_S}{r^3} \tag{1.24}$$

According to the nature of the nuclei involved in the interaction there are two types of direct dipole-dipole interaction: heteronuclear and homonuclear. In heteronuclear dipole-dipole interaction, when the Hamiltonian is transformed into the rotating frame only the first terms of equation 1.23 survives. The heteronuclear dipolar Hamiltonian in the rotating frame is given by the equation

$$\hat{H}_D^{I,S} = -\frac{\mu_0 \hbar}{4\pi} \cdot \frac{1}{2} \cdot \frac{\gamma_I \gamma_S}{r^3} (3cos^2\vartheta - 1) 2\hat{I}_z \hat{S}_z \tag{1.25}$$

The equation shows the interaction is coaxial to inter nuclear vector and is independent of the external magnetic field ($B_0$). It is inversely proportional to the cube of internuclear distance ( $r^3$) and hence is used as a probe for bond distance. Common hetero nuclei where dipolar interaction observed is between $^1$H and $^{13}$C, here a bond distance of 1.1 Å shows a heteronucler dipole-dipole coupling of 22.0 kHz. In solids different orientation of internuclear vector with respect to external magnetic field produces a dipolar line shape pattern called the Pake pattern. The dipolar powder pattern for a nucleus with a coupling constant 22.0 kHz is shown in the figure 1.6.

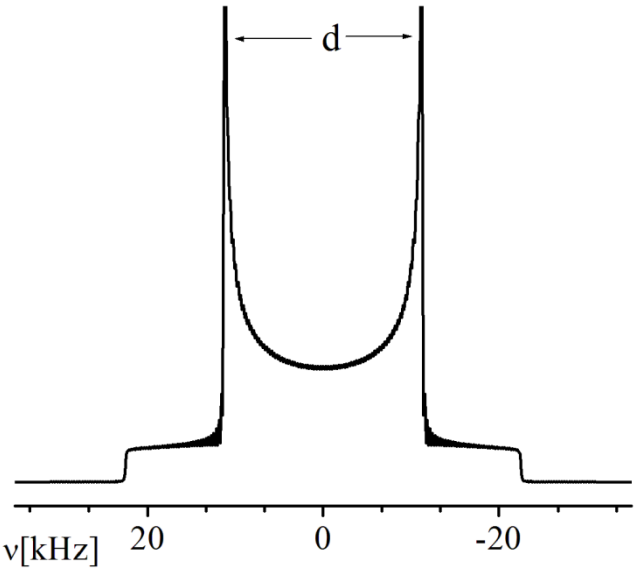


*Figure 1.6: The heterouclear dipole-dipole coupling line shape for a nucleus with a coupling constant of 22.0 kHz.*

In homonuclear dipolar interaction, when the Hamiltonian is transformed to the rotating frame, the first two terms of eq. 1.21 survives and remaining terms are averaged to zero. The homonculear dipole-dipole Hamiltonian is then express as

$$\begin{aligned}\widehat{H}_{DD} &= -\frac{\mu_0\hbar}{4\pi}.\frac{\gamma_I\gamma_S}{r^3}[\left(\hat{I}_z\hat{S}_z(3\,cos^2\vartheta-1\right)\\ &\quad -\tfrac{1}{4}\left(\hat{I}_+\hat{S}_- + \hat{I}_-\hat{S}_+\right)(3\,cos^2\vartheta-1)]\\ &= -\frac{\mu_0\hbar}{4\pi}\frac{1}{2}\frac{\gamma_I\gamma_I}{r^3}(3cos^2\vartheta-1)(3\hat{I}_z\hat{I}_z-\hat{I}.\hat{I})\end{aligned} \tag{1.26}$$

$^1$H-$^1$H dipolar coupling is a commonly observed in solid-state NMR. Nuclei having $^1$H-$^1$H distance of 1.77 Å has a dipolar coupling of 21.5 kHz.

### 1.1.2.4. Scalar coupling (*J*)

The scalar coupling is also called the through bond coupling or indirect coupling where magnetically active nuclei interact through intervening chemical bonds. This interaction is mediated through the electrons which come across the bonds. The heteronuclear *J*-coupling interaction Hamiltonian is given by

$$\widehat{H}_J^{I,S} = -2\pi\, J_{IS}\, \hat{I}.\hat{S} \tag{1.27}$$

where $J_{IS}$ is the heteronuclear *J*-coupling constant. The homonuclear *J*-coupling interaction Hamiltonian is given by

$$\widehat{H}_J^{I,I} = -2\pi\, J_{II}\, \hat{I}.\hat{I} \tag{1.28}$$

The *J*-coupling interaction is very small in comparison to other internal spin interactions and usually is of the order of a few 100s of Hz. In the solution-state, all the anisotropic interactions average out due to Brownian motions, hence *J*-coupling is observed as a splitting in the isotropic chemical shift. However, in the solid-state, the *J*-coupling is suppressed inside the direct dipolar interaction which usually is of the order of 10-22.5 kHz. The large value of direct dipolar coupling attenuates the possibility for detection of scalar coupling in solid-state NMR. However, introduction of 2D experiments such as COSY, HSQC etc from solution-state NMR and mechanical sample spinning made possible the measurement of *J*-coupling in solid-state NMR. Experiments such as insensitive nuclei enhanced by polarization transfer (INEPT) [52], *J*-resolution by 2D [53], HMQC [54] are used for the heteronuclear *J*-coupling information while experiments such as incredible natural-abundance double-

quantum transfer experiment (INADEQUATE) [55], TOCSY [56] etc are used for the homonuclear $J$-coupling information.

### 1.1.2.5. Quadrupolar interaction

Quadrupolar interaction is observed in nuclei whose spin quantum number is greater than ½ (I> ½). It originates from the interaction of the nuclear quadrupolar moment with the surrounding electric field gradient (EFG) tensor, and the coupling observed is called the nuclear quadrupolar coupling [51; 57]. Nuclear quadrupolar coupling is a function of both nuclei (nuclear quadrupolar moment) and electric field environment (EFG). The quadrupolar Hamiltonian in the Cartesian coordinate system is given by

$$\widehat{H}_Q = \frac{eQ}{6I(2I-1)\hbar} \sum_{\alpha,\beta=x,y,z} V_{\alpha\beta}[\frac{3}{2}(\hat{I}_\alpha \hat{I}_\beta + \hat{I}_\beta \hat{I}_\alpha) - \delta_{\alpha\beta}\hat{I}^2] \tag{1.29}$$

where $\delta_{\alpha\beta}$ is the Kronecker delta function, $V_{\alpha\beta}$ is the component of the electric field gradient tensor and $eQ$ is called the nuclear quadrupolar moment. The mathematical representation of electric field gradient tensor in the principle axis system is given by

$$V = \begin{pmatrix} V_{xx} & 0 & 0 \\ 0 & V_{yy} & 0 \\ 0 & 0 & V_{zz} \end{pmatrix} \tag{1.30}$$

The EFG tensor elements follow the convention $V_{zz} \geq V_{yy} \geq V_{xx}$. In the quadrupolar interaction, the sum of principle values of EFG tensor is zero ie. $V_{xx} + V_{yy} + V_{zz} = 0$. Hence, isotropic component does not exist in the quadrupolar interaction. The two important parameters in quadrupolar interactions are the anisotropy and asymmetry which is expressed as

$$eq = V_{zz} \tag{1.31a}$$

$$\eta = \frac{V_{xx} - V_{yy}}{V_{zz}} \tag{1.31a}$$

where the asymmetry parameter takes values in between 0 and 1. When the EFG is in the principle axis frame, the quadrupolar Hamiltonian in the Cartesian co-ordinate system is given by the equaiton

$$\widehat{H}_Q = \frac{e^2qQ}{4I(2I-1)\hbar}) \sum_{\alpha,\beta=x,y,z} [3\hat{I}_z^2 - \hat{I}^2 + \eta(\hat{I}_x^2 - \hat{I}_y^2)] \tag{1.32}$$

where the quadrupolar coupling constant of the nucleus is defined as $C_q = e^2qQ$. The quadrupolar coupling may vary from few 10s of kHz to 10s of MHz depending on the

strength of quadrupole moment and electric field gradient tensor. For example, $\alpha - Al_2O_3$ have an octahedral structure, with aluminum having a quadrupolar coupling constant of the order of ~1.2 MHz.

The transformation of the quadrupolar Hamiltonian from the PAF to LF is done using the two polar angles $\varphi$ and $\theta$. The Quadruplar Hamiltonian is given by

$$\hat{H}_Q = \frac{e^2qQ}{4I(2I-1)\hbar})\left(3\hat{I}_z^2 - \hat{I}^2\right)[\frac{1}{2}(3cos^2\vartheta - 1) + \eta\, sin^2\vartheta.cos2\varphi] \tag{1.33}$$

About 74% of NMR active nuclei in the periodic table are quadrupolar in nature. In a quadrupolar system, each transitions from $m$ to $m \pm 1$ state results in a resonance peak in the spectrum. Based on the spin number of the nuclei, the quadrupolar interaction is divided into two, they are half-integer spin (spin is integral multiple of ½) and integer-spin (spin is integral multiple of 1) quadrupolar interaction. Nuclei such as $^{7}$Li, $^{11}$B, $^{23}$Na (3/2 spin system), $^{27}$Al, $^{25}$Mg (5/2 spin system), $^{51}$V (7/2 spin system) have half-integer spins. When quadrupolar coupling constant is of the order of MHz, Zeeman energy levels need correction with both 1$^{st}$ and 2$^{nd}$ order quadrupolar interaction. Figure 1.7 shows the energy level splitting diagram of $^{27}$Al,

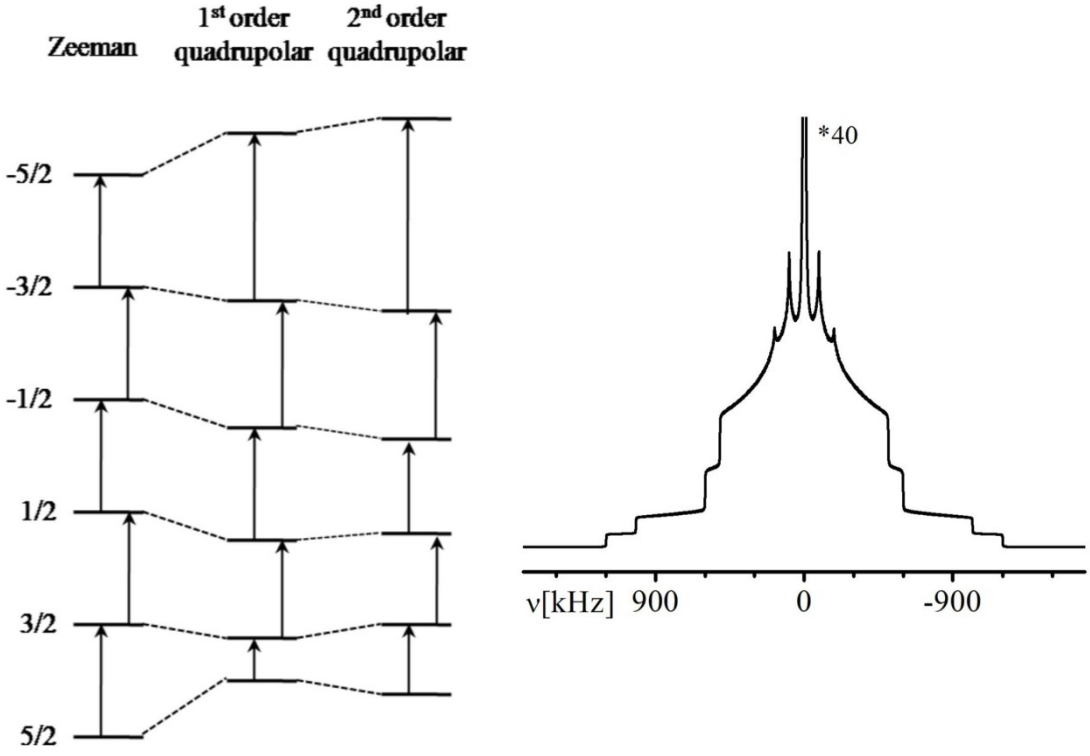


*Figure 1.7: The energy level diagram (left) and corresponding simulated static spectrum (right) of $^{27}$Al nuclei, a 5/2 spin system with a quadrupolar coupling constant of 3.0 MHz in 800 MHz spectrometer.*

the 5/2 spin system, in presence of Zeeman, 1st and 2nd order quadrupolar interaction and corresponding simulated quadrupolar line shape obtained with a coupling constant of 3.0 MHz in a 800 MHz spectrometer.

Nuclei such as $^{2}H$, $^{6}Li$, $^{14}N$ (spin system-1), $^{3}B$ (spin sytem-3) etc. have integer-spins. Among these $^{2}H$ nuclei is used in solid-state NMR experiments for obtaining information about polymer dynamics. The $^{2}H$ quadrupolar coupling constant has a maximum value of 250 kHz, hence the line shape of spectra is determined by only first order quadrupolar interaction. In organic molecules, $^{2}H$ quadrupolar interaction have cylindrical symmetry ($\eta = 0$) hence deuterium spectrum gives a symmetric quadrupolar pattern. The Energy level diagram and corresponding static quadrupolar line shape obtained for $^{2}H$ nuclei with a quadrupolar coupling constant of 250 kHz in a 300 MHz spectrometer is shown figure 1.8

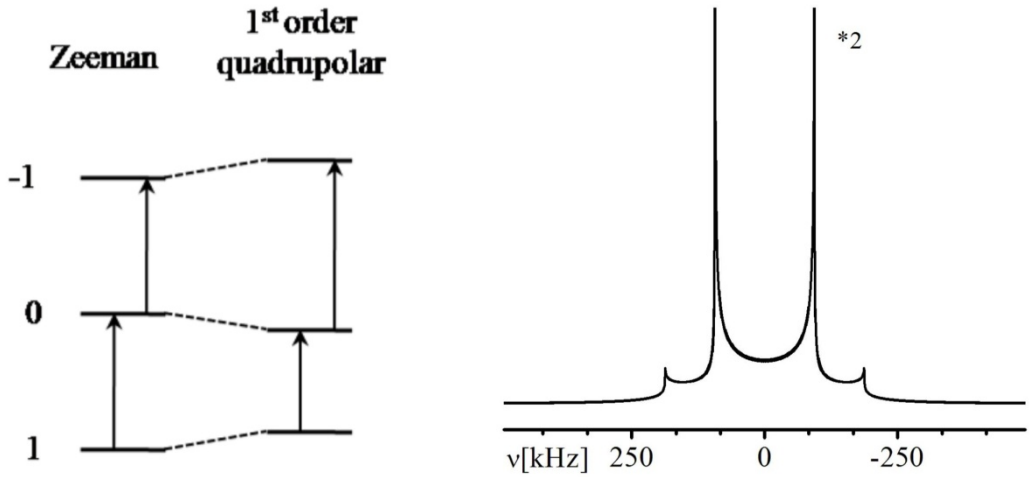


*Figure 1.8: The energy level diagram (left) and corresponding simulated static spectrum (right) of $^{2}H$ nuclei, a spin-1 system with a quadrupolar coupling constant of 250 kHz in 300 MHz spectrometer.*

### 1.1.3. Magic angle spinning

In solution-state NMR, the anisotropic interactions are averaged by fast tumbling motions of the molecules inside the solvent. When the tumbling rates are faster than the width of nuclear spin interactions, a narrow spectrum is generated. In the solid-state, the tumbling motions of molecules are absent; hence the anisotropic interactions survive resulting in a broad NMR spectrum. Andrew and Lowe [25] introduced mechanical spinning technique called Magic Angle Spinning (MAS) for resolution enhancement in solid-state NMR, where the sample is spun at an axis inclined $\vartheta_m = 54.74^{o}$ with respect to the external magnetic field. With magic angle

spinning, sharp peaks similar to that of solution-state are achieved in solid-state NMR. MAS achieve this by averaging the anisotropic part of different internal spin interactions such as chemical shift, direct dipole-dipole coupling etc. The schematic representation of magic angle spinning setup is shown in figure 1.9.

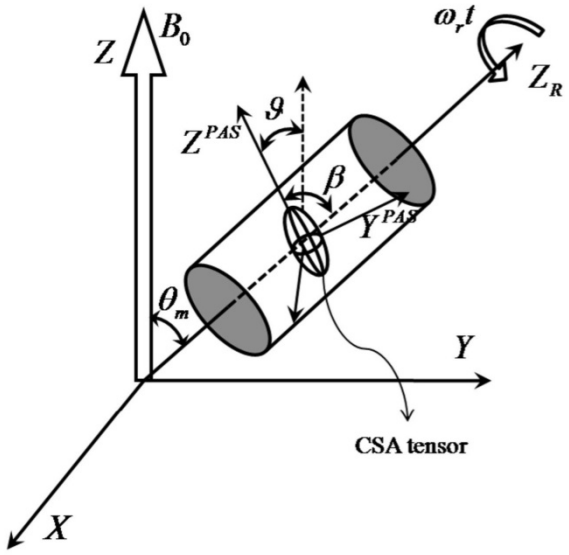


*Figure 1.9: Schematic representation of a magic angle spinning setup in solid-state NMR, where the rotor is kept at an angle of 54.74$^o$ with respect to the external magnetic field and spun with a frequency of $\omega_r$ for averaging the different anisotropic interaction.*

The orientation dependence of nuclear spin interaction in an external magnetic field has terms of the form $(3cos^2\vartheta - 1)$ as seen in equation 1.19. In a powder sample, each nuclei have different orientation $\vartheta$ with respect to the external magnetic field and therefore results in the powder pattern under static condition. If the sample is spun at an angular velocity $\omega_r$ at an angle $\vartheta_m$ inclined with respect to the external magnetic field, the CSA tensor orientation $\vartheta$ changes continuously. The transformation of single chemical shift tensor from principal axis system into the lab frame through an intervening rotor spinning axis is given by the equation

$$\cos\vartheta = \cos\beta \,.\cos\vartheta_m + \sin\beta \,.\sin\vartheta_m \cos\omega_r t \qquad (1.34)$$

where $\beta$ is the angle between $Z^{PAS}$ of CSA tensor and $Z^R$ while $\vartheta$ is the angle between $Z^{PAS}$ and the external magnetic field. Due to the mechanical spinning, the value of $\vartheta$ changes continuously and the average value of $(3cos^2\vartheta - 1)$ term can be represented by the equation

$$\langle 3cos^2\vartheta - 1\rangle = \frac{1}{2}(3cos^2\vartheta_m - 1)(3cos^2\beta - 1) \tag{1.35}$$

In Solid-state NMR the angle $\vartheta_m$ is usually kept at $54.74^0$. At this angle the equation 1.35 averages to zero resulting in the narrowing of NMR spectrum. But this happens only when the sample is spun with a spinning speed greater than the width of the anisotropic interaction. If the spinning speed is lower than the width of the anisotropic interaction, spinning side bands are obtained. The $^{13}C$ spectra obtained for a sample with definite CSA, at different spinning speeds is shown in figure 1.10. It can be seen that the spinning side bands are separated by sample spinning frequency and the separation between them increases as the spinning speed increases. The isotropic chemical shift does not change its position with spinning speed and therefore it can be easily identified by changing the spinning speed of the sample. As the spinning speed exceeds the width of chemical shift anisotropy, the spinning side bands disappear.

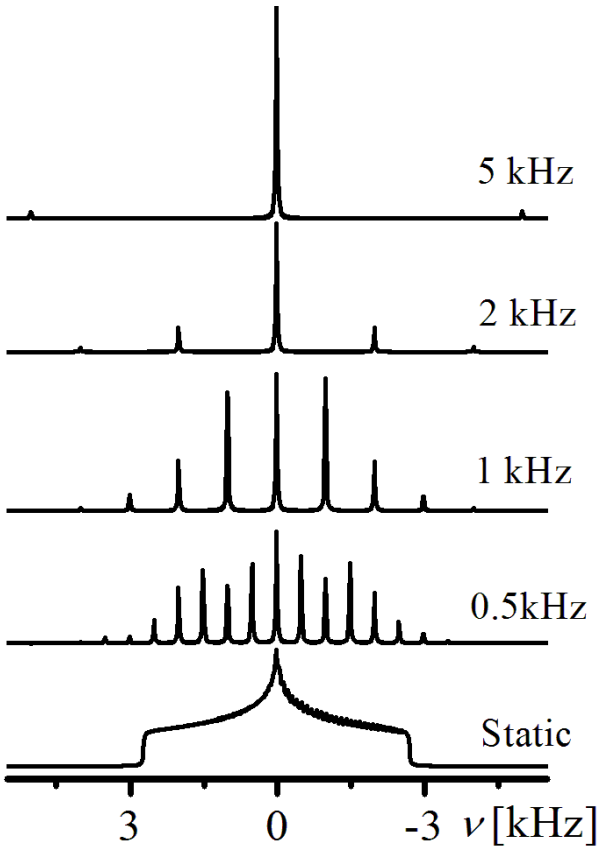


*Figure 1.10: The spinning side bands obtained at different spinning speeds (simulation). The sample has a chemical shift anisotropy ($\delta_{aniso}$) and asymmetry value ($\eta$) of 36 ppm and 1.0 respectively.*

### 1.1.4. Decoupling

As discussed in the earlier sections, static solid-state NMR spectrum is broadened due to chemical shift anisotropy, heteronuclear dipolar coupling, and homonuclear dipolar coupling. The magic angle spinning with spinning speeds of 5-10 KHz is able to remove the chemical shift anisotropy from the spectrum. However, the heteronuclear dipolar coupling and homonuclear dipolar coupling which are usually of the order of 10-23 kHz cannot be removed completely by magic angle spinning. Sample spinning of 50-70 kHz is necessary for the complete removal of direct dipolar interactions. As a result, decoupling techniques have been introduced in solid-state NMR, where spectral resolution is achieved by the spin space manipulation of dipolar Hamiltonian. According to the nature of nuclei involved in dipolar interaction there are two types of decoupling techniques: heteronuclear dipolar decoupling and homonuclear dipolar decoupling. Brief descriptions of both are given below.

#### 1.1.4.1. Heteronuclear dipolar decoupling

The simplest heteronuclear dipolar decoupling technique is high power decoupling (HPDEC), where a decoupling frequency of 80-90 kHz is applied on the proton channel to remove the coupling observed on the nearby $^{13}C$ nuclei. The irradiation of $^{1}H$ channel with HPDEC saturates the $|\alpha\rangle$ and $|\beta\rangle$ energy levels equally. The strength of $^{1}H$-$^{13}C$ heteronuclear dipolar coupling is determined by the time average observation of two $^{1}H$ energy levels $|\alpha\rangle$ and $|\beta\rangle$ by $^{13}C$ nucleus. The irradiation of $^{1}H$ channel by HPDEC cause a fast transition of spins between two energy levels ie $|\alpha\rangle \leftrightarrow |\beta\rangle$. This result in a time average observation of two $^{1}H$ energy levels by $^{13}C$ nucleus as zero and hence heteronuclear dipolar decoupled $^{13}C$ spectra is obtained. A schematic representation of the pulse sequence used for heteronuclear dipolar decoupling and the effect of decoupling on $^{13}C$-$^{1}H$ spin system is shown in figure 1.11.

A series of continuous pulses with $180^{o}$ flip angle and zero phases are used in $^{1}H$ channel for heteronuclear dipolar decoupling. HPDEC generally needs very high RF power for efficient heteronuclear decoupling. A combination of magic angle spinning with spinning frequency 5-10 kHz and RF irradiation frequency of 70 kHz on $^{1}H$ channel averages majority of heteronuclear dipolar coupling.

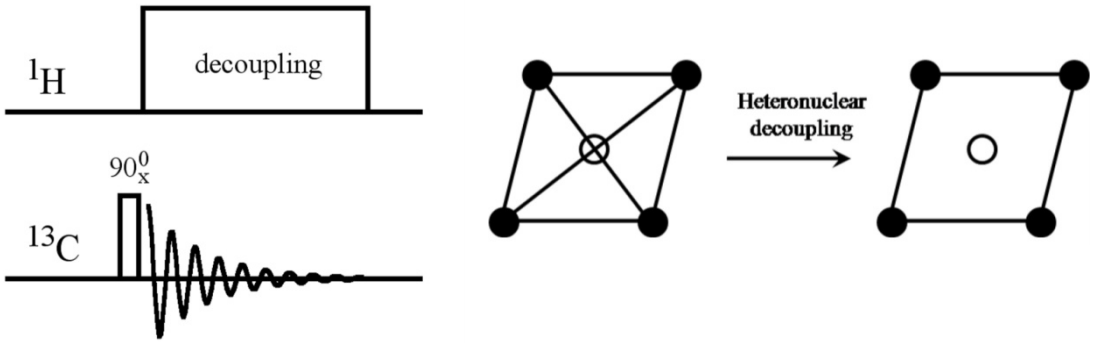


*Figure 1.11: High power decoupling pulse sequence is shown on the left. The $^1$H channel decoupling pulse removes the dipolar coupling and a schematic representation of decoupling in $^{13}$C-$^1$H spin system is shown (right).*

Sequences such as WALTZ [58], two pulse phase modulation (TPPM) [59], X inverse-X (XiX) [60], small phase incremental alteration (SPINAL) [61] and its modified versions have better heteronuclear dipolar decoupling efficiencies compared to HPDEC sequence. Among these TPPM and SPINAL are commonly used decoupling sequences. In TPPM, decoupling pulses with 170$^o$ flip angle are used, where the phase of the pulse is alternated between $\pm\phi$. The optimum value of phase in TPPM is between 5$^o$ and 15$^o$. In SPINAL sequences, pulses with flip angle of 165$^o$ is used and the phases of the pulses are incremented cyclically between $\pm 10, \pm 15, \pm 20, \pm 15$ degrees for better decoupling efficiency.

### 1.1.4.2. Homonuclear dipolar decoupling

Spinning rates of the order of 70-80 kHz are required to remove homonuclear dipolar interaction. Since most of the commercial probes do not have the facility to achieve such high spinning rates, different pulse sequences were developed for homonuclear dipolar decoupling. Waugh Huber Haeberlen (WAHUHA) [62] and MREV-8 [63] were two successful pulse sequences developed for homonuclear dipolar decoupling. In both these sequences, a set of 90$^o$ pulses with a definite time delay between them is used for better decoupling efficiency. These sequences achieve homonuclear dipolar decoupling in a small window after every decoupling pulse cycles, where the Hamiltonian due to homonuclear dipolar coupling averages to zero. It generally needs high RF power for efficient decoupling of homonuclear dipolar interaction. The schematic representation of homonuclear dipolar decoupling is shown in figure 1.12.

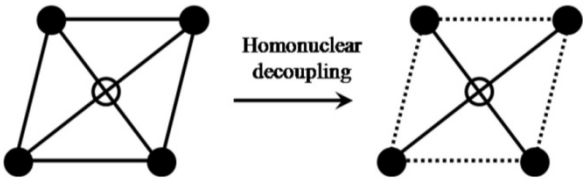


*Figure 1.12: The schematic representation of Homonuclear dipolar decoupling.*

Introduction of magic angle spinning improved the efficiency of homonuclear dipolar decoupling sequences. One of the first techniques that introduced for spinning samples was the Combined Rotation And Multiple Pulse Sequences (CRAMPS)[64]. A spinning speed of 10 kHz removes the chemical shift anisotropy in the CRAMPS experiment, while simultaneous RF irradiation removes homonuclear dipolar interaction. Later, it was distinguished that the introduction of MAS severely attenuate the decoupling efficiency of dipolar interaction and it was identified that careful rotor synchronization of pulse sequences are necessary for better decoupling efficiency. The restriction of windowed acquisition was overcome by the introduction of 2D sequences where the decoupling is achieved in the indirect dimension of the experiment. Frequency Switched Lee-Goldberg (FSLG) [65] and Phase-Modulated Lee-Goldberg (PMLG) [66] are the two well known 2D experiments that comes under this category. In the FSLG sequence, a pair of $360^{o}$ pulses is used for decoupling. The FSLG pulses are applied on the $^{1}H$ channel with a resonance offset of $\Delta\omega$ to produce an effective $^{1}H$ magnetization at the magic angle. At this position the pulses applied with an alternating phase produces homonuclear decoupled spectra. In the Polarization Inversion Spin Exchange at Magic Angle (PISEMA) experiment, which will be described in section 1.2.4, FSLG sequence is used for the suppression of homonuclear dipolar interaction.

### 1.1.5. Cross polarization (CP)

Since the natural abundance of $^{13}C$ nuclei is very low (1.1 %), their detection is very poor by the direct single pulse experiment. A technique called cross polarization (CP) was introduced for the sensitivity enhancement of $^{13}C$ nuclei in solid-state NMR [28]. The signal enhancement in CP is achieved by transferring the magnetization from 100% naturally abundant $^{1}H$ nuclei into the rare $^{13}C$ nuclei by making use of direct dipolar coupling between them.

The larmour frequency of $^{1}H$ nuclei is about four times higher than the larmour frequency of $^{13}C$ nuclei in the laboratory frame. Therefore, a direct transfer of magnetization from $^{1}H$ to $^{13}C$ nuclei is not possible in this frame because of the corresponding high energy gap. Hence the transfer of magnetization from $^{1}H$ to $^{13}C$ nuclei is made possible by first transferring both $^{1}H$ and $^{13}C$ magnetization into a frame called doubly rotating frame. In this frame, the frequency of both nuclei can be made equal by continuous RF irradiation on both channels with suitable amplitudes. When the frequency of both channels matches, a continuous flow of magnetization happens from the $^{1}H$ to $^{13}C$ nuclei. The pulse sequence used for cross polarization with constant RF amplitude (square CP) is shown in figure 1.13.

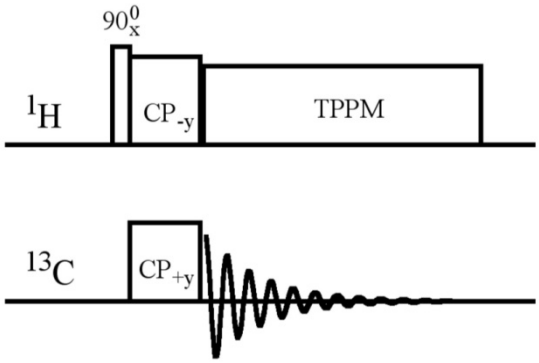


*Figure 1.13: The cross polarization pulse sequence with constant amplitude condition. This CP condition is called square CP condition and applied to static samples.*

In the cross polarization pulse sequence, a $90^0_x$ pulse is first applied on the proton channel to create coherence in the $-y$ axis. This is followed by a contact pulse with phase $-y$ applied in the $^{1}H$ channel to spin lock the $^{1}H$ magnetization in the $xy$ plane. Simultaneously, a continuous RF pulse with phase $\pm y$ transfers the magnetization from $^{1}H$ channel to $^{13}C$ channel. The cross polarization happens when the amplitude of the two magnetization reaches the Hartmann-Hahn condition[67],

$$\gamma^{13C} \times B_{RF}^{13C} = \gamma^{1H} \times B_{RF}^{1H} \tag{1.36}$$

where $\gamma^{1H}$ and $\gamma^{13C}$ are the gyromagnetic ratios of $^{1}H$ and $^{13}C$ nucleus while $B_{RF}^{1H}$ and $B_{RF}^{13C}$ are the corresponding RF fields applied in each channel. Experimentally, the resonance condition is achieved by varying the power of the RF pulses applied on $^{1}H$ channel by keeping the $^{13}C$ RF power constant; hence obtain maximum signal intensity for the spectrum. Cross polarization happens through the $^{1}H$-$^{13}C$

heteronuclear dipolar interactions, where the $^{1}H$ magnetization flows into $^{13}C$ when the Hartmann-Hahn condition is reached. For a static sample, constant amplitude CP condition is used for maximum cross polarization transfer.

The cross polarization is influenced by the strength of heteronuclear and homonuclear dipolar coupling, anything which interrupts dipolar coupling strength decrease the cross polarization efficiency. In mobile systems due to the fast motion of molecule, the dipolar coupling strength reduces drastically resulting in the reduction of CP efficiency. Magic angle spinning is another instant in solid-state NMR, where the mechanical spinning of the sample reduces the cross polarization efficiency. The mechanical spinning of the sample produce a mismatch in the Hartmann-Hahn condition which is given by $\Delta = \omega_{13C} - \omega_{1H}$ and the maximum CP takes place when the mismatch will be equal to $\pm\omega_r$ or $\pm 2\omega_r$. A technique called ramp-CP has been introduced to remove the spinning rate influence on the cross polarization efficiency. In the ramp-CP, the amplitude of $^{1}H$ channel is ramped through all possible mismatch condition so that maximum signal transfer occurs which is independent of spinning speed [68]. The pulse sequence which used in ramped-CP is shown in figure 1.14.

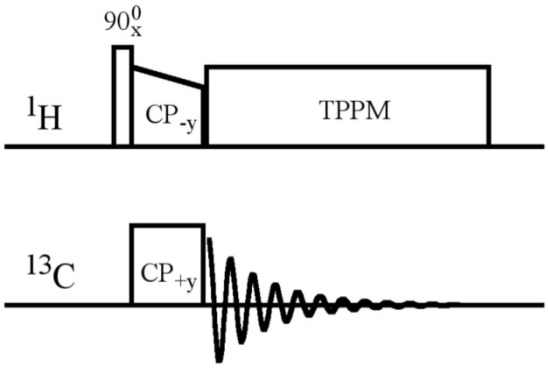


*Figure 1.14: The cross polarization pulse sequence with ramped amplitude in $^{1}H$ channel.*

### 1.1.6. Re-coupling techniques

In solid-state NMR, different anisotropic interactions provide information such as orientation, geometry and dynamics, while magic angle spinning and different decoupling sequences removes most of these interactions. Therefore, different recoupling techniques have been introduced in solid-state NMR for the re-introduction of anisotropic interactions which are averaged during magic angle spinning and high power decoupling. These reintroduction techniques vary from

sequence to sequence based on the anisotropic interaction which is to be reintroduced and its recoupling efficiency. Thus, several sequences have emerged for the reintroduction of chemical shift anisotropy, heteronuclear dipolar interaction, and homonuclear dipolar interactions. In this thesis CODEX and PISEMA experiments are used for obtaining information about polymer dynamics, where chemical shift anisotropy and heteronuclear dipolar coupling are used to probe the dynamics. Therefore, brief descriptions about important CSA and heteronculear dipolar recoupling sequences are given in the following sections.

#### 1.1.6.1. CSA re-coupling

One of the first experiments to recouple the chemical shift anisotropy (CSA) in a spinning sample was proposed by Maricq and Waugh [69; 70]. They used spinning sideband intensities of the one dimensional spectrum to obtain chemical shift anisotropy information. In relatively big molecules, overlap of spinning side bands from chemically distinct environments made this method very complex. Hertzfield and Berger derived an analytical expression for the correlation of the spinning side band intensity with the chemical shift anisotropy and demonstrated graphical and numerical methods for extraction and visualization of chemical shift anisotropy [71]. In 1981, Aue *et al.* introduced 2D experiments for recoupling CSA, where they were able to separate the spinning side bands of magnetically distinct nuclei based on the isotropic chemical shift [12]. Poor resolution of isotropic dimension which is acquired in the indirect dimension was a major limitation of this sequence. A basic requirement for spinning side band based CSA recoupling experiments is the presence of sufficient number of spinning side bands which is not achieved in systems which have small CSA.

In 1983 Bax *et al.* introduced magic angle hopping experiments for the reintroduction of CSA [72]. The experiment was designed under static conditions with isotropic chemical shift obtained in the indirect dimension and CSA in the direct dimension. Since it is a non-spinning experiment, it has severe limitation in signal sensitivity. Bax *et al.* later proposed an off-magic angle spinning sequence and demonstrated the CSA recoupling efficiency on p-dimethoxy-benzene systems by mechanically flipping the sample into $xy$ plane during the experiment [73]. The loss

in signal intensity during the mechanical flipping and lack of stable spinning units were the major disadvantages of the off-magic angle experiments.

Yarim-Ageav *et al.* proposed an experiment containing six $\pi$ pulse with a definite time interval in between them for CSA recoupling, which was successfully demonstrated on dimethylsulfone [74]. Later, Bax *et al.* proposed another rotor synchronized pulse sequence with four $\pi$ pulses for CSA recoupling [75]. A better RF inhomogeity compensation was the advantage of the proposed sequences but a distorted CSA line shape obtained by these sequences made the CSA extraction difficult. Tycko *et al.* introduced a sequence, using a series of $\pi$ pulse trains with a definite delay in between them [32], which was able to achieve a static CSA line shape, making the extraction of CSA easier. This sequence was designed for slow spinning speeds and the implementation to high spinning speeds was a major limitation of this sequence. In 1998, Ishii *et al.* developed an amplitude and phase modulated pulse sequences [76] and was able to extract the CSA pattern at spinning speeds upto 10 kHz. Gan *et al.* proposed a pulse sequence based on rotary resonance method [77], which also works at high spinning speeds although the recoupled pattern does not look like the static powder pattern. Gross *et al.*, using a series of tilted $C_n$ pulses, showed that CSA recoupling is possible at spinning speeds of 8 kHz [78]. However, the recoupled CSA pattern does not look like a normal static pattern, making the CSA extraction difficult by this method.

A modified version of Tycko's experiment was proposed by Schmidt-Rohr *et al.* named Separation of Undistorted Powder pattern by Effortless Recoupling (SUPER), in which $360^o$ pulses with different time delays were used to obtain a static like CSA line shape [79]. The limitation of this sequence was that, it did not work for spinning rates above 5 kHz. In 2003, Chan *et al*. proposed a symmetry based sequence to obtain CSA and used it for conformation analysis in peptides and proteins [80]. The pulse sequence is known as Recoupling of Chemical Shift Anisotropy (ROCSA) and was able to produce static CSA pattern at spinning speeds $\geq$ 10 kHz. In 2006 Nishiyama *et al.* proposed an amplitude and phase modulated symmetry based sequence at a spinning speed of 10 kHz, where they obtained accurate information about shielding tensor values with the use of on and off magic angle 2D experiments [81].

In this thesis, the CODEX experiment have been used for the measurement of slow motions in polymers which use two sets of rotor synchronized $180^{o}$ pulses trains separated by half rotor period to recouple CSA. A detailed description about the CODEX experiment is given in section 1.2.3. In the fifth chapter, different symmetry based CSA recoupling sequence have been introduced [47] and were tested for its recoupling efficiency with the aim to find an alternative CSA recoupling scheme for the CODEX experiment. A detailed description about the theory of symmetry based CSA recoupling sequences is given in section 1.3.

### 1.1.6.2. Hetero-nuclear dipolar recoupling

Heteronuclear dipolar coupling is an important source of structural information in solid-state NMR. This is directly proportional to the inverse of the cube of inter-nuclear distance and hence gives information about bond distance. In addition to structural information, a comparison of reduced dipolar coupling observed in polymer system with respect to the dipolar coupling measured for solid crystalline system is used as a measure of molecular and functional group dynamics [44; 46]. Muller *et al.* made the first observation of transient oscillations due to $^{1}H$-$^{13}C$ hetronuclear dipolar coupling in ferrocene single crystal [82]. With the introduction of 2D Separated Local Field (SLF) NMR experiment by Waugh *et al.,* it became possible to separate the heteronuclear dipolar information based on isotropic chemical shift [83]. One of the first experiments developed for the reintroduction of dipolar coupling with magic angle spinning was Rotational Echo Double Resonance (REDOR) and they have used it for obtaining $^{13}C$-$^{15}N$ dipolar coupling information in alanine [31]. Major problem encountered in REDOR experiment was the presence of large $^{1}H$-$^{1}H$ homonuclear dipolar interaction which hampered the recoupling efficiency of heteronuclar dipolar coupling. SLF technique was first applied to single crystals and oriented polymer systems to obtain their structural information [84; 85]. Later SLF experiments were modified to obtain $^{1}H$-$^{15}N$ heteronuclear distance information in polycrystalline solids of amino acids [86], where the distance information achieved by this was comparable to that from the neutron scattering. It was the first time a heteronuclear recoupling sequence was developed in NMR for determining the bond distance in amorphous solids. In this experiment, the dipolar coupling is determined from the spinning sideband intensity which requires slow spinning speed which is a severe restriction of this method. The $^{1}H$-$^{1}H$ homo-nuclear

dipolar coupling cause severe line broadening in the SLF spectrum which makes the accurate measurement of heteronuclear dipolar coupling difficult.

Wu *et al.* modified the SLF experiment by incorporating the frequency switched Lee-Goldberg (FSLG) sequence and extracted the heteronuclear dipolar coupling information in amino acids under static conditions [45]. This experiment called the polarization inversion spin exchange at magic angle (PISEMA), have the advantage that it suppress $^{1}$H-$^{1}$H homonuclear dipolar interaction. PISEMA is used in the study of peptides, proteins and lipid bilayer systems to extract order parameter and hetero-nuclear bond lengths information [87-89]. Van Rossum *et al.* introduced another hetero-nuclear dipolar recoupling sequence called Lee-Goldberg Cross Polarization (LG-CP), where the LG sequence suppresses the $^{1}$H-$^{1}$H homo-nuclear dipolar coupling and results in a better resolution of hetronculear dipolar coupling [90]. This experiment is carried out at spinning rates of 10 kHz and the recoupled dipolar coupling pattern looks like a pake pattern, making the analysis of bond distances easy. Mei Hong *et al.* introduced a modified LG-CP based SLF experiment for effective decoupling of $^{1}$H-$^{1}$H homonuclear dipolar coupling and the recoupled heteronuclear dipolar coupling is used to obtain information about dynamics in polymers and biomolecules [44].

The $C_7$ sequence, based on symmetry principles, is an important sequence developed by Lee *et al.* in 1995 for recoupling the heteronuclear dipolar coupling in spinning samples in which they used a basic pulse element $360_{\varphi}360_{\varphi+180}$ [91]. Hohwy *et al.* showed that the $C_7$ sequence which uses the pulse element $360_{\varphi}360_{\varphi+180}$ have less stability towards offset and they proposed an offset instability compensated sequence by introducing a new basic pulse element $90_{\varphi}360_{\varphi+180}270_{\varphi}$ [92]. Zhao *et al.* proposed two sequences $R18_1^7$ and $R18_2^5$ with simultaneous suppression of $^{1}$H-$^{1}$H homonuclear dipolar interaction [93]. This sequence is applied in a two dimensional mode, making the extraction of dipolar coupling information easier in complex systems. Wang *et al.* proposed an ultrafast spinning sequences based on the symmetry sequence $R12_3^5$ [94] where a 60 kHz spinning speed removes the homonuclear dipolar interaction.

The Dipolar Chemical Shift correlation (DIPSHIFT) experiment is a two dimensional experiment recouple the dipolar coupling in the indirect dimension and

the isotoropic chemical shift in the direct dimension [95; 96]. The DIPSHIFT experiments are used for obtaining information about fast dynamics in polymers, collagen fibrils etc [97-99]. Dvinskikh and group modified the PISEMA experiment for magic angle spinning samples [46] where fast spinning along with the spin exchange at magic angle (SEMA) suppress the homonuclear dipolar coupling with simultaneous reintroduction of heteronuclear dipolar coupling. In this thesis, we use the PISEMA experiment for obtaining information about polymer dynamics and a detailed description is given in the section 1.2.4.

Since the major topic of this thesis is the study of dynamics in polymers, a brief description about the different SSNMR experiments used for studying dynamics is given below.

## 1.2. SSNMR Experiments for measuring Dynamics in Polymers

Specific application of an engineering polymer depends on its mechanical property and the mechanical property of a polymer is a function of many factors such as chemical structure, morphology, molecular and segmental motions in the polymer chains. At the molecular level, all polymers have motions such as vibration, rotation, chemical exchange, segmental and functional group reorientations, and cooperative mobility. Different techniques such as x-ray diffraction, dielectric spectroscopy, neutron scattering, and solid-state NMR are used to probe different kinds and ranges of motions in polymers. Solid-state NMR has a clear advantage over the other available techniques since there are different experiments to probe different ranges of motions, ability to resolve different functional groups which is responsible for the mobility and therefore correlation to macroscopic property. The time-scales that can be probed by solid-state NMR are shown in the figure 1.15.

Some of the common SSNMR experiments used for measuring motions in polymers are deuterium NMR, 2D exchange NMR, line shape analysis, relaxation measurements, SLF-PISEMA and CODEX experiments. Deuterium NMR is a very efficient method for the investigation of dynamics in polymers. However, this requires deuterated polymer samples which are usually difficult to prepare. One of the main aims of this project is to investigate molecular motions in polymers which are readily available without any special synthetic procedure like $^{2}H$ or $^{13}C$ labeling. $^{13}C$ exchange experiment provides information about the geometry and time-scale of

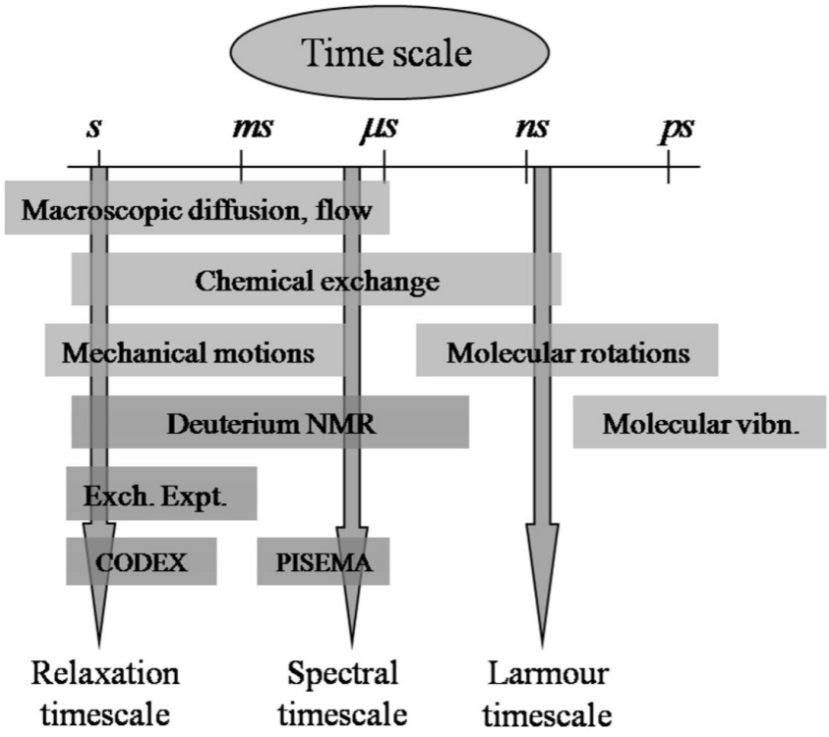


*Figure 1.15: Different ranges of motion that can be probed by NMR[1]*

motion but has the disadvantage that it is a static or quasi static (very slow spinning) experiment and require large amount of experimental time. Line shape analysis and relaxation experiments also have difficulties because the extraction of dynamics from them is not straight forward. The book by Schmidt-Rohr and Spiess [100] has a detailed discussion about some of the important experiments that are used to obtain information about dynamics in polymers.

Our aim is to use solid-state NMR techniques that can be applied on naturally abundant $^{13}C$ nuclei within reasonable experimental times. The SLF-PISEMA and CODEX are such experiments and we have chosen them for our studies on polymers. CODEX experiment have been used for detecting motions in the range of 0.1 Hz to 1000 Hz while PISEMA experiment is used for measurement of motion in the range of 100s of kHz. The major part of this thesis deals with the determination of functional group and segmental motion in three polymers, polyoxymethylene (POM), polysulfones (PSF) and poly D-L lacticacid (PDLLA). Before discussing the details of the CODEX and PISEMA experiments, a brief review of the reports in the literature where techniques such as deuterium NMR and exchange NMR experiments were used for studying dynamics in polymers are given.

### 1.2.1. Deuterium NMR

As the complexity of a system increases, the spectral overlap increases and analysis of dynamics become difficult by one dimensional NMR experiment. By selective introduction of deuterium nuclei in the main chain or side chain of a polymer segment, determination of functional groups motions become easier.

Deuterium is a quadrupolar nucleus with spin I=1 and the Hamiltonian is determined by the interaction of the nuclear quadrupole moment with the electric field gradient (EFG) tensor. In organic molecules containing C-$^2$H moiety, the EFG tensor lies in the direction of the bond axis. As a result, the tensor is axially symmetric and the quadrupolar pattern will be a symmetric pake pattern. Deuterium has a quadruplar coupling of 250 kHz in a rigid molecule. $^2$H SSNMR gives information about different kinds of motions along with its frequency which are in the range of $10^8$ to $10^{-2}$ Hz. It is also used for determining the relative percentage of amorphous and crystalline regions in semi-crystalline polymers. Deuterium ($^2$H) NMR became a major technique for measurement of dynamics in polymers with the introduction of experiments such as deuterium line shape analysis, solid echo and spin alignment echo by Spiess and group [33; 101; 102]. In deuterium NMR, $T_1$ relaxation monitor fast dynamics of the order of $10^8$ Hz, $T_2$ relaxation monitor intermediate dynamics which is of the order of $10^6$ to $10^3$ Hz and spin alignment technique give information about slow and ultra slow motions which are in the range of $10^3$ to $10^{-2}$ Hz.

Deuterium NMR line shape analysis can be used for the determination of molecular motions in polymers. Analysing the deuterium line shapes of linear polyethylene, Spiess and group studied the effect of temperature on the chain dynamics, especially belonging to the amorphous region [103]. At 120 K they found that polyethylene C-$^2$H bond possess two site jump motion in a tetrahedral site of diamond lattice. As the temperature approaches 200 K, 3 sites jump motion is observed and at 300 K, all the 4 sites become mobile. Later, it was shown that in amorphous polystyrene there are two dynamically distinct regions, one is rigid and the other mobile [104]. It was interpreted that the chain posses spin diffusional motion along with aromatic 180$^o$ flips ($\pi$), and even at well below the glass transition temperature, 20% of the sample undergoes 180$^o$ flips. Temperature dependent line shape study on bisphenol A polycarbonates showed that aromatic groups are

undergoing 180° flips motions around its $C_1 - C_4$ axis along with small angle fluctuation motions with the amplitude of slow motion varying from $\pm 15^o$ to $\pm 35^o$ [105]. At the room temperature, the whole phenyl group undergoes 180° flip motions resulting in a motionally averaged line shape and as the temperature is lowered to 160 K, deuterium NMR shows the presence of both rigid and mobile regions.

Deuterium NMR study on poly(para-phenylene) showed that there are two distinct regions present in the polymer at 23°C, amorphous and crystalline and it is found that 25% of the amorphous region undergoes continuous 180° flip motions along with complex liberational motions[106]. In another study on blends of polyacetylene-polystyrene revealed that 20% of poly acetylene is amorphous in nature and undergoes complex motions involving lengths of 3, 5 and 10 bonds. Deuterium NMR study on poly(butylenes-terephthalate) showed the presence of morphologically intermediate component along with crystalline and amorphous component [107]. A line shape analysis on bisphenol A polysulfone -an amorphous polymer- by Dumais

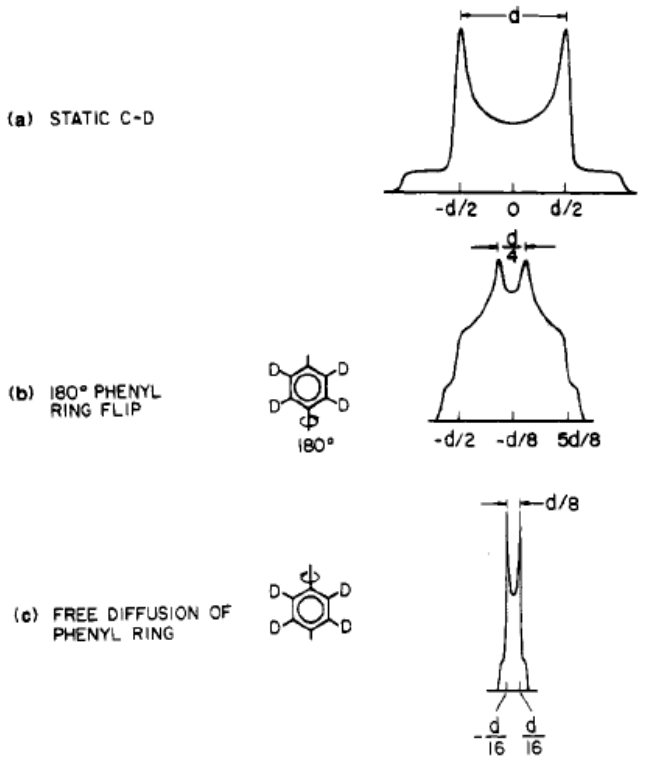


*Figure 1.16: Deuterium line shapes obtained due to a).static, b).180° phenyl flips and c).free diffusion [108].*

*et al.* revealed the presence of intermediate mobile component along with rigid and mobile components with each environment having different motional characteristics [108]. Examples of $^{2}H$ line shapes obtained for different types of motion a). static b). $180^{o}$ phenyl flip and c). free diffusion of phenyl ring are shown in figure 1.16.

### 1.2.2. Exchange NMR

One dimensional NMR experiments gives limited information about the correlation time and geometry of motions. Static and spinning $^{2}H$ and $^{13}C$ exchange experiments have been developed which gave more insight into polymer dynamics. There are four important components present in an exchange experiment: they are preparation, evolution, mixing, and detection periods. During the preparation period, the magnetization is prepared for evolution; this is generally done by cross polarizing the $^{1}H$ magnetization into $^{13}C$ for carbon exchange experiments. In $^{2}H$ exchange NMR experiments, the magnetization is prepared by an initial $90^{o}$ pulse. During the evolution period, the spin system evolves under different nuclear spin interactions which give indirect dimension to the spectrum. A mixing time is applied between the evolution and the detection periods, during which a reorientation or mixing of different energy levels occurs. The redistribution of magnetization happens due to the molecular motions and magnetization that has evolved after the mixing period is acquired during the detection period. The schematic representation of $^{2}H$ exchange pulse sequence is shown in figure 1.17a. The $^{2}H$ exchange line shape obtained for a motion with a reorientation angle of $109.5^{o}$ is shown in figure 1.17b [109]. The axis length of the ellipse is correlated to the reorientation angle giving the geometry of motional dynamics.

2D exchange experiments with appropriate mixing time gives information about the geometry of motions and from a series of 2D exchange experiments with different mixing times, the correlation time can be calculated. Exchange experiments are used to obtain information about the slow molecular dynamics which are in the range of 1 $msec$ to 10 $sec$.

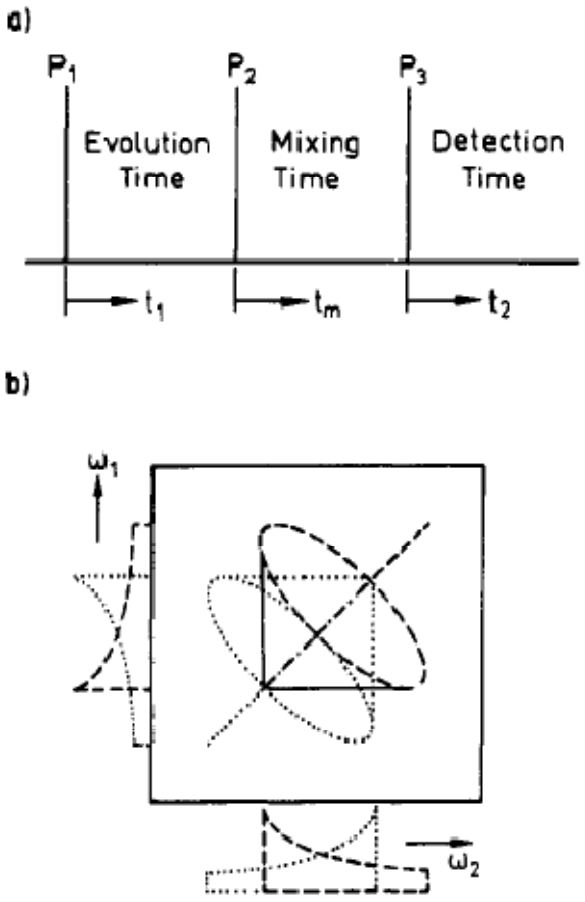


*Figure 1.17: a).The pulse sequence used in a $^{2}H$ exchange NMR experiments. b).The exchange spectrum modeled with a reorientation angle of 109.5$^{o}$ [109].*

One of the first studies using 2D $^{13}C$ exchange experiment was done on a semicrystalline polyethylene and it was reported that both jump motion and spin exchange contribute to the dynamics in the crystalline region [110]. Spectral overlap in complex molecules was a major limitation of the exchange experiments. Kentgens *et al.* introduced exchange experiments on slow magic angle spinning samples to determine the correlation time of the motions in crystalline region of polyoxymethylene [2; 111]. The spinning side band analysis showed that the crystalline regions of POM undergo $0, \pm 200, \pm 400, \pm 600, \pm 800$ degree jump motions about the chain axis and the activation energy of crystalline motion was estimated as 83 kJ/mol.

To understand the geometry of motions in polypropylene, Schaefer *et al.* carried out $^{2}H$ 2D static exchange experiments [112]. The exchange experiments revealed that atactic polypropylene has a distribution in reorientation angle and hence confirmed that the major motion in atactic polypropylene is spin diffusion while in

isotactic polypropylene, the exchange spectra shows separate ridge patterns indicating that there are some well defined helical jump motions. The motional geometry of the dynamic process in deuterium labeled polyoxymethylene was confirmed by Spiess and group using static two dimensional deuterium exchange experiments [3; 113]. The geometry of different crystalline motions such as $0, \pm 200, \pm 400, \pm 600, \pm 800$ degree jumps were observed as ridge patterns around the diagonal peak. The advantage of static 2D exchange experiments was that direct visualization of motional geometry is possible from the distinct ridge patterns that are obtained. For different angles of jump motions, different ridge pattern is observed and the ridge pattern observed in the case of semicrystalline POM is shown in figure 1.18.

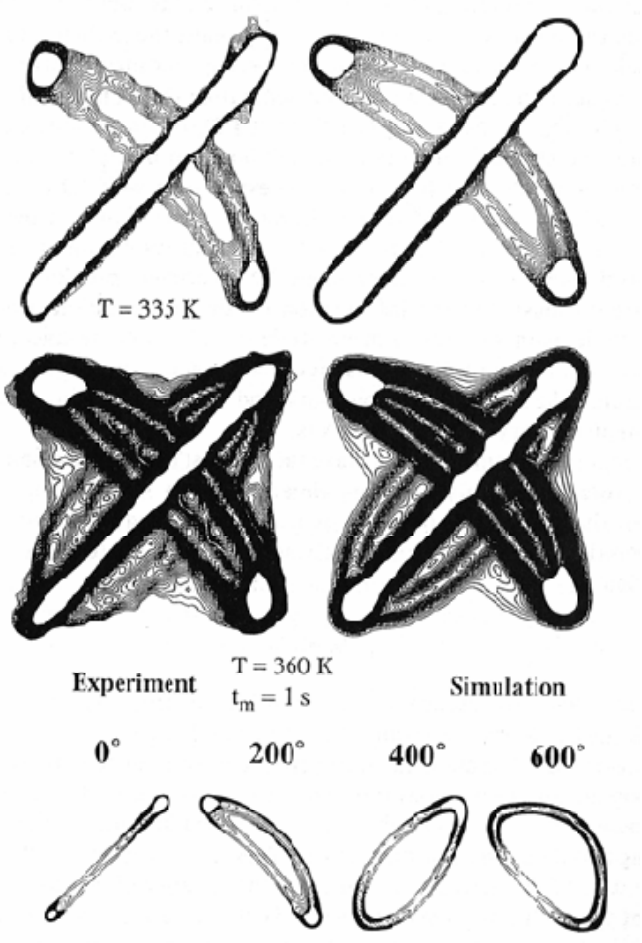


*Figure 1.18: Experimental and simulated $^2H$ Exchange NMR spectra of Polyoxymethylene at 335 and 360 Kelvin. The ridges indicates a jump angle of* $0, \pm 200, \pm 400, \pm 600$ *degrees which is in agreement with the theoretical simulations [3].*

Since the major part of this thesis is studies on industrial polymers, $^{13}C$ or $^2H$ enrichment was not viable and hence NMR experiments on $^2H$ or $^{13}C$ labeled samples

were not carried out. In addition, exchange experiments require long experimental times which consumes tremendous amount of spectrometer time. Hence we have used experiments such as CODEX, and PISEMA which give segmental and functional group motions of the order of 0.1 Hz to 100s of kHz with naturally abundant $^{13}C$ nuclei. Spin lattice relaxation time ($T_1$) experiments, $T_1$ and $T_2$ filtered PISEMA experiments were also used in our study, which gives insights about dynamic heterogeneity of a polymer. The experiments which were used in this study are described below.

### 1.2.3. Center band Only Detection of Exchange (CODEX)

One dimentional experiments such as Toss-exchange, ODESSA, time reverse ODESSA, SELDOM-ODESSA, PATROS were introduced in place of 2D experiments for measuring dynamics in polymers [36-38; 40; 114]. These sequences use the changes in spinning sidebands intensity as a function of the mixing time to obtain information about correlation time. As mentioned in the earlier section, the disadvantage of these experiments is that at least 5 spinning side bands are required to get a reasonable estimate of the dynamics which are not possible in most of the aliphatic environments. Alternatively, in these techniques the minimum number of spinning side bands is achieved by reducing the spinning speed to well below 1 kHz, but it results in severe reduction in signal to noise ratio. The Center band Only Detection of Exchange (CODEX) experiment, proposed by Schdmit-Rohr and group, uses the center band intensity for the study of slow dynamics in polymers [41; 115] is a good alternative to such spinning sideband based experiments.

CODEX uses chemical shift anisotropy (CSA) as the probe for slow dynamics in polymers. Orientational reordering of the polymer chains ie. fluctuations in the polymer chain units changes the orientation of the CSA tensor during the experiment. This CSA reorientation causes a dephasing in the CODEX NMR signal and it is used as a measure for dynamics in polymers. The pulse sequence used for the CODEX experiment is shown in the figure 1.19.

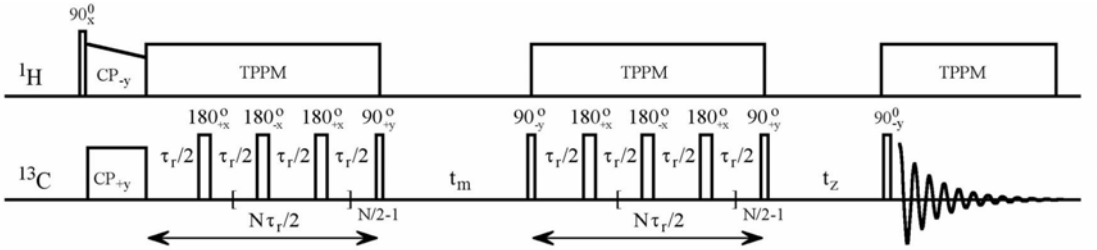


*Figure 1.19: The pulse sequence of the CODEX experiment, consisting of two sets of 180° pulse trains separated by a mixing time, along with a z-filter at the end of the sequence. The $N\tau_r$ dependence is measured by changing the 180° pulse loop by keeping a fixed mixing time ($\tau_m$) during which we expect enough motion to happen in the polymer. The $\tau_m$ dependence experiment is carried out by changing mixing time $\tau_m$ with an optimized $N\tau_r$ value.*

The CODEX experiment uses two sets of rotor synchronized pulses to recouple the CSA. The basic components of a CODEX experiment are the preparation period, two evolution periods which is of the duration of $N/2$ rotor periods, a mixing time and a $z$-filter time followed by a detection period. During the preparation period, the proton magnetization is transferred to the carbons by cross polarization. The carbon magnetization placed in the $xy$ plane by cross polarization is allowed to evolve during the subsequent evolution period. During each $N/2$ rotor periods, the chemical shift anisotropy is refocused by 180° pulses trains, where the 180° pulses are separated from each other by a half rotor period ($\tau_r/2$). Since anisotropic interactions depends on the orientation of the molecule, mixing time ($\tau_m$) period will always be kept as a multiple of the rotor period ($\tau_r$). After the first 180° pulse block, the spin magnetization is stored in the $z$ axis by a 90° pulse called the storage pulse and after the $\tau_m$ period the magnetization is restored back into the $xy$ plane by another 90° pulse called readout pulse. A second 180° pulse train with half rotor period delay between the 180° pulses is applied to the spin system after the readout pulse. The magnetization evolved after the second 180° pulse train is allowed to evolve for a short $z$-filter period before detection. The $z$-filter period is made as small as possible to ensure that no motions happen during that time.

After the first 180° pulse train the signal acquires a phase $\Phi_1$. Similarly, after the second 180° pulse train also the signal acquire a different phase $\Phi_2$. The total phases $\Phi_1$ and $\Phi_2$ obtained after each 180° pulse train is given by

$$\phi_1 = \frac{N}{2}(-\phi_{A1} + \phi_{B1}) \tag{1.37a}$$

$$\phi_2 = \frac{N}{2}(+\phi_{A2} - \phi_{B2}) \tag{1.37b}$$

where $\phi_{A1}$ and $\phi_{B1}$ are the phases acquired by the magnetization before and after each 180° pulse during the first 180° pulses train while $\phi_{A2}$ and $\phi_{B2}$are the phases acquired by the magnetization before and after the each 180° pulses in the second pulse train. Hence the total phase acquired after each 180° pulse train is give by

$$\phi_{A,n} = \int_0^{\tau_r/2} \omega_n(t)dt \tag{1.38a}$$

$$\phi_{B,n} = \int_{\tau_r/2}^{\tau_r} \omega_n(t)dt \tag{1.38b}$$

where $\omega_1(t)$ and $\omega_2(t)$ are the frequency of the evolved magnetization before and after the mixing time. It can be observed that the 180° pulses reverse the phase of magnetization evolved during the evolution time, hence $\phi_{A,n}$ and $\phi_{B,n}$ will have opposite sign. In addition, the two 90° pulses before and after the mixing time reverses the phases of magnetization $\phi_{A,1}$ and $\phi_{A,2}$, $\phi_{B,1}$ and $\phi_{B,2}$ with each other.

The chemical shift anisotropy averaged during MAS is refocused by 180° pulses applied at half rotor periods. The total phase acquired by the signal before the mixing time can be expressed as

$$\phi_1 = \frac{N}{2}(-\int_0^{\frac{\tau_r}{2}} \omega_1(t)dt + \int_{\frac{\tau_r}{2}}^{\tau_r} \omega_1(t)dt) \tag{1.39}$$

The chemical shift anisotropy with the same frequency acquired before and after the 180° pulses add up. This can be easily visualized from the fact that the chemical shift anisotropy phase acquired during the MAS is zero. ie.

$$\int_0^{\tau_r} \omega_n(t)dt = 0$$

$$\Rightarrow \int_0^{\tau_r/2} \omega_n(t)dt + \int_{\tau_r/2}^{\tau_r} \omega_n(t)dt = 0$$

$$\Rightarrow \int_{\tau_r/2}^{\tau_r} \omega_n(t)dt = -\int_0^{\tau_r/2} \omega_n(t)dt$$

$$\Rightarrow \phi_{A,n} = -\phi_{B,n} \tag{1.40}$$

Inserting this into eq 1.39, the total phases obtained before and after the evolution time can be rewritten as

$$\phi_1 = -\frac{N}{2} 2 \int_0^{\tau_r/2} \omega_1(t)dt \tag{1.41a}$$

$$\phi_2 = \frac{N}{2} 2 \int_0^{\tau_r/2} \omega_2(t)dt \tag{1.41b}$$

If a reorientation of CSA does not take place during the mixing time, the total phase acquired over the whole $180^o$ pulse train will be $\phi_1 + \phi_2 = 0$ ($\phi_{A,1} = -\phi_{B,1}$ & $\phi_{A,2} = -\phi_{B,2}$). On the other hand, if a reorientation takes place, the total phase acquired over the full pulse sequence will not be zero and that will give information about the segmental motion in the sample. In the CODEX experiment, the signal observed is a function of the mixing time and the CSA recoupling time represented as $S(\tau_m, \delta N\tau_r)$. To remove the effects of spin lattice relaxation ($T_1$) during $\tau_m$ and spin-spin relaxation ($T_2$) during $N\tau_r$, a reference spectrum is recorded by interchanging $\tau_m$ and the $z$-filter time with each other in the CODEX experiment. The signal intensity obtained during reference experiment is represented by $S(0, \delta N\tau_r)$. During the reference experiment, influence of the relaxation time will be same as that of the CODEX experiment but influence due to the change in the orientation of the CSA tensor due to motions during mixing time is completely absent. The ratio of $S(\tau_m, \delta N\tau_r)/S(0, \delta N\tau_r)$ removes relaxation effects, gives information about motions alone and a variation of $\tau_m$ and $N\tau_r$ is used to determine the correlation time (time constant) and geometry of segmental motions respectively. The normalization of the CODEX spectrum with the reference spectrum removes the non-exchanging signals from the spectrum and hence the signal intensity obtained is a function of motions alone.

If the number of sites available for exchange is given by $M$and the fraction of the groups that undergo segmental motion is represented by $f_m$, the final exchange intensity obtained $E_\infty$ during $E(\tau_m \gg \tau_c, \delta N\tau_r \gg 1)$ is expressed by the equation

$$E_\infty = f_m(M-1)/M \tag{1.42}$$

The ratio of the intensity of the CODEX to the reference spectra $S/S_0$ is plotted as a function of $N\tau_r$ and is fitted using the model [41; 116], from which information about the geometry of motions can be obtained. The $N\tau_r$ at which the $S/S_0$ reaches a plateau in the $N\tau_r$ dependence experiment is used in the CODEX $\tau_m$ dependence experiment in which the mixing time is varied. The ratio of the intensity $S/S_0$ is plotted as a function of $\tau_m$ and the decay curve can be fitted with a Kolhrash's William Watt (KWW) function (equation 1.43) to obtain the frequency of motion.

$$\left(\frac{S}{S_0}\right)_{motion,diff} = (1-M) + M * exp(-\frac{\tau_m}{\tau_c})^\beta \tag{1.43}$$

The $\left(\frac{S}{S_0}\right)_{motion,diff}$ is the ratio of the CODEX to reference signal intensity which is a function of both motion and diffusion, $\tau_c$ is an inverse of the frequency of dynamics called the correlation time, $\beta$ the distribution in the frequency of dynamics and $M$ is the fraction of sites involved in the dynamics which is dependent on the availability of polymer segments for motions.

In the CODEX experiment, spin diffusion causes a decay in the $^{13}C$ signal even without the presence of molecular motion [117]. The spin diffusion can be removed systematically from the CODEX experiment, since diffusion is independent of the temperature while molecular motion is temperature dependent. The CODEX experiment is carried out at a temperature which is as low as possible where only spin diffusion is expected. Hence the spin diffusion at elevated temperatures is removed by using the equation 1.43

$$\left(\frac{S}{S_0}\right)_{motion} = \left(\frac{S}{S_0}\right)_{motion,diff} / exp(-\frac{\tau_m}{\tau_{diff}})^\beta \tag{1.44}$$

where $\left(\frac{S}{S_0}\right)_{motion}$ is the ratio of the CODEX to the reference signal intensity which is a function of motion alone, $\tau_m$ is the mixing time used and $\tau_{diff}$ is the correlation time of the spin-diffusion process obtained at low temperature. The fitting of $\left(\frac{S}{S_0}\right)_{motion}$ vs

the mixing time using KWW function gives the frequency of motion devoid of diffusion. In the study of POM and PDLLA which are described in chapters 2 and 4 the CODEX curve at 23$^{o}$C is treated as a function of diffusion alone because motions are absent in these systems at this temperature.

The CODEX experiment has been used by different groups to obtain information about slow molecular and segmental motions in polymers. Schmidt-Rohr and group studied the influence of the side group bulkiness on the correlation time and geometry of dynamics in poly(n-alkyl methacrylates) [118]. Detlef and group have used this experiment for correlating the origin of mechanical relaxation to different segmental and functional group motions in poly(methyl methacrylates) [117], study of motional geometry in isotactic Poly(4-methyl-1-pentene) [119], and protein dynamics information [120]. In this thesis CODEX experiments have been used on three polymers POM, PSF and PLA to obtain information about slow range dynamics.

### 1.2.4. Polarization Inversion Spin Exchange at Magic Angle (PISEMA)

As discussed in section 1.1.5, in the cross polarization (CP) experiment, a magnetization transfer takes place from $^{1}$H to $^{13}$C nuclei during the contact time through heteronuclear dipolar coupling. The separated local field (SLF) experiment is a 2D version of the CP experiment where the cross polarization time is varied linearly in the indirect dimension to obtain information about the strength of the heteronuclear dipolar coupling. The $^{13}$C CP intensity undergoes a transient oscillation and hence the frequency of the oscillation is a direct measure of the heteronuclear dipolar coupling. The first observation of transient oscillation due to heteronuclear dipolar coupling was observed by Muller *et al.* [82], where the buildup of $^{13}$C magnetization as a function of dipolar coupling strength is expressed by the equation

$$M_{sx}(\tau) = \frac{1}{2}\beta\hbar\omega_{0I}[1 - \frac{1}{2}\exp(-R\tau) - \frac{1}{2}\exp\left(-\frac{3R\tau}{2}\right) * \cos\left(\frac{b\tau}{2}\right)] \qquad (1.45)$$

where $b/2$ is the heteronuclear dipolar coupling factor, $R$ is determined by the homo nuclear spin diffusion and $\beta$ is a constant $1/k_BT$ where $k_B$ is the Boltzmann constant. The $^{1}$H-$^{13}$C dipolar oscillations and the corresponding Fourier Transform spectra is shown in figure 20. The Fourier Transformed spectrum has the advantage that the

distance between the outer peaks gives direct information about the heteronuclear dipolar coupling.

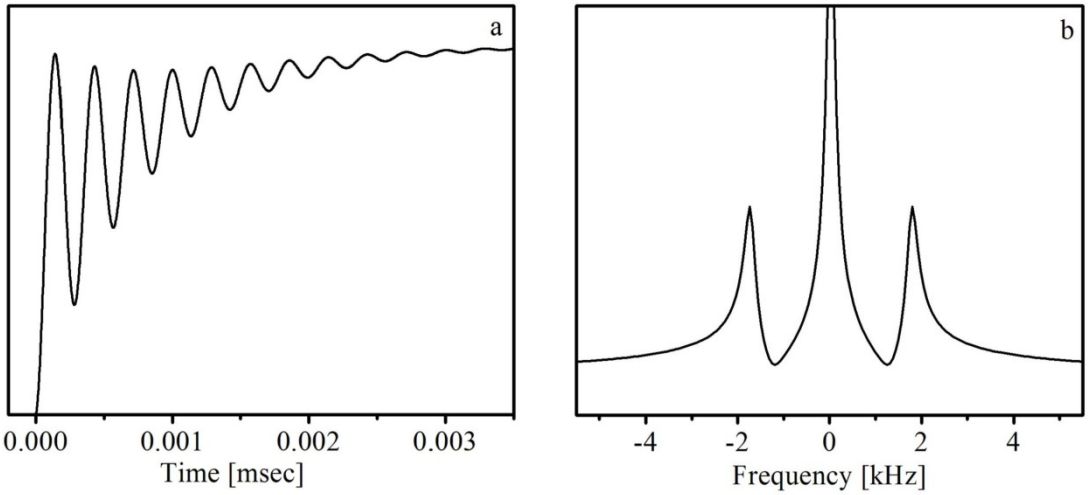


*Figure 1.20: a).The transient oscillation observed due to $^{1}H$-$^{13}C$ dipolar coupling and b).the corresponding Fourier Transformed spectrum.*

A thermodynamic mechanism for the transfer of magnetization from $^{1}H$ to $^{13}C$ nuclei during cross polarization was proposed by Levitt *et al.* using the density matrix formalism [121]. For a two spin system $I-S$, having heteronuclear dipolar coupling, the total Hamiltonian can be represented in a doubly rotating frame by the equation

$$H = H_I + H_S + H_{IS} \tag{1.46a}$$

$$H = (\Omega_I \mathrm{I}_Z + \omega_{1I}\mathrm{I}_X) + (\Omega_S \mathrm{S}_Z + \omega_{1S}\mathrm{S}_X) + 2dI_Z\mathrm{S}_Z \tag{1.46b}$$

where $\Omega_I$ and $\Omega_S$ are the offset of RF pulse applied to $I$ and $S$ spins respectively and $d$ is the dipolar coupling. In the presence of high RF pulses, the offset terms become small and can be neglected from the above equation. Hence the total Hamiltonian in the presence of RF pulses applied on the $y$ axis is given by

$$H_T = \exp\left[-i\frac{\pi}{2}(\mathrm{I}_Y + \mathrm{S}_Y)\right] * H * \exp\left[i\frac{\pi}{2}(\mathrm{I}_Y + \mathrm{S}_Y)\right] \tag{1.47a}$$

$$= \omega_{1I}\mathrm{I}_Z + \omega_{1S}\mathrm{S}_Z + 2dI_X\mathrm{S}_X \tag{1.47b}$$

This Hamiltonian can be expressed in terms of double quantum($H^{\Sigma}$) and zero quantum ($H^{\Delta}$) terms by rearranging the terms of equation 1.47

$$H_T = \frac{1}{2}[(\omega_{1I} + \omega_{1S})(\mathrm{I}_Z + \mathrm{S}_Z) + d(I^+S^+ + I^-S^-)] + \frac{1}{2}[(\omega_{1I} - \omega_{1S})(\mathrm{I}_Z - \mathrm{S}_Z) + d(I^+S^- + I^-S^+)] \quad (1.48a)$$

$$= \frac{1}{2}[(\omega_{1I} + \omega_{1S})I_Z^\Sigma + dI_X^\Sigma] + \frac{1}{2}\left[(\omega_{1I} - \omega_{1S})I_Z^\Delta + dI_X^\Delta\right] \quad (1.48b)$$

$$H_T = H^\Sigma + H^\Delta \quad (1.48c)$$

The initial density matrix and density matrix at the beginning of the strong RF pulse is given by

$$\sigma_0 = I_z \quad (1.49a)$$

$$\sigma^\Sigma(0) + \sigma^\Delta(0) = I^\Sigma(0) + I^\Delta(0) \quad (1.49b)$$

In the doubly rotating frame, under the influence of the strong RF pulse, under the exact Hartmann-Hahn condition, $H^\Sigma = \omega^\Sigma I_Z^\Sigma$ and $H^\Delta = d.I_X^\Delta$. Hence the evolution of the density matrix in presence of dipolar coupling is given by

$$\sigma(t_1) = I_Z^\Sigma + I_Z^\Delta \cos(dt_1) + I_Y^\Delta \sin(dt_1) \quad (1.50)$$

This equation shows that the oscillating term due to dipolar coupling is arising only from the zero quantum space, while the non-oscillatory term originates from the double quantum space. Hence on Fourier Transformation, the oscillatory term results in the dipolar peaks on the outer side while non-oscillatory term results in the zero frequency peak at the center of spectrum(figure 1.20).

In a multi spin system, presence of homonuclear dipolar coupling severely attenuates the recouping efficiency of the heteronuclear dipolar interaction in the SLF experiment. For removing the effects of homonuclear dipolar coupling, frequency switched Lee-Goldberg (FSLG) techniques have been introduced in the SLF experiments. The PISEMA is an experiments introduced to obtain heteronuclear dipolar coupling information with simultaneous decoupling of homonulcear dipolar coupling. This was first introduced as a heteronuclear dipolar recoupling technique to obtain structural information such as bond distances, order parameter, particularly in oriented gel systems. Dvinskikh *et al*. modified the sequence for MAS solid samples and the pulse sequence developed is shown figure 1.21 [46].

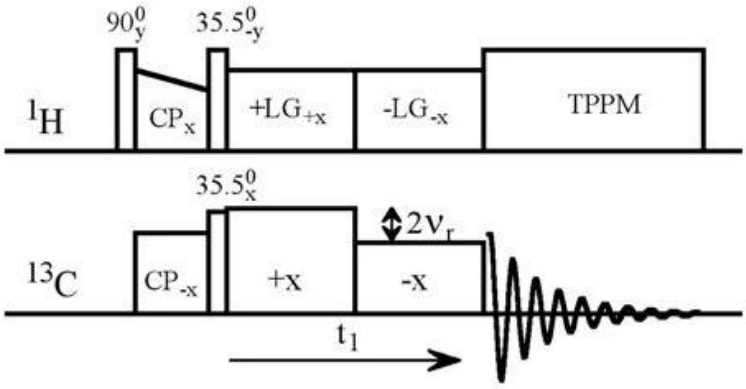


*Figure 1.21: The pulse sequence of the PISEMA experiment for recoupling the $^{1}H$-$^{13}C$ heteronuclear dipolar coupling in solid samples with magic angle spinning.*

A brief summary of the theory of the Lee Goldberg sequence which is available in the literature is presented [90; 122; 123]. The total Hamiltonian in the doubly rotating frame with the application of the Lee-Goldberg sequence is given by the equation

$$H = \omega_{1I}\mathrm{I}_X + \omega_{1S}\mathrm{S}_X + \Delta\omega_I\mathrm{I}_z + 2d(t)I_Z\mathrm{S}_Z \qquad (1.51)$$

The first two terms corresponds to RF pulse applied on I and S spins respectively and third term corresponds to the RF offset on I channel due to Lee-Goldberg condition, where $\Delta\omega_I = \omega_{1H}/\tan(54.74)$. The fourth term corresponds to the heteronuclear dipolar coupling between I and S spin and the orientation of the dipolar coupling in the rotor frame is given by

$$d(t) = \omega_d\left(\frac{3}{4}\sin 2\theta_m \,.\, sin\theta_{ij}.\cos\left(\omega_r t + \phi_{ij}\right)\right.$$
$$\left. -\frac{3}{4}sin^2\theta_m.sin^2\theta_{ij}.\cos\left(2\omega_r t + 2\phi_{ij}\right)\right) \qquad (1.52)$$

where $\omega_d = \frac{\mu_0\hbar}{4\pi}.\frac{\gamma_I\gamma_S}{r^3}$. The total Hamiltonian is then transformed into a tilted frame using the transformation equation $\exp(-i\theta_m I_y)\exp(-i.\pi/2.S_y)$ and resulting Hamiltonian is given by

$$H_T = -\omega_{\mathrm{eff},I}\mathrm{I}_Z - \omega_{1S}\mathrm{S}_Z - 2d(t)(\sin(\theta_m)\,\mathrm{I}_X\mathrm{S}_X - \cos(\theta_m)\,\mathrm{I}_Z\mathrm{S}_X) \qquad (1.53)$$

where $\omega_{\mathrm{eff,I}} = (\Delta\omega^2 + \omega_1^2)^{1/2}$. This equation can be simplified by a double transformation using a toggling frame, imposing the Hartmann-Hahn condition $\omega_{\mathrm{eff,H}} - \omega_{1,C} = \pm n\omega_r$, and neglecting the time dependent terms $\cos(\omega_r t)$, $\cos(2\omega_r t)$ etc., and the resulting dipolar Hamiltonian is given by

$$H_1^* = \frac{\delta}{4}(I_+S_- \exp(i\phi) + I_-S_+ \exp(-i\phi)) \tag{1.54}$$

where $\delta = \frac{3}{4}\sin 2\theta_m \,.\, sin\theta_{ij}.\,\omega_d.\, sin\theta_m$. In the density matrix form, the spin system in the beginning of the LG sequence is represented by $\rho_0 = -Z^{-1}\beta\omega_{0I}\mathrm{I}_Z$, where $\beta = 1/k_bT$. Now the evolution of density matrix in the presence of the dipolar Hamiltonian $H_1^*$ is given by $\rho(t) = \exp(-iH_1^*t)\,.\,\rho_0.\exp(iH_1^*t)$ and the resulting signal can be evaluated by the equation $\langle S_z(t)\rangle = Tr(\rho(t)\mathrm{S}_Z)$ and expanded as

$$S(t) = -\frac{1}{4}\,Z^{-1}\beta\omega_{0I}(1 - \cos(\frac{1}{2}\delta t)) \tag{1.55a}$$

$$= -\frac{1}{4}\,Z^{-1}\beta\omega_{0I}(1 - iexp\,(+\frac{i}{2}\delta t) - iexp\,(-\frac{i}{2}\delta t)) \tag{1.55b}$$

On Fourier Transformation of the above equation, two singularities will be produced in the spectra at frequencies of $\pm\frac{1}{2}\delta$. The difference between these singularities will give the scaled dipolar coupling with the scaling factor determined by $\delta$. In the PISEMA experiment, the scaling factor is 0.577.

The implementation of the PISEMA experiment is carried out as follows. After the cross polarization, the $^1$H magnetization in the $xy$ plane is placed into magic angle by a $35.5^0$ pulse, followed by a Lee-Goldberg sequence applied on the $^1$H channel for an efficient suppression of the $^1$H-$^1$H homonuclear dipolar coupling. The schematic representation of FSLG is shown in figure 1.22. In the Lee-Goldberg sequence, a spin lock pulse at the magic angle is applied, which is achieved by the application of $^1$H RF of frequency $\omega_{1H}$ with an offset $\Delta\omega$, so that an effective field with a frequency ($\omega_{\mathrm{eff},H}$) will be created exactly along the magic angle. The Lee-Goldberg sequence efficiently spin locks the $^1$H magnetization at the magic angle with continuous application of phase alternated 360$^o$ pulses. The $\omega_{\mathrm{eff}}, \omega_{1H}$ and $\Delta\omega_H$ are interrelated by the equation

$$\Delta\omega = \omega_{1,H}/\tan(54.74) \tag{1.56a}$$

$$\omega_{\mathrm{eff},H} = (\Delta\omega^2 + \omega_{1,\mathrm{H}}^2)^{1/2} \tag{1.56b}$$

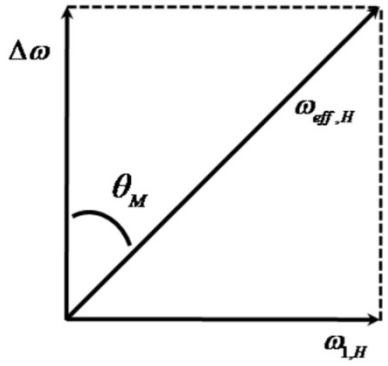


*Figure 1.22: The schematic representation of the spin locking during the FSLG pulses.*

For the static case, with the Lee-Goldberg decoupling condition, an effective transfer of magnetization from proton to carbon takes place when the effective frequency on $^{1}$H channel ($\omega_{\text{eff,H}}$) and carbon channel ($\omega_{1,C}$) are equal. But for magic angle spinning sample there is a mismatch ($\Delta$) in the resonance between the $^{1}$H and $^{13}$C channel for effective transfer of magnetization through dipolar coupling. This mismatch is a function of spinning frequency ($\omega_r$) and is compensated by changing the $^{13}$C channel frequency by first multiple of rotor frequency($\pm\omega_r$).

$$\omega_{\text{eff,H}} - \omega_{1,C} = \pm n\omega_r \tag{1.57}$$

When the frequency of the carbon channel is matched to $\omega_{1,C} + \omega_r$ ($n = 1$ sideband) and $\omega_{1,C} - \omega_r$ ($n = -1$ sideband) with alternate phases a continuous transfer of magnetization from proton to carbon takes place. During the free induction decay a high power TPPM-15 sequence is used for heteronuclear dipolar decoupling. However, SIMPSON simulations on PISEMA sequence reveled that a slight increase in carbon frequency $\omega_{1,C}$ ($\omega_{1,H} * \tan(54.74^0)$) from the exact Hartman-Hahn condition, keeping the resonance condition to $\pm\omega_r$ the same, a decrease in the intensity of zero frequency peak was observed without affecting the recoupled dipolar line shape. So for all the PISEMA experiments we have used this slight mismatch condition in the RF power for the $^{13}$C channel.

Polymers containing aromatic groups such as Bisphenol-A posses 180$^{o}$ ($\pi$) flips motions around the chain axis. These flip motions are in the range of hundreds of kHz and PISEMA experiments are used in SSNMR for tracking these fast motions. The distance between the horns of the resulting Pake pattern give the heteronuclear dipolar coupling and hence used for information about dynamics in polymers. Crystalline alanine is a rigid system and it has a CH dipolar coupling of 21.5 kHz.

Any decrease in hetero nuclear dipolar coupling with respect to the CH dipolar coupling of alanine indicates that there are motions of the order of hundreds of kHz. In our studies on polymers, the heteronuclear dipolar coupling obtained from the polymers have been compared with the dipolar coupling of alanine to obtain information about dynamics. Mei Hong *et al.* reported a reduction in dipolar coupling for the aromatic carbons of BPA which undergoes 180$^{o}$ flips. The PISEMA spectra of the CH carbon of alanine and the aromatic CH carbon of BPA are shown in figure 1.23. (At spinning speeds above 12 kHz the PISEMA experiment is observed to have a scaling factor of 0.56 and at 8 kHz the scaling factor of 0.52 is observed. Since all the PISEMA experiments were recorded at 8 kHz, the spectra have been scaled with 0.52 so that the actual dipolar coupling read out directly). Our study is one of the first reports on applications of PISEMA experiments for studying dynamics in polymers.

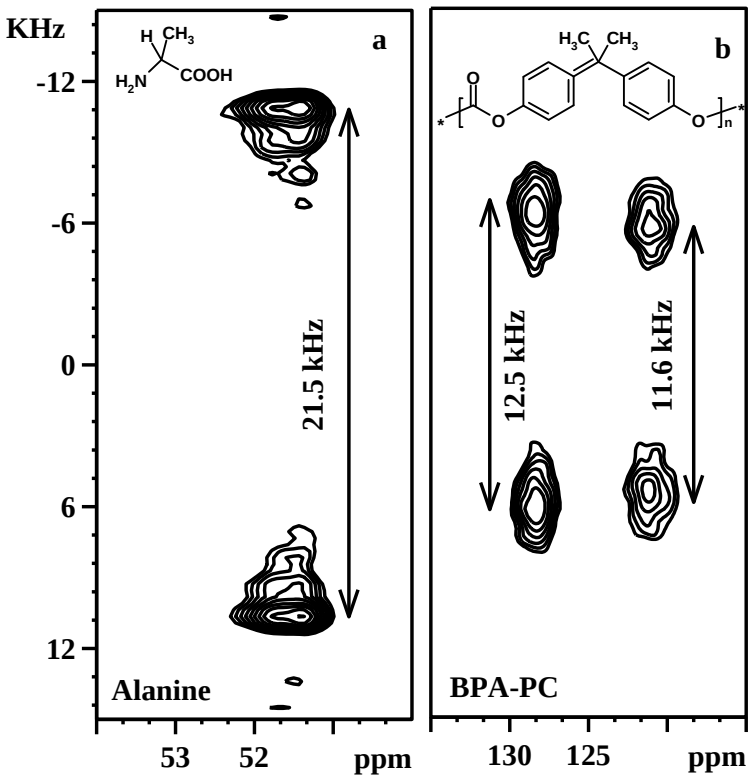


*Figure 1.23: The PISEMA spectra obtained for the a).CH carbon of alanine and the b).aromatic CH groups of bisphenol A PC. The CH group of alanine has a dipolar coupling of 21.5 kHz while the aromatic CH group of Bisphonol-A-PC has a dipolar coupling of ~11.5-12.5 kHz.*

Zhang *et al.* have shown that the peaks in the PISEMA spectrum can be separated based on the differences in the spin-lattice relaxation time ($T_1$) [124]. This

experiment is very useful for distinguishing sites with dynamical heterogeneity since the environments with small $T_1$ usually have high mobility and can be first removed from the spectra. Using this experiment, the environments with small $T_1$ relaxation time can be removed from the PISEMA spectrum and that with high value of $T_1$ can be retained. The pulse sequence of the $T_1$ filtered experiment is shown in figure 1.24a where a $T_1$ filter is introduced after the PISEMA sequence, which is sandwiched between two $90^o$ pulses. The $T_2$ filtered PISEMA experiments have also been used in this study, where peaks with small spin-spin relaxation time ($T_2$) are removed based on the differences in their mobility. The pulse sequence used for $T_2$ filtered PISEMA experiment is shown in figure 1.24b. In the $T_2$ filtered PISEMA pulse sequence, a delay is introduced between the Lee-Goldberg sequence and the acquisition time, so that the magnetization evolves in the transverse plane during this period. The components with small $T_2$ relaxation time is removed first in the $T_2$ filtered PISEMA experiment. The $T_1$ and $T_2$ filtered PISEMA experiments have been used to separate out the amorphous and crystalline regions in semicrystalline polymers.

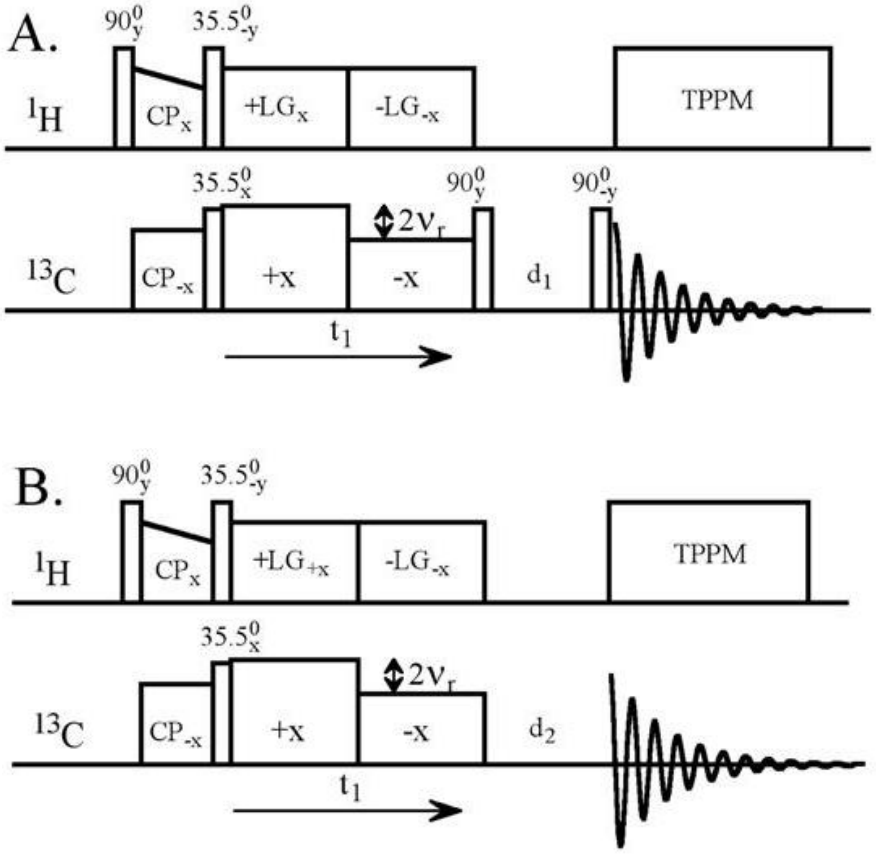


*Figure 1.24: a).The pulse sequence of the $T_1$ filtered PISEMA and b).$T_2$ filtered PISEMA.*

### 1.2.5. $^{13}C$ $T_1$ relaxation Experiment

Spin-lattice relaxation is measured by the inversion recovery method developed by Torchia [125]. The pulse sequence of this experiment is shown in figure 1.25. A CP sequence is followed by a delay which is sandwiched between two 90$^o$ pulses before acquiring the signal. The delay is varied from 1 $msec$ to 300 $sec$ logarithmically. The peak intensity obtained is plotted against the delay and fitted with an exponential decay to extract the $T_1$ relaxation times using the equation

$$S = \sum_n A_n \exp\left(-\frac{t}{T_n^C}\right) \tag{1.58}$$

where n is the no of components, $A_n$ is the amplitude of the n$^{th}$ component, and $T_n^C$ is its spin lattice relaxation time.

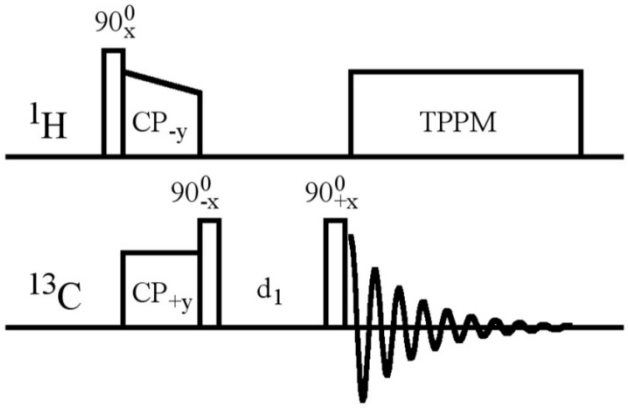


*Figure 1.25: Pulse sequence used for the $T_1$ relaxation experiments. The $d_1$ delay is incremented logarithmically from 1 msec to 300 sec and the data obtained is fitted with an exponential decay to extract the $T_1$ relaxation times.*

In this thesis different ranges of molecular dynamics in three polymers, poloxymethyline (POM), polylacticacid (PLA) and Polysulfones (PSU) have been studied. POM and PLA are semicrystalline polymer while PSU is an amorphous polymer. The NMR studies that have been carried out on these three polymers are discussed in chapters 2, 3 and 4. In chapter 5, an alternative for the CODEX experiment has been proposed by replacing the CSA recoupling sequence in the CODEX experiment with symmetry based CSA recoupling sequences. A brief overview about symmetry sequences is given below.

## 1.3. Symmetry sequences

As discussed in section 1.2.3, the CODEX experiment is an advanced solid-state NMR experiment used for measuring motions which are in the range of $msec$ to $sec$ with the advantage that it can be applied to samples without isotope enrichment [41]. The mechanical relaxation process of a polymer is determined by the main chain or/and side chain or/and functional group motions [117; 118; 126]. Chemical shift anisotropy is used to probe motions in the CODEX experiment, hence the $180^{o}$ pulse trains that refocus the CSA is a crucial component in the CODEX experiment. An alternative to the CSA recoupling element in the CODEX experiment is developed using the symmetry based R sequences which would have a better CSA recoupling efficiency. A brief introduction to the symmetry based sequences is given below [47; 49].

The symmetry based approach to the design of rotor synchronized pulse sequences exploits the rotational properties of nuclear spin interactions. In general, each internal spin interactions can be expressed as a product of three terms, transformation properties of interaction with respect to rotation in space, spin and external magnetic field. The external magnetic field is kept constant in the $z$ axis and therefore its rotational properties are not usually manipulated. The rotational properties of each interaction can be summarized in terms of the space and the spin rank which are given in table 1.1.

| Interaction | Space rank ($l$) | Spin rank ($\lambda$) |
|---|---|---|
| Isotropic chemical shift | 0 | 1 |
| Chemical shift anisotropy | 2 | 1 |
| J coupling | 0 | 0 |
| Dipole-dipole coupling | 2 | 2 |

*Table 1.1: The ranks of different internal spin interactions in NMR*

If an interaction has $'s'$ orbital symmetry then it is a 0 ranked tensor, if the interaction has $'p'$ orbital symmetry then it is a tensor having rank of 1 and if the interaction has $'d'$ orbital symmetry then it is a tensor with rank 2. An irreducible spherical tensor of rank $l$ has $2l$+1 components with index ranging from $-l$ to $+l$ in

integer steps. Rotations inter converts these $2l$+1 components according to the transformation equation

$$R(\Omega)A_{lm}R(\Omega)^{\dagger} = \sum_{m'=-l}^{+l} A_{lm'}D^{l}_{m'm}(\Omega) \tag{1.59}$$

where $R(\Omega)$ represents the rotation operator with Euler angles of $\Omega = [\alpha, \beta, \gamma]$ and $D^{l}_{m'm}(\Omega)$ are the elements of the Wigner matrix. In space, this is achieved by the physical rotation of the sample. The physical rotation of any interaction from one reference frame $[\mathrm{X}, \mathrm{Y}, \mathrm{Z}]$ to another reference frame $[\mathrm{x}, \mathrm{y}, \mathrm{z}]$ using the Euler angles $[\alpha, \beta, \gamma]$ is shown in figure 1.26.

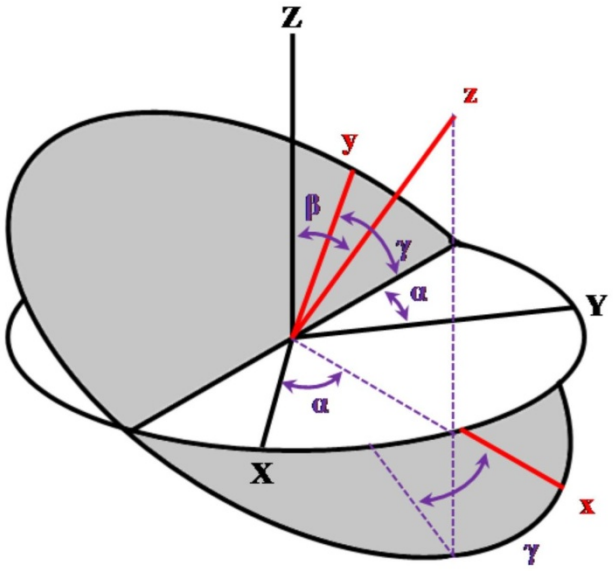


*Figure 1.26: Euler angle rotation of any interaction from the initial reference frame* $[X, Y, Z]$ *to the final reference frame* $[x, y, z]$ *using the Euler angles* $[\alpha, \beta, \gamma]$. *Initially, a rotation by* $\alpha$ *degree about* $Z$ *axis is carried out followed by a rotation of* $\beta$ *degrees about the newly generated intermediate* $y$ *axis and finally a rotation by* $\gamma$ *degree about* $z$ *axis transforms the spin interaction into the new reference frame*$[x, y, z]$.

Similar to the rotation in space, there is a rotation in the nuclear spin polarization also which is produced by the external RF field. The application of the RF field which induces a rotation of the resonant spins may be expressed as

$$U_{RF}(t, t^0) = \exp\left[-i\alpha_{RF}(t)I_z\right] \exp\left[-i\beta_{RF}(t)I_y\right] \exp\left[-i\gamma_{RF}(t)I_z\right] \tag{1.60}$$

The propagator for the RF rotation is determined by the solving the Schrodinger equation

$$\hbar \frac{d}{dt} U_{RF}(t, t^0) = -iH_{RF}(t) U_{RF}(t, t^0) \tag{1.61}$$

The spin interactions have a space rank $l$ and spin rank $\lambda$ in the mechanical space and the spin space respectively. Simultaneous application of magic angle spinning and RF irradiation induces a mixing of space and spin interaction components resulting in a total of (2$l$+1)*(2$\lambda$+1) components. The total Hamiltonian of the internal spin interaction is given by the equation

$$\widehat{H} = \sum_{-l}^{+l} \sum_{-\lambda}^{+\lambda} \widehat{H}_{lm\lambda\mu} \tag{1.62}$$

Any composite pulses that suppress all the components in the above Hamiltonian except $l = 2$ and $\lambda = 1$ results in the reintroduction of chemical shift anisotropy. Likewise any composite pulses that suppress all the components except $l = 2$ and $\lambda = 2$ result in the reintroduction of direct dipolar coupling. Levitt has proposed two symmetry classes of composite pulses for the selective reintroduction of internal spin interactions. They are the C sequences and the R sequences and notated as $CN_n^\nu$ and $RN_n^\nu$ respectively.

### 1.3.1. Reference Frames

Before discussing the details of spin and space manipulation, a brief introduction about different reference frames in which the internal spin interactions are represented in solid-state NMR are necessary. For a better understanding of the interaction and their manipulations, these different frames and their inter conversions are used. There are four reference frames used in solid-state NMR.

#### 1.3.1.1. The Principle Axis Frame (PAF)

This is the frame in which the internal spin interactions are defined. In section 1.1.2.2, it is mentioned that the CSA tensor is diagonal in the PAF. Similarly dipolar and quadrupolar interactions can also be represented in its PAF. Even if each interaction have a PAF, it may not be common to all the spin interactions in a molecule. Therefore, a common reference frame is necessary to define all the interactions and hence the molecular frame is introduced.

### 1.3.1.2. The Molecular frame (MF)

All molecules are represented in a specific frame, which is determined by the orientation of the molecular structure and is called molecular reference frame. Different internal spin interactions can be represented in this common reference frame. The PAF and MF are related through three Euler angles $[\alpha_{PM}, \beta_{PM,}\gamma_{PM}]$, which inter convert the spin interactions between these frames. The transformation of the internal spin interaction from one reference frame to another is shown in figure 1.26. For each internal spin interaction, the set of Euler angles will be the same or different depending on whether the PAF is the same or different. For any manipulation in solid-state NMR, it is necessary to transform all the spin interactions first from the PAF frame to the MF.

### 1.3.1.3. The Rotor Frame (RF`)

This is the frame in which the sample is spun at the magic angle. In poly crystalline solids, each molecule orient in different directions with respect to the rotor frame. Therefore, a set of Euler angles are needed to transform each molecular frame interaction into the rotor frame. The Euler angles $[\alpha_{MR}\beta_{MR}\gamma_{MR}]$ are used for the conversion of the internal spin interaction from the MF to the RF`.

### 1.3.1.4. The Lab Frame (LF)

This is the frame at which the NMR experiments are carried out. Here, the Euler angles $[\alpha_{RL}\beta_{RL}\gamma_{RL}]$ will transform the internal spin interactions from the rotor frame into the direction of the external magnetic field axis ie. the LF.

## 1.3.2. Transformation between different frames

The interactions are transformed between different frames using the Wigner rotation matrix. The Wigner rotation matrix which transforms the interaction from the PAF to the MF is given by the equation

$$D^{l}(\alpha_{PM}\beta_{PM}\gamma_{PM}) = \exp\left(-i\,\alpha_{PM}\hat{I}_Z\right)\exp\left(-i\,\beta_{PM}\hat{I}_Y\right)\,\exp\left(-i\,\gamma_{PM}\hat{I}_Z\right) \qquad (1.63)$$

where $\exp\left(-i\,\alpha_{PM}\hat{I}_z\right)$ is the rotation operator which transforms the nuclear spin interaction through $\alpha_{PM}$ with respect to the Z axis, $\exp\left(-i\,\beta_{PM}\hat{I}_Y\right)$ is the rotation operator which transforms the nuclear spin interaction through the angle $\beta_{PM}$ with

respect to Y axis and $\exp\left(-i\,\gamma_{PM}\hat{I}_z\right)$ is the rotation operator which transforms the nuclear spin interaction through $\gamma_{PM}$ with respect to the Z axis.

### 1.3.3. Symmetry classes

The spin and space trajectories are synchronized in such a way that it generates an average Hamiltonian that contains only desired combination of quantum numbers $[l, m, \lambda, \mu]$ while other combinations are suppressed. This is done by setting up a periodic relationship between the mechanical and RF rotation.

Consider two arbitrary time points separated by intervals $n\tau_r/N$ where $N$ represent the number of basic C/R elements in $n$ rotor cycles. $\tau_r = 2\pi/\omega_r$ is the rotational period of the sample. A continuous rotation of the sample imposes the following relationship for the spatial Euler angles which is common for both C and R sequences.

$$\alpha_{RL}\left(t + \frac{n\tau_r}{N}\right) = \alpha_{RL}(t) - \frac{2\pi n}{N} \tag{1.64a}$$

$$\beta_{RL}\left(t + \frac{n\tau_r}{N}\right) = \beta_{RL}(t) \tag{1.64b}$$

It gets more complicated by the introduction of RF pulses on the nuclear spin. In case of the $CN_n^\nu$ sequence, the Euler angle symmetry imposed by RF pulse is given by

$$\beta_{RF}\left(t + \frac{n\tau_r}{N}\right) = \beta_{RF}(t) \tag{1.65a}$$

$$\gamma_{RF}\left(t + \frac{n\tau_r}{N}\right) = \gamma_{RF}(t) - \frac{2\pi\nu}{N} \tag{1.65b}$$

where $\nu$ represents the spin winding number, which represents the number of times the spin polarization advances during the $n$ rotor rotations. In the case of $RN_n^\nu$ sequence, the Euler angles follow the symmetry

$$\beta_{rf}\left(t + \frac{n\tau_r}{N}\right) = \beta_{rf}(t) \pm \pi \tag{1.66a}$$

$$\gamma_{rf}\left(t + \frac{n\tau_r}{N}\right) = \gamma_{rf}(t) - \frac{2\pi\nu}{N} \tag{1.66b}$$

The symbols $CN_n^\nu$ and $RN_n^\nu$ are called the Symmetry classes and $N$, $n$ and $\nu$ are called symmetry numbers of the pulse sequence. In the next section, different

symmetry classes are defined and how they are used for decoupling and re-coupling of different interactions by averaging of the spin Hamiltonians are explained.

### 1.3.4. Designing of $CN_n^\nu$ and $RN_n^\nu$ sequences

The $CN_n^\nu$ sequence is designed in such a way that $n$ rotational periods of the sample is divided into $N$ equal intervals, with each of these $N$ intervals containing composite pulses. The radio frequency phases of the subsequent $N$ pulses are shifted by an angle of $2\pi\nu/N$. The symmetry properties are independent of the internal structure of the composite pulse, provided that each basic element accomplishes a full $360^0$ rotation of magnetization. Two common $C$ basic elements used in $CN_n^\nu$ pulse sequence are $360_0360_{180}$ and $270_0360_{180}90_0$, where the amplitude of the sequence is chosen in such a way that the entire pulse element fits exactly into $n$ rotational periods of the rotor.

The $RN_n^\nu$ sequence is chosen in such a way that each basic $R$ element must rotate the nuclear spin through $180^0$ about the $x$ axis. The phase of the $R$ element in a particular $RN_n^\nu$ sequence is given by $\phi = \pi\nu/N$. A reversal of R elements phase results in complementary element $R'$. Hence a full $RN_n^\nu$ sequence contain $N/2$ number of $R_\phi R_{-\phi}$ elements which are enclosed in $n$ rotor periods. The RF amplitude is chosen in such a way that $N$ elements of $R$ occupy exactly $n$ rotational periods. In $RN_n^\nu$ sequence $N$ is always an even number. Three commonly used basic $R$ elements in $RN_n^\nu$ sequence are $180_0$, $90_{45}90_{-45}90_{45}$ and $90_0270_{180}$.

The advantages of $RN_n^\nu$ sequences over the $CN_n^\nu$ sequences are that the former is more selective towards recoupling, suppresses most of the unwanted internal spin interactions (dipolar, and $J$-coupling), and recouple the desired one (CSA in our study).

### 1.3.5. Effective Hamiltonian

The behavior of nuclear spin interaction under the influence of pulse sequences are described using the time independent Hamiltonian called the Effective Hamiltonian, $\bar{H}^0(t^0)$. The effective Hamiltonian is approximated using the Magnus expansion as

$$\bar{H}(t^0) \cong \bar{H}^{(1)}(t^0) + \bar{H}^{(2)}(t^0) + \cdots \tag{1.67}$$

where the first two terms of Magnus Expansion is given by

$$\bar{H}^{(1)}(t^0) = T^{-1} \int_{t^0}^{t^0+T} dt\, H_{int}(t) \tag{1.68a}$$

$$\bar{H}^{(2)}(t^0) = (2iT)^{-1} \int_{t_0}^{t_0+T} dt_2 \int_{t^0}^{t_2} dt_1 [H_{int}(t_2), H_{int}(t_1)] \tag{1.68b}$$

where $T = n\tau_r$, is the duration of the pulse sequence. The term $\overline{H}^{(1)}$ is called the average Hamiltonian and $\overline{H}^{(2)}$ is called the second order correction to average Hamiltonian and $H_{\text{int}}$ is the Hamiltonian of different internal spin interactions. CSA and dipolar coupling Hamiltonian is small in magnitude and hence vanishes after the first order term.

### 1.3.6. First order selection rules

In the interaction frame of the RF field with magic angle spinning, the spin Hamiltonian is the sum of the spatial and spin rotational components, the average Hamiltonian may therefore be written as

$$\bar{H}^{(1)}(t^0) = \sum_{l,m,\lambda,\mu} \bar{H}^{(1)}_{l,m,\lambda,\mu}(t_0) \tag{1.69}$$

The symmetry sequences impose selection rules on the average Hamiltonian during recoupling. For a particular $CN^{\nu}_{n}$ sequence, the following selection rules apply

$$\bar{H}^{(1)}_{l,m,\lambda,\mu} = 0 \; if \; mn - \mu\nu \neq NZ \tag{1.70}$$

where Z is an integer. The components which satisfy the above condition are recoupled while all other terms varnish. In the case of $RN^{\nu}_{n}$ sequence, the recoupling follows the selection rule

$$\bar{H}^{(1)}_{l,m,\lambda,\mu} = 0 \; if \; mn - \mu\nu \neq \frac{N}{2} Z_\lambda \tag{1.71}$$

where $Z_\lambda$ is any integer with the same parity as the spin rank $\lambda$. The components which satisfy above condition survive while the other components are suppressed. Since the R sequences are more selective for specific reintroduction of anisotropic interactions they have been used in all our studies.

### 1.3.7. Space-Spin Selection (SSS) Diagrams

The selection rules that determine which interaction is reintroduced during a pulse sequence can be schematically visualized by space-spin selection diagrams. The space-spin selection diagram for the $R10_1^3$ sequence is shown in figure 1.27. It shows that the CSA with components $(l, m, \lambda, \mu) = (2, -2, 1, 1)$ and $(2, 2, 1, -1)$ recouples (two arrows), while all the other CSA components, dipolar and isotropic chemical shift interaction averages to zero.

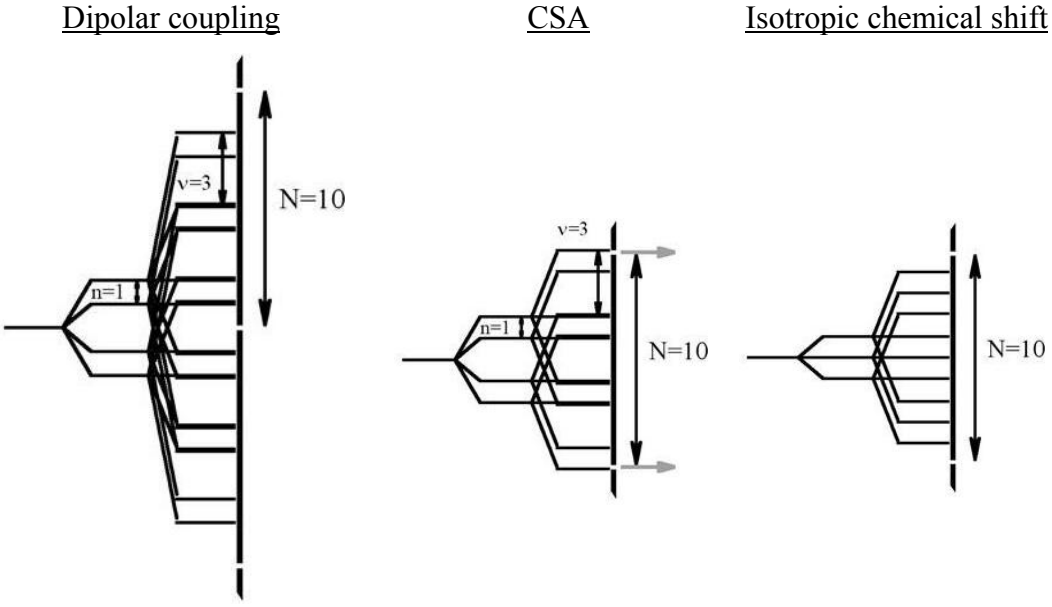


*Figure 1.27.The SSS diagrams for $R10_1^3$ shows that only CSA is re-coupled. All the components of dipolar and isotropic chemical shift interactions are blocked, while the $(l, m, \lambda, \mu) = (2,2,1,-1)$ and its mirror component (shown by arrows) of the chemical shift anisotropy recouples.*

The objective of our study is to improve the CODEX experiment by replacing the CSA recoupling element of the CODEX experiment with symmetry based R sequences.

### 1.3.8. Scaling factor

In NMR experiments, the recoupling of different interactions is achieved with a reduction or scaling in the anisotropic interactions, with respect to the actual value. The ratio of the value of reduced anisotropic interaction obtained in a pulse sequence with respect to the actual value of the anisotropic interaction is called as the scaling

factor of the sequence. The scaling factor is specific for each NMR experiment. The scaling factor ($k$) of the symmetry based R sequence is determined by the equation

$$k_{lm\lambda\mu} = \tau^{-1} d^{l}_{m0}(\beta_{RL}) \int_0^{\tau} dt d^{\lambda}_{\mu 0}(-\beta_{RF}(t)) \exp\left[i\left(\mu\gamma_{RF}(t) - \mu\frac{\pi\nu}{N} + m\omega_r t\right)\right] \quad (1.72)$$

where $d_{m,0}(\beta_{RL})$ is the reduced Wigner matrix element for space transformation, $d^{\lambda}_{\mu 0}(-\beta_{RF}(t))$ is the Wigner matrix element for spin transformation. Euler angle, $\beta_{RF}$ and $\gamma_{RF}$ are RF Euler angles and $\tau$ is the duration of basic R element. The scaling factor of each components of a specific interaction can be calculated numerically by the MATHEMATICA notebook SPINDYNAMICA developed by Levitt and Brinkman [127].

The huge number of possibilities to recouple the anisotropic interactions make the symmetry based sequences a fascinating area of research in SSNMR. Brouwer *et al.* used symmetry based CSA recoupling sequences to obtain information about the hydrogen bond in Maleic acid and Citric acid[128]. Hou *et al.* introduced ultrafast magic angle spinning symmetry based CSA recoupling sequences to extract CSA parameters in biological solids HIV-1 CA proteins [129]. However, there are not many reports on the use of symmetry sequences for recoupling CSA and dipolar interaction for measuring dynamics in polymers. In this thesis, symmetry sequences are used for reoupling of CSA and are explored to replace the CSA recoupling element in the CODEX experiment.

## 1.4. Simulation programs used in SSNMR

In Solid-state NMR spectroscopy several simulation programs have been introduced, which can mimic the behavior of nuclear spin interaction in actual spectrometer using a desktop computers. This helps in understanding the performance of new experiments before they are actually implemented into the spectrometer and thus saves valuable spectrometer time. Some of the popular simulation programs used in SSNMR are GAMMA[23], SIMPSON[24], SPINEVOLUTION[130] and which can be used to calculate the spin evolution in all kinds of experimental conditions and generate the NMR spectra. SPINDYNAMICA [127] is a specialized MATHEMATICA notebook developed for the analysis of nuclear spin interactions in the presence of symmetry based pulse sequence developed by Malcolm H. Levitt.

In this thesis we have used the SIMPSON program for the evaluating the recoupling efficiency of different symmetry based CSA recoupling sequences. SPINDYNAMICA has also been used for evaluating the scaling factors of different recoupling sequences, in particular to identify the components which recouple during a specific sequence and to calculate the scaling factor of different recouping sequences.

# CHAPTER 2

# Crystalline motions and morphology of POM

## 2.1. Abstract

Mechanical Property of melt crystalized polyoxymethylene (POM) shows a deviation at around 97$^{o}$C, which is considered as the softening point of the sample, while it has a melting temperature of around 175$^{o}$C. According to the reports available in the literature, helical jump motions in the crystalline phase are believed to be responsible for the softening observed in POM at elevated temperatures. A recent report by Guruswami *et al*. showed that softening in POM occur only when it is prepared through melt crystallization and this is absent in a solution crystallized sample [4]. Using techniques such as Differential Scanning Calorimetry (DSC), Atomic Force Microscopy (AFM), Dynamic Mechanical Analyzer (DMA), Small Angle X-ray Scattering (SAXS) and Solid-State NMR (SSNMR), it was concluded that softening in the melt crystallized POM is due to the lamellar melting and not because of crystalline motions. However, a complete picture about the nature of crystalline motions and morphology of the different regions in both melt crystallized (MC) and solution crystallized (SC) POM was not provided in that paper. In this chapter, advanced solid-state NMR experiments such as CODEX, PISEMA, $T_{1,}$ and $T_2$ filtered PISEMA and spin-lattice relaxation were carried out on MC and SC POM samples for precise measurement of crystalline motions and information about the morphology and hence a deeper understanding about softening in MC POM. From our investigations, it is observed that the MC and SC POM have crystalline motions with similar activation energies and the nature of the amorphous region in the MC and SC POM are different from each other. The amorphous region of MC POM have high mobility with a distribution, while the amorphous region of SC POM has less mobility and the distribution of motion is absent in comparison to MC sample.

## 2.2. Introduction to POM

Homopolymer polyoxymethelne (POM) is a semi crystalline thermoplastic polymer, having good hardness, rigidity and strength. They are electrically resistant

and impermeable to gases and water. Because of these properties, this polymer is widely used in the automotive sector, electrical, mechanical and industrial applications [131]. POM is observed to have 4 different types of relaxation at the macroscopic level; δ relaxation is observed at -223$^{o}$C, γ transition with a wide range from -120 to -70$^{o}$C, a weak β transition around 0$^{o}$C, and finally an α transition is also observed in the range of 50 to 150$^{o}$C [4; 132; 133]. The β transition is assigned as the glass transition temperature ($T_g$) of the POM polymer. Suzuki *et al.* showed that the percentage of crystalline phase in POM is largely determined by the preparation condition of the sample [133]. Through heat capacity measurements, they showed for the first time the presence of a rigid amorphous phase in POM along with mobile amorphous and crystalline phases. Later, using dielectric relaxation measurements and dynamical mechanical analysis Read *et al*. showed that it is the disordered regions, not the crystalline part of POM that are responsible for any mechanical relaxation at room temperature [134]. They concluded that the chain segmental motion in the amorphous phase is responsible for this relaxation. Later, Hama *et al.*, in a series of papers analyzed the crystal structure growth in POM when it is cooled from 195$^{o}$C to RT [135-137]. While cooling from melt, at around 156$^{o}$C they observed the crystals of POM with folded chain crystal (FCC) morphology, having a period of 14 nm. As the temperature decreases to 140$^{o}$C, a new crystalline lamellae with extended chain crystal (ECC) morphology having a period 7 nm is observed. The new crystals are observed between the crystals which are already generated at 156$^{o}$C.

Based on the difference in spin lattice relaxation time ($T_1$) and rotating frame spin lattice relaxation time ($T_{1\rho}$) obtained from solid-state NMR, Veeman *et al.* identified the presence of crystalline and amorphous phases in POM [138]. Using cross polarization magic angle spinning solid-state $T_{1\rho}$ NMR experiments, Cholli *et al.* confirmed the presence of separate amorphous and crystalline phases in MC POM [139]. Using $^{1}$H spin diffusion and spin-spin relaxation solid-state NMR experiments, Tekely *et al.* showed the presence of three morphologically different regions in POM [140]. More details about dynamics and geometry of motions were obtained by the development of 2D experiments. From 2D exchange experiments at slow spinning speeds (700 Hz), Kentgens *et al.* estimated the nature of crystalline motions in the MC POM in the temperature range of 63 $^{o}$C to 87$^{o}$C and calculated the activation energy of motions as 83 kJ/Mol [2; 141]. Hagmeyer *et al.* also estimated the nature of the

crystalline motions using static exchange NMR experiments and calculated the activation energy of crystalline motion as 75±8 kilo Joules/Mol [3], which was similar to that estimated by Kentgens *et al.* Using a simulation of the 2D exchange spectra, they identified the geometry of the crystalline motions as a $9_5$ helical jump with jump angles of 0, ±200, ±400, ±600 and ±800 and the population of the jump angle is determined by the temperature. The activation energies estimated from these experiments were similar to those obtained from mechanical measurements and therefore it was concluded that the softening observed in MC POM is due to the onset of crystalline motions at these elevated temperatures.

The MC polymer soften at around 97$^{o}$C, which is called as the deflection temperature/softening point, although the melting point of the sample (175$^{o}$C) is far above the deflection temperature [142]. The low deflection temperature compared to the melting point restricts POM from its high temperature industrial applications. Recently, Guruswamy *et al*. obtained fresh insights into this problem by studying the macroscopic and microscopic behavior near the deflection temperature of MC and SC POM using techniques such as DSC, AFM, DMA and SAXS, in addition to Solid-State NMR [4]. Two morphologically different POM samples: injection molded (melt crystallized) and solution crystallized samples were used for the comparison. Using modulated DSC, it was shown that, melting and recrystallization in the crystalline part of MC POM occurs above 70$^{o}$C, while for SC sample this melting and recrystallization is absent till 140$^{o}$C. SAXS on the MC sample show a distribution in the lamellar crystal stacks and an irreversible melting and recrystalization happens when heated to 135$^{o}$C, while in case of SC POM the crystals are uniform in thickness and the melting and recrystallization process is reversible till it is heated to 150$^{o}$C. Using AFM it was observed that the softening is present only in MC POM, while in case of SC POM the softening is completely absent. DMA measurements also showed a decrease in elastic modulus in MC POM at high temperatures. The $^{13}$C MAS solid-state NMR spectra showed that the line shape of crystalline region for both the samples were similar at all the temperatures indicating that the crystalline motions are similar at all the temperatures. At high temperatures (100$^{o}$C), a narrowing of the amorphous peak in the MC sample was observed, while it was not seen in SC POM. Using $^{13}$C spin-lattice relaxation experiments at room temperature, it was also inferred

that a rigid amorphous phase is present in the molded sample along with crystalline and amorphous phases.

Advanced solid-state NMR experiments were carried out on MC and SC POM samples for getting a deeper understanding about the molecular dynamics which is responsible for the observed difference in mechanical property are described in this chapter. Three sets of investigations that were carried out are 1) correlation times of the slow crystalline motions were measured for both MC and SC sample by the CODEX experiment for different temperatures through its softening point and the activation energy calculated using the Arrhenius equation, 2) $T_1$ and $T_1$ filtered PISEMA experiments were carried out at different temperatures through its softening point for analyzing the nature of the components in the sample, 3) $T_1$ and $T_2$ filtered PISEMA experiments were carried out at different temperature through its softening point to analyze the differences in morphology between crystalline and amorphous regions of the MC and SC samples.

## 2.3. Material

The Polyoxymethylene pellets having molecular weight of 112700 g/mole received from DELRIN was used for the preparation of MC and SC sample. The MC and SC POM was prepared according to the protocol described by Guru *et al*. [4].

**Melt Crystallized (MC) Sample**: 20 g of DELRIN POM pellets were kept in an oven for 4 hrs at 80$^{o}$C for the complete removal of moisture from the pellets. The dried sample was slowly fed into the injection molding machine (DSM Microinjection Molder) which was kept at 215$^{o}$C with the screw rpm of 20. The thick solution of POM was then injected into an injection mold kept at 90$^{o}$C. The thick bars of MC sample obtained were used for all further experiments.

**Solution Crystallized (SC) sample:** About 0.4 g of POM was weighed and dissolved in 40 ml of cyclohexanol at 160$^{o}$C. The hot transparent solution was slowly cooled to 140$^{o}$C. When a polymer suspension was observed at this temperature, it was heated back to 155$^{o}$C and suddenly transferred to 400 ml cyclohexanol kept in a 135$^{o}$C thermal oil bath. This isothermal solution was kept for 24 hrs for maximum crystallization. The micro crystals obtained was filtered after 24 hrs using a porcelain funnel using silk sieves. The micro crystal of POM collected in the sieve was first

washed with hot cyclohexanol at 120°C, and then with hot water and finally with boiled acetone. The material obtained was kept in the vacuum oven for 80°C for 24 hrs and then used for NMR measurements.

## 2.4. Experimental

The purity of MC and SC POM samples were confirmed by DSC, SAXS, CPMAS-SSNMR before carrying out advanced SSNMR experiments. All measurements were carried out on 300 MHz Bruker Avance solid-state NMR spectrometer with carbon frequency of 75 MHz. A triple resonance 4 mm DVT probe in a double resonance mode with a magic angle set up was used for all measurements. The MC sample was cut into small pieces and filled in the 4 mm Zirconia rotor, and small pieces of SC sample obtained during crystallization was packed into the rotor with a gentle push without changing the macroscopic crystalline morphology. All the CODEX experiments were carried out at a spinning speed of 3 kHz while the PISEMA and spin-lattice relaxation measurements were carried out at spinning speed of 8 kHz with a spinning stability of ±1 Hz. The temperatures for the measurements were calibrated using methanol [143] and $PbNO_3$ [144] at spinning speeds of 3 kHz and 8 kHz separately. The sample temperature was calibrated from 25°C to 100°C. CODEX experiment were carried out with $^1$H RF power of 79.6 kHz, $^{13}$C RF power of 66 kHz and a cross polarization time of 2.5 $msec$ for both the MC and SC samples. During $N\tau_r$ evolution period of CODEX, a low power $^1$H decoupling is used. A gradual increase in $^1$H spin-lattice relaxation time was observed in case of the MC sample, while for the SC sample, it showed a gradual decrease. A recycle delay of five times the $^1$H spin-lattice relaxation time was used for all the CODEX experiments. The CODEX experiments were carried out at 23, 60, 70, 80, 85, 90, 95, 100 and 105°C for the MC and SC samples. At each temperature $\tau_m$ dependence experiments were carried out with a mixing time of 1 $msec$ to 12.3 $sec$ with 14 points in between. A $z$-filter time ($\tau_z$) of 1 $\mu sec$ is used for all the CODEX experiments. During the signal acquisition, a high power decoupling with TPPM-15 was used in the $^1$H channel. All the CODEX experiments with mixing times ($\tau_m$) of 1 $msec$ to 2 $sec$ were done with 128 transients and the remaining $\tau_m$ measurements were done with 512 transients because of low signal to noise ratio at longer mixing times.

The PISEMA and $^{13}C$ spin-lattice relaxation ($T_1$), the $T_1$ and $T_2$ filtered PISEMA experiments were carried out at 29, 50, 70 and 100$^oC$. PISEMA experiments were carried out with a Lee-Goldberg pulse block, in which the $^1H$ magnetization was spin locked at magic angle (54.74$^o$) with an effective RF field of 73.5 kHz. During the Lee Goldberg pulses in the $^1H$ channel, RF pulses with frequency of $\upsilon_{13C} + \upsilon_r = 92.9$ kHz and $\upsilon_{13C} - \upsilon_r = 76.9$ kHz were applied in the $^{13}C$ channel at a spinning speed of 8 kHz. At each temperature, the spin-lattice relaxation time of the proton was measured and the recycle delay was set to five times of this. All the PISEMA experiments were carried out with the STATES acquisition mode [145]. $^{13}C$ $T_1$ relaxation data at each temperature was measured using the Torchia experiment [125] and the data obtained was fitted with an exponential decay (equation 1.58) to obtain the $T_1$ values. The $T_1$ filtered PISEMA experiments were carried out with different $T_1$ filters for obtaining information on the morphology. For the $T_2$ filtered PISEMA experiments a $T_2$ filter of 150 $\mu sec$ was used. For SC and MC samples, the $T_1$ filtered PISEMA experiments were carried out with 192 $t_1$ increments with 16 scans. For the MC sample, all the $T_2$ filtered PISEMA experiments were carried out with 350 $t_1$ increments with 16 scans while for the SC sample, 64 scans were collected for each 192 $t_1$ increments. All the spectra were processed using 'QFIL' (topspin) dc offset correction routine in the indirect dimension for removing the center frequency.

## 2.5. Results and Discussion

The $^{13}C$ CPMAS spectra of the MC and SC samples which were recorded at 23, 60, 80 and 100$^oC$ are shown in figure 2.1. The spectra of MC and SC samples at 23$^oC$ shows a prominent peak at about 88.5 ppm which has a splitting and a broad peak centered around 90 ppm at the base. The peak with a splitting seen at 88.5 ppm is assigned to the crystalline region and the broad peak is assigned to the amorphous region [4; 138]. As the temperature increases to 100$^oC$, a merging of the two crystalline peaks is observed, at the same time the broad amorphous peak narrows down and become well separated from the crystalline region. This is in agreement with the results from Guru *et al*. where the $^{13}C$ spectra were acquired by dipolar decoupled magic angle spinning (DDMAS) experiment. A merging in the crystalline peak is observed for both MC and SC sample near softening point. In Guru *et al.*, the merging of the two crystalline peaks at 100$^oC$ in both the samples was attributed to the crystalline motions at these temperatures. Due to the similarity of the crystalline

peak, it was concluded that the crystalline motions are similar for both the MC and SC POM. However, it is not possible to measure the frequency and activation energy of the crystalline motions using a simple one-pulse NMR experiment. In this chapter, the geometry and frequency of the crystalline motions have been determined and the activation energy of the crystalline motions is calculated for both the MC and SC POM around the softening point using the CODEX experiments. Further, the nature of the amorphous phase have been explored from 29°C to 100°C using a combination of PISEMA, $^{13}C$ spin-lattice relaxation time ($T_1$), $T_1$ and $T_2$ filtered PISEMA experiments.

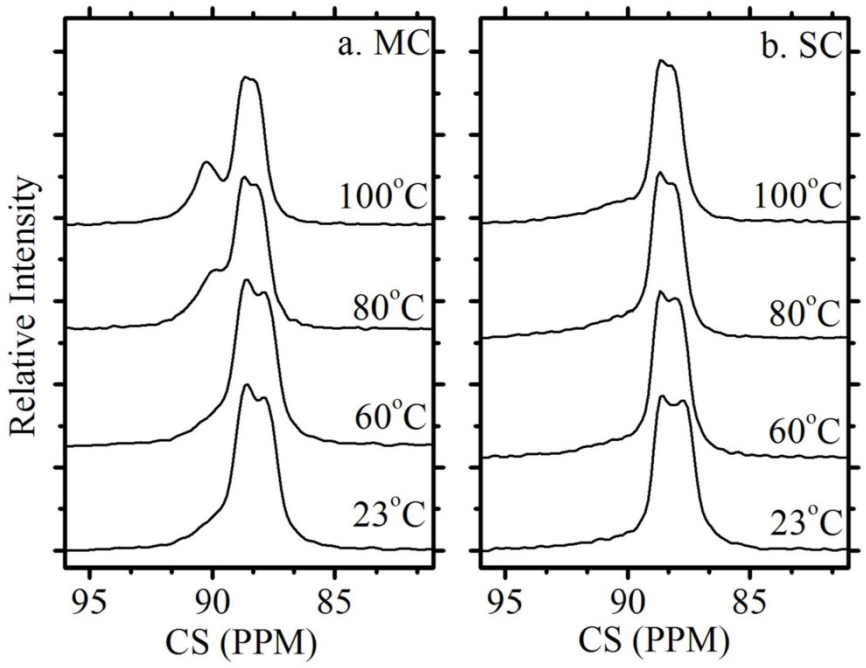


*Figure 2.1: The $^{13}C$ CPMAS spectra of a).MC and b).SC POM at temperatures 23, 60, 80 and 100°C. In MC POM, a shoulder peak is observed for the crystalline region at higher temperatures and it becomes a separate narrow peak when the temperature reaches 100°C. This behavior is not seen in the amorphous region of the SC POM sample. In addition, for both MC and SC POM samples, the crystalline peaks merge at 100°C.*

### 2.5.1. Crystalline motions in POM using CODEX experiment

From the CODEX experiments, it is possible to estimate the geometry and frequency of slow motions. In the CODEX $N\tau_r$ dependence experiment, the mixing time is kept constant while the recoupling time $N\tau_r$ is varied for the determination of the geometry of motion and also used to find out the $N\tau_r$ value at which the dephasing attains a plateau which is used for the $\tau_m$ dependence experiment. For all

the CODEX $N\tau_r$ dependence experiments, a mixing time of 4.1 $sec$ and z-filter time of 1 $\mu sec$ were used. At 23°C, $N\tau_r$ dependence measurements does not show any decay in the crystalline peak in both MC and SC POM indicating that crystalline motions are absent. As the temperature was increased to 70°C, the CODEX $N\tau_r$ dependence measurements show a decay indicating the onset of crystalline motions. The CODEX $N\tau_r$ dependence measurements obtained at 100°C for the MC and SC samples are shown in figure 2.2. The CODEX $N\tau_r$ dependence measurements attains a plateau of ~0.2 when $N\tau_r$ reaches 2 $msec$ and this value is used as the $N\tau_r$ for all the CODEX $\tau_m$ dependence experiments. Using a $9_5$ symmetry with a jump angle of 200° between the sites, the CODEX $N\tau_r$ curve simulated using the model proposed by Schmidt-Rohr [41] is in excellent agreement with the experimental values as shown in figure 2.2. This is in accordance with the motional models proposed by Kentgens *et al.*[2] and later by Hagemeyer *et al.*[3] where the crystalline part of POM show helical jump motions with $9_5$ symmetry, ie. during 5 complete rotation of the helix, the -$OCH_2$- group passes through 9 equivalent sites with a jump angle of 200° each. The important observation made from this experiment is that, the geometry of motion at 100°C for the MC and SC POM is same.

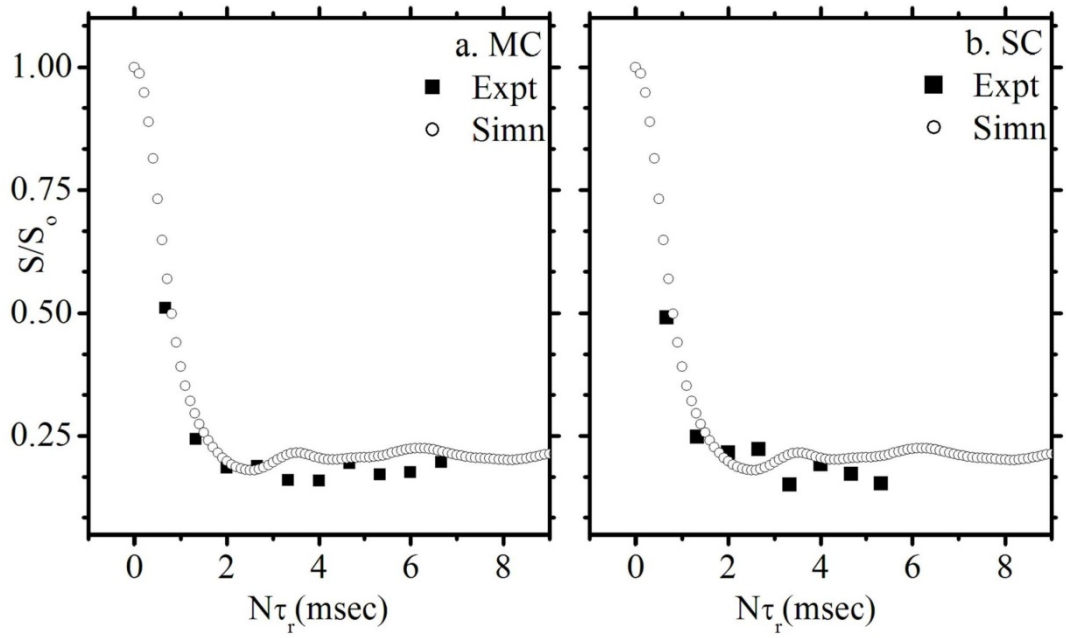


*Figure 2.2: The CODEX $N\tau_r$ curve dependence measurements for a).MC and b).SC POM at 100°C with simulated dephasing curves. A model with $9_5$ helical jump having jump angle of 200° matches with the experimental results. The dephasing curve reaches a plateau value at $N\tau_r$ of ~2msec.*

The CODEX $\tau_m$ dependence experiments were carried out for the MC and SC POM at 23, 60, 70, 80, 85, 90, 95, 100 and 105°C. All the CODEX $\tau_m$ dependence experiments were carried out with a fixed value of 2 $msec$ as the recoupling time ($N\tau_r$). No significant difference was observed between the CODEX and the reference spectra at 23°C. But appreciable differences in spectra were seen as the temperature was increased beyond 70°C. The difference spectra of MC and SC POM at 100°C with mixing times of 1, 128, 1024, and 8192 $msec$ are shown in the figure 2.3.

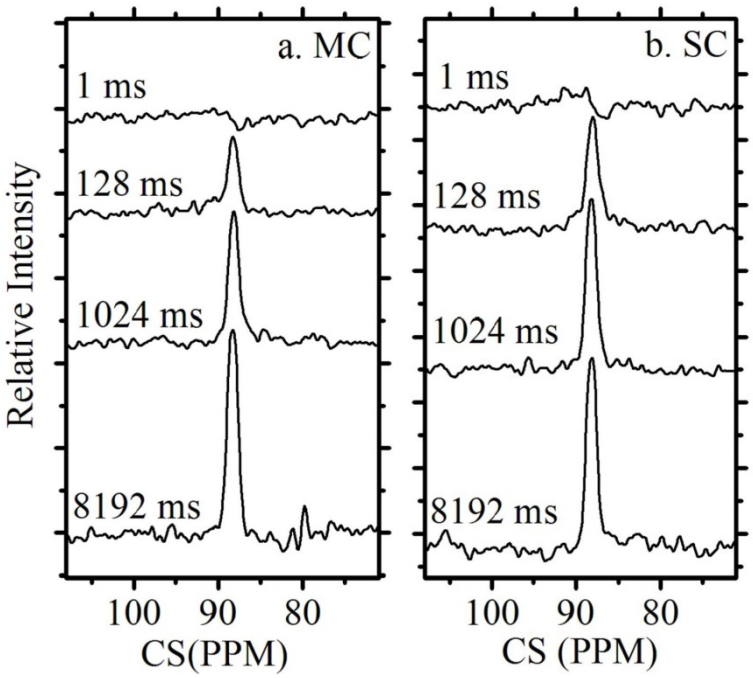


*Figure 2.3: The CODEX difference spectra of a)MC and b)SC POM at 100°C with mixing times of 1 msec, 128 msec, 1024 msec and 8192 msec with $N\tau_r$ time of 2 msec.*

The CODEX $\tau_m$ dependence measurements for the MC and SC sample from 23°C to 105°C are shown in figure 2.4. The $\tau_m$ dependence at the 23°C shows that the dephasing in the CODEX signal is low indicating that the crystalline motions are either very slow or completely absent. As the temperature increases, the CODEX $\tau_m$ dependence measurements show more decay indicating that rates of the crystalline motions are increasing. The decay does not reach a plateau till 70°C indicating that the motions at these moderate temperatures are very slow. The $\tau_m$ dependence measurements obtained from 80°C to105°C shows a plateau and the data points obtained is fitted with the KWW function to extract the correlation time.

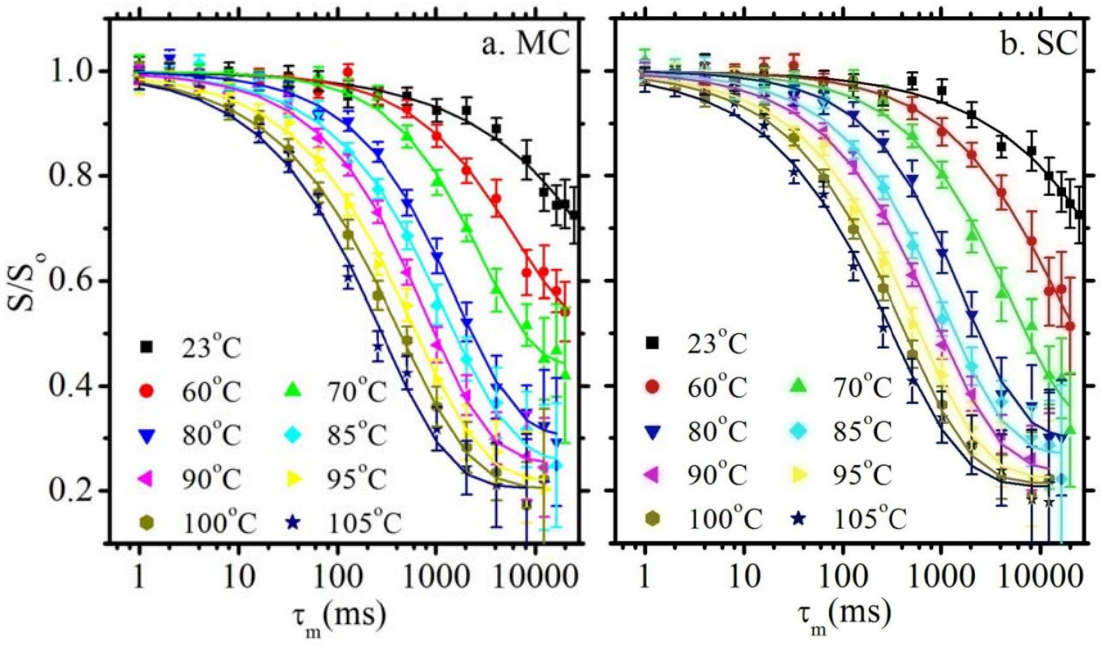


*Figure 2.4: The results of the CODEX mixing time ($\tau_m$) dependence experiments fitted with the KWW function at different temperatures for a. MC and b. SC POM samples. Till 70°C the curve does not show much dephasing, from 80°C to 105°C, it shows significant dephasing with a clear plateau value.*

The values obtained from KWW fit are tabulated in table 1. The MC and SC sample show similar correlation times ($\tau_c$) at each temperature indicating that the crystalline regions in both the samples have similar motional frequency. A gradual

| Temp (°C) | Melt Crystallized POM | | | Solution Crystallized POM | | |
|---|---|---|---|---|---|---|
| | $M$ | $\tau_c\ (msec)$ | $\beta$ | $M$ | $\tau_c\ (msec)$ | $\beta$ |
| 80 | 0.70±0.01 | 1648±105 | 0.71±0.02 | 0.70± 0.01 | 1773±130 | 0.76±0.04 |
| 85 | 0.74±0.02 | 1314±24 | 0.65±0.03 | 0.73±0.01 | 1128±124 | 0.69±0.05 |
| 90 | 0.75±0.01 | 831±38 | 0.68±0.02 | 0.76±0.01 | 896±55 | 0.66±0.02 |
| 95 | 0.78±0.01 | 615±41 | 0.62±0.02 | 0.78±0.01 | 577±50 | 0.64±0.03 |
| 100 | 0.80±0.01 | 444±39 | 0.59±0.03 | 0.78±0.01 | 429±27 | 0.63±0.02 |
| 105 | 0.80±0.02 | 286±31 | 0.62±0.04 | 0.79±0.02 | 322±35 | 0.59±0.04 |

*Table 2.1: The percentage of crystalline components available for motions ($M$), the correlation time ($\tau_c$), and the distribution in correlation time ($\beta$) obtained for a).MC and b).SC POM at 80, 85, 90, 95, 100 and 105°C using CODEX $\tau_m$ dependence experiment. Both the MC and SC samples have similar correlation time at near the softening temperature.*

decrease in the correlation time with temperature indicates an increase in the frequency of motion. A gradual increase in M with respect to temperature is observed for both the MC and SC samples, which indicates that the fraction of the polymer chain units contributing to crystalline motion is increasing. A gradual decrease in the stretched exponential factor $(\beta)$ indicates that the distribution in the correlation time increases with temperature.

The activation energy of the crystalline motion can be determined using the Arrhenius equation 2.1 [117].

$$\ln(\nu) = -\frac{E_a}{RT} + \ln(A) \tag{2.1}$$

where $\nu$ is the frequency of motion at a temperature T (Kelvin), R is the universal gas constant, $E_a$ is the activation energy and $A$ is the amplitude which is a constant. The inverse of the correlation time is plotted against the inverse of the temperature (Kelvin) and fitted with the Arrhenius equation. The Arrhenius plots of the MC and SC samples are shown in figure 2.5. The slope of the fit gives the activation energy of the crystalline motions as 77.9 kJ/mol and 75.4 kJ/mol for the MC and the SC

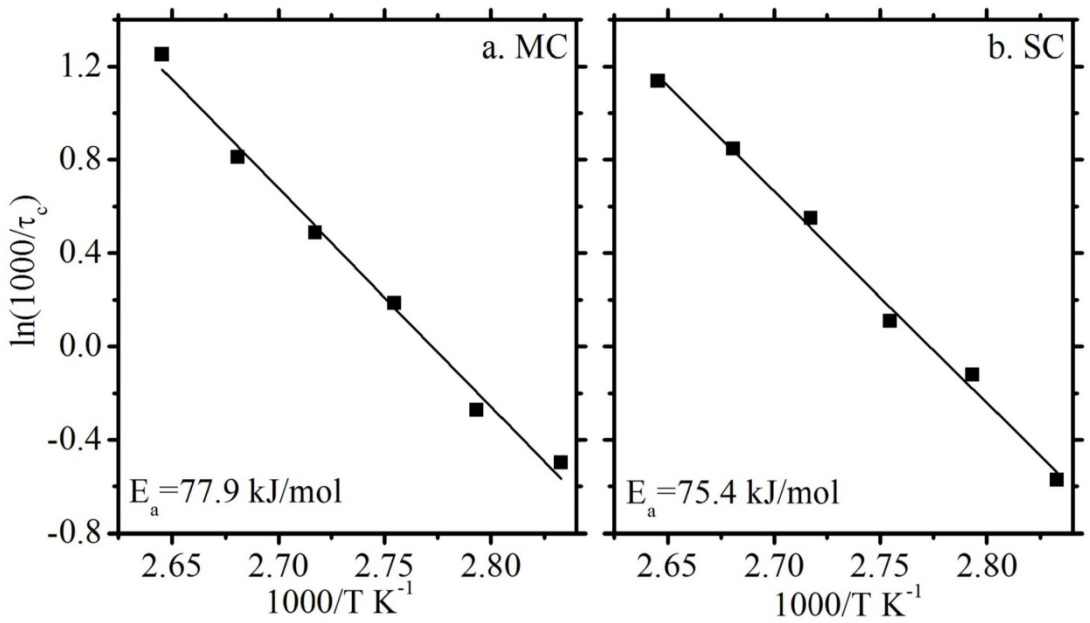


*Figure 2.5: Arrhenius plot of a).MC and b).SC POM obtained during the temperature range of 80 to 105°C, through the softening point. The log of correlation time (sec) is plotted against 1/T (Kelvin). Activation energy of 77.9 kJ/mol and 75.4 kJ/mol were estimated for the crystalline motions in MC and SC POM respectively.*

samples respectively. This shows that the crystalline motions in both MC and SC have similar activation energy and hence indicate that even if crystalline motions are present in the MC sample it is not responsible for the softening. If the crystalline motions are responsible for the softening in POM both MC and SC should show softening, but the softening is observed only in SC samples. The activation energy of the crystalline motions calculated by the CODEX experiment is comparable to that reported in literature [2; 3].

### 2.5.2. $^{13}$C Spin-lattice relaxation measruements ($T_1$)

Using AFM, DMA and SSNMR Guru *et al.* showed that the softening in POM happens when it is prepared through the melt crystallization [4]. The CODEX experiment results discussed in this chapter confirm that MC and SC POM have similar activation energy for crystalline motions and it indicates that the origin of softening in MC POM is not from the crystalline region. Using SAXS, Guru *et al.* showed that lamellar melting of imperfect crystals which are present between the main crystals is responsible for the softening in MC POM at 97$^o$C. Using $^{13}$C spin-lattice relaxation ($T_1$) experiment at 29$^o$C, it was also shown that there is a rigid amorphous phase which has mobility in between that of the amorphous and crystalline phases. A $^{13}$C $T_1$ experiment was carried out using the saturation recovery method which was fitted to a model with 3 components for the relaxation time and they were 0.47 $sec$, 2.2 $sec$ and 23.5 $sec$ which were assigned to amorphous, rigid amorphous and crystalline region respectively. In this study, the $^{13}$C $T_1$ measurements were carried out at different temperatures using CP based $^{13}$C $T_1$ relaxation experiment developed by Torchia [125] since this is much more sensitive than the $^{13}$C saturation recovery experiments.

The data from $^{13}$C $T_1$ relaxation experiment using the Torchia method is carried out on the MC POM at 29$^o$C was fitted with three component exponential decay function and the relaxation times obtained 0.28 $sec$, 1.34 $sec$ and 25 $sec$ was assigned to the amorphous ($T_A$), rigid amorphous ($T_{RA}$) and crystalline phases ($T_C$) respectively. However, it is observed that the error in the estimation of the relaxation time of the rigid amorphous phase was very high. A similar error is seen in the estimation of $T_1$ of the amorphous region at higher temperatures also. For SC sample only amorphous and crystalline regions are expected, hence a two component

exponential decay fit gives a $T_1$ relaxation time of 0.53 *sec* ($T_A$) and 25 *sec* ($T_C$) respectively at RT. The experimental results and the fit using a three component (MC) and two component (SC) models for different temperatures are shown in figure 2.6a and 2.6b. The corresponding $T_1$ values obtained are tabulated in table 2.2.

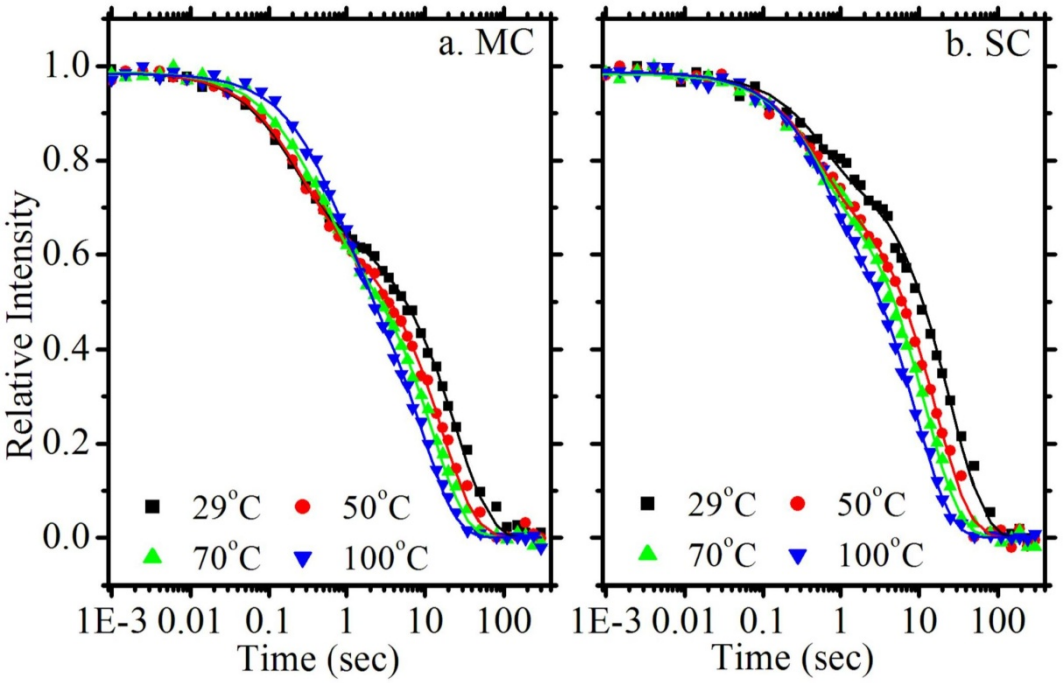


*Figure 2.6: The $^{13}C$ spin lattice relaxation data of a).MC and b).SC sample fitted with 3 components and 2 component exponential decay equation respectively at different temperatures 29°C, 50°C, 70°C and 100°C.*

| Temp (°C) | MC POM (3 component) | | | SC POM (2 component) | |
|---|---|---|---|---|---|
| | $T_A$ | $T_{RA}$ | $T_C$ | $T_A$ | $T_C$ |
| 29 | 0.19±0.03 | 1.34±0.57 | 25.15 | 0.53±0.07 | 25.15±0.78 |
| 50 | 0.19±0.06 | 0.75±0.37 | 16.56 | 0.48±0.05 | 16.56±0.47 |
| 70 | 0.19±0.13 | 0.62±0.20 | 12.44 | 0.48±0.04 | 12.44±0.34 |
| 100 | 0.31±0.56 | 0.84±0.32 | 9.39 | 0.57±0.04 | 9.39±0.22 |

*Table 2.2: The $^{13}C$ spin lattice relaxation times of the amorphous ($T_A$), rigid amorphous ($T_{RA}$) and crystalline phases ($T_C$) of MC POM and that of amorphous ($T_A$) and crystalline phases ($T_C$) of SC POM at different temperatures.*

In order to verify the presence of the rigid amorphous phase with the above $T_1$ values, $T_1$ filtered PISEMA experiments were carried out which is described below.

### 2.5.3. $T_1$ filtered PISEMA

A clear evidence for the presence of rigid amorphous phase is still an open issue in polymer science [146-148]. The aim of the PISEMA experiments was to obtain further insights into the nature of the amorphous region and in particular to obtain a clear proof for the existance of a rigid amorphous phase which has mobility in between that of the amorphous and the crystalline phase. To investigate the presence of rigid amorphous phase in MC POM [4; 133] $T_1$ filtered PISEMA with different $T_1$ filters 0.0 $sec$ (without $T_1$ filter), 0.25 $sec$, 0.75 $sec$ and 1.5 $sec$ at different temperatures were carried out. The pulse sequence of the $T_1$ filtered PISEMA experiments is shown in figure 1.24a.

The results of $T_1$ filter PISEMA experiments carried out on the MC sample at 29, 50, 70 $^oC$ are shown in figure 2.7 and at 100$^oC$ is shown in figure 2.8. The 2D spectra without the $T_1$ filter for different temperatures show two separate sets of contours (figure 2.7a, 2.7d, 2.7g, 2.8a). The separation between the sets of contours in the $F_1$ axis indicates two separate regions with different dipolar coupling. The contours with a separation of 21.5 kHz is assigned to the crystalline region in MC POM, which has the same dipolar width as that of the CH environment in crystalline alanine. This similar dipolar coupling indicates, motions in the ranges of hundreds of kHz are absent in crystalline region of MC POM at these temperatures. From the CODEX experiment, it has already been established that the crystalline region experiences slow motions (100s of $Hz$), and the results from PISEMA experiment shows that the crystalline regions does not have any fast motions. The contours with smaller separation of ~5 kHz is assigned to the amorphous region.

A $T_1$ filtered PISEMA experiment with a $T_1$ filter $\geq$ 2-4 times the $T_1$ of the amorphous region should supress the contours corresponding to the amorphous regions and hence only rigid amorphous and crystaline region should survive. The amorphus regions of MC samples have $T_1$ relaxation times of 0.19 $sec$ (table 2.2) at 29$^oC$ according to the 3 component model and a $T_1$ filtered PISEMA experiment with a $T_1$ filter of 0.75 $sec$ ($\sim$ 3*$T_1$ of amorphus region) should remove the amorphous region from the spectrum and hence only rigid amorphous and cyrstaline region is expected to survive.

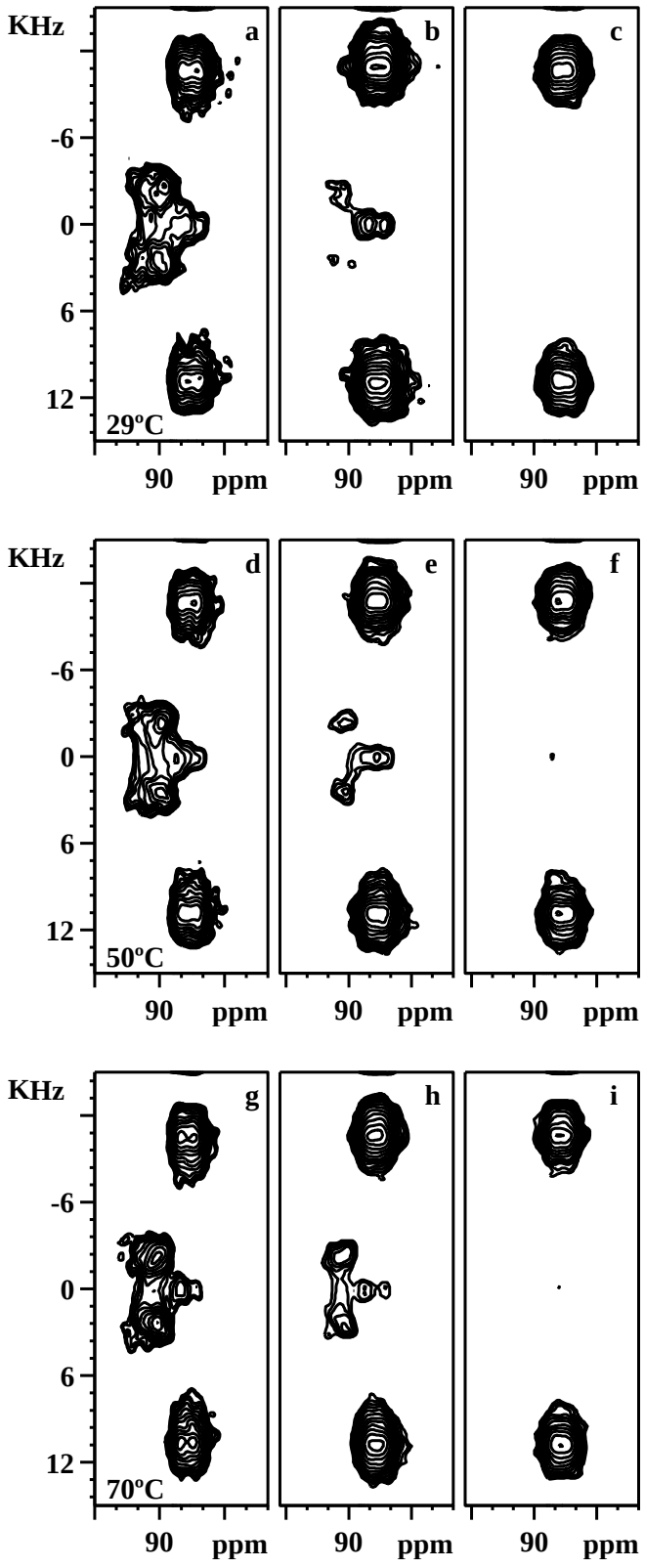


*Figure 2.7: PISEMA and $T_1$ filtered PISEMA spectra of MC samples at $T_1$ filters of 0 sec (a,d,g), 0.25 sec (b,e,h), 0.75 sec(c,f,i) for the temperatures 29°C, 50°C and 70°C.*

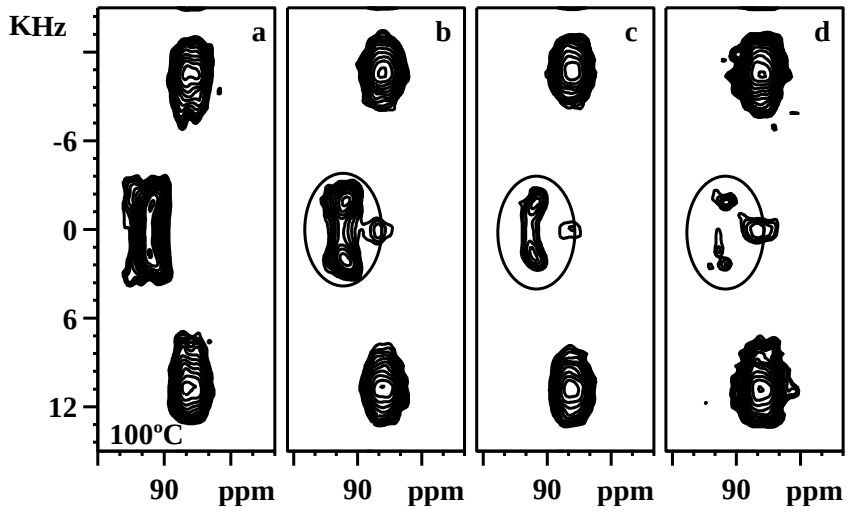


*Figure 2.8: PISEMA and $T_1$ filtered PISEMA spectra of MC samples with $T_1$ filters of a).0 sec b).0.25 sec, c).0.75 sec d).1.5 sec at 100°C. The amorphous region does not vanishes even with $T_1$ filter of 1.5 sec, while at lower temperatures it vanishes with a $T_1$ filter of 0.75 sec indicating that the $T_1$ relaxation time of amorphous region has increased at 100°C.*

The $T_1$ filtered PISEMA spectra at different temperatures with a $T_1$ filter of 0.25 *sec* shows the contours of the inner region has not vanished (figure 2.7b, 2.7e, 2.7h, 2.8b) indicating that the $T_1$ of the amorphous region calculated from the three component model could be correct. However, the $T_1$ filtered PISEMA spectra with a $T_1$ filter of 0.75 *sec* at 29, 50, 70°C, all the inner regions vanishes (figure 2.7c, 2.7f, 2.7i) indicating that a separate rigid amorphous phase with a $T_1$ of 1.35 *sec* - 0.8 *sec* are not possible. If a component with $T_1$ relaxation value of 1.35 *sec* - 0.8 *sec* is present (intermediate region) it should survive the $T_1$ filtered PISEMA with filter time of 0.75 sec. An exception is seen only at 100°C (figure 2.8c). At 100°C, the PISEMA experiment with $T_1$ filter of both 0.75 *sec* and 1.5 *sec* shows contours with amorphous region (figure 2.8c, 2.8d), indicate the $T_1$ relaxation value of amorphous region increases with temperature. This indicates the nature of the amorphous phase of MC POM around the softening temperature is different from that at lower temperatures. Since the $T_1$ filtered PISEMA with a $T_1$ filter time of 0.75 *sec* at temperatures 29, 50 and 70°C show only contours with dipolar coupling of 21.5 kHz, it can be concluded that the rigid amorphous phase is absent in MC POM.

Based on the results from $T_1$ filtered PISEMA experiments which showed that a three component model is incorrect, the $T_1$ relaxation data of MC POM were fitted with a two component exponential decay model and the results had lesser error bars. The experimental $^{13}C$ $T_1$ data for MC POM at different temperatures and their fit using a two component model are shown in figure 2.9. The $^{13}C$ $T_1$ relaxation times obtained for the amorphous and crystalline phases of MC sample at different temperatures is tabulated in table 2.3.

The values of $T_1$ obtained from the two components fit are in excellent agreement with the results of $T_1$ filtered PISEMA experiments. The $T_1$ of the amorphous region are 0.28, 0.32, and 0,47 *sec* at 29, 50, and 70°C respectively. The $T_1$ filtered PISEMA spectra with a $T_1$ filter of 0.25 *sec* at these temperatures show that the amorphous region is present since the $T_1$s are larger than the $T_1$ filter. For the $T_1$ filtered PISEMA spectra with a filter time of 0.75 *sec*, the amorphous region have vanished since the $T_1$ is smaller than the $T_1$ filter values. However, the $T_1$ filtered PISEMA spectra with a $T_1$ filter of 0.75 *sec* at 100°C shows the presence of the amorphous region since the $T_1$ is 0.77 *sec* and the amorphous region is barely visible

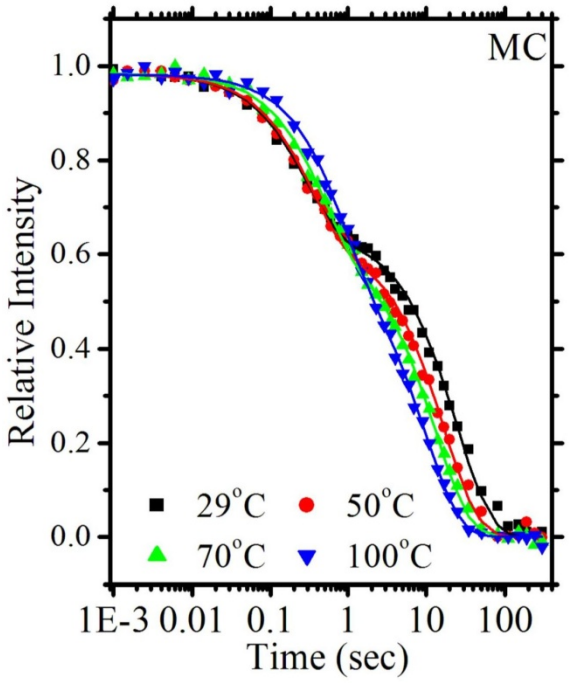


*Figure 2.9: The results of the $^{13}C$ spin lattice relaxation experiment fitted with exponential decay for MC (2 components) POM obtained at different temperatures from 29°C to 100°C.*

in the $T_1$ filtered PISEMA spectra with this $T_1$ filter of 1.5 *sec* which is less than 2 times the $T_1$ at this temperature. It is likely that at 100°C the amorphous region is visible even at the $T_1$ filter of 1.5 *sec* since there is larger population of the amorphous region at this temperature.

| Temp (°C) | MC POM (2 component) | |
|---|---|---|
| | $T_A$ | $T_C$ |
| 29 | 0.28±0.02 | 24.80±0.73 |
| 50 | 0.32±0.02 | 17.02±0.48 |
| 70 | 0.47±0.02 | 13.33±0.36 |
| 100 | 0.77±0.04 | 10.00±0.33 |

*Table 2.3: The $^{13}C$ spin lattice relaxation times of MC POM amorphous phases obtained with two component fit at different temperatures.*

The $T_1$ relaxation times of the amorphous and crystalline phases obtained from the MC and SC POM samples obtained with a two component model is plotted against the temperature and is shown in figure 2.10. The crystalline part of both MC and SC POM shows a decrease in $^{13}C$ $T_1$ relaxation time with increase in temperature but at each temperature both samples shows similar relaxation times. But the amorphous region of MC and SC POM shows completely different behavior. The $^{13}C$ $T_1$ relaxation times of MC amorphous region show an increase in relaxation time with temperature, while the SC amorphous $^{13}C$ $T_1$ relaxation time is almost constant throughout the temperature up to the deflection point. This reiterates the fact that the origin of softening observed in MC POM may is not from the crystalline part, but from the amorphous region.

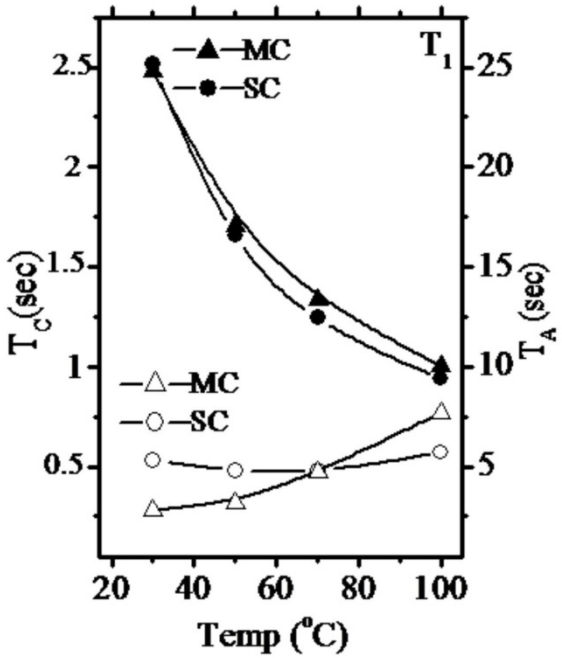


*Figure 2.10: A plot of spin lattice relaxation times of crystalline $T_C$ and amorphous region $T_A$ of MC and SC POM. Filled symbols correspond to crystalline region while hollow symbol corresponds to the amorphous region.*

To obtain further insights into nature of the crystalline and amorphous region, the $T_1$ filtered and $T_2$ filtered PISEMA were carried out at different temperature and the results are discussed below.

## 2.5.4. Nature of crystalline and amorphous phase

To monitor the nature of the crystalline regon at different temperatures, $T_1$ filtered PISEMA experiments were carried out for the MC and SC POM, and the results are shown in figure 2.11. A $T_1$ filter of 1.5 $sec$ was used at all the temperatures except at 100$^o$C for MC POM, where it was 2.5 $sec$. A dipolar coupling of 21.5 kHz was observed for the MC and SC POM at these temperaures. Since there is no change in the dipolar coupling for the crystaline region with respect to the C-H diplar coupling in alanine, motions in the range of hundreds of kHz is absent in the crystalline region of MC and SC POM at these temperatures. It is also seen that the two crysalline peaks of both MC and SC sample merges at 100$^o$C, which similar to that obseved in the case of CPMAS spectra discussed earlier.

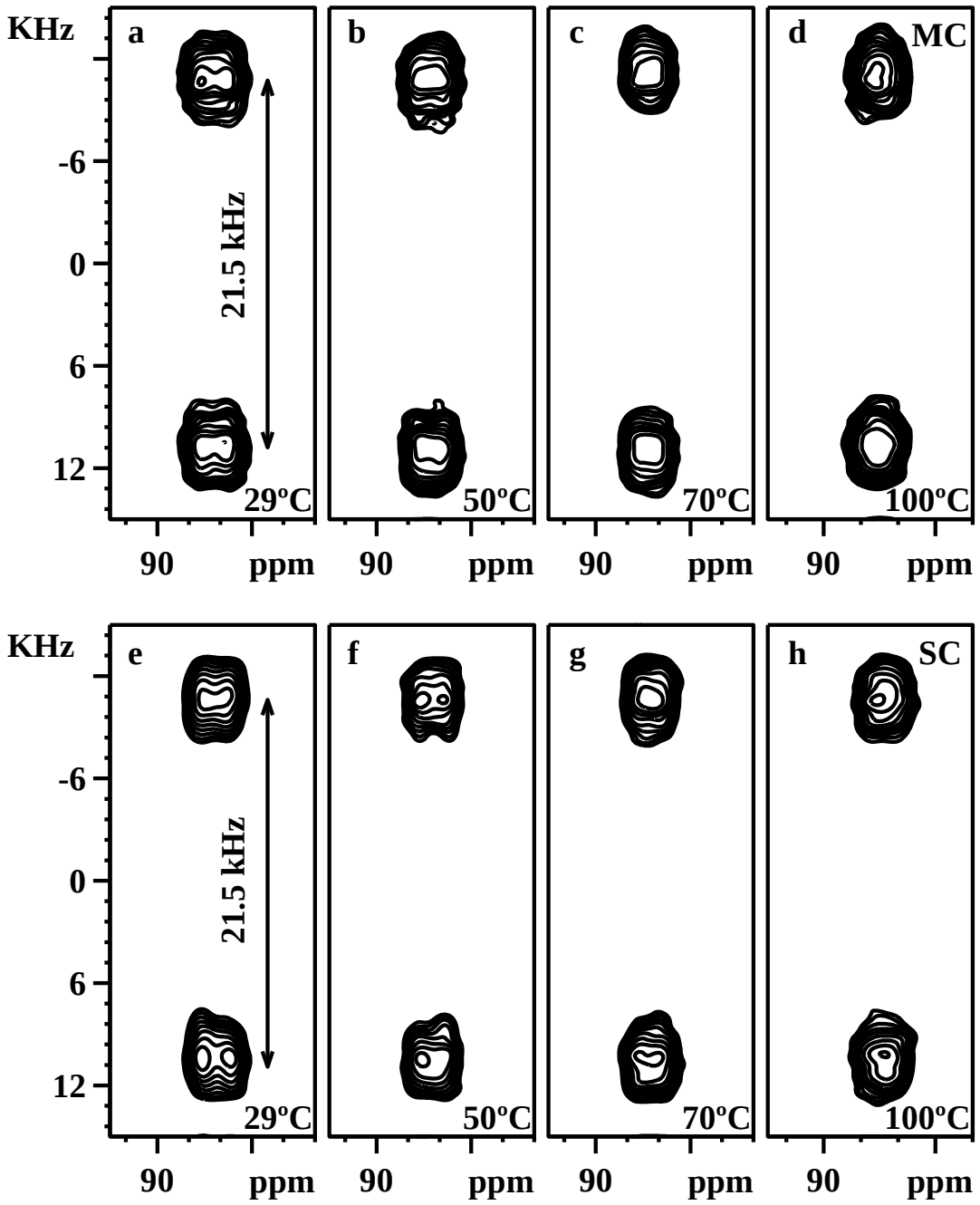


*Figure 2.11: $T_1$ filtered PISEMA spectra showing the contours corresponding to the crystalline region in MC and SC POM at 29 $^oC$ (a,e), 50 $^oC$ (b,f), 70 $^oC$ (c,g) and 100$^oC$ (d,h). $T_1$ filter was 1.5 sec for all the temperatures except for MC at 100$^oC$. At 100$^oC$ the $T_1$ filter was 2.5 sec for the MC sample. The dipolar coupling width of 21.5 KHz is observed for both the samples at different temperatures.*

The $T_2$ filtered PISEMA spectra of the MC and SC POM with a $T_2$ filter of 150 $\mu sec$, filters out the contours from the crystalline region and the contours corresponding to the amorphous region only survive (figure 2.12). In figure 2.11 the contours corresponding to the crystalline region of the SC and MC POM are shown,

which are parallel to the $F_2$ axis implying that the distance between the peaks are constant and hence it has uniform dipolar coupling. However, for the amorphous region of the MC POM, a distribution in the dipolar coupling is observed and width between the contours varies from 5 kHz to 6 kHz at 29°C. The values of the dipolar coupling indicate that the amorphous region have mobility in the range 100s of kHz, while the distribution in dipolar coupling indicates the amorphous region of MC POM have a distribution in mobility. For the MC POM, a decrease in dipolar coupling is observed with an increase in temperature. At 100°C, the distribution vary from

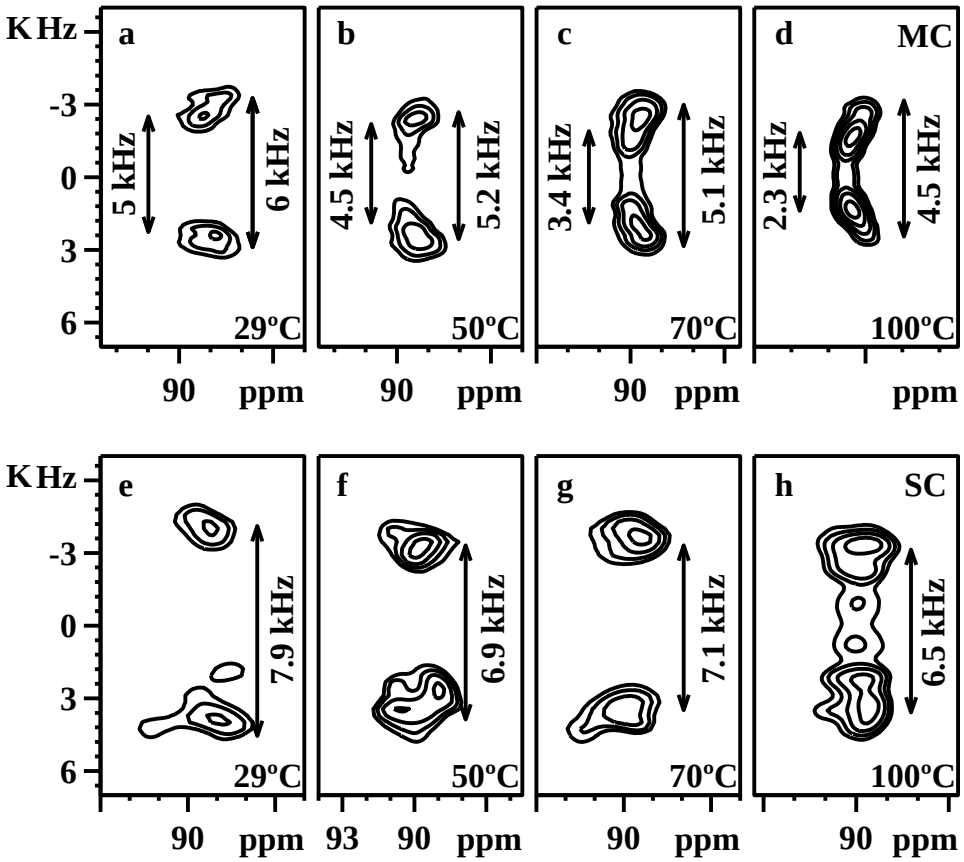


*Figure 2.12: Amorphous peak of MC and SC POM obtained by $T_2$ filtered PISEMA at 29 °C (a,e), 50 °C (b,f), 70 °C (c,g) and 100°C (d,h). A distribution in dipolar coupling is observed for MC POM at all the temperatures. At 29°C the distribution vary from 5 kHz to 6 kHz, a gradual decrease in dipolar coupling is observed with increase in temperature and at 100°C the distribution become 2.3 kHz to 4.5 kHz. In SC POM, dipolar coupling of 7.9 kHz at 29°C and 6.5 kHz at 100°C is observed. The distribution of dipolar coupling is absent in the amorphous phase of the SC POM. In addition, the dipolar coupling of the amorphous phase of MC POM is always lower than that of the amorphous phase of SC POM at each temperature.*

2.3 kHz to 4.5 kHz indicating that there is substantial increase in mobility which was already observed in the CPMAS spectra as separate region, where the region of amorphous phase separate out completely from crystalline region. For the SC POM, we see only a reduction in the dipolar coupling: from 7.9 kHz at 29$^{o}$C to 6.5 kHz at 100$^{o}$C and the distribution of dipolar coupling observed in MC sample is totally absent in the SC POM. It must also be noted that at each temperature, the dipolar coupling of the MC POM sample is always lower than the SC POM sample, which indicate that the amorphous region of MC POM are more mobile compared to the amorphous region of SC POM.

Thus the $T_2$ filtered PISEMA experiments on MC POM confirms that there is a continuum in dipolar coupling in the amorphous region at each temperature but there is no indication of separate mobile amorphous and rigid amorphous phases.

## 2.6. Conclusion

Till recently it was believed that torsional motions in the crystalline chains are responsible for the softening in MC POM [2; 3]. By comparing MC and SC POM, in a recent study by Guru *et al.* it was shown that MC POM shows the softening near 100$^{o}$C while SC POM does not show this softening [4]. Based on the observations from SAXS, AFM and SSNMR, it was concluded that lamellar melting is responsible for softening in MC POM. In this chapter, a deeper understanding to the softening in MC POM is provided using SSNMR techniques such as CODEX, PISEMA, $T_1$ and $T_2$ filtered PISEMA experiments.

The CODEX experiments were carried out from 23$^{o}$C to 105$^{o}$C through its softening temperature. The correlation time obtained shows that the frequency of motion are in the range of few 100s of $msec$ near its softening points and they are of similar order for both MC and SC POM at each temperature. Activation energies of 77.9 kJ/mol and 75.4 kJ/mol was observed for MC and SC POM samples respectively. A similar value of activation energy for crystalline motions for both the samples concludes that the crystalline motions are not the cause for softening in MC POM.

Insights into the morphology of POM have been obtained using the spin-lattice relaxation ($T_1$) and $T_1$, $T_1$ filtered PISEMA experiments. The spin lattice

relaxation experiments in combination with $T_1$ filtered PISEMA experiments at different temperatures were able to unambiguously show that a third phase, the rigid amorphous phase, does not exist in the MC POM. However, in the $T_2$ filtered PISEMA experiments on MC POM at various temperatures show a distribution in the heteronuclear dipolar coupling, while such a distribution was absent in the amorphous region of the SC POM sample. A reduction in the dipolar coupling is observed for the amorphous region of MC and SC sample with temperature, indicating that the mobility of amorphous phase increases. The reduction of dipolar coupling seen in the case of the MC POM sample is more than that seen in the SC sample indicating that the amorphous region of the MC POM is more mobile.

# CHAPTER 3

# Phenyl group motions in Polysulfones

## 3.1. Abstract

The origin and nature of different intra and intermolecular segmental motions and its influence on mechanical properties in amorphous polymers is an intense area of research in polymer science and engineering. Various studies using Dielectric Analysis (DEA), Dynamic Mechanical Analysis (DMA) and Neutron Scattering (NS) on high-end engineering amorphous polymers such as polycarbonates and polysulfones, having bisphenol A unit in common, reveals that both the aromatic $180^{o}$ flips and small or large amplitude chain oscillational motions contribute to $\gamma$ relaxation and correspondingly to high impact strength and stiffness. The SOLVAY technical reports on three grades of polysulfones, PESU (polyethersulfone with trade name VERADEL), PSU (polysulfone with trade name UDEL) and PPSU (polyphenylsulfone with trade name RADEL) says that the Notched Izod impact strength of PPSU is an order of magnitude higher than PESU and PSU. In this chapter, the functional group, and segmental motions in the three different grades of polysulfone polymers PESU, PSU and PPSU are probed using Solid-State NMR experiments to obtain insights into the superior ductility of PPSU. A temperature dependent Polarization Inversion Spin Exchange at Magic Angle (PISEMA) experiment is carried out to differentiate the dynamic heterogeneity between the three polymers. A combination of $^{13}C$ spin lattice relaxation time ($T_1$) and $T_1$ filtered PISEMA experiments were performed at $29^{o}C$ in order to get deeper insights into the dynamic heterogeneity in the polysulfone polymers. Center band Only Detection of Exchange (CODEX) experiment was carried out to monitor the slow motions in PESU, PSU and PPSU.

## 3.2. Introduction to Polysulfones

Sulfone functional group containing aromatic polymers such as PESU, PSU and PPSU are known for its high ductility, thermal stability, toughness and resistance to water and used in medicinal, engineering, and food processing applications [149]. Among these, PSU is an extensively studied polymer in terms of thermo mechanical

properties and is observed to have a glass transition temperature ($T_g$), assigned as the α relaxation, of 185°C, a sub-$T_g$-β relaxation observed around 85°C and another sub-$T_g$-γ relaxation which is observed in a wide range centered around -80°C [150]. PESU and PPSU are polysulfone polymers which are observed to have comparable or even better mechanical properties than PSU (UDEL), having a $T_g$ of 225°C, which is 40°C higher than that of PSU, no β transition have been reported for either of the samples and a sub-$T_g$ γ transition is observed in the region centered around -75 to -80°C which is almost similar to that of PSU [150]. In all aromatic polymers, sub-$T_g$ γ relaxation plays a vital role in the ductility and correspondingly high stiffness and impact resistance to an external force. In commercially important aromatic amorphous polymers such as bisphenol A polycarbonates (BPA-PC) and bisphenol A polysulfones (BPA-PSU or PSU), having similar structural unit BPA, the γ relaxation is greatly influenced by the functional group and segmental motions [150-152]. Several studies have been carried out using SSNMR, DES, DMA, NS and computer simulations to correlate the functional group and segmental motion of polymers with γ relaxation [35; 43; 108; 150-160]. Since BPA-PC is a well studied aromatic polymer and has structural similarity to polysulfone polymers, a brief review of the literature on studies on BPA-PC related to its mechanical property and molecular dynamics is presented here before the discussion about poly-sulfone polymers.

Several studies on BPA-PC have been reported where molecular and segmental motions of the chains of the aromatic polymers are correlated to the γ relaxation. By systematic substitution of aromatic, carbonate and isopropylyden units in BPA-PC Yee *et al.* have reiterated that both intermolecular and intra molecular motions play equal contribution to the $\gamma$ relaxation hence to ductility [151]. Jho *et al.* carried out a systematic study of the influence of intra molecular cooperative chain motion on $\gamma$ relaxation of BPA-PC [152]. They prepared a series of block copolymers of BPA-PC and bulky tetra methyl bisphenol A poly carbonate (TMBPA-PC) and observed that the γ relaxation peaks are restored in BPA-PC only when there is six to nine repeat BPA units in the chain. Dynamic mechanical measurements on a blend of BPA-PC and TMBPA-PC indicate that with relatively less percentage of a bulky group itself the γ relaxation of BPA-PC is fully suppressed. From these observations, Jho *et al.* concluded that, in poly carbonates along with inter molecular motion, intra

molecular motion is also contributing to the γ relaxation. Xiao *et al.* later established that the contribution from intra molecular interaction is stronger than intermolecular relaxation in BPA-PC and found that the correlation distance of at least seven repeat units are necessary for the restoration of the γ relaxation peak of BPA-PC polymer when it is copolymerized with TMBPA-PC [157]. Using dipolar rotational spin echo (DRSE) NMR experiments Schaefer *et al.* proved the presence of 180$^o$ flip motions in poly carbonate aromatic rings along with small angle chain oscillation, with amplitude of 30$^o$ [43; 153; 155]. This indicates that 180$^o$ flips are not the only motions in poly carbonates responsible for $\gamma$ relaxation. They found out that the frequency of aromatic 180$^o$ flip motions are of the order of 100s of kHz. Using neutron scattering measurements by Arrese-Igor *et al.* revealed the presence of 180$^o$ flip motions along with ~90$^o$ rotations and large amplitude oscillation in the poly carbonate chains [161]. Arrese-Igor *et al.* using NS and DES later showed that the phenyl, carbonyl and methyl group motion in poly carbonates are coupled to each other [162]. Therefore, based on these reports, it can be concluded that the high impact strength of poly carbonate is a result of local and cooperative motion of the polymer chains.

Polysulfone (PSF) polymers are amorphous engineering plastics structurally similar to poly carbonates containing a bisphenol-sulfone unit in place of the carbonate group. Deuterium Solid-state NMR study by Dumais et al. showed that BPA-PSF possess 180$^o$ phenyl flips as it is observed in BPA-PC polymer. However, large amplitude chain oscillational motion which are observed in polycarbonates are absent in polysulfones at room temperature [108]. Arrese-lgor *et al.* was able to observe aromatic 180$^o$ flips in PSU (BPA-PSF) along with small angle chain oscillational motions using neutron scattering experiments [163-165]. There are also a few studies reported in the literature correlating structural modification of polysulfones to molecular motions and hence to mechanical property. Aitken *et al.* monitored the dynamical mechanical relaxation behavior of polysulfone polymers by substitution of bulky tetra-methyl bisphenol A polysulfone and hexamethyl bisphenol A polysulfone separately and found two separate $\gamma$ relaxation peaks assigned to the bisphenol A and the bulky tetra or hexa methyl bisphenol A groups [150]. This indicates the absence of intra molecular correlated motions in polysulfone polymers. This is in complete contrast to the molecular motions observed in bisphenol A polycarbonates where motional correlation extends over seven repeating units [158].

They have interpreted that the flexibility of polymer units around oxygen linkage suppresses the long range correlation distance in polysulfones and have a major role in the high ductility and toughness.

PESU and PPSU are structural modifications of PSU, where the bisphenol A units of PSU is replaced with bisphenol sulfone, and biphenyl group respectively as shown in figure 3.1. Although all the three polymers have similar sub-$T_g$ relaxation, PPSU is reported to have high impact strength compared to PESU and PSU. In this chapter, the reason for high impact strength of PPSU in comparison to PSU and PESU has been investigated. To obtain deeper insights into this issue, the molecular motion and dynamic heterogeneity of all three polymers were obtained using advanced solid-state NMR experiments. The chapter is divided into three parts. In the first part the dynamic heterogeneities in the polymers and its variation with temperature were investigated using advanced solid-state NMR experiments. In the second part, the dynamic heterogenity of the polymers were studied using the longitudinal relaxation time ($T_1$) and $T_1$ filtered PISEMA experiments. In the third part slow segmental and cooperative motions which are of the order of $msec$ to $sec$ were studied using CODEX experiments.

## 3.3. Experimental section

### 3.3.1. Preparation of the Samples for SSNMR

The solid bars of the samples, PESU, PSU and PPSU were received from SOLVAY chemicals and used as such without any thermal or physical modification. Cylindrical rods of each sample were machined from the solid bars to a diameter of 2.9 mm so as to snuggly fit into the 4 mm NMR rotor. The entanglement molecular weight of PESU, PSU and PPSU which we used in our studies are 3600 gm/mol, 3020 gm/mol and 2550 gm/mol respectively. The chemical structures of all three polymers are shown in figure 3.1. PESU is the repeating unit of bisphenol sulfone unit, PSU contains both bisphenol sulfone and bisphenol A polycarbonate and PPSU contain bisphenol A sulfone and biphenyl groups.

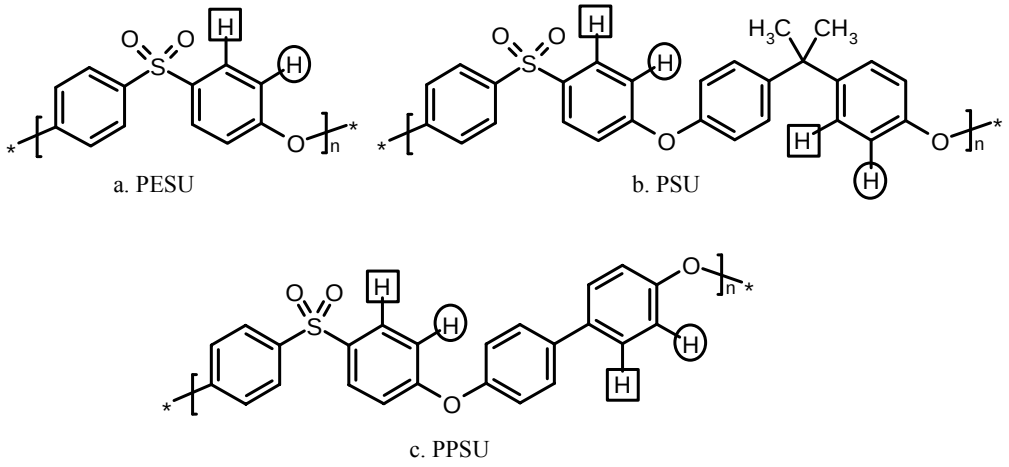


*Figure 3.1: Chemical structure of three different polysulfone polymers a)PESU, b).PSU and c).PPSU*

### 3.3.2. SSNMR Methods

All the solid-state NMR experiments were carried out on a Bruker Avance 300 MHz spectrometer with a 4 mm magic angle spinning probe head. For all the NMR experiments, the cross polarization contact time of 800 $\mu sec$ was used. $^{1}H$ and $^{13}C$ 90$^{o}$ pulses of RF frequency 85 kHz and 68 kHz used respectively. $^{1}H$ longitudinal relaxation time ($T_1$) of all the three polysulfone samples were measured and 4-5 times of this is used as recycle delay (PPSU) for each experiment. The PISEMA $^{13}C$ $T_1$ relaxation and $T_1$ filtered PISEMA experiments were carried out at a spinning rate of 8 kHz. An effective field of 73.5 kHz was used during LG decoupling. $^{13}C$ $T_1$ relaxation times were measured using the Torchia experiment[125]. The CODEX experiments were carried out with a spinning speed of 4.5 kHz. The $N\tau_r$ dependence experiment was carried out to determine the plateau of the CODEX dephasing measurements for each sample. Using the optimum $N\tau_r$ value that was obtained from $N\tau_r$ dependence experiment, the CODEX mixing time ($\tau_m$) dependence experiment was carried out. In the mixing time dependence experiment, the mixing time ($\tau_m$) was varied from 1 $msec$ to 8 $sec$ with 16 points in between them. The temperature of the sample was calibrated at spinning speeds of 4.5 kHz and 8 kHz, using methanol and $PbNO_3$ [143; 144].

## 3.4. Results and Discussions

### 3.4.1. Spectrum assignments

The $^{13}C$ spectrum assignments of all the three polymers PESU, PSU and PPSU were first done using solution-state experiments such as $^{13}C$ single pulse experiment, COSY, HMBC and HSQC. The solution-state $^{13}C$ NMR spectrum is then compared with the solid-state $^{13}C$ CPMAS spectrum. The $^{13}C$ CPMAS spectra obtained for PESU, PSU, and PPSU are shown in figure 3.2. In the $^{13}C$ CPMAS spectrum of **PESU** four different carbon environments are observed, the peaks centered around 120 ppm and 129 ppm are assigned as the carbons directly attached to the protons. The peaks at 120 ppm is identified as the CH moiety near the ether linkage (the carbons attached to the circled hydrogen, figure 3.1a) while the peak at 129 ppm is assigned as the CH moiety near to the sulfone unit (the carbons attached to the squared hydrogen, figure 3.1a). The other two peaks centered around 137 ppm and 160 ppm are assigned as the quaternary carbon in the aromatic ring near to the sulfone unit and the ether linkage respectively. In **PSU**, the peaks centered around 120 ppm and 129 ppm are the carbons that are directly attached to the protons. Each peak has contributions from two different $^{13}C$ environments. The peak at 120 ppm is assigned to the carbons near the ether linkage (the carbons attached to the circled hydrogen, figure 3.1b) while the peak at 129 ppm is assigned as the sum of the carbons near to the isopropylidene and sulfone linkages (the carbons attached to the squared hydrogen, figure 3.1b). The remaining carbons at 136 ppm, 147 ppm, 152 ppm and 162 ppm are quaternary carbons assigned to the $^{13}C$ environments directly attached to the sulfone unit, isopropylidene unit, quaternary carbons attached to the ether unit which are in the bisphenol A unit and quaternary carbons attached to the ether unit which are in the bisphenol sulfone unit respectively. In addition, PSU contain two more $^{13}C$ environments at 31 ppm and 42 ppm assigned as the isopropylidene methyl and quaternary carbons respectively. In **PPSU**, four distinct carbon environments are observed. The peaks at 120 ppm and 129 ppm are assigned as the carbons which are directly attached to the protons. The peak at 120 ppm is assigned to the $^{13}C$ moiety which is near to the ether linkage (the carbons attached to the circled hydrogen, figure 3.1c) and the peak at 129 ppm is assigned to the $^{13}C$ moiety which is near to the biphenyl and sulfone linkages (the carbons attached to the squared hydrogen, figure 3.1c). The peaks at 135, 152 and 162 ppm are the quaternary carbons in the aromatic

ring assigned to the carbons near to biphenyl and sulfone units, carbons attached to ether linkage which is in the biphenyl unit, carbons attached to ether linkage which is in the bisphenol sulfone unit respectively. It is also observed that in PSU and PPSU, SSNMR is unable to differentiate between the CH environments having different ether environments. The peaks from the CH environment near the isopropylidene and bisphenol sulfone groups are indistinguishable in PSU, similarly the CH environments near the biphenyl and bisphenol-sulphone in PPSU is also indistinguishable.

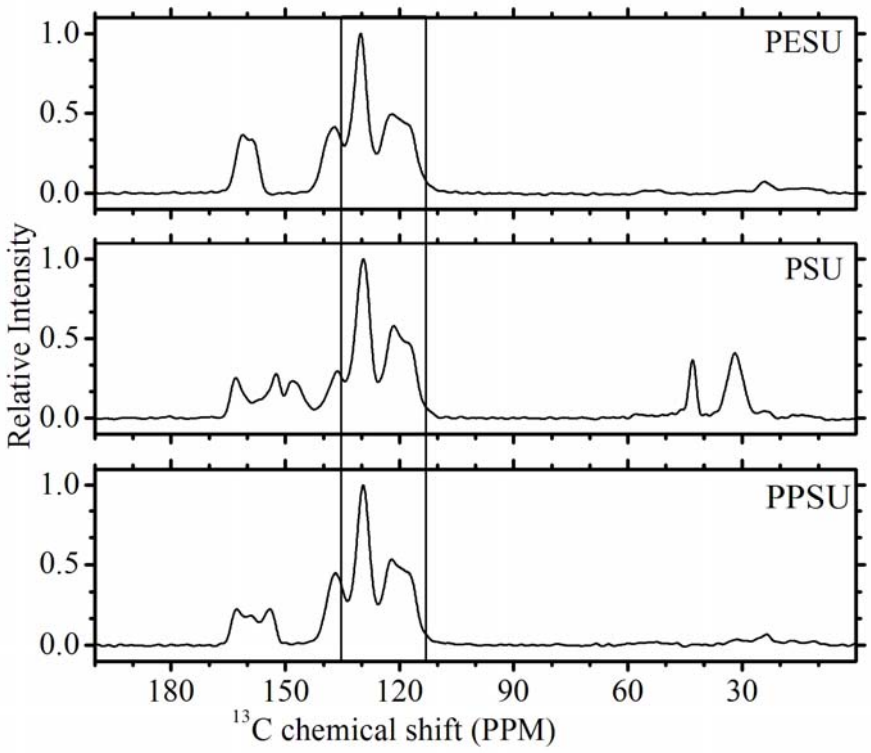


*Figure 3.2: The CPMAS spectrum of PESU, PSU and PPSU at 29°C. The carbons corresponding to the peaks in the box in the spectrum are used as the probe for dynamics in the polymers, in PISEMA and CODEX experiments.*

The aim of this study is to understand the origin of the superior mechanical property of PPSU, which is almost an order of magnitude higher than PESU and PSU. SSNMR, DMA, DEA and NS measurements on PSU already shows that molecular motions play a vital role in its mechanical property. In this study, the ranges and heterogeneity of motions in these polymers are characterized using different SSNMR techniques such as PISEMA, $^{13}C$ $T_1$ relaxation experiments, $T_1$ filtered PISEMA experiment and CODEX experiments. The PISEMA experiment monitor fast motions

of the order of hundred of kHz and the dynamic heterogeneity in the polymer, the CODEX experiment measure the slow segmental motions.

### 3.4.2. The PISEMA experiments

The PISEMA experiment is meaningful only for carbons which are directly attached to the protons. Hence in the polysulfone samples, PISEMA experiments are used to monitor only the carbons at 120 and 129 ppm as a function of temperature. At 29$^{o}$C, the PISEMA spectra of the carbons at 120 ppm (CH environment near ether linkage in the aromatic ring) for PESU, PSU and PPSU are shown in figure 3.3a, 3.3b and 3.3c respectively. The spectra show two sets of contours with dipolar coupling of 21.5 kHz for the outer region and 11.7 kHz for the inner region. Dipolar coupling of 21.5 kHz indicates that all the 3 polymers contain immobile regions, while the reduced dipolar coupling of 11.7 kHz indicate the presence of mobile regions, which originates from the 180$^{o}$ flips of aromatic rings. Two separate dipolar couplings is an evidence for dynamic heterogeneity in all the three polymers at 29$^{o}$C. Similarly, the PISEMA spectra at 29$^{o}$C for the carbons around 129 ppm for PESU, PSU and PPSU are shown in figure 3.3j, 3.3k, 3.3l respectively. These are the CH groups close to sulfonyl/isopopylidene/biphneyl environments in PESU, PSU and PPSU respectively. As seen for the carbons at 120 ppm, the carbons at 129 ppm also shows two sets of contours, the outer region with dipolar coupling of 21.5 kHz corresponds to the immobile part and an inner region with dipolar coupling of 11.7 kHz corresponds to the mobile part.

The PISEMA spectra of PESU, PSU and PPSU at 60$^{o}$C for the carbons at 120 ppm are shown in figures 3.3d, 3.3e and 3.3f. The immobile region of PPSU has almost vanished at 60$^{o}$C, while in PESU and PSU some traces of immobile regions are still present. This indicates that at 60$^{o}$C almost all the aromatic units in the PPSU sample are activated for 180$^{o}$ flips motion, but in PESU and PSU the full activation of the immobile region does not happen. A similar behavior is shown by the carbons at 129 ppm also where the immobile part of PPSU is almost converted to the mobile part while in PESU and PSU some immobile regions are still present (figure 3.3m, 3.3n, 3.3o).

The PISEMA spectra obtained at 100$^{o}$C for PESU, PSU and PPSU are shown in figures 3.3g, 3.3h, 3.3i. At 100$^{o}$C, the immobile regions of all the three polymers

have almost disappeared. This indicates that at 100°C all the aromatic immobile units of PESU, PSU and PPSU are almost fully activated for 180° flips motion and only mobile components are present. A similar behavior is seen from the carbons at 129 ppm where also the immobile components are almost completely converted into the mobile part at 100°C (figure 3.3p, 3.3q, 3.3r).

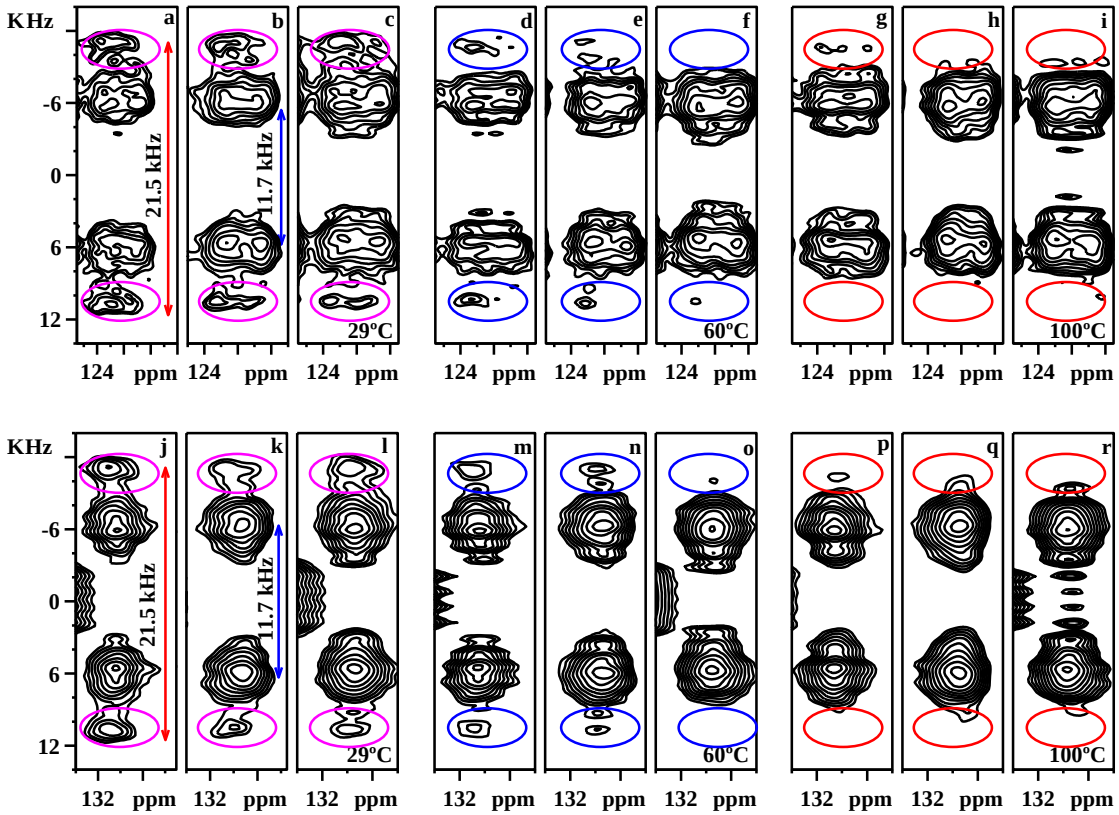


*Figure 3.3: The $^{13}C$ PISEMA spectra of the carbons centered at 120 ppm (carbons which are near to the ether linkage in the chain) at 29°C (a,b,c), 60°C(d,e,f) and 100°C(i,j,k). Two distinct regions are observed at 29°C with dipolar coupling of 21.5 kHz and 11.7 kHz. At 60°C the immobile region of PPSU vanishes while traces of the immobile region are present for both PESU and PSU. At 100°C, the immobile regions in all the three polymers merge with the mobile region. The $^{13}C$ PISEMA spectra of the carbons centered at 129ppm for PESU, PSU and PPSU at 29°C (j,k,l), 60°C(m,n,o) and 100°C(p,q,r). Similar to the carbons at 120 ppm, here also at 60°C the immobile region of PPSU vanishes while traces of the immobile region are present for both PESU and PSU. At 100°C the immobile regions in all the three polymers merges with mobile region.*

### 3.4.3. $^{13}C$ $T_1$ relaxation time and $^{13}C$ $T_1$ filtered PISEMA experiments.

From the PISEMA experiments, it is clear that all the three polymers PESU, PSU and PPSU have immobile and mobile environments. To investigate if there are regions with mobility in between mobile and rigid components, a combination of $^{13}C$ relaxation ($T_1$) experiments and $^{13}C$ $T_1$ filtered PISEMA experiments were carried out for all the three polymers. The data obtained from the $^{13}C$ relaxation experiment using the Torchia method is iteratively fitted using a two component exponential decay equation (Equation 1.58) and the $T_1$ values that were obtained are tabulated in table 3.1. The fast relaxing components were observed to have an average $T_1$ value of 1 $sec$ for all the 3 polymers, which are assigned to the mobile regions. The slow relaxing component has an average relaxation time of 16 $sec$ for all the three polymers, which are assigned to the immobile regions.

| | CS(environment) | Sample | $T_{1C}$ $(sec)$ | $T_{3C}$ $(sec)$ |
|---|---|---|---|---|
| Two component fit | 120ppm (ether link) | PESU | 0.99±0.08 | 18.0±0.9 |
| | | PSU | 0.82±0.07 | 15.0±0.8 |
| | | PPSU | 0.74±0.06 | 13.4±0.7 |
| | 130 ppm (sulphone, Aliphatic, biphenyl) | PESU | 1.23±0.90 | 20.6±1.0 |
| | | PSU | 0.8±0.06 | 14.9±0.7 |
| | | PPSU | 0.76±0.05 | 15.3±0.6 |
| Average values | | | ~1 $sec$ | ~16 $sec$ |

*Table 3.1: The $^{13}C$ Spin-lattice relaxation times of PESU, PSU and PPSU obtained using a 2 component model.*

Based on the $T_1$ values obtained from the relaxation experiments, the $T_1$ filtered PISEMA experiments (figure 1.24) were carried out. The PISEMA spectrum of the carbons at 120 ppm (CH moiety near to the ether linkage) without the $T_1$ filter and with a $T_1$ filter of 5 $sec$ for PESU, PSU and PPSU are shown in figure 3.4. If the polymers contain only mobile and immobile region with distinct relaxation times for each, a $T_1$ filter time of 2 to 4 times the $T_1$ relaxation time of mobile region should filter out the inner contours from the $T_1$ filtered PISEMA spectra. It is clear from figures 3.4b, 3.4d and 3.4f that with a $T_1$ filter of 5 $sec$ (>4*$T_1$ relaxation time of mobile region) the inner peaks are still present in the PISEMA spectra for all the

polysulfone polymers (circled spectra, figure 3.4). This is an evidence for the presence of an intermediate component in all the three polymers with a $T_1$ relaxation time greater than 1 *sec*. Figure 3.4a, 3.4c and 3.4e are the PISEMA spectra without a $T_1$ filter for PESU, PSU and PPSU respectively. Similar spectra are observed for the carbons centered at 129 ppm in all the three polymers. The $T_1$ filtered PISEMA spectra with a $T_1$ filter of 5 *sec* for the carbons centered at 129 ppm on PESU, PSU and PPSU are shown in figures 3.4h, 3.4j and 3.4l respectively show that contours with a dipolar coupling of 13.7 kHz are present (circled portion in the spectra). Hence

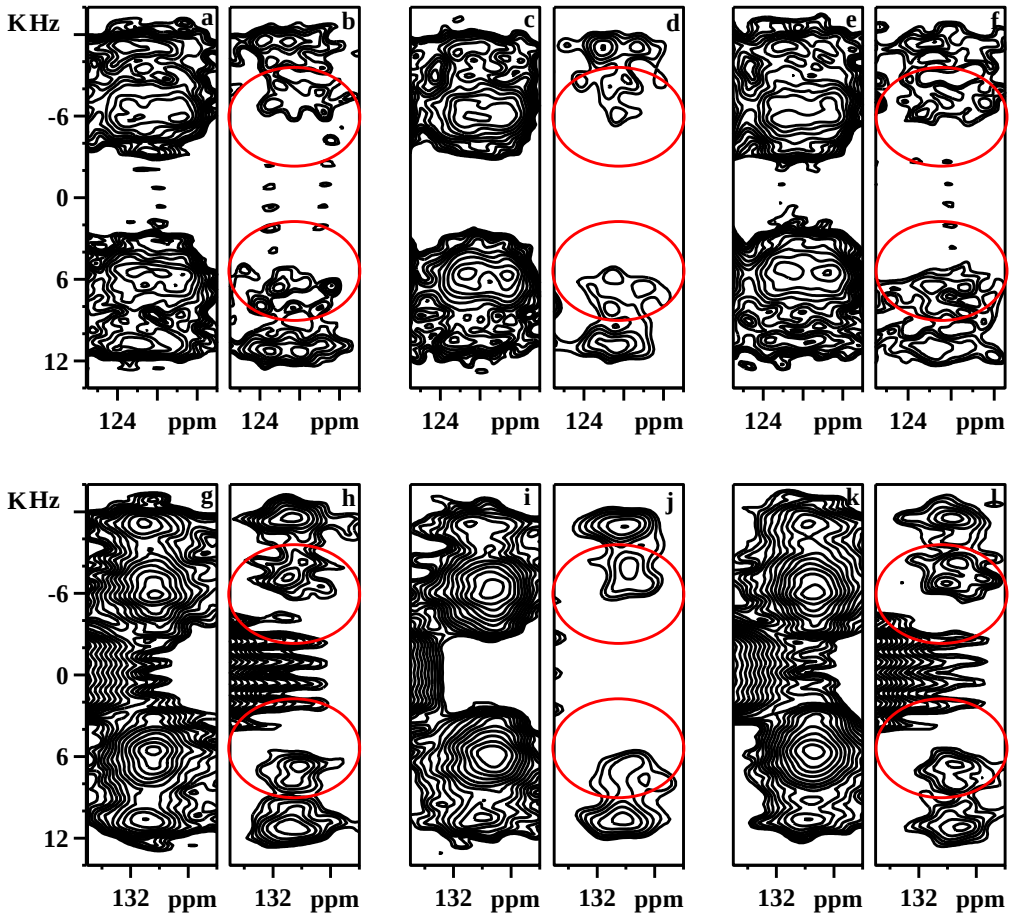


*Figure 3.4: The PISEMA spectra of PESU, PSU, PPSU for carbons at 120 ppm without a $T_1$ filter (a,c,e) and with a $T_1$ filter of 5 sec (b,d,f). The $T_1$ filtered PISEMA spectra with a $T_1$ filter of 5 sec shows residual contours of intermediate regions (red circle). Similarly, the PISEMA spectra of PESU, PSU, PPSU for carbons at 129 ppm without a $T_1$ filter (g, i, k) and with a $T_1$ filter of 5 sec (h, j, l). The $T_1$ filtered PISEMA spectra with a filter of 5sec shows residual contours of intermediate regions in all the three polymers.*

it is evident that an intermediate region with relaxation times greater than 1 $sec$ is present in all the three polymers.

Since the $T_1$ filtered PISEMA experiments shows the presence of a component other than a fast and a slow relaxing component, the data from the Torchia $T_1$ relaxation experiment was fitted again using a three component exponential decay (Equation 1.58). The relaxation values obtained for the carbons at 120 and 129 ppm are tabulated in Table 3.2. The fastest relaxing component, attributed to the mobile region has an average $T_1$ of 0.45 $sec$. The slow relaxing component has an average $T_1$ of 25 $sec$ and it is assigned to the immobile regions. The $T_1$ of 4 $sec$ which is between the mobile and immobile regions is assigned to the intermediate region.

| | CS(environment) | Sample | $T_{1C}$ $(sec)$ | $T_{2C}$ $(sec)$ | $T_{3C}$ $(sec)$ |
|---|---|---|---|---|---|
| Three component fit | 120ppm (ether link) | PESU | 0.41±0.07 | 3.2±0.6 | 25.6±1.9 |
| | | PSU | 0.33±0.05 | 2.7±0.4 | 20.3±1.3 |
| | | PPSU | 0.46±0.04 | 4.5±0.7 | 25.8±3.0 |
| | 130ppm (sulphone, Aliphatic, biphenyl) | PESU | 0.55±0.05 | 5.1±0.7 | 31.6±2.2 |
| | | PSU | 0.44±0.04 | 3.3±0.6 | 19.7±1.3 |
| | | PPSU | 0.48±0.04 | 5.1±0.6 | 30.8±3.2 |
| Average values | | | ~0.45 $sec$ | ~4 $sec$ | ~25 $sec$ |

*Table 3.2: The Spin-lattice relaxation time of PESU, PSU and PPSU obtained using a 3 component exponential decay equation. (Equation 1.58)*

To confirm the presence of the intermediate region, $^{13}C$ $T_1$ filtered PISEMA experiments were carried out with $T_1$ filter times of 2.5 $sec$, 5 $sec$, 10 $sec$ and 15 $sec$. The $T_1$ filter times were chosen based on the $T_1$ values obtained from the $T_1$ data which are tabulated in table 2. The results of the $T_1$ filtered PISEMA experiments for the carbons at 120 ppm (peak near the ether linkage) and 129 ppm are shown in figures 3.5 and 3.6 respectively. The $T_1$ filtered PISEMA spectra of PESU, PSU, PPSU with a $T_1$ filter of 2.5 $sec$ are shown in Figures 3.5b, 3.5g, 3.5l respectively. A $T_1$ filter time of 2.5 $sec$ completely removes the mobile regions from the spectra which have a relaxation time 0.45 $sec$. Thus, the inner contours seen in the $T_1$ filtered PISEMA spectra with a $T_1$ filter of 2.5 $sec$ are attributed to the intermediate region. It is also seen that the center of gravity of inner contour of the spectra has moved apart from each other and hence a dipolar coupling of 13.7 kHz is observed for this region.

Since the dipolar coupling of this region is higher than that of the mobile region (11.7 kHz) it can be confirmed that a region with mobility lower than mobile region is present in all the three polymers. The $T_1$ filtered PISEMA with a $T_1$ filter time of 2.5 $sec$ for the carbons around 129 ppm is shown in figure 3.6b, 3.6g and 3.6l. As seen in the case of the $T_1$ filtered PISEMA for the carbons at 120 ppm, the inner contours does not vanish in any of the three polymers. In addition, the center of gravity of the inner peaks increases to 13.7 kHz for all the three polymers confirming the presence of the intermediate regions in all the three polymers.

The $T_1$ filtered PISEMA spectra with a $T_1$ filter of 5 $sec$ of the carbons at 120ppm in PESU, PSU and PPSU are shown in figure 3.5c, 3.5h and 3.5m respectively. Since the $T_1$ of the intermediate region is 4 $sec$, a $T_1$ filter with 5 $sec$ is not sufficient to remove this component from the $T_1$ filtered PISEMA spectra and the contours with a dipolar coupling of ~13.7 kHz is observed in this spectra which is from the intermediate region. The $T_1$ filtered PISEMA spectra with a $T_1$ filter of 5 $sec$ for the carbons at 129ppm in PESU, PSU and PPSU are shown in figure 3.6c, 3.6h and 3.6m respectively and an inner contour with a dipolar coupling of 13.7 kHz is observed indicating the presence of intermediate regions in all the three polymers.

The $T_1$ filtered PISEMA experiments with a $T_1$ filter of 10 $sec$ for the carbons at 120 ppm are shown in figures 3.5d, 3.5i and 3.5n respectively. The contours with a dipolar coupling of 13.7 kHz have almost completely vanished indicating that the $T_1$ relaxation time of this phase should be below 4 $sec$. This is in excellent agreement with the $T_1$ values obtained from Torchia experiment where the average $T_1$ value of 3 to 4 $sec$ was observed. The $T_1$ filtered PISEMA experiments with a $T_1$ filter of 10 $sec$ for the carbons at 129 ppm is shown in figure 3.6d, 3.6i and 3.6n respectively. Here the inner contour with dipolar coupling of 13.7 kHz does not vanish completely with 10 $sec$ filter time, indicating that the relaxation time of the intermediate region of CH carbons near to sulfone group/bisphenol-A/biphenyl group is higher than carbons near ether linkage (>4 $sec$).

Figures 3.5e, 3.5j and 3.5o show the $T_1$ filtered PISEMA spectra with a $T_1$ filter of 15 $sec$ of the carbons at 120 ppm, in PESU, PSU and PPSU respectively and the inner contours have completely disappeared. The $T_1$ filtered PISEMA spectra with $T_1$ filter time of 15 $sec$, the inner contours of carbons at 129 ppm also disappeared

(figure 3.6e, 3.6j and 3.6o) confirming that the intermediate region have a $T_1$ relaxation of 4-5 *sec* in all three polymers.

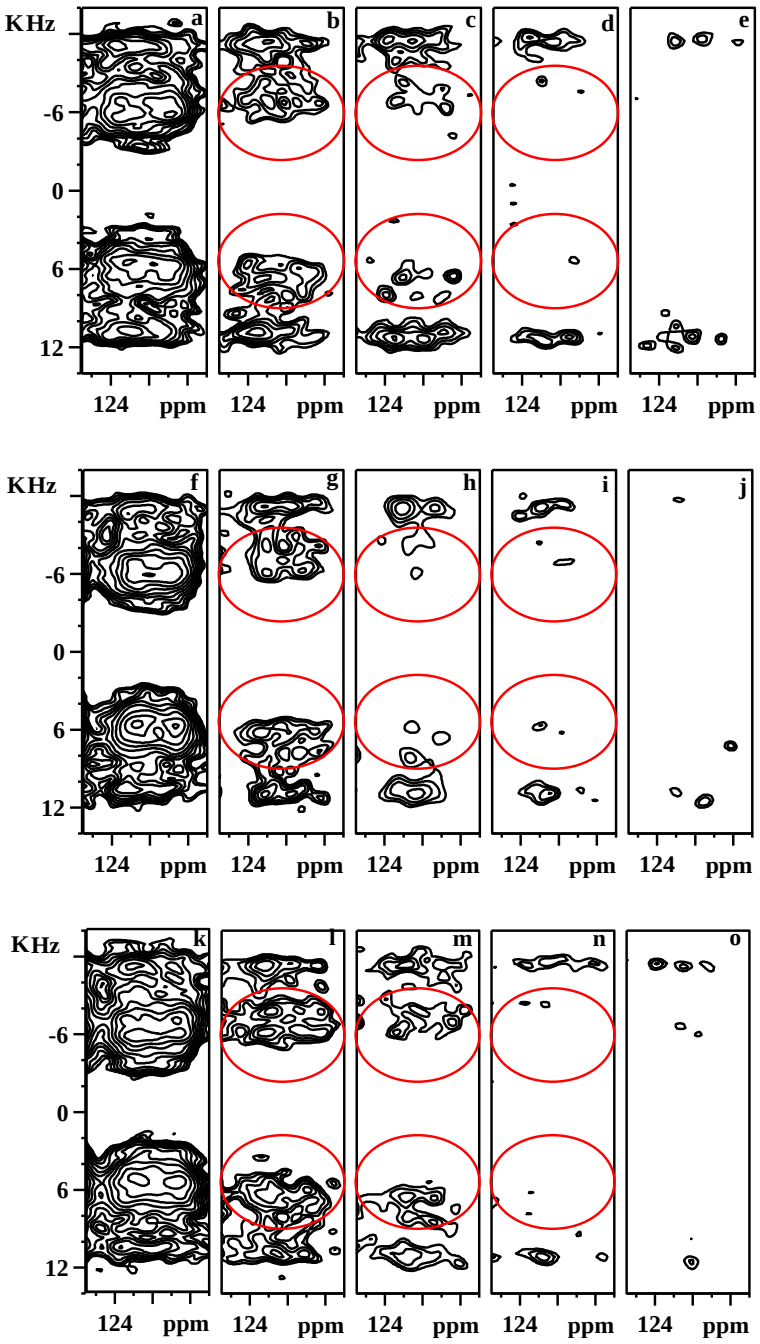


*Figure 3.5: The $T_1$ filtered PISEMA spectra of the carbons at 120 ppm in PESU, PSU and PPSU at 29°C with a $T_1$ filter of 0 sec (without $T_1$ filter) 2.5 sec, 5 sec, 10 sec and 15 sec respectively. A dipolar coupling of 11.7 kHz is observed for the inner region and 21.5 kHz for outer region without a $T_1$ filter. The dipolar coupling of 13.7 kHz is observed for the inner contours with a $T_1$ filter of 2.5 sec and this peak vanishes with a filter time of 10 sec.*

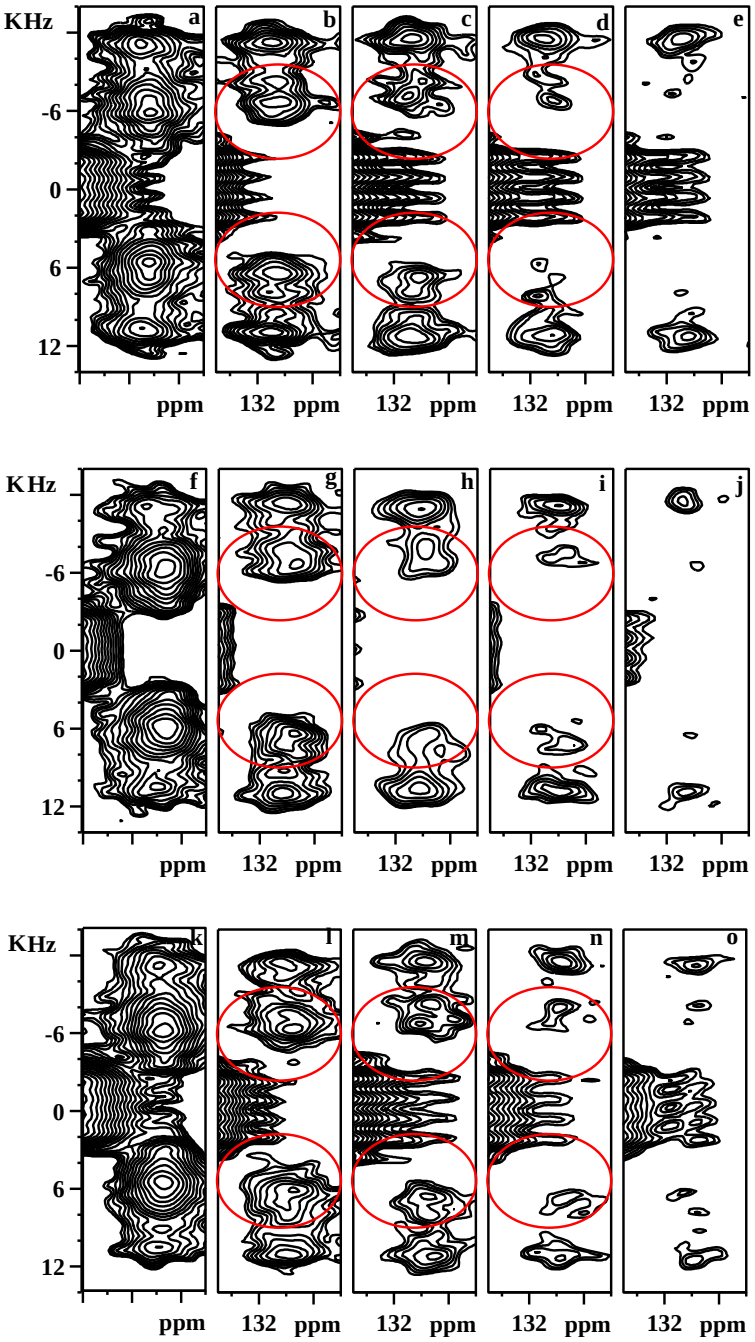


*Figure 3.6: The $T_1$ filtered PISEMA spectra of the carbons at 129ppm in PESU, PSU and PPSU at 29°C with a $T_1$ filter time of 0 sec (without $T_1$ filter) 2.5 sec, 5 sec, 10 sec and 15 sec respectively. A dipolar coupling of 11.7 kHz is observed for the inner region and 21.5 kHz for outer region without $T_1$ filter. A dipolar coupling of 13.7 kHz is observed for the inner region with a $T_1$ filter of 2.5 sec. This peak vanishes with a $T_1$ filter time of 15 sec.*

The intermediate regions of the CH moiety near ether linkage have lower $T_1$ compared to the CH moiety near the sulfone /bisphenol-A/biphenyl environment. This indicates that the ether linkage in polysulfone polymers are more flexible compared to

sulfone group/bisphenol-A/biphenyl linkages. A similar behavior is also shown by the immobile regions also.

### 3.4.4. Slow motions by the CODEX experiments

The CODEX experiments were carried out on all the three polymers to measure slow segmental dynamics in the polymer chains at 26°C and 100°C. The results of the $N\tau_r$ dependence experiment with a mixing time ($\tau_m$) of 4 $sec$ resulted in a dephasing with a plateau at $N\tau_r$ of 1.33 $msec$. The $\tau_m$ dependence experiments were carried out using this $N\tau_r$ value for PESU, PSU and PPSU. The dephasing obtained for the carbons (CH) near to the ether linkage (120 ppm) and isopropyl/sulfone/biphenyl linkage (129 ppm) for PESU, PSU, PPSU at 26°C are shown in figure 3.7a and 3.7b respectively. The CODEX curve shows a gradual dephasing indicating the presence of slow motions in the polymer chains. However it can be seen that the dephasing is not reaching a plateau value indicating that the motions are very slow of the order of 10s of $sec$. Therefore the extraction of the correlation time is difficult from this data.

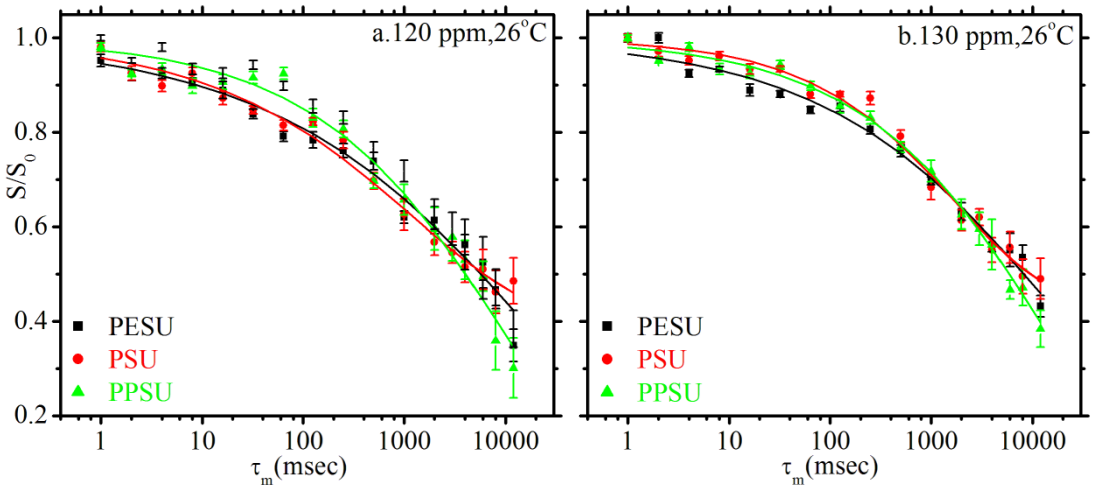


*Figure 3.7: The result of the CODEX $\tau_m$ dependence experiments for the CH moiety a) near the ether linkage (120 ppm) and b) near to the sulfonyl/isopropylydene/biphenyl group (129 ppm) in PESU, PSU and PPSU at 26°C showing that there is a gradual decrease in the CODEX intensity as a function of mixing time but does not reach a plateau till a mixing time of 12sec.*

At 26°C all the three polymers PESU, PSU and PPSU shows mobile, intermediate and rigid component. In ordered to distinguish the component which is

contributing to the slow motions, CODEX experiments were carried out at 100°C. The CODEX $\tau_m$ dependence of the carbons near to the ether linkage (120 ppm) and isopropyl/sulfone/biphenyl linkage (129 ppm) in the PESU and PPSU samples at 100°C are shown in figure 3.8a and 3.8b. At 100°C both the samples shows similar CODEX dephasing as seen at 26°C indicating the presence of slow motions. The PISEMA experiments at 100°C has already established that the immobile regions in all the three polymers merges with the mobile regions, hence we cannot expect that the slow motions observed in the CODEX experiment has originated from the immobile regions. The frequency of motion in the mobile regions is expected to be of the order of 100s of kHz and the CODEX experiment cannot detect such fast motions. Therefore, it can be confirmed that the dephasing observed in the CODEX experiment in the polysulfones should be from the intermediate region. At 100°C also the dephasing curve does not reach a plateau making the extraction of the correlation time impossible.

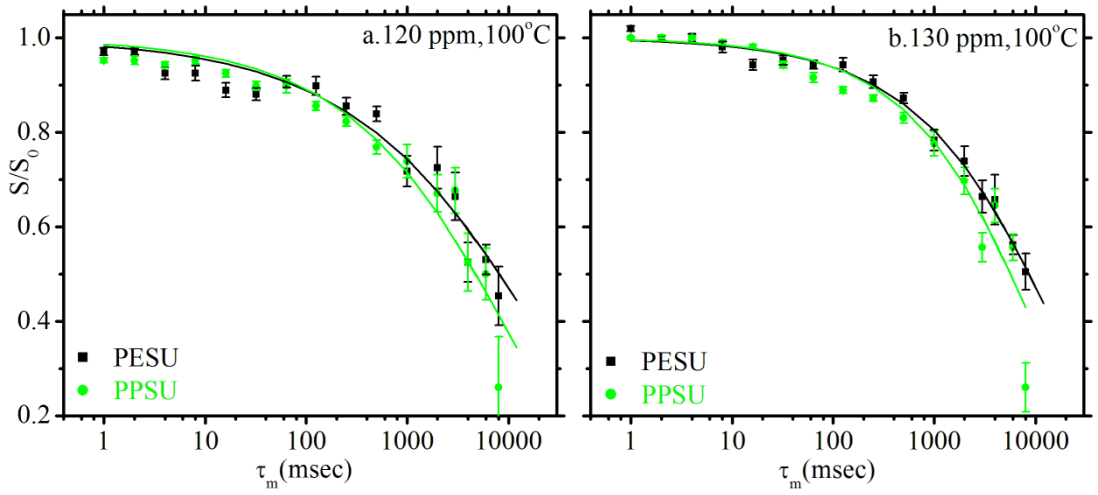


*Figure 3.8: The results of the CODEX $\tau_m$ dependence experiments for the CH moiety a) near the ether linkage (120 ppm) and b) near to the sulfonyl/isopropylydene/biphenyl group (129 ppm) in PESU, PSU and PPSU at 100°C showing a gradual decrease in CODEX intensity as a function of mixing time and does not reaches a plateau till a mixing time of 12 sec.*

## 3.5. Conclusion

An order of magnitude ductility difference for PPSU in comparison with PESU and PSU reported is rationalized by monitoring their functional group, and segmental motions. The solid-state NMR techniques PISEMA, $^{13}C$ $T_1$ relaxation

experiments, $^{13}C$ $T_1$ filtered PISEMA experiments and CODEX experiments were used to monitor different ranges of motions. The PISEMA experiment is used to monitor motions which are of the order of 100s of kHz by monitoring the reduction in dipolar coupling. The PISEMA experiments at 29$^oC$ reveal the presence of two dynamically distinct regions. One is attributed to the mobile component which has a dipolar coupling of 11.7 kHz and the other to the immobile component with a dipolar coupling of 21.5 kHz. The reduced dipolar coupling 11.7 kHz confirms the mobile components have motions of the order of 100s of kHz, present in all the three polymers PESU, PSU and PPSU. Temperature dependent PISEMA experiments are carried out on PESU, PSU and PPSU to differentiate the change in dynamical heterogeneity as a function of temperature. It is observed that the immobile components of PPSU completely vanish at 60$^oC$ while traces of the immobile component are present in PESU and PSU at this temperature. This indicate that the presence of higher percentage of the immobile region may be the reason for the lower ductility observed in PESU and PSU. However, at 100$^oC$, the outer contours have vanished in the PISEMA spectra of PESU, PSU and PPSU indicating that the immobile regions are completely converted to mobile regions.

A combination of $T_1$ relaxation and $T_1$ filtered PISEMA experiments on PESU, PSU and PPSU shows that there are three dynamically distinct regions. The mobile region has $T_1$ value of the order of ~0.5 $sec$, the intermediate component have a $T_1$ value of the order of ~4 $sec$ and a rigid region have $T_1$ value of ~25 $sec$ is obtained through Torchia $T_1$ relaxation experiment. The presence of each region is confirmed by $T_1$ filtered PISEMA experiments with different $T_1$ filters of 2.5 $sec$, 5 $sec$, 10 $sec$ and 15 $sec$. $T_1$ filtered PISEMA experiments with a $T_1$ filter of 2.5 $sec$ shows that the inner contours have a dipolar coupling of 13.7 kHz. A residual dipolar coupling is assigned for the intermediate regions of the polymers. A $T_1$ filter of 10 $sec$ is observed to remove the intermediate region of PISEMA peak centered at 120 ppm while a 15 $sec$ $T_1$ filter is necessary for complete removal of inner contour region for peak centered at 129 ppm. This indicates that the phenyl group around the ether link has relatively more flexibility compared to the phenyl group around the sulfonyl/isopropylidene/biphenyl.

The CODEX experiment is used to monitor slow segmental motions in all the polymers. At 26$^{o}$C CODEX curves show dephasing indicating the presence of slow segmental motion in all the three polysulfone polymers. Since at 26$^{o}$C the polymer contains the mobile, intermediate and immobile components, CODEX experiments at 100$^{o}$C were carried out to probe which component contributes to the slow motions. These slow motions are present at 100$^{o}$C indicating that they are from the intermediate regions because immobile regions disappear at this temperature (results from the temperature dependent PISEMA experiments) and the motions from the mobile regions are faster than that can be detected by the CODEX experiment.

# CHAPTER 4
# Segmental motions in PLA at the *Tg*

## 4.1. Abstract

At a molecular level, the origin of ductility in an amorphous polymer may be traced to cooperative segmental mobility, which is driven by motions of the functional groups in repeat units. Enantiomerically pure poly lactic acid is semicrystalline in nature and always gives a high percentage of crystallinity to the material, while a recemic mixture of PDLA and PLLA give amorphous poly D-L lactic acid (PDLLA). DMA and DES studies on poly lactic acid show an induction of crystallanity in the amorphous polymer cause reduction in the intensity of the $\alpha$ transition called glass transition ($R_g$). It is revealed that in addition to the induction of crystallinity, the microstructure of crystallinity causes a change in the glass transition. In the present work, the segmental motions of different thermally aged PDLLA are probed using the Center band Only Detection of Exchange (CODEX) experiment at the glass transition temperature. The crystallinity of the polymer is also measured as a function of annealing time using DSC. Therefore, the aim of work is to correlate aging effect observed in poly lactic acid with the segmental and functional group motions.

## 4.2. Introduction

Over the past few decades, several biodegradable polymers have been investigated as green alternatives to non-degradable polymers. Poly lactic acid (PLA) is a chief contender to be a commercial success among biodegradable plastics. It is a thermoplastic aliphatic polyester derived entirely from renewable resources, by fermentation of agricultural products such as corn starch, tapioca, maize, sugar, and wheat [166; 167]. Since PLA has very low or no toxicity, it is used as structural scaffolds in human body for reconstruction of damaged organs, sutures for wound closure, drug delivery applications, orthopeadic devises for surgical applications etc [167-170].

PLA is synthesized from lactic acid. The ring opening polymerization or condensation polymerization of lactic acid gives high molecular weight poly-lactic-acid. Homo polymer Poly lactic acid has a glass transition temperature of 55-60$^{o}$C ($\alpha$

transition) and melting temperature of 180$^{o}$C [166]. According to the monomer used for the preparation, there are three different kinds of poly lactic acids, poly D lactic acid (PDLA), poly L lactic acid (PLLA) and poly D-L lactic acid (PDLLA). Enantiomerically pure poly lactic acid is semicrystalline in nature and always gives a high percentage of crystallinity to the material while PDLA and PLLA together form recemic or meso poly lactic acid. PDLLA is amorphous and transparent in physical appearance. The mechanical properties of semicrystalline PLA are better compared to amorphous PLA. The high molecular mass of polymer chain, presence of crystallinity and high entanglement density all give good mechanical property to PLLA [171]. In the semicrystalline PLA the polymer chains are more entangled compared to amorphous state and results in cross linking between the chains. This result in high molecular weight polymers and the tensile strength of the polymer increases. It is observed that a PLLA with relatively small amount of D isomer having 65% crystallanity is reported to have the highest impact strength. Recemization decrease the melting temperature of poly lactic acid by 20-30$^{0}$C, while it has the advantage of high mechanical processibility. Poly lactic acid is being used in variety of applications including interior parts of vehicles, electric appliances, bio-absorbable bone fixation devices etc [172; 173]. However, the low heat resistance and poor toughness of PDLLA limit its wider applicability.

Poly lactic acid is used in many biomedical applications, structural implantation, wound closure etc. Since the glass transition temperature of poly lactic acid, 60$^{o}$C, comes very close to the body temperature; there is particular interest in understanding the dynamics behavior of poly lactic acid in and around the glass transition temperature. Different techniques such as DSC, DMA, DES, Thermally stimulated recovery (TSR) are used to obtain information about the dynamics in the polymer. Using dielectric relaxation spectroscopy(DES), Mijovic *et al.* tried to understand the effect of crystalline region on chain dynamics of PLLA amorphous region [174]. They observed that the amorphous phase in PLLA undergoes cooperative chain motions with motional lengths that are shorter than the distance between the crystalline lamellae. Kanchanasopa *et al.* proposed the existence of a rigid amorphous phase in PLLA along with amorphous and crystalline phases and interpreted that the crystallinity induction along with the microcrystalline structure influence the $\alpha$ process [175]. Mano has studied the glass transition dynamics in PLLA using DMA and TSR techniques and found that at the glass transition

temperature the polymer chains are undergoing cooperative chain mobility [176]. Majority of the studies on the dynamics of poly lactic acid is performed based on mechanical property measurements and hence give macroscopic information.

To understand the mechanical behavior of polymers, it is very important to understand the contribution of the segmental and functional group motions. Theoretically, the random arrangement of coils results in motions at the molecular level. If the molecular scale of motions can be probed by solid-state NMR, and a correlation to the macroscopic behavior can be found, then probably more insight into the molecular origin for the mechanical property in poly lactic acid sample can be addressed. The aim of this study is to understand the thermo-mechanical behavior of PDLLA as a function of thermal ageing and correlate these with segmental and functional group dynamics.

## 4.3. Sample preparation

The amorphous PDLLA used for the SSNMR study was prepared by compression molding. The crystalline sample of PDLLA (6% D-L Lactic Acid), having a molecular weight of 256000 g/mol, was first heated to 200$^o$C, kept for 2 minutes in the compression die and then compressed to a narrow thin film. The thin film formed inside the die was then quickly put into cold water for quenching. The sample obtained after the process was hard and transparent in physical appearance. To check the nature of the sample Differential Scanning Calorimetry (DSC) was carried out.

The DSC graph of a fresh PDLLA is shown in figure 4.1. As the temperature rises, the curve goes linearly until 55$^o$C. In the region between 55$^o$C and 60$^o$C, the graph shows a dip indicating its glass transition ($T_g$). After the $T_g$ the DSC curve is linear until 200$^o$C. The melting temperature of PDLLA is expected to be around 150$^o$C-160$^o$C, if there is a crystalline component present. Since no peak is observed in this region, it can be confirm that the sample is purely amorphous.

## 4.4. Experimental

### 4.4.1. Differential Scanning Calorimetry (DSC)

All the DSC measurements have been carried out on a Q-100 differential scanning calorimeter from TA instruments. The DSC cell was first calibrated with

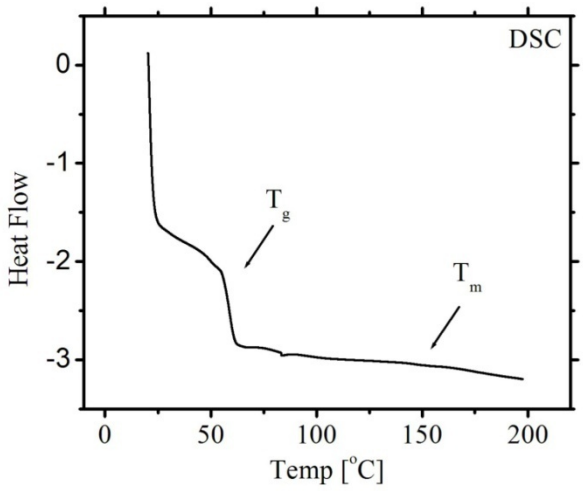


*Figure 4.1: DSC curve of a freshly prepared poly DL lactic acid obtained from Q-100 TA instrument. Its shows a $T_g$ around 55-60°C, while the melting temperature ($T_m$) peak expected at 150°C-160°C range is completely absent.*

99.99% pure indium. About 3-7 mg of sample was placed in an aluminum pan and used for the measurement. The thermal behavior of the sample was scanned from 0°C to 200°C with the rate of temperature increment at 10°C/min. The % of crystallinity of the sample is determined by the comparison of melting temperature peak areas of amorphous PLA and 100% pure crystalline PLA sample. It is given by the equation

$$\%\, crystallinity = 100 * {}^{\Delta H}/_{93} \tag{4.1}$$

where 93 J/g is the heat of fusion of an infinitely large crystal of poly lactic acid.

### 4.4.2. Solid-state NMR

The NMR measurements were carried out on Bruker Avance 300MHz spectrometer in a 4 mm triple resonance probe which is used in the double resonance mode. The processed PDLLA films were cut into small pieces and perfectly packed in 4 mm rotor. All the experiments were carried out at a spinning rate of 3 kHz. The RF frequencies of the $^{1}H$ and $^{13}C$ channels were 85 kHz and 67.5 kHz respectively. A mixing time of 2.5 $msec$ was used during the cross polarization. The TPPM-15 decoupling sequence with decoupling frequency of 85 kHz was used during the acquisiton. $^{1}H$ longitudinal relaxation time ($T_1$) was measured using the saturation recovery experiment and a recycle delay of five times $T_1$ was used for all the NMR experiments. The probe temperature was calibrated using Methanoal and $PbNO_3$ for the spinning rate of 3 kHz [143; 144]. A description about CODEX experiment is given in section 1.2.3. The CODEX mixing time ($\tau_m$) dependence experiment was

carried out by varying the mixing time from 1 $msec$ to 2048 $msec$ in a logarithmic scale with 12 data points in between. Each experiment was carried out with 1152 transients.

The samples which were thermally aged for 9 and 15 days were prepared by heating the sample in a vacuum oven at 65$^o$C which is ~5$^o$C above the glass transition temperature. One portion of the sample was used for the CODEX experiments and the other portion for the DSC measurements. All the CODEX experiments were carried out at 60$^o$C, at the glass transition temperature of poly lactic acid.

## 4.5. Results and Discussion

The chemical structure of PDLLA is shown in figure 4.2a. PDLLA contain three chemically distinct carbons: CO, CH and $CH_3$. The CPMAS spectrum of PDLLA at 23$^o$C is shown in figure 4.2 and the chemical shift observed at 170.0, 69.5 and 16.9 ppm is assigned to the environments CO, CH and $CH_3$ respectively. The CPMAS spectra clearly indicates that the centre band do not overlap with the spinning sidebands at a spinning speed of 3 kHz.

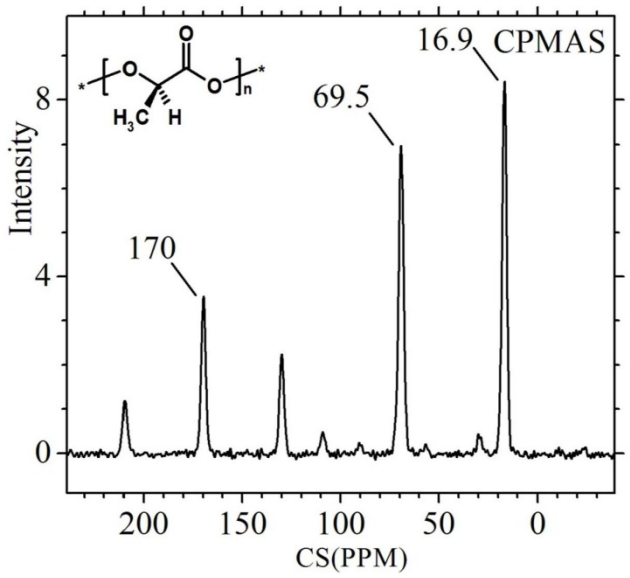


*Figure 4.2: The CPMAS spectrum of poly D-L lactic acid at 60$^o$C. The peak at 16.9 ppm, 69.5 ppm, and 170 ppm corresponds to $CH_3$, CH and CO environments respectively. The structure of polylacticacid is shown in the inset.*

The CODEX $N\tau_r$ dependence experiments were carried out with a mixing time of 100 $msec$. The CODEX $N\tau_r$ dephasing attains a plateau when $N\tau_r$ is equal to

3.33 $msec$ and therefore, all the CODEX $\tau_m$ dependence experiments were carried out with this $N\tau_r$. The results of the CODEX $\tau_m$ dependence experiments are discussed below. The CODEX $\tau_m$ dependent experiments were analyzed for both CH and $CH_3$ moiety, while the CO moiety was not analyzed due to poor signal to noise ratio.

It was observed that from 23°C to 50°C, the CODEX $\tau_m$ dependence does not show much dephasing in the difference signal, indicating that slow segmental motions are either absent or very slow. But as the temperature approaches 60°C, the CODEX $\tau_m$ dependence experiment shows dephasing indicating the onset of slow segmental and cooperative motions in the main chain. The CODEX difference spectrum obtained for the fresh PDLLA at 60°C with mixing times of 1, 8, 64 and 1024 $msec$ are shown in the figure 4.3. A gradual change in intensity of the CODEX difference spectrum indicates the presence of slow segmental motions at 60°C.

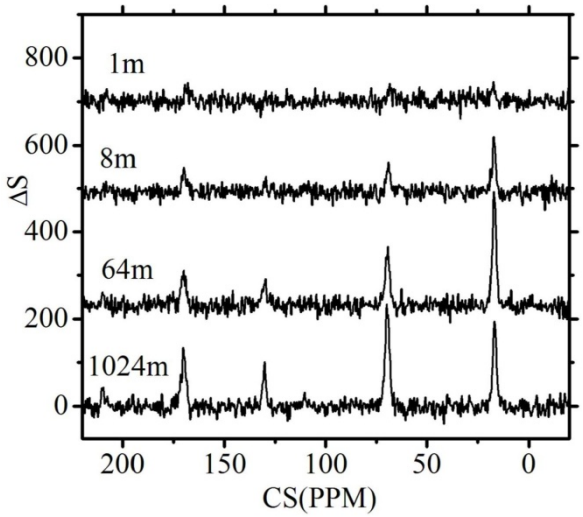


*Figure 4.3: The CODEX difference spectrum obtained for a fresh PDLLA sample at mixing times 1 msec, 8 msec, 64 msec and 1024 msec. The spectra show a gradual increase in the dephasing signal with the increase in mixing time.*

The results of CODEX $\tau_m$ dependence experiments obtained for the $CH_3$ and CH environments in PDLLA are shown in figures 4.4a and 4.4b respectively. The CODEX $\tau_m$ dependence experiments were carried out on fresh, 9 days and 15 days thermally aged sample. The normalized signal intensity ($S/S_0$) is fitted using the KWW function (Equation 1.44) to extract the correlation time of motion. It is

observed that the CODEX dephasing curves for both the $CH_3$ and CH environment show an upward shift with an increase in the annealing time.

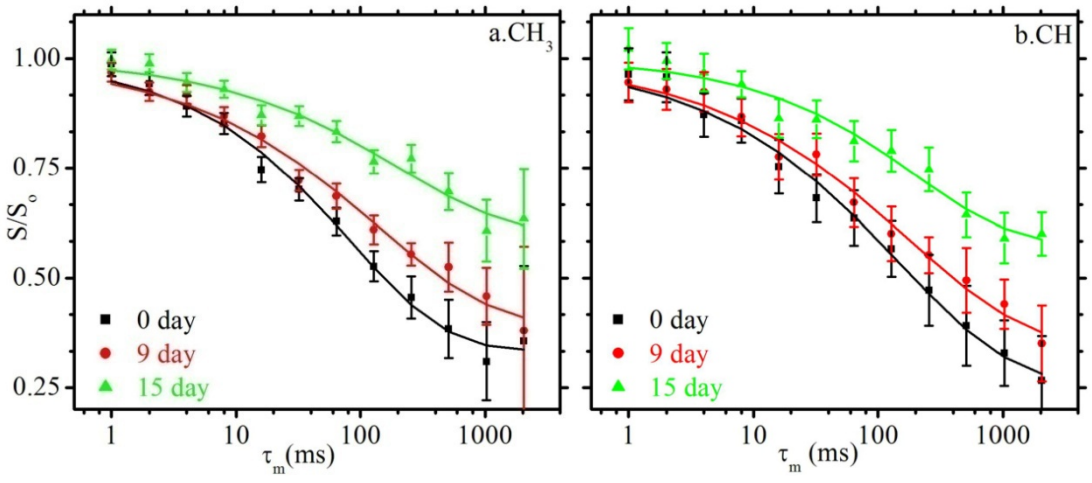


*Figure 4.4: The results of the CODEX $\tau_m$ dependence experiments of a).$CH_3$ b).CH moieties in PDLLA samples. The experiments were carried out on a fresh sample, 9 and 15 days thermally aged sample. It can be confirmed that at 60°C the chains possess slow segmental motions and the CODEX curve show an upward shift with annealing time. The CODEX signal intensity obtained was fitted with the KWW function to obtain correlation time.*

The fitting of CODEX de-phasing intensity against mixing time gave the correlation time, degree of distribution in correlation time and the fraction of segments available for motion and the values obtained for the $CH_3$ and CH moieties in PDLLA are tabulated in table 1. The $CH_3$ moiety of freshly prepared sample have a correlation time of 85.4 $msec$. This indicates slow segmental motions are present in PDLLA at 60°C. For the 9 days thermally aged sample a correlation time of 140.4 $msec$ was observed which indicates that there is a slowing down in segmental motion with respect to annealing. A correlation time of 205 $msec$ was obtained for the 15 days aged sample which confirms the slowing down of chain motion in the polymer with respect to thermal aging. The value of $M$ indicates the amount of segments available for motion which decreases as the thermal aging increases. A similar trend is observed for the CH group also, where the correlation time increases from 150.9 $msec$ to 203.5 $msec$, as the annealing time increases. The correlation time of both the CH and $CH_3$ group increases with annealing time, indicates that the rate of motions is decreases as annealing time increases.

| Aging (days) | $CH_3$ | | | CH | | |
|---|---|---|---|---|---|---|
| | $M$ | $\tau_m\ (msec)$ | $\beta$ | $M$ | $\tau_m\ (msec)$ | $\beta$ |
| 0 | 0.67±0.02 | 85.4±12.9 | 0.57±0.04 | 0.74±0.03 | 150.9±37.5 | 0.48±0.03 |
| 9 | 0.60±0.03 | 140.4±40.3 | 0.47±0.04 | 0.66±0.04 | 180.8±59.9 | 0.45±0.04 |
| 15 | 0.40±0.04 | 210.7±103.5 | 0.50±0.08 | 0.42±0.04 | 203.5±79.9 | 0.56±0.08 |

*Table 4.1: The correlation time $\tau_m$ of $CH_3$ and CH groups for different thermally aged samples along with the fraction of sample undergoing the dynamics ($M$) and the distribution in the correlation time ($\beta$).*

DSC measurements were also carried out on all the samples to determine the % of crystallinity accumulated (Figure 4.5a). It is seen that for the fresh sample the % of crystallinity is zero and it reaches 4% and 5% for the 9 and 15 days annealed samples.

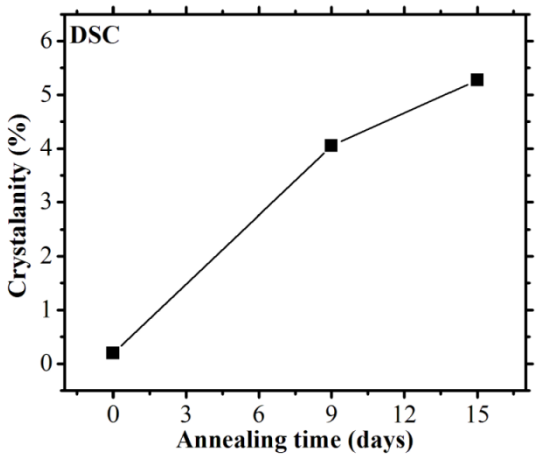


*Figure 4.5: a. The crystallinity obtained from the DSC measurements for different annealing times. The crystallinity increases with increase in the annealing time.*

## 4.6. Conclusion

The influence of thermal aging on the segmental and cooperative motion in poly lactic acid was studied using the CODEX experiment. Different thermal aged samples were prepared and the CODEX and DSC experiments were carried out on them. The CODEX experiments show that there are no slow motions in the polymer at low temperatures (23°C to 50°C). However, the slow motions were observed as the temperatures approaches to the glass transition temperature, 60°C. Slow motions of the order of 100s of Hz were detected through the CH and $CH_3$ moieties of the polymer and the rate of motions decreases with the aging of the sample. The DSC

measurements show that there is an increase in crystallinity with annealing time. Therefore, it is concluded that the increase in crystallinity in polymer chain decreases the rate of slow segmental motions in poly D-L lactic acid.

# CHAPTER 5

# Modification of the CODEX experiments using symmetry sequences

## 5.1. Abstract

The center band only detection of exchange (CODEX) NMR experiment, which was developed by deAzevedo *et al.* is an effective technique for determination of segmental and functional group motions in the range of 0.1 Hz to 1 kHz, in materials such as polymers, proteins etc [41]. The crucial component of the CODEX experiment is a series of 180$^o$ pulses separated by half rotor period which recouples the chemical shift anisotropy (CSA) and used as a probe for information on dynamics. In this chapter, an alternative approach for CODEX experiment using symmetry sequences developed by M. H. Levitt [47] is proposed, where the CSA recoupling element of CODEX is replaced with symmetry sequences $R10_1^3$, $R10_1^4$, $R18_2^5$, $R18_2^7$, $R18_4^5$ and $R14_4^3$. The experiment is called the R-CSA CODEX experiments. These sequences were first evaluated for their robustness to RF offset and RF power mismatch using SIMPSON simulations [24] and the efficiency of CSA recoupling of these sequences were tested at spinning speeds of 3 kHz and 10 kHz using a two dimensional experiment before implementing them in the R-CSA CODEX experiment. The R-CSA CODEX $N\tau_r$ dependence and mixing time ($\tau_m$) dependence experiments were carried out on a standard sample dimethylsulfone (DMS) and it is shown that this is a very effective alternative to the CODEX experiment.

## 5.2. Introduction

Functional group and main chain segmental motions play vital roles in the mechanical property of polymers, enzymatic activity of proteins etc [177; 178]. These motions usually have a wide range; very fast motions which are of the order of $10^9$ Hz and very slow motions which are of the order $10^{-2}$ Hz. Some of the motions that are generally observed are the methyl group rotations which are of the order of few $nsec$, 180$^o$ flips of aromatic rings which are of the order of 100s of kHz, conformational changes in the protein chains which occur in a wide range of 100s of kHz to few Hz and long chain oscillational and cooperative segmental motions of

polymers backbone which are of the order of few 100s of Hz. Different techniques such as Dynamic mechanical analysis (DMA) [150; 151], dielectric spectroscopy (DES) [175; 179], time resolved x-ray crystallography, neutron scattering (NS)[165; 180], solid-state NMR[177; 181-183] etc. are used to probe different types and ranges of motions. Solid-state NMR has a clear advantage over the other current available techniques since it can probe different ranges of motions and can resolve different functional groups which are responsible for its mobility [178; 182; 184]. The CODEX experiment is an advanced solid-state NMR technique which is used to measure motions in the range of $msec$ to $sec$ and has the advantage that it can be applied to samples without isotope enrichment [41]. In this chapter, an alternative to the CSA recoupling element in the CODEX experiment using symmetry based R sequences the R-CSA CODEX experiment is proposed. Before implementing the symmetry elements into the CODEX pulse sequence, the CSA recoupling efficiency of the sequence is verified using a 2D CSA recoupling experiment.

The CODEX experiment was developed as a technique for measurement of slow dynamics in polymers [41; 115]. Schmidt-Rohr and group used the CODEX experiments for studying the geometry of side chain dynamics in systematically substituted poly(n alkyl methacrylates) [118; 126]. They observed large amplitude $180^{o}$ flips motions along with small amplitude chain fluctuations in poly(n alkyl methacrylates). The CODEX experiments were able to measure quantitatively the fraction of molecule flip in the polymer. According to the measurements, they interpreted that 34% of the side groups in poly(methyl methacrylates) undergoes flip motions and it reduces with an increase in the side group bulkiness and reaches 10 % in case of poly(n hexyl methacrylates). Ovidiu *et al.* were able to correlate mechanical relaxation to the main chain and side group segmental motions in the polymer Poly(n hexamethyl methacrylate) using the CODEX experiments and could identify that the side chain motions contribute mainly to the $\beta$ relaxation and both the side chain and main chain contribute to the $\alpha$ relaxation[117].

There are reports on improvements in the CODEX experiment called SCODEX and CONTRA experiments [185; 186], where a better understanding to geometry of motions is possible by these sequences. The important issue for the determination of motional geometry by these sequences is, the need for CSA parameters for the system under study. Krushelnitsky *et al*. developed a heteronuclear

dipolar recoupling version of the CODEX experiment to study complex systems like peptide and proteins and identified the side chain motions in α-Spectrin SH3 proteins [120]. Another modification of the CODEX experiment is the R-CODEX, which also uses hetero nuclear dipolar coupling as the probe for information about dynamics where efficient suppression of homonuclear dipolar coupling is made possible by symmetry based R sequences [187; 188]. Hence the efficiency and accuracy of information about dynamics in the CODEX experiments are determined by the CSA or dipolar recoupling pulse sequences.

In solid-state NMR, the CSA gives information about the molecular structure, conformation, dynamics and functional properties of organic and inorganic materials. Polymer dynamics is one of the areas where CSA is frequently used, directly or indirectly for determining the geometry, frequency and activation energy of segmental and functional group motions [114; 182]. From the analysis of CSA line shape, Roy *et al.* proposed that in polycarbonates simultaneous $180^{o}$ flips and small angle rotational diffusional motion with a distribution in the correlation time are present [156]. The activation energy obtained from the correlation time is in very good agreement with that obtained from dielectric spectroscopy (DES) and dynamic mechanical analysis (DMA). Kentgens *et al.* used CSA based exchange experiments for characterizing the chain motions of polyoxymethylene and measured the activation energy of crystalline motions and found that it matches with the results from mechanical relaxation methods [2]. In proteins and peptides, CSA is used for the assignment of functional groups, and information about the secondary structure since the conformational arrangement of proteins produces helix and $\beta$-sheet structure which produces entirely different CSA line shape [189; 190]. Many of the techniques use CSA directly or indirectly for obtaining information about dynamics in polymers.

Levitt and group proposed symmetry based C and R sequences for the reintroduction of different internal spin interactions using simultaneous manipulation of spin and space Hamiltonian [47; 49; 191]. The advantage of these sequences is that it can be applied at high spinning speeds which were not possible for many of the other present sequences. Hou *et al.* applied symmetry sequences into biological systems for the reintroduction of heteronuclear dipolar and chemical shift anisotropy interactions and hence to obtain structural information such as bond angle, bond length etc [129; 190]. In this chapter, the recoupling of the CSA using symmetry

based sequences are explored and suitable sequences for CODEX experiments are identified and demonstrated on a standard sample dimethysulphone (DMS).

## 5.3. Methods

The principle of the symmetry based pulse sequences is that a combination of mechanical rotation of the sample and simultaneous rotation of the nuclear spin magnetization in the spin space recouple the desired interaction in a very elegant way with simultaneous suppression of the undesired ones. As discussed in section 1.3., Levitt has proposed two classes of symmetry sequences to recouple the internal spin interactions, the $C$ and $R$ sequences [47]. The $R$ sequences have advantages over the $C$ sequences in terms of selectivity. The $R$ sequence suppress majority of unwanted internal spin interactions (dipolar, *J*-coupling etc. here) with the recoupling of the desired one (CSA).

The symmetry based $R$ sequence, $RN_n^\nu$ [47], used for CSA recoupling experiments are shown in figure 5.1a and 5.1b. The CSA recoupling sequence is divided into three periods; the preparation period during which the cross polarized (CP) $^{13}C$ magnetization is generated, the evolution period during which the spin system evolves under the rotor synchronized $RN_n^\nu$ sequence, the detection period during which the NMR signal is acquired. R sequences are $z$ rotation sequence (rotation of magnetization start from $z$ axis), therefore the magnetization obtained after cross polarization is put into the $z$ axis by a 90$^o$ pulse present at the beginning of

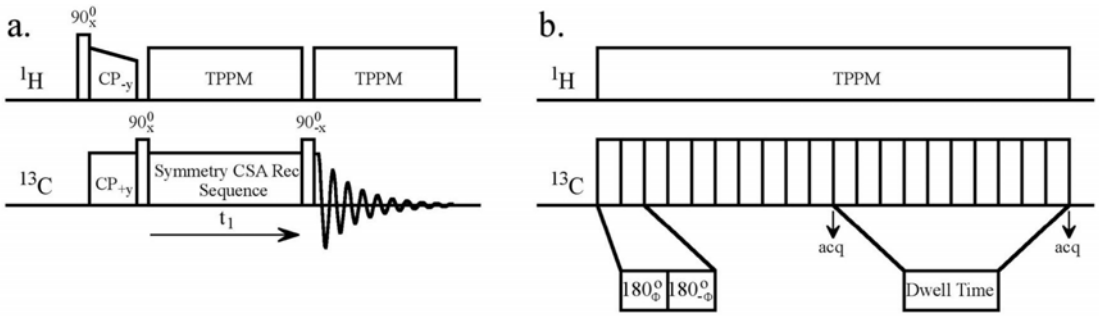


*Figure 5.1: a) 2D Pulse sequence for CSA recoupling using Symmetry based R sequence. b) The $t_1$ dimension of a particular 2D symmetry sequence $R10_1^3$ is shown. A basic element of $180_\Phi$, with $\phi = 54^o$ is used here. The signals are acquired after every complete rotation of the rotor.*

the $RN_n^\nu$ recoupling period. At the end of $RN_n^\nu$ period the magnetization is put back into the $xy$ plane using another 90$^o$ pulse and then follows the detection period.

A detailed description of symmetry R sequences is given in section 1.3. In short, the $RN_n^\nu$ sequence contains $N/2$ repetition of the basic element $R_{\pi\nu/N}R_{-\pi\nu/N}$ which is enclosed in '$n$' rotor periods. The radio frequency (RF) power of the sequence depends on the spinning rate and is designed in such a way that '$N$' number of basic elements must be included in $n$ rotor periods. In general, the Hamiltonian recoupled during a particular $RN_n^\nu$ sequence is determined by the selection rule

$$\widehat{H}_{l,m,\lambda,\mu} \neq 0 \quad \text{if} \quad mn - \mu\nu = NZ_\lambda/2 \tag{5.1}$$

where $m$ and $\mu$ are the spin and space component of the internal spin interaction recoupled respectively and $Z_\lambda$ is any integer having value of same parity as that of the spin rank tensor value. The interaction with components which satisfy the above condition survives during $RN_n^\nu$ scheme while other components are suppressed. The effective Hamiltonian of the above interaction can be simplified by the Magnus expansion and the first order Hamiltonian of the interaction is given by the equation

$$\hat{H} = K_{m,\lambda,\mu}\hat{A_{lm}}(\Omega_{PR})\, d^l_{m0}(\beta_{RL})\, \hat{T_{\lambda,\mu}} \tag{5.2}$$

where $K_{m,\lambda,\mu}$, $\hat{A_{lm}}$, $\hat{T_{\lambda,\mu}}$ represents the scaling factor, the spatial component and spin component of the internal spin interaction respectively.

During the mechanical spinning of the sample, the spatial part of the second rank tensor, here it is CSA tensor, is split into components $m = [-2, -1, 0, 1, 2]$ while under the influence of the external RF field the spin part of the first rank CSA tensor splits into components $\mu = [-1, 0, 1]$. The symmetry number of $RN_n^\nu$ sequence determines if the recoupling component of the CSA interaction is 1$^{st}$ order or 2$^{nd}$ order or both in the spatial part. The second rank tensor for the CSA interaction in the lab frame is given by the equation [129; 190]

$$\begin{aligned}\widehat{H}_{CSA} &= \widehat{H}_0^{CSA} + \widehat{H}_1^{CSA} + \widehat{H}_2^{CSA} \\ &= \widehat{H}_{2,0,\lambda,\mu}^{CSA} + \widehat{H}_{2,\pm1,\lambda,\mu}^{CSA} + \widehat{H}_{2,\pm2,\lambda,\mu}^{CSA} \\ &= \sum_{m=0,\lambda,\mu} K_{m,\lambda,\mu}\hat{A_{lm}}(\Omega_{PR})d^l_{m0}(\beta_{RL})\hat{T_{\lambda,\mu}}\end{aligned}$$

$$+\sum_{m=\pm1,\lambda,\mu} K_{m,\lambda,\mu}\hat{A_{lm}}(\Omega_{PR})d^{l}_{m0}(\beta_{RL})\hat{T_{\lambda,\mu}}$$

$$+\sum_{m=\pm2,\lambda,\mu} K_{m,\lambda,\mu}\hat{A_{lm}}(\Omega_{PR})\, d^{l}_{m0}(\beta_{RL})\, \hat{T_{\lambda,\mu}} \quad (5.3a)$$

$$= \gamma B_0\sigma_0 I_z + \gamma B_0\sigma_1 \cos(\gamma_{PR} + \omega_r t + \delta_1)\, I_z$$

$$+ \gamma B_0\sigma_2 \cos 2(\gamma_{PR} + \omega_r t + \delta_2)\, I_z \quad (5.3b)$$

where the second element of equation 5.3a corresponds to 1st order term ($\sigma_1$) while third element corresponds to 2nd order term ($\sigma_2$). The expression for $\sigma_0$, $\sigma_1$, $\sigma_2$ are given by

$$\sigma_0 = \sigma^{iso} + P_2(\cos\beta_{RL})[P_2(cos\beta_{PR})\left(\sigma_{zz}^{PAS} - \sigma^{iso}\right) + \frac{1}{2}sin\beta_{PR}\cos 2\alpha_{PR}(\sigma_{xx}^{PAS} - \sigma_{yy}^{PAS})] \quad (5.4a)$$

$$\sigma_1 = sin\beta_{RL}cos\beta_{RL}sin\beta_{PR}\Big[sin\beta_{PR}\big[-3\left(\sigma_{zz}^{PAS} - \sigma^{iso}\right) + 3cos2\alpha_{PR}\left(\sigma_{xx}^{PAS} - \sigma_{yy}^{PAS}\right)\big]^2 + [sin2\alpha_{PR}\left(\sigma_{xx}^{PAS} - \sigma_{yy}^{PAS}\right)]^2\Big]^{1/2} \quad (5.4b)$$

$$\sigma_2 = \frac{1}{2}\, sin^2\beta_{RL}\Bigg[\Big[\frac{3}{2}\, sin^2\beta_{PR}\left(\sigma_{zz}^{PAS} - \sigma^{iso}\right) + \frac{1}{2}(1 + cos2\beta_{PR})\, cos2\alpha_{PR}\left(\sigma_{xx}^{PAS} - \sigma_{yy}^{PAS}\right)\Big]^2 + [sin\beta_{PR}sin2\alpha_{PR}\left(\sigma_{xx}^{PAS} - \sigma_{yy}^{PAS}\right)]^2\Bigg]^{1/2} \quad (5.4c)$$

The scaling factor of these recoupled components are evaluated by integrating the equations 35 given in reference [47] or equation 50 in ref [49]. It can also be calculated using the Mathematica notebook SPINDYNAMICA[127]

## 5.4. The R sequences used in this study

Several CSA recoupling sequences can be designed based on the symmetry selection rule and the spin-space selection diagram. CSA recoupling sequences for which $N \leq 20, n \leq 10$ and $\nu \leq 10$ are listed in the article by Levitt in the Encyclopedia of Magnetic Resonance [47]. After evaluating several sequences listed in the article for its robustness by simulating their performance using the SIMPSON program [24] and calculating their scaling factor using MATHEMATICA notebook

SPINDYNAMICA [127], six sequences $R10_1^3$, $R10_1^4$, $R18_2^5$, $R18_2^7$, $R18_4^5$ and $R14_4^3$ were selected for further study. The six sequences can be grouped into two based on the CSA component that is recoupled. The $R10_1^4$, $R18_2^7$, $R18_4^5$, $R14_4^3$ recouple the 1st order component ($\sigma_1$) while $R10_1^3$, $R18_2^5$ recouple the 2nd order component ($\sigma_2$) of the CSA. The basic building blocks of the $RN_n^\nu$ sequences are the $R$ elements which is a pulse or series of pulses which give an effective 180° rotation about the x axis. There are three common R elements that are reported in the literature: $180_0$ $90_{45}90_{45}90_{45}$ and $90_0270_{180}$ [47; 49]. The parameters of the sequences for different R elements are shown in Table 5.1. The RF frequency for a particular $RN_n^\nu$ sequence at a particular spinning speed is calculated using the method mentioned in section 1.3/5.3.

For example, the $R10_1^3$ sequence contains ten R elements in one rotor period and the symmetry number $\nu = 3$ determine the phase at which the pulses are applied. This sequence recouples the 2nd order component of the spatial CSA tensor ($\sigma_2$). When the R element is 180°, this sequence has five $[180_{54}180_{306}]$ pulse pairs in one rotor period. For spinning speeds of 3 kHz and 10 kHz, the RF powers are 15 kHz and 50 kHz respectively. The scaling factor of the sequence is 0.17. When the R element is $90_{45}90_{-45}90_{45}$ the sequence contains five repeating units of $[90_{99}90_{9}90_{99}90_{261}90_{351}90_{261}]$ pulses in one rotor period. For spinning speeds of 3 kHz and 10 kHz this sequence have RF powers of 22.5 kHz and 75 kHz respectively. The scaling factor of this sequence is 0.20. When the R element is $90_0270_{180}$, this sequence contains five repeating units of $[90_{54}270_{234}90_{306}270_{126}]$ pulses in one rotor period. For spinning speeds of 3 kHz and 10 kHz the RF powers of the sequence are 30 kHz and 100 kHz respectively. The scaling factor of the sequence is very low at 0.06.

From Table 5.1, it is seen that the sequences with R elements $90_{45}90_{-45}90_{45}$ have the best scaling factor, $180_0$ have good and $90_0270_{180}$ have the least scaling factor. However from studies using simulations, it is seen that the $180_0$ is more robust to the RF-offset, RF-power mismatch and easier to implement because there are lesser number of pulses (details are given in the appendix). Hence the R element $180_0$ is used in the R sequences for CSA recoupling and the R-CSA CODEX experiments. The simulation of the sequences have been restricted to RF power $\leq$ 50 kHz. The RF

| R sequence | Compt. Rec. $(\sigma_1/\sigma_2)$ | R element | RF power at | | Scaling Factor |
|---|---|---|---|---|---|
| | | | 3 kHz | 10 kHz | |
| $R10_1^3$ | $\sigma_2$ | $180_0$ | 15 | 50 | 0.18 |
| | | $90_{45}90_{-45}90_{45}$ | 22.5 | (75) | 0.20 |
| | | $90_0270_{180}$ | 30 | (100) | 0.06 |
| $R10_1^4$ | $\sigma_1$ | $180_0$ | 15 | 50 | 0.26 |
| | | $90_{45}90_{-45}90_{45}$ | 22.5 | (75) | 0.27 |
| | | $90_0270_{180}$ | 30 | (100) | 0.04 |
| $R18_2^5$ | $\sigma_2$ | $180_0$ | 13.5 | 45 | 0.18 |
| | | $90_{45}90_{-45}90_{45}$ | 20.25 | (67.5) | 0.20 |
| | | $90_0270_{180}$ | 27 | (90) | 0.06 |
| $R18_2^7$ | $\sigma_1$ | $180_0$ | 13.5 | 45 | 0.26 |
| | | $90_{45}90_{-45}90_{45}$ | 20.25 | (67.5) | 0.27 |
| | | $90_0270_{180}$ | 27 | (90) | 0.06 |
| $R18_4^5$ | $\sigma_1$ | $180_0$ | 6.75 | 22.5 | 0.25 |
| | | $90_{45}90_{-45}90_{45}$ | 10.01 | 33.75 | 0.29 |
| | | $90_0270_{180}$ | 13.1 | 45 | 0.09 |
| $R14_4^3$ | $\sigma_1$ | $180_0$ | 5.25 | 17.5 | 0.24 |
| | | $90_{45}90_{-45}90_{45}$ | 7.9 | 26.25 | 0.3 |
| | | $90_0270_{180}$ | 10.5 | 35 | 0.11 |

*Table 5.1: The parameters of the symmetry based CSA recoupling sequences used in this study.*

power of $R10_1^3, R10_1^4, R18_2^5, R18_2^7$ seqeunces with $90_{45}90_{-45}90_{45}$ and $90_0270_{180}$ pulse element at 10 kHz spinning speed exceeds 50 kHz. Simulations showed that when the RF power exceeds 50 kHz, the rcoupled line shape is distorted for these sequences and hence not used for further studies.

## 5.5. Experimental

All the NMR experiments were carried out on a Bruker AV 300 MHz spectrometer with a carbon frequency of 75 MHz. A 4 mm triple resonance magic angle spinning probe head was used. The cross polarization contact time of 2.5 $msec$ and 1.2 $msec$ was used for DMS and alanine respectively for all measurement. A

recycle delay of 2 $sec$ was enough for DMS and alanine for the complete equilibration of $^{1}$H magnetization during cross polarization experiments. The CODEX 180$^{o}$ pulses were applied with an RF frequency of 67.5 kHz and 95 kHz at 3 and 10 kHz respectively. During the refocusing period of the CODEX experiment $^{1}$H deoupling using TPPM was applied with low power. For a specific spinning speed and a pulse element each R sequence has a constant pulse width. The RF power used in the R sequence is calibrated using a $^{13}$C 90$^{o}$ pulse which is introduced just after a cross polarization sequence. Keeping the pulse width constant, the RF power is varied linearly and the RF power corresponding to the first null point of the $^{13}$C peak is RF power for which the pulse width is 90$^{o}$. During the evolution and the detection periods of the R CSA sequence, $^{1}$H-$^{13}$C decoupling is achieved by TPPM-15 [59] with a $^{1}$H RF power of 85 kHz.

The spectral width of the indirect dimension in the 2D CSA recoupling experiment is determined by the rotor frequency $\nu_R$, the span of $RN_n^\nu$ sequence $n$ and is given by $\nu_R/n$. The acquisition point of the signal after every $RN_n^\nu$ block, $\left[R_{\pi\nu/N}R_{-\pi\nu/N}\right]_{N/2}$, is represented by a circle in the figure 5.2b. This mode of acquisition has low spectral width and therefore will not be able to study systems with a large anisotropy such as the aromatic CH or carbonyl groups, especially at low spinning speeds. The possibility of acquiring the signal after every $R_{\pi\nu/N}R_{-\pi\nu/N}$ element was explored using SIMPSON simulations. The acquisition after every $R_{\pi\nu/N}R_{-\pi\nu/N}$ pulse element has the advantage that it increases the spectral width of the experiment $N/2$ times in the indirect dimension. An implementation of the $R10_1^3$ sequence with the R element $180_0$ is shown in figure 5.2b, where the acquisition after every pair of basic symmetry elements (two $180_0$ pulses) is called an $N/2$ mode acquisition, while the FID points acquired after every $n$ rotor period (ten $180_0$ pulses) is called an $n$ mode acquisition. The $N/2$ mode is called so because $N/2$ points are acquired in each $n$ rotor cycle. The spectral width of $N/2$ mode acquisition in the indirect dimension of 2D experiment is given by $N\nu_R/2n$. All the 2D experiments were implemented in the phase insensitive mode.

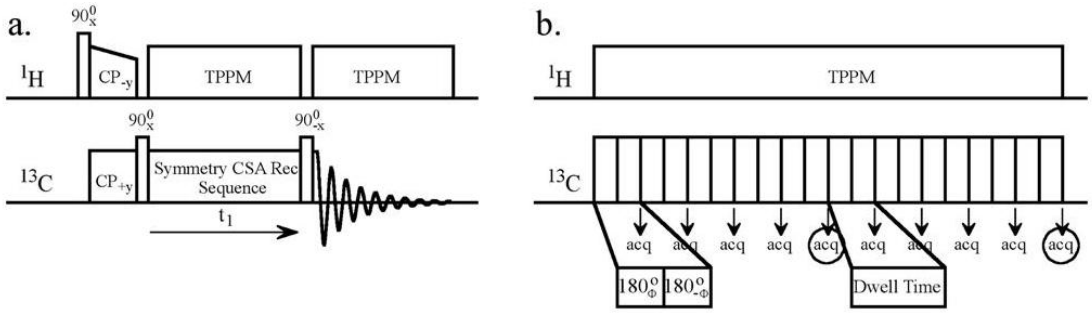


*Figure 5.2: a) The 2D pulse sequence for recoupling the CSA using R sequences. b) The $t_1$ dimension of $R10_1^3$ 2D sequence. A basic element of $180_\Phi$, with $\phi = 54^o$ is used. The signals are acquired after every $180_\Phi 180_{-\Phi}$ element which is shown by the arrows ($N/2$ mode) and the acquisition of signal after every $RN_n^\nu$ sequence is indicated by arrow with a circle ($n$ mode).*

Simulations of the $R10_1^3, R10_1^4, R18_2^5$ and $R18_2^7$ sequences in the $N/2$ and the $n$ mode were carried out using SIMPSON for the carbonyl environment of alanine at a spinning speed of 10 kHz and the results are shown in figure 5.3. The simulated spectra show that the line shape of the recoupled CSA pattern from the $N/2$ mode is similar to that from the $n$ mode. This shows that the R sequences implemented in the $N/2$ mode are better CSA recoupling experiments since they have better resolution. At a spinning speed of 3 kHz, the spectral width of the CSA recoupling sequences $R10_1^3, R10_1^4, R18_2^5$ and $R18_2^7$ implemented in the $n$ mode are 3.33, 3.33, 1.66 and 1.66 kHz respectively and therefore not sufficient to observe the CSA line shape of the carbonyl environment of alanine which has an anisotropy of 71 ppm (5.2 kHz in a 300 MHz spectrometer). The advantage of the CSA recoupling sequences implemented in the $N/2$ mode is that its spectral width is $N/2$ times as that of the sequence implemented in the $n$ mode. The spectral width of CSA recoupling sequences using $R10_1^3, R10_1^4, R18_2^5$ and $R18_2^7$ sequences in the $N/2$ mode are 16.66, 16.66, 14.94, 14.94 kHz respectively, and has enough spectral width to observe the CSA line shape at a spinning speed of 3 kHz. Since the spectral width of the CSA recoupling sequences using the selected R sequences implemented in the $n$ mode are not enough to recouple the full CSA at a spinning speed of 3 kHz, a comparison of the CSA line shape with the sequence implemented in the $N/2$ mode is not possible. For the CSA recoupling sequences using the $R18_4^5, R14_4^3$ sequences implemented in the $N/2$ mode, at a spinning speed of 3 kHz the spectral widths are 6.75 and 5.25 kHz

respectively which are lower than the other four sequences and from the simulations using SIMPSON it is seen that the recoupling efficiencies are very poor since the RF power of the sequences are 6.75 kHz and 5.25 kHz respectively. Therefore the experimental implementations of $R18_4^5, R14_4^3$ sequences have not been carried out at the spinning speed of 3.

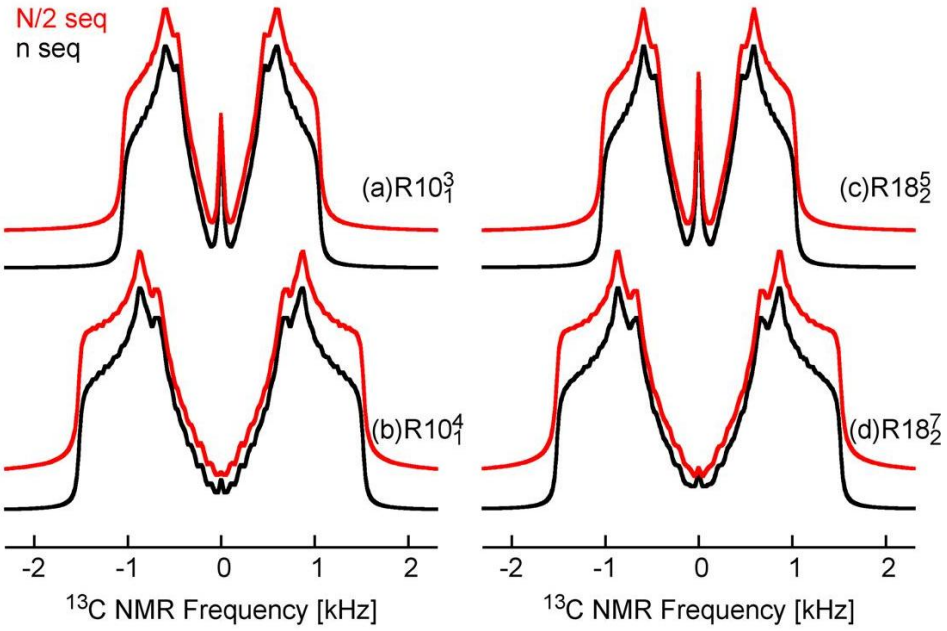


*Figure 5.3: Comparison of the simulated CSA line shape obtained by the n mode and the N/2 mode at a spinning speed of 10 kHz for the carbonyl environment of alanine.*

## 5.6. The R-CSA CODEX experiment

The CODEX experiments that are modified using the $R$ sequences are called the R-CSA CODEX experiments. A detailed description of the CODEX experiment is given in section 1.2.3. In the R-CSA CODEX experiments, the RR′ pulse pair is applied during $N\tau_r$ period. For example the R-CSA CODEX pulse sequence used for $R10_1^3$ sequence is shown in figure 5.4. As described in section 1.2.3, two kinds of measurements were carried out in the CODEX experiments. The first experiment is the $N\tau_r$ dependence, where the $N\tau_r$ at which the CODEX dephasing reaches plateau is used for mixing time dependence experiment. In the second experiment, the recoupling time $N\tau_r$ is kept fixed and the dephasing is measured as a function of the mixing time($\tau_m$). The $N\tau_r$ dependence experiment is carried out in both the $n$ and $N/2$ mode. In the $n$ mode the $N\tau_r$ is incremented as function of $R_{\pi\nu/N}R_{-\pi\nu/N}$, while

for $N/2$ mode the $N\tau_r$ is incremented as function of $\left[R_{\pi\nu/N}R_{-\pi\nu/N}\right]_{N/2}$. The normalized spectrum intensity (CODEX to REFERENCE) is plotted as a function of the $N\tau_r$ duration in both the $n$ and $N/2$ modes. The main difference between the CODEX and $R$-CSA CODEX experiments is the evolution of magnetization during the $N\tau_r$ period. In the CODEX experiment the magnetization evolves with respect to $z$ axis, ie in the $xy$ plane, during $N\tau_r$ period. In the R-CSA CODEX experiment, the magnetization evolves about an axis which is placed in the $xy$ plane; with the starting point of magnetization evolution is $z$ axis. The axis of evolution of $RN_n^\nu$ sequence is determined by the symmetry numbers of the sequence, $\pm\pi\nu/N$. In the CODEX experiment, since the magnetization evolves in the $xy$ plane during $N\tau_r$ period, two $90^o$ pulses called store pulse and read out pulses are used before and after the mixing time while in the R-CSA CODEX experiment the magnetization starts and ends at $z$ axis of lab frame and hence the store and read out pulses are not needed.

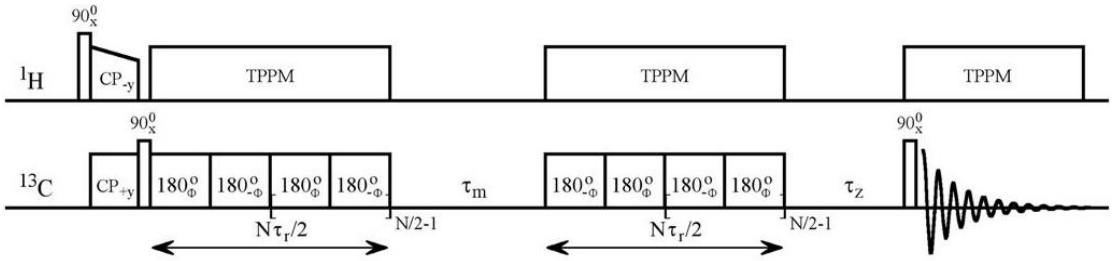


*Figure 5.4: The pulse sequence for the R-CSA CODEX experiment with $R10_1^3$ sequence where the R element used is $180_\Phi$ with $\phi = 54$.*

## 5.7. Results and discussion

The 2D experiments are carried out on alanine using different R sequences with $180^o$ pulse as the basic R element at spinning speeds of 3 and 10 kHz. Since the RF power of $R18_4^5$ and $R14_4^3$ sequences at a spinning speed of 3 kHz, are less than 10 kHz (table 5.1), and simulation showed that they have a very inefficient recoupling, they were not used for the 2D experiments and the R-CSA CODEX experiments. At a spinning speed of 10 kHz, the RF powers of all the sequences $R10_1^3$, $R10_1^4$, $R18_2^5$, $R18_2^7$, $R18_4^5$, $R14_4^3$ are ≤ 50 kHz and were used in the 2D experiments and the R-CSA CODEX experiments. The 2D spectrum acquired in the $N/2$ mode for the carbonyl environment of alanine using the $R10_1^3$ sequence at a spinning speed of 10 kHz is shown in figure 5.5. From the 2D experiment, the sum projection of the spectra

into the indirect spectral dimension is obtained and is shown in the indirect dimension of the 2D spectrum. This projection spectrum is iteratively fitted with a simulated CSA line shape to extract the CSA parameters.

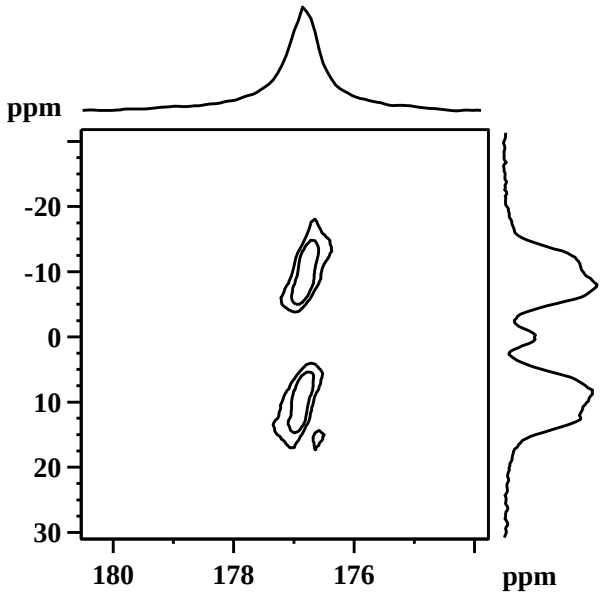


*Figure 5.5: 2D CSA spectrum obtained using the* $R10_1^3$ *sequence at a spinning speed of 10 kHz. The sum projection of the indirect dimension gives the recoupled CSA lineshape and is shown in the 2D projection.*

## 5.7.1. Extraction of the CSA parameters

The extraction of the CSA parameters was carried out using the OPT package in SIMPSON, which iteratively fits the experimental spectra with the simulated spectrum. The CSA parameters of the carbonyl environment of alanine were extracted using this method. The CSA values of the carbonyl environment of alanine: $\delta_{iso}$= 176 ppm, $\delta_{aniso}$= -70 ppm and $\eta$=0.85 were used as the initial values. Then $\delta_{iso}$, $\delta_{aniso}$ and $\eta$ were varied iteratively between 169 & 180 ppm, -90 & -40 ppm, 0.5 & 1.0 respectively with iteration intervals of 0.3, 0.4 and 0.02 respectively. The experimental spectra along with the iteratively fitted spectra for the 4 sequences $R10_1^3, R10_1^4, R18_2^5$ and $R18_2^7$ at a spinning speed of 3 kHz are shown in figure 5.6 and that of the 6 sequences $R10_1^3, R10_1^4, R18_2^5, R18_2^7, R18_4^5$ and $R14_4^3$ at a spinning speed of 10 kHz are shown in figure 5.7.

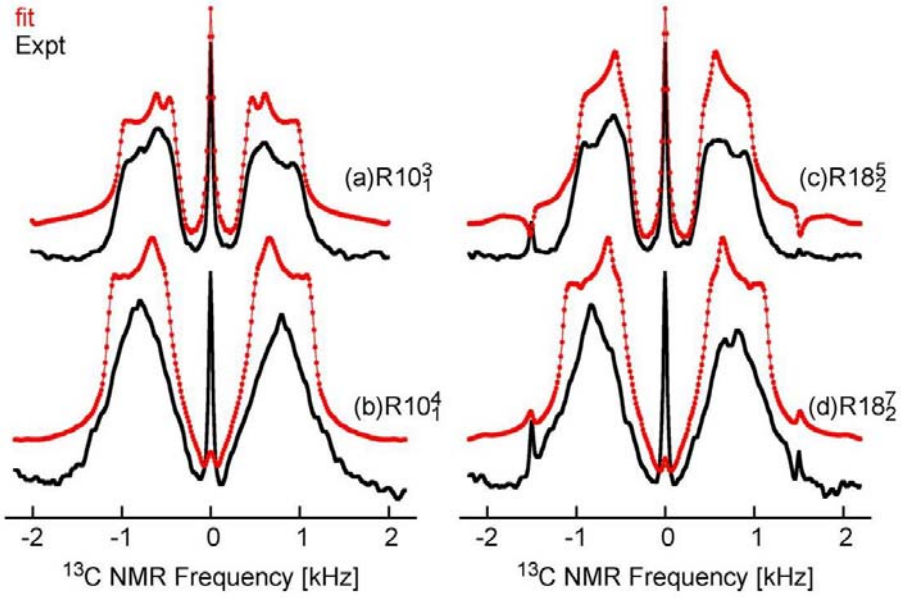


*Figure 5.6: The experimental and the fitted spectrum of the carbonyl environment of alanine at a spinning rate of 3 kHz using* $a).R10_1^3$, $b).R10_1^4$, $c).R18_2^5$ *and* $d).R18_2^7$ *sequences with the R element* $180_0$.

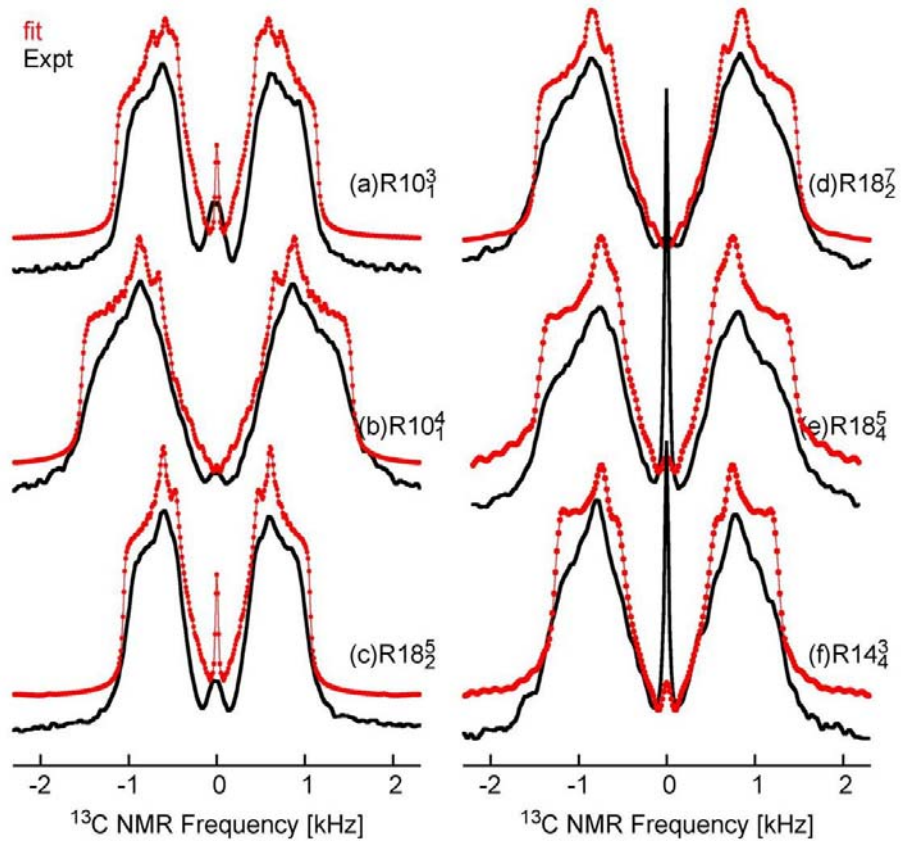


*Figure 5.7: The experimental and fitted spectra of the carbonyl environment of alanine, at a spinning speed of 10 kHz using* $a).R10_1^3$, $b).R10_1^4$, $c).R18_2^5$, $d).R18_2^7$, $e).R18_4^5$ *and* $f).R14_4^3$ *sequences with the R element* $180_0$.

At a spinning speed of 3 kHz, the experimental spectrum of the $\sigma_2$ CSA recoupling sequences such as $R10_1^3, R18_2^5$ shows a similar line shape to the fitted spectra (figure 5.6a, 5.6c). The extracted CSA parameters tabulated in table 5.2 indicate that the experimental and simulated spectra are very close to each other except the $\sigma_1$ seequences. A large deviation was observed between the experimental and the fitted spectra for the $\sigma_1$ CSA recoupling sequences $R10_1^4, R18_2^7$ (figure 5.6b, 5.6d). The anisotropy value of the fitted spectra is -54 ppm which largely deviated from the expected anisotropy value of -71 ppm. (table 5.2).

At the spinning speed 10 kHz also the experimental spectra of the $\sigma_2$ CSA recoupling sequences $R10_1^3$, $R18_2^5$ show a similar line shape to the fitted spectra (figure 5.7a, 5.7c) and the calculated CSA values are very close to the expected values which are tabulated in table 5.2. For the $\sigma_1$ CSA recoupling sequences $R10_1^4, R18_2^7$-

| Sequence | $\sigma_1/\sigma_2$ | Spinning rate | CSA parameters | | |
|---|---|---|---|---|---|
| | | | $\delta_{iso}$ | $\delta_{aniso}$ | $\eta$ |
| $R10_1^3$ | $\sigma_2$ | 3 kHz | 173.5±18.9 | -68.6± 3.6 | 0.77± 0.15 |
| | | 10 kHz | 175.6±0.01 | -76.7±3.7 | 0.77±0.19 |
| $R10_1^4$ | $\sigma_1$ | 3 kHz | 177.6± 8.6 | -54.1± 3.5 | 0.85± 0.22 |
| | | 10 kHz | 176.6±0.01 | -71.7±3.5 | 0.82±0.16 |
| $R18_2^5$ | $\sigma_2$ | 3 kHz | 180.0±19.3 | -67.0± 3.5 | 0.83± 0.16 |
| | | 10 kHz | 176.1±0.01 | -72.7± 3.5 | 0.83±0.16 |
| $R18_2^7$ | $\sigma_1$ | 3 kHz | 176.3±7.4 | -54.1±3.3 | 0.71±0.09 |
| | | 10 kHz | 176.4±0.01 | -69.5± 3.6 | 0.83±0.17 |
| $R18_4^5$ | $\sigma_1$ | 3 kHz | -- | -- | -- |
| | | 10 kHz | 176.9±12.3 | -69.8± 4.7 | 0.85± 0.15 |
| $R14_4^3$ | $\sigma_1$ | 3 kHz | -- | -- | -- |
| | | 10 kHz | 171.1±15.04 | -65.1± 4.2 | 0.82± 0.17 |
| Expected values of the CSA | | | 178 | -71 | 0.83 |

*Table 5.2: The CSA parameters of the carbonyl environment of alanine extracted from the experimental spectra using SIMPSON at spinning rates of 3 and 10 kHz for the sequences $R10_1^3, R10_1^4, R18_2^5, R18_2^7, R18_4^5$ and $R14_4^3$. The values obtained are compared with the expected CSA values except $\sigma_1$ sequences at 3 kHz .*

there is an improvement in the CSA line shape (figure 5.7b, 5.7d) compared to that at 3 kHz and this is reflected in the CSA values extracted, which are closer to the expected values (table 5.2). The experimental spectrum of $\sigma_1$ CSA recoupling sequences $\mathrm{R18}_4^5, \mathrm{R14}_4^3$ also show a good CSA line shape at 10 kHz which is very close to the iteratively fitted spectrum (figure 5.7e, 5.7f), and the CSA values obtained from the fitting confirm this.

The recoupled CSA line shape shows that the $\sigma_1$ recoupling sequences $\mathrm{R10}_1^4, \mathrm{R18}_2^7$ are less efficient at 3 kHz while the recoupling efficiency of these sequences improved at 10 kHz. The $\sigma_2$ recoupling sequences $\mathrm{R10}_1^3, \mathrm{R18}_2^5$ show that they are efficient for CSA reocupling both at 3 and 10 kHz spinning speeds. The $\sigma_1$ CSA recoupling sequences such as $\mathrm{R18}_4^5, \mathrm{R14}_4^3$ also have better recoupling efficiency at a spinning speed of 10 kHz.

The aim of carrying out the 2D experiments and extracting the CSA parameters was to demonstrate the capability of the R sequences to recouple the CSA efficiently before it is used in the R-CSA CODEX experiment.

### 5.7.2. R-CSA CODEX at 3 kHz

The R-CSA CODEX experiments were first carried out at a spinning speed of 3 kHz to test the validity of this approach by comparing with the CODEX experiment at 3 kHz, before implementing it at higher spinning speeds. The efficiency of the CODEX experiment depends on maintaining the ideality of the 180$^o$ pulses used in the 180$^o$ pulse train and the total pulse length in a rotor period should be less than 10% [41]. At a spinning speed of 3 kHz with $^{13}$C RF power of 67.5 kHz, this ratio is around 4% and satisfy above condition. The R-CSA CODEX $N\tau_r$ and $\tau_m$ dependence experiments were carried out on the standard sample DMS. As mentioned earlier, the 180$^o$ pulses trains with half rotor period delay in the CODEX experiment is replaced with the $R10_1^3$, $R10_1^4$, $R18_2^5$, $R18_2^7$ sequences in the R-CSA CODEX experiments. The experiments were carried out in the $n$ mode and $N/2$ mode. For $n$ mode sequence the $N\tau_r$ evolution is a function of full R element, ie. $[R_{\pi\nu/N}R_{-\pi\nu/N}]_{N/2}$, while for the $N/2$ mode sequence the $N\tau_r$ evolution is a function of $R_{\pi\nu/N}R_{-\pi\nu/N}$ element. For the $N\tau_r$ dependence experiments, a mixing time ($\tau_m$) of 100 $msec$ ($\tau_m$>>$\tau_c$) and a $z$ filter time of 1 $\mu sec$ is used. The $\tau_m$ dependence experiment was carried out by

varying the mixing time from 0.33 $msec$ to 128 msec. At a spinning speed of 3 kHz the sample temperature was 26°C. The $N\tau_r$ dependence experiments were carried out to identify the plateau value to be used in the $\tau_m$ dependence experiments. As mentioned in the section 1.2.3, the $N\tau_r$ dependence experiments are also used to determine the geometry of motion of the system. This aspect of the $N\tau_r$ dependence experiments were not explored in this study and this experiment was used only to identify the $N\tau_r$ value at which the $S/S_0$ attain the plateau. The $N\tau_r$ dependence curves obtained from different R-CSA CODEX experiments in the $n$ mode (green circle) and the CODEX $N\tau_r$ dependence curves (black points) are shown in figure 5.8. In the R-CSA CODEX experiments, the resolution of $N\tau_r$ experiment depends on the particular $n$ value and the spinning speed of the sample. At a spinning speed of 3 kHz R-CSA CODEX experiments using the $R10_1^3$, $R10_1^4$, $R18_2^5$, $R18_2^7$ sequences in the $n$ mode have $N\tau_r$ resolutions of 0.666 $msec$, 0.666 $msec$, 1.333 $msec$ and 1.333 $msec$ respectively. The CODEX experiment at the same spinning speed have $N\tau_r$ resolution of 0.666 $msec$.

The CODEX $N\tau_r$ dependence experiment at 3 kHz is shown in figure 5.8, where the first dephasing point itself reaches the plateau with $S/S_0$ of 0.54 at $N\tau_r$ of 0.666 $msec$. After reaching the plateau, the dephasing point oscillates between 0.53 and 0.55 as $N\tau_r$ is increased. For the R-CSA CODEX $N\tau_r$ dependence experiment using $R10_1^3$ in the $n$ mode (figure 5.8a), the $S/S_0$ decreases from 1 to 0.45 and then oscillate between 0.5 and 0.65. The $N\tau_r$ at which the $S/S_0$ reaches plateau is 2.66 $msec$. For the R-CSA CODEX $N\tau_r$ dependence experiment using $R10_1^4$ in the $n$ mode (figure 5.8b), it is observed that the $S/S_0$ decreases from 1 to 0.55 and then oscillates between 0.52 and 0.58. The $N\tau_r$ at which the $S/S_0$ reaches plateau is 1.33 $msec$. The $N\tau_r$ dephasing curve of $R10_1^4$ CODEX experiment is similar to that of the CODEX, after it reaches the plateau. It can be seen that the resolution of CODEX, and R-CSA CODEX using $R10_1^3$ and $R10_1^4$ are the same because the $N\tau_r$ evolution in this case is a function of 2 rotor periods. For R-CSA CODEX $N\tau_r$ dependence experiment using $R18_2^5$ in the $n$ mode (figure 5.8c), the $S/S_0$ intensity decreases from 1 to 0.65 and then oscillate between 0.5 and 0.65. However since the $N\tau_r$ resolution $R18_2^5$-CODEX sequence is $2n$ times the rotor period (4 rotor periods) the oscillations are not very evident. The $N\tau_r$ at which the $S/S_0$ reaches saturation is 2.66 msec. For R-CSA

CODEX $N\tau_r$ dependence experiment using $R18_2^7$ in the $n$ mode (figure 5.8d), the $S/S_0$ decreases from 1 to 0.55 and then oscillates between 0.52 and 0.58. The $N\tau_r$ at which the $S/S_0$ reaches saturation is 1.33 $msec$. Here also the resolution of the sequence is low since $N\tau_r$ evolution is a function of 4 rotor periods. However, the $N\tau_r$ dephasing curve obtained is similar to the CODEX $N\tau_r$ dephasing curve. -

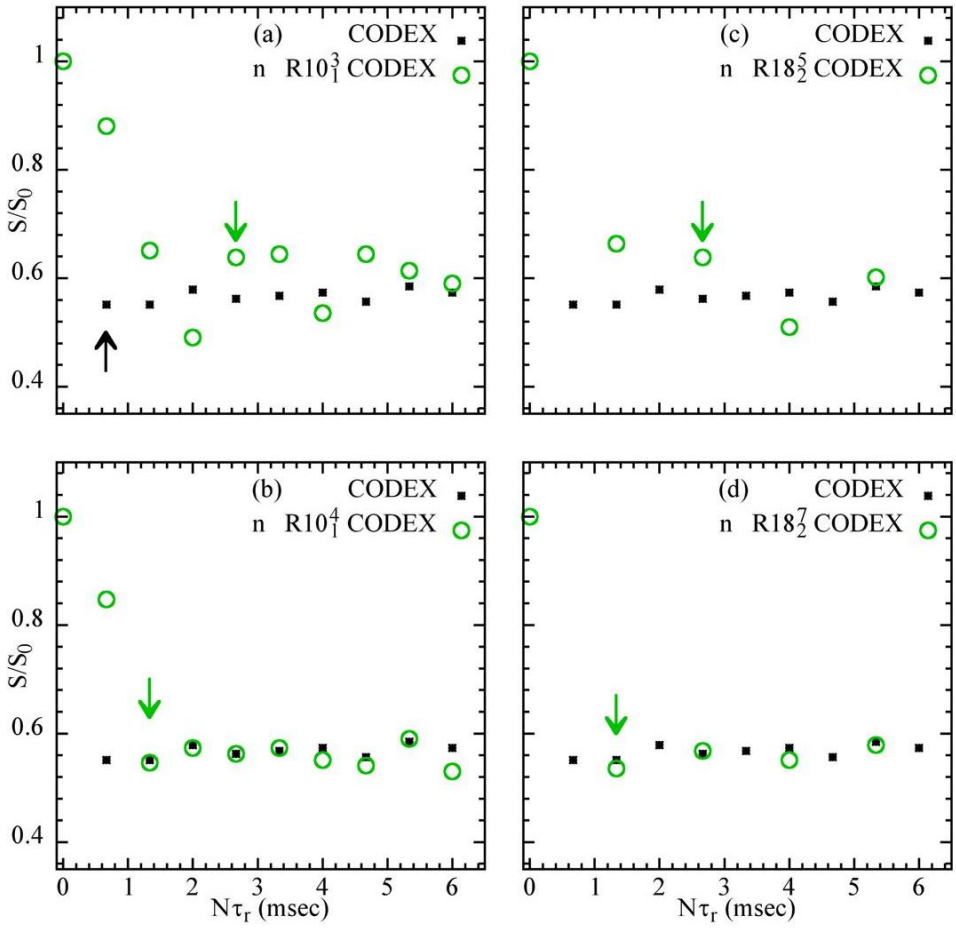


*Figure 5.8: The results of the CODEX $N\tau_r$ dependence experiment plotted along that from the R-CSA CODEX $N\tau_r$ dependence experiment using $(a)R10_1^3$, $(b)R10_1^4$, $(c)R18_2^5$, $(d)R18_2^7$ sequences in the n mode (green circle) at a spinning speed of 3 kHz. For all the experiments, the R element was 180₀, the mixing time ($\tau_m$) 100 $msec$ and the z-filter time 1 $\mu sec$. The $R10_1^4, R18_2^7$ CSA CODEX $N\tau_r$ dephasing curves are similar to that of the CODEX experiment (black points) after it reaches the plateau. The green arrows indicate the first point of the plateau in the $N\tau_r$ dephasing curves in the $n$ mode which was used for the $\tau_m$ dependence experiment. The black arrow indicate the $N\tau_r$ value used in the CODEX $\tau_m$ dependence experiment.*

Comparing the results from all the experiment at 3 kHz spinning speed, it is observed that the $N\tau_r$ dephasing curve of R-CSA CODEX experiment using $\sigma_1$ CSA recoupling sequences $R10_1^4$ and $R18_2^7$ are similar to the CODEX $N\tau_r$ dephasing curve, while that using of $\sigma_2$ CSA recoupling sequences $R10_1^3$ and $R18_2^5$ deviate from the CODEX $N\tau_r$ dephasing curve. The green arrow in the figure 5.8 indicates the plateau value for each R-CSA CODEX $N\tau_r$ dependence experiment and these were used in $\tau_m$ dependence experiments.

For all the R-CSA CODEX experiments, the $N\tau_r$ at which the $S/S_0$ saturates has increased compared to that from the CODEX experiment. This is probably because the CSA is scaled by the symmetry sequences. For the R-CSA CODEX $N\tau_r$ dependence experiments using $R10_1^3$, $R10_1^4$, $R18_2^5$, $R18_2^7$ sequences, the first plateau value observed are at 2.66 $msec$, 1.33 $msec$, 2.66 $msec$ and 1.33 $msec$ respectively. Using these $N\tau_r$ values, the R-CSA CODEX $\tau_m$ dependence experiments were carried out and the dephasing curves obtained are shown in figure 5.9. For the CODEX $\tau_m$ dependence experiment, an $N\tau_r$ of 0.666 $msec$ was used. The dephasing points are iteratively fitted with the KWW function (equation 1.44) to obtain the correlation time of motion and the values obtained for R-CSA CODEX and the CODEX experiments are tabulated in table 5.3. The fitted curves of the R-CSACODEX experiments using $R10_1^4$, $R18_2^7$ sequences ($\sigma_1$) are similar to the CODEX experiments since they have similar $S/S_0$ at the plateau. The fitted curves from the R-CSA CODEX experiments using $R10_1^3$, $R18_2^5$ sequences ($\sigma_2$) are different from CODEX experiment because their $N\tau_r$ curves have different $S/S_0$ at the plateau. However correlation times of 3.0 $msec$, 2.9 $msec$, 3.1 $msec$, 3.0 $msec$ were obtained for R-CSA CODEX experiments using $R10_1^3$, $R10_1^4$, $R18_2^5$, $R18_2^7$ respectively, while 3.1 $msec$ was obtained from the CODEX experiment. This shows that even if the $N\tau_r$ at which the $S/S_0$ reaches plateau are different for different sequences the correlation time obtained is within ±0.2 $msec$ of that obtained from CODEX, indicating that R-CSA CODEX experiments are as good as the CODEX experiments at 3 kHz. In particular, the R-CSA CODEX experiments using $R10_1^4$, $R18_2^7$ sequences ($\sigma_1$) are very similar to the CODEX experiments for both the $N\tau_r$ and $\tau_m$ dependence experiments.

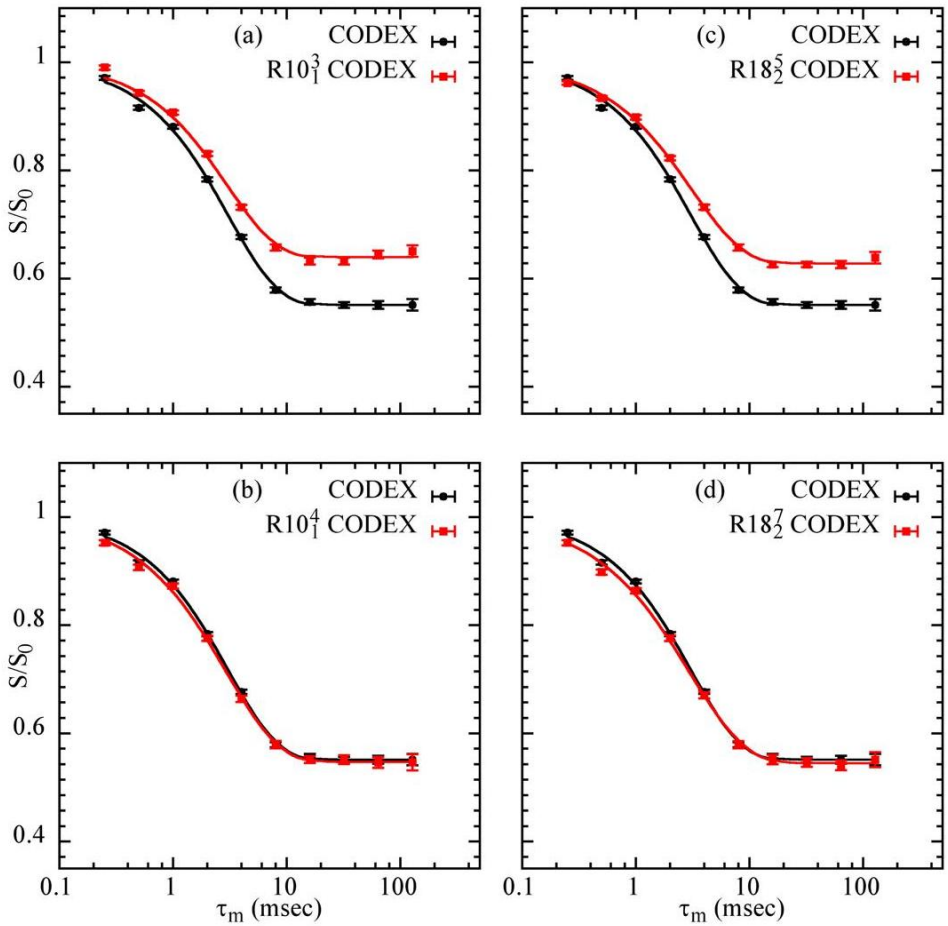


*Figure 5.9: R-CSA CODEX $\tau_m$ dependence curves obtained using sequences $R10_1^3$, $R10_1^4$, $R18_2^5$, $R18_2^7$ at a spinning speed of 3 kHz. The dephasing curves are fitted with the KWW function to extract the correlation time of motion. The $N\tau_r$ value for the experiment was taken from the first plateau value of $N\tau_r$ dephasing curve (green arrow of figure 5.8).*

| Sequence | $N\tau_r$ $(msec)$ | $\tau_c$ $(msec)$ |
|---|---|---|
| CODEX | 0.66 | 3.1 |
| $R10_1^3$ | 2.66 | 3.0 |
| $R10_1^4$ | 1.33 | 2.9 |
| $R18_2^5$ | 2.66 | 3.1 |
| $R18_2^7$ | 1.33 | 3.0 |

*Table 5.3: The correlation time obtained from the CODEX and the R-CSA CODEX experiments with corresponding $N\tau_r$ value in the n mode at a spinning speed of 3 kHz.*

The R-CSA CODEX $N\tau_r$ dependence curves obtained using $N/2$ mode are shown in figure 5.10. This experiment using $R10_1^3$, $R10_1^4$, $R18_2^5$, $R18_2^7$ sequences have $N\tau_r$ resolutions of 0.133 $msec$, 0.133 $msec$, 0.148 $msec$ and 0.148 $msec$ respectively. As mentioned earlier, the CODEX $N\tau_r$ dependence experiment at this spinning speed has an $N\tau_r$ resolution of 0.666 $msec$.

For the R-CSA CODEX $N\tau_r$ dependence experiments using $R10_1^3$ (figure 5.10a), it is observed that the $S/S_0$ decreases from 1 to 0.4 and then oscillates between 0.5 and 0.65. The $N\tau_r$ at which the $S/S_0$ reaches saturation is 2.66 $msec$. For the R-CSA CODEX $N\tau_r$ CODEX dependence experiments using $R10_1^4$ (figure 5.10b), the $S/S_0$ decreases from 1 to 0.45 and then oscillates between 0.5 and 0.6. The $N\tau_r$ at which the $S/S_0$ reaches saturation is 2.0 $msec$. For the R-CSA CODEX $N\tau_r$ dependence experiments using $R18_2^5$ (figure 5.10c), the $S/S_0$ decreases from 1 to 0.45 and then oscillates between 0.5 and 0.65. Large oscillations are observed here with $N/2$ modes which were not seen in the $n$ mode. For the the R-CSA CODEX $N\tau_r$ dependence experiments using $R18_2^7$ (figure 5.10d), the $S/S_0$ decreases from 1 to 0.5 and then oscillate between 0.54 and 0.6. The $N\tau_r$ at which the $S/S_0$ reaches saturation is 2.0 $msec$. The results from the $n$ mode acquisition are shown as green circles for a comparison with $N/2$ mode acquisition (red points). R-CSA CODEX $\tau_m$ dependence experiments were carried out using a plateau value from $N\tau_r$ curve obtained in the $N/2$ mode which is different from that in the $n$ mode.

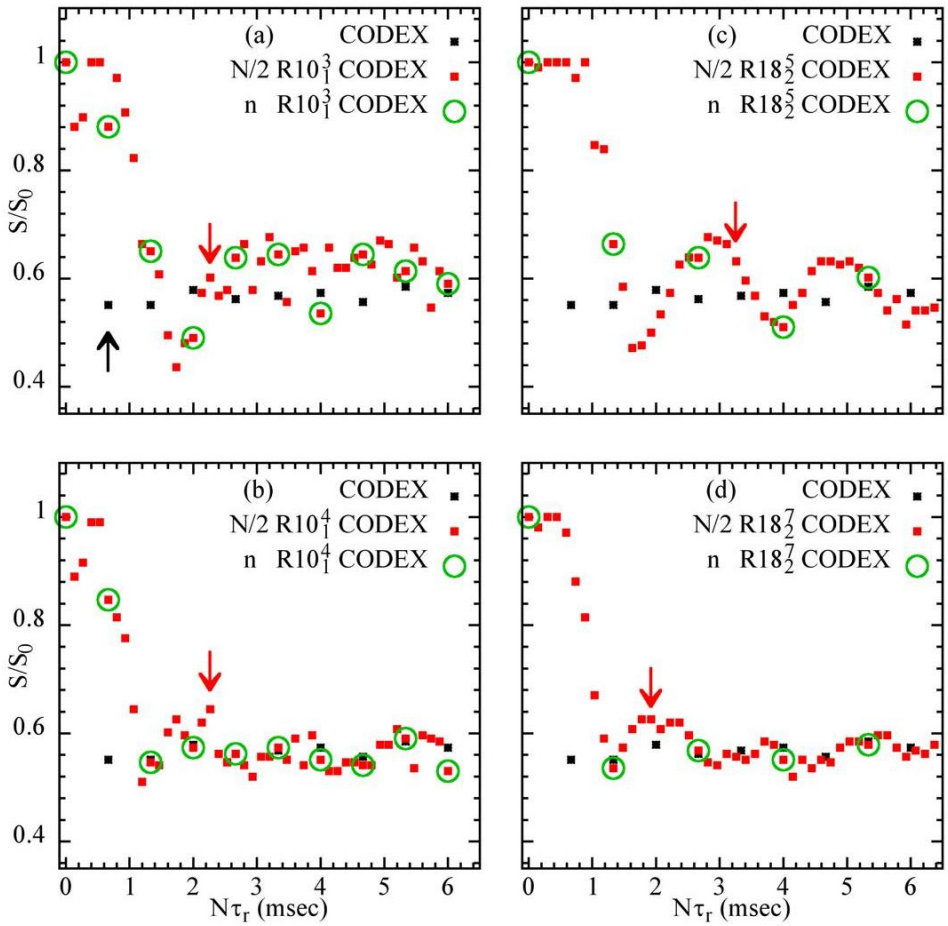


*Figure 5.10: The results of the CODEX $N\tau_r$ dependence experiment plotted along with that from the R-CSA CODEX $N\tau_r$ dependence experiment using $a).R10_1^3$, $b).R10_1^4$, $c).R18_2^5$, $d).R18_2^7$ sequences in the N/2 mode (red points) at a spinning speed of 3 kHz. For all the experiments, the R element was $180_0$, the mixing time ($\tau_m$) 100 $msec$ and the z-filter 1 $\mu sec$ used. The dephasing curves of R-CSA CODEX experiments using $R10_1^4$, $R18_2^7$ are similar to that of the CODEX experiment (black points) after the plateau. The green circle indicates n mode points. The red arrows are the $N\tau_r$ value selected for $\tau_m$ dependence experiment while black arrow is the $N\tau_r$ value selected for CODEX $\tau_m$ dependence experiment.*

The results of the R-CSA CODEX $\tau_m$ dependence experiments carried out using the $R10_1^3$, $R10_1^4$, $R18_2^5$, $R18_2^7$ sequences with $N\tau_r$ values of 2.26 $msec$, 2.26 $msec$, 1.92 $msec$ and 1.92 $msec$ respectively are shown in figure 5.11. The $\tau_m$ dependence curves of the R-CSA CODEX experiments are compared with that from the CODEX experiments obtained with $N\tau_r$ value of 0.666 $msec$. The dephasing curves are fitted with the KWW function to extract the correlation time of motion (equation 1.44) and the values obtained for the R-CSA CODEX along with the

CODEX experiments are tabulated in table 5.4. All the R-CSA CODEX $\tau_m$ dependence curves deviate from the CODEX $\tau_m$ dependence curves. For R-CSA CODEX using the $R10_1^3$, $R10_1^4$, $R18_2^5$, $R18_2^7$ sequences, correlation times of 3.3 $msec$, 3.2 $msec$, 3.4 $msec$, 3.4 $msec$ were obtained respectively which are within $\pm 0.3$ $msec$ of the correlation time of 3.1 $msec$ obtained from the CODEX experiments. Thus it is observed that even if R-CSA CODEX $\tau_m$ dependence curves deviate from the CODEX $\tau_m$ dependence curves, the correlation time obtained are very close.

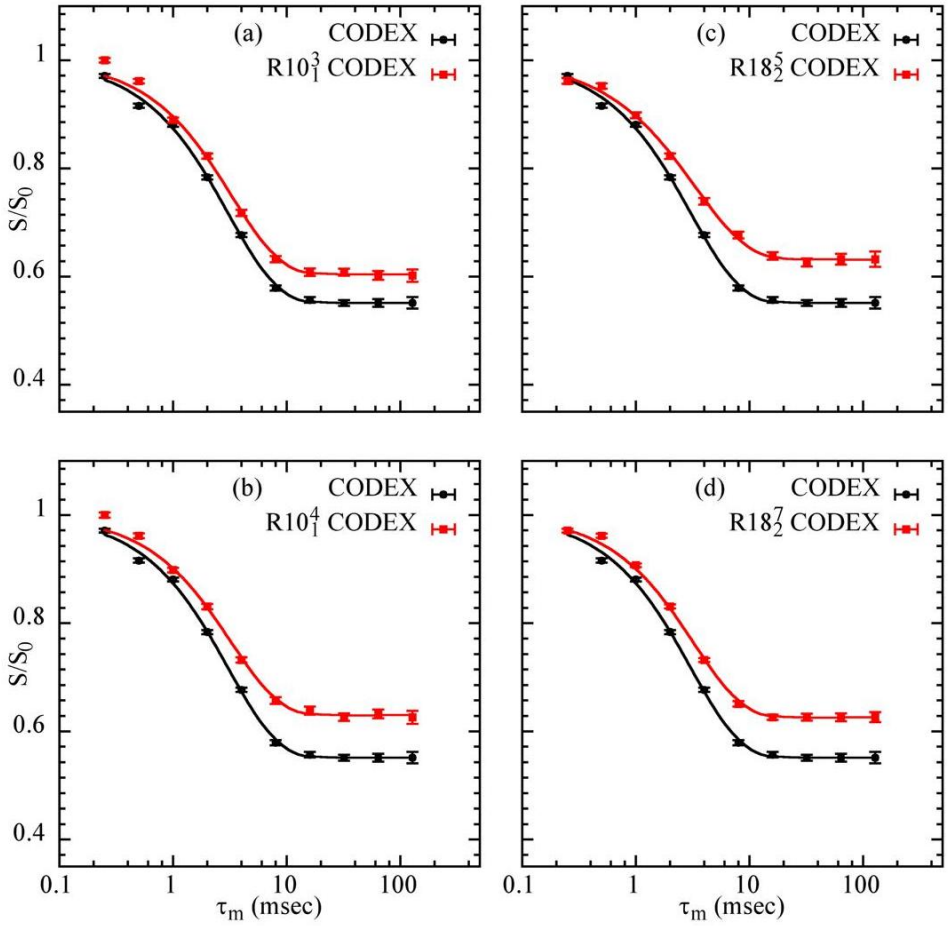


*Figure 5.11: R-CSA CODEX $\tau_m$ dependence curves obtained with R-CSA CODEX experiments using $R10_1^3$, $R10_1^4$, $R18_2^5$, $R18_2^7$ sequences at a spinning speed of 3 kHz. They are fitted with the KWW function to extract the correlation time of motion. The $\tau_m$ dependence experiments were carried out with the $N\tau_r$ values obtained from the: R-CSA CODEX experiments in the $N/2$ mode.*

| Sequence | $N\tau_r\ (msec)$ | $\tau_c\ (msec)$ |
|---|---|---|
| CODEX | 0.66 | 3.1 |
| $R10_1^3$ | 2.26 | 3.3 |
| $R10_1^4$ | 2.26 | 3.2 |
| $R18_2^5$ | 1.92 | 3.4 |
| $R18_2^7$ | 1.92 | 3.4 |

*Table 5.4: The correlation times obtained from the CODEX and the R-CSA CODEX experiments with the corresponding $N\tau_r$ value which are acquired in $N/2$ mode at spinning speed of 3 kHz.*

From the results of the R-CSA CODEX experiments at 3 kHz, it is clear that the approach of using R sequences to recouple the CSA in the CODEX experiment is an effective method. Among the $N\tau_r$ dependence experiments in the $n$ mode, there is a clear difference between the R-CSA CODEX experiments using the $\sigma_1$ CSA recoupling sequences and the $\sigma_2$ recoupling sequences. But the correlation times obtained from these experiments are similar to the value that is obtained from the CODEX experiment when the $N\tau_r$ value is used from the $n$ mode as well $N/2$ mode. Thus it may be concluded that the R-CSA CODEX experiment in the $n$ mode acquisition is clearly as effective as the CODEX experiment.

The main aim of this study was to probe the effectiveness of symmetry based approach for dynamics measurements in CODEX at higher spinning speeds, where the CODEX require short 180$^o$ pulses (high RF power) to maintain ideal nature of pulses, which is difficult to achieve.

### 5.7.3. R-CSA CODEX at 10 kHz

The efficiency of a CODEX experiment is determined by 180$^o$ RF pulse length. Each rotor period of the CODEX experiment contains two 180$^o$ pulses. The CODEX experiment will be efficient if the total 180$^o$ pulses length is less than 10% of rotor period [41] and the efficiency will be best if they are ideal pulses. At a spinning speed of 3 kHz with an RF power of 67.5 kHz, ratio of the 180$^o$ pulse length to the rotor period is 4% and hence CODEX works very well as shown in the section 5.7.2. However at a spinning speed of 10 kHz with an RF power of 67.5 kHz this ratio is around 15%. This affects the performance of the CODEX experiment and it is seen in

the CODEX $N\tau_r$ dependence experiments. The results of CODEX $N\tau_r$ dependence experiments on DMS at a spinning speed of 10 kHz with RF powers of 67.5 kHz and 95 kHz are shown in figure 5.12. The ratio of the pulse length to the rotor period for 67.5 kHz and 95 kHz of RF power are 15% and 10.4 % respectively. For both the experiments, the $S/S_0$ decreases from 0.93 to 0.59 and reaches the minimum at $N\tau_r$ of 0.8 $msec$, and then the dephasing curve shows an upward shift as $N\tau_r$ increases. However, the deviation is less when the RF power of 180$^o$ pulse is 95 kHz compared to 67.5 kHz since the pulse length to the rotor period ratio is smaller at 95 kHz. The only way to achieve the best $N\tau_r$ dephasing curve is to increase the RF power to get close to an ideal pulse which is not possible with the RF powers available in standard 4 mm probes.

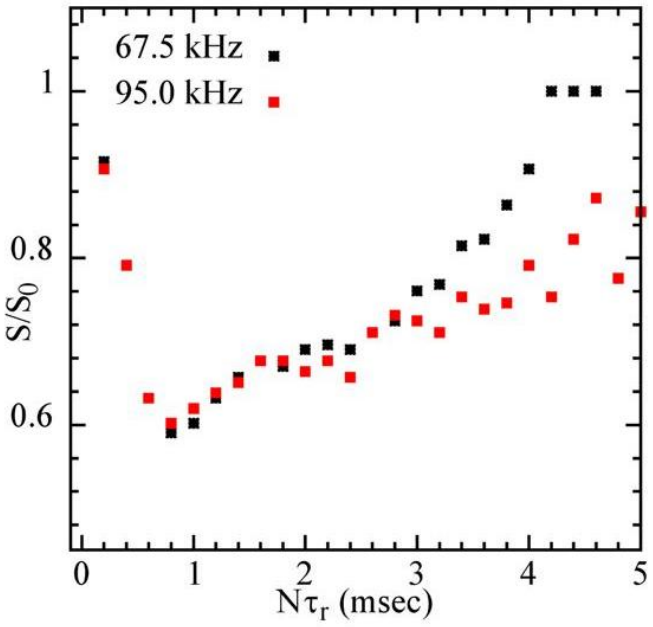


*Figure 5.12: Results of the CODEX $N\tau_r$ dependence experiments carried out with 180$^o$ pulses at RF powers of 67.5 kHz and 95 kHz at a spinning speed of 10 kHz. The dephsaing curves from both the experiments show an upward shift after reaching the minimum. The shift seen when the RF power is 95 kHz is less compared to that when it is 67.5 kHz.*

The R-CSA CODEX experiments have the advantage that the recoupling of CSA is achieved by composite RF pulses alone and ideal RF pulses are not needed.

The R-CSA CODEX $N\tau_r$ and $\tau_m$ dependence experiments were carried out at a spinning speed of 10 kHz using $R10_1^3$, $R10_1^4$, $R18_2^5$, $R18_2^7$, $R18_4^5$, $R14_4^3$

sequences in the $n$ mode and $N/2$ mode. A mixing time ($\tau_m$) of 100 $msec$ ($\tau_m$>>$\tau_c$) and a $z$ filter of 1 $\mu sec$ is used for $N\tau_r$ dependence experiments. The $\tau_m$ dependence experiment were carried out by varying the mixing time from 0.1 $msec$ to 128.0 $msec$. At a spinning speed of 10 kHz the sample temperature was 309 K.

The $N\tau_r$ dependence experiments were carried out to identify the plateau to be used in the $\tau_m$ dependence experiments. The $N\tau_r$ dependence curves obtained from different R-CSA CODEX experiments in the $n$ mode (green circle) along with that from the CODEX $N\tau_r$ dependence curve (black points) obtained with an RF power of 95 kHz is shown in figure 5.13. The R-CSA CODEX $N\tau_r$ dependence experiments using $R10_1^3$, $R10_1^4$, $R18_2^5$, $R18_2^7$, $R18_4^5$, $R14_4^3$ sequences in the $n$ mode have $N\tau_r$ resolutions of 0.2 $msec$, 0.2 $msec$, 0.4 $msec$, 0.4 $msec$, 0.8 $msec$, and 0.8 $msec$ respectively, while the CODEX $N\tau_r$ dependence experiments have an $N\tau_r$ resolution of 0.2 $msec$.

The $N\tau_r$ dependence curves obtained from R-CSA CODEX $N\tau_r$ dependence experiments using the sequences $R10_1^3$, $R18_2^5$ in the $n$ mode reaches a plateau at $N\tau_r$ of 2.0 $msec$ with $S/S_0$ intensity of 0.6. After the minimum, the $N\tau_r$ dephasing curve shows an upward shift (figure 5.13a, 5.13c). For the $N\tau_r$ dependence curves using $R10_1^4$ sequence in the $n$ mode (figure 5.13b), the $S/S_0$ decreases from 1 to 0.6 and then oscillate between 0.6 and 0.7. The $N\tau_r$ at which the $S/S_0$ reaches saturation is 1.4 $msec$. For the $N\tau_r$ dependence curve using $R18_2^7$ sequence in the $n$ mode (figure 5.13d), the $S/S_0$ decreases from 1 to 0.6 and then oscillate between 0.6 and 0.65. The $N\tau_r$ at which the $S/S_0$ reaches saturation is 1.6 $msec$. For the $N\tau_r$ dependence curves using $R18_4^5$ in the $n$ mode (figure 5.13e), the $S/S_0$ decreases from 1 to 0.6 and then oscillate between 0.6 and 0.63. The $N\tau_r$ at which the $S/S_0$ reaches saturation is 1.6 $msec$. For the $N\tau_r$ dependence curves using $R14_4^3$ in the $n$ mode (figure 5.13f) the $S/S_0$ decreases from 1 to 0.6 and then oscillate between 0.57 and 0.6. The $N\tau_r$ at which the $S/S_0$ reaches saturation is 1.6 $msec$. The $N\tau_r$ dephasing curves of the R-CSA CODEX experiments using $R10_1^4$, $R18_2^7$, $R18_4^5$, $R14_4^3$ does not show any upward shift in the depshasing curve. The green arrows in figure 5.13 indicate the $N\tau_r$ values selected for the $\tau_m$ dependence experiments.

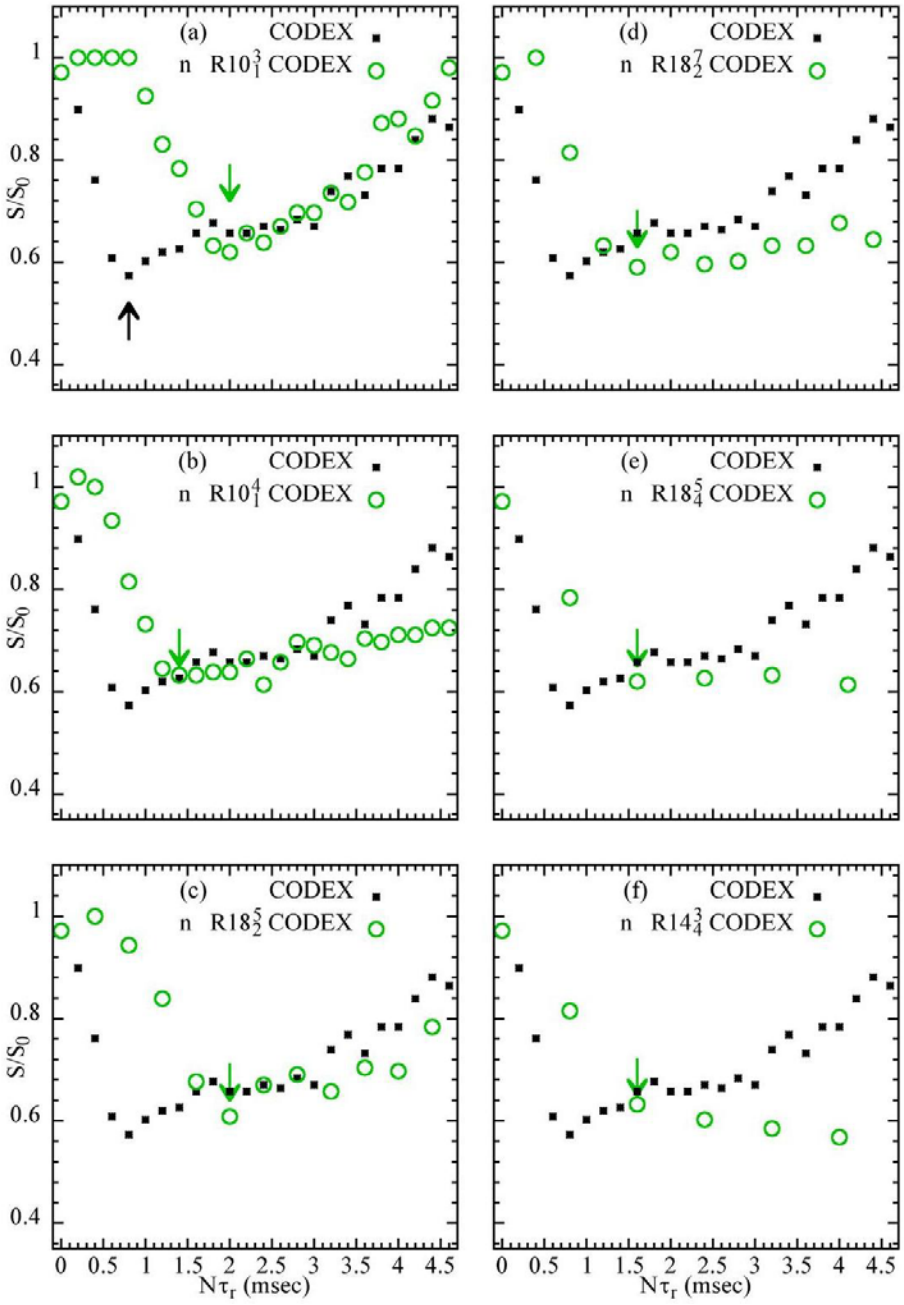


*Figure 5.13: The CODEX $N\tau_r$ dependence curves along with that from the R-CSA CODEX $N\tau_r$ dependence curves using $a).R10_1^3,\ b).R10_1^4,\ c).R18_2^5,\ d).R18_2^7,\ e).R18_4^5,$ $f).R14_4^3$ sequences in the $n$ mode (green circle) at a spinning speed of 10 kHz. For all the experiments, the R element was $180_0$, the mixing time ($\tau_m$) 100 msec and the z-filter 1 $\mu$sec used. The $N\tau_r$ dependence curves from the R-CSA CODEX using $R10_1^3,\ R18_2^5$ sequences shows an upward shift which is very similar to that of the CODEX experiment (black points). The green arrows indicate the first point of the plateau from the $N\tau_r$ dependence experiment in the $n$ mode which was selected for the $\tau_m$ dependence experiments. The black arrow indicates the $N\tau_r$ value selected for the CODEX $\tau_m$ dependence experiment.*

The plateau value obtained from the R-CSA CODEX $N\tau_r$ dependence experiments were used for the $\tau_m$ dependence experiments. The $N\tau_r$ values of 2.0 $msec$, 1.4 $msec$, 2.0 $msec$, 1.6 $msec$, 1.6 $msec$ and 1.6 $msec$ were used for R-CSA CODEX $\tau_m$ dependence experiments using $R10_1^3$, $R10_1^4$, $R18_2^5$, $R18_2^7$, $R18_4^5$, $R14_4^3$ respectively. The corresponding dephasing curves are shown in figure 5.14. For the CODEX $\tau_m$ dependence experiments $N\tau_r$ of 0.8 $msec$ was used. The correlation time is obtained by iterative fitting of dephasing curve with KWW function (equation 1.43) and the values obtained for CODEX and different R-CSA CODEX are tabulated in table 5.5. Since the dephasing intensity of the plateau value ($S/S_0$) of the R-CSA CODEX experiments were higher than that from the CODEX experiments, the fitted curves of the R-CSA CODEX experiments saturates at higher $S/S_0$. Correlation times of 1.3 $msec$, 1.2 $msec$, 1.6 $msec$, 1.2 $msec$, 1.3 $msec$, 1.3 $msec$ were obtained for R-CSA CODEX experiments using $R10_1^3$, $R10_1^4$, $R18_2^5$, $R18_2^7$, $R18_4^5$, $R14_4^3$ respectively, while a correlation time of 1.2 $msec$ was obtained from the CODEX experiments. All the correlation times obtained from the R-CSA CODEX experiments except that using $R18_2^5$ are very close to that obtained from CODEX experiment. It is also noteworthy that even if the plateau value of $S/S_0$ is different from that of the CODEX experiment, the correlation time obtained are similar. The correlation time obtained from the CODEX $\tau_m$ dependence experiments at 10 kHz is different from that obtained at 3 kHz. This decrease in correlation time is due to the increase in temperature due to mechanical heating of the sample at the high spinning speeds and Kay *et al.* have shown that the correlation time in DMS is very sensitive to the temperature [116].

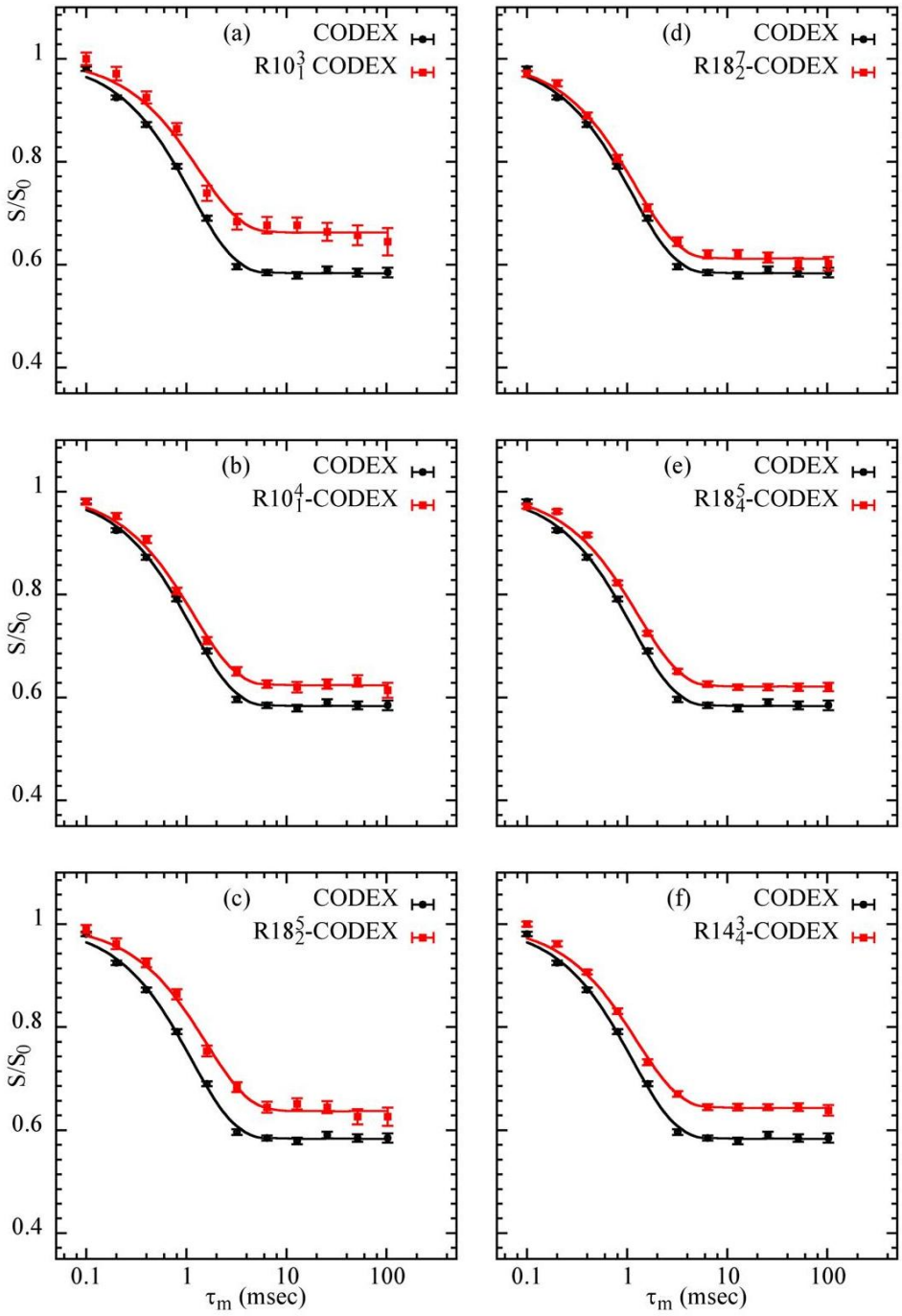


*Figure 5.14: Results of the R-CSA CODEX $\tau_m$ dependence experiments using $R10_1^3$, $R10_1^4$, $R18_2^5$, $R18_2^7$, $R18_4^5$, $R14_4^3$ sequences at a spinning speed of 10 kHz. The dephasing curves are fitted with the KWW function to extract the correlation time. The $N\tau_r$ value was taken from the plateau value of the R-CSA CODEX $N\tau_r$ dependence experiments in the n mode (green arrow of figure 5.13).*

| R sequence | $N\tau_r$ $(msec)$ | $\tau_c$ $(msec)$ |
|---|---|---|
| CODEX | 0.8 | 1.2 |
| $R10_1^3$ | 2.0 | 1.3 |
| $R10_1^4$ | 1.4 | 1.2 |
| $R18_2^5$ | 2.0 | 1.6 |
| $R18_2^7$ | 1.6 | 1.2 |
| $R18_4^5$ | 1.6 | 1.3 |
| $R14_4^3$ | 1.6 | 1.3 |

*Table 5.5: The correlation times extracted from the CODEX and the R-CSA CODEX experiments with the $N\tau_r$ value obtained from $N\tau_r$ dependence experiment in the n mode with a spinning speed of 10 kHz.*

The results of the $N\tau_r$ dependence experiment in $N/2$ mode are shown in figure 5.15. Since at the spinning speed of 10 kHz the resolution of the experiment in the $n$ mode acquisition is already good, hence only selective points are used for $N/2$ mode acquisition. At this spinning speed the R-CSA CODEX experiment using $R10_1^3$, $R10_1^4$, $R18_2^5$, $R18_2^7$, $R18_4^5$, $R14_4^3$ sequences in the $N/2$ mode have a maximum $N\tau_r$ resolution of 0.04 $msec$, 0.04 $msec$, 0.044 $msec$, 0.044 $msec$, 0.088 $msec$, 0.0114 $msec$ respectively, while CODEX experiment have an $N\tau_r$ resolution of 0.2 $msec$ $N\tau_r$ resolution.

As seen in the case of the $N\tau_r$ dephasing curves obtained in the $n$ mode, the $N\tau_r$ dephasing curves obtained in the $N/2$ mode using $R10_1^3$, $R18_2^5$ sequences show an upward shift in dephasing curve (figure 5.15a, 5.15c), while this is not seen when $R10_1^4$, $R18_2^7$, $R18_4^5$, $R14_4^3$ (figure 5.15b, 5.15d, 5.15e, 5.15f) sequences are used. The $N\tau_r$ dephsasing curves obtained using $R18_4^5$, $R14_4^3$ sequences show a large oscillation around plateau.

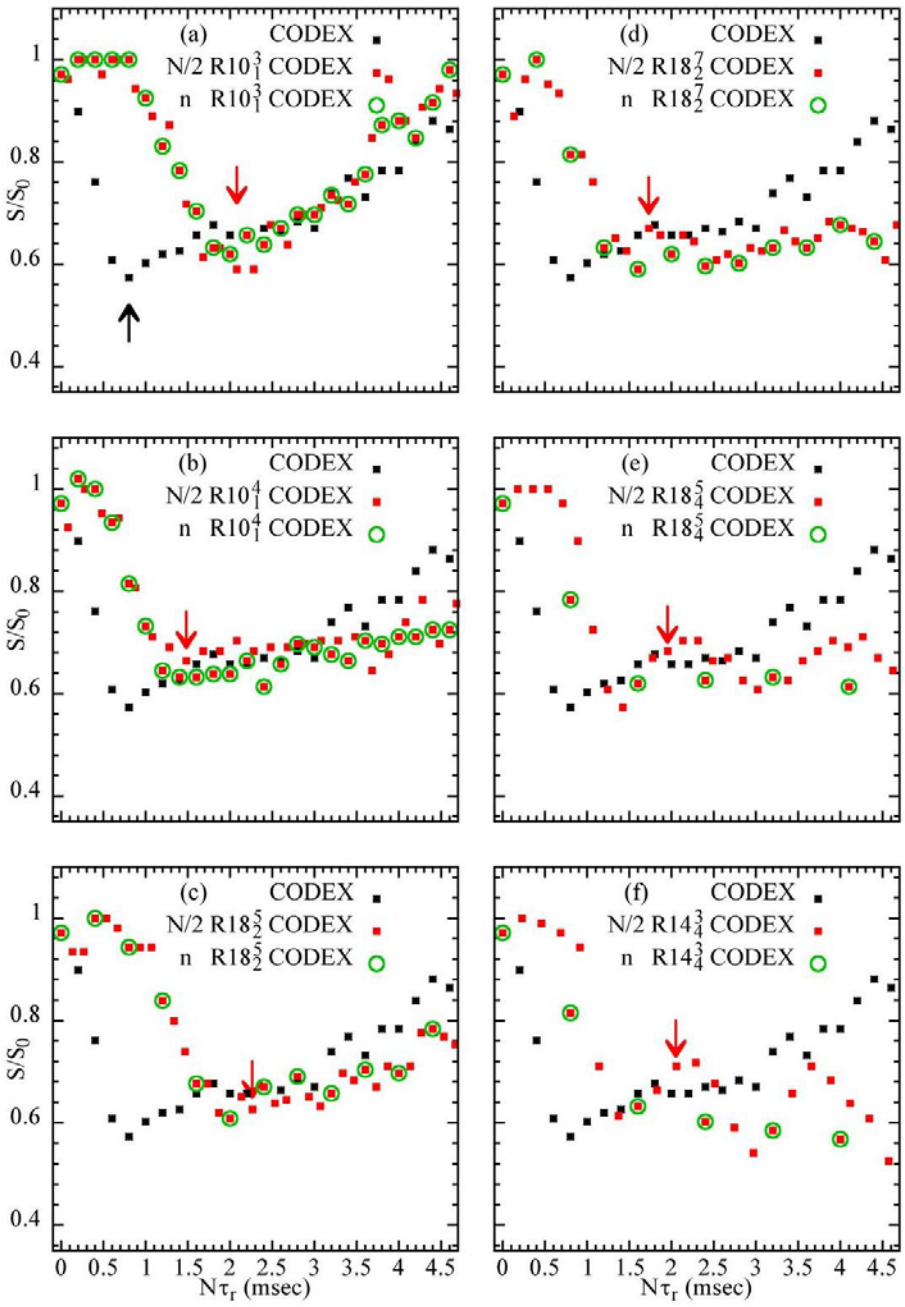


*Figure 5.15: The results of the CODEX $N\tau_r$ dependence experiments plotted along with that from the R-CSA CODEX $N\tau_r$ dependence experiment using $a).R10_1^3$, $b).R10_1^4$, $c).R18_2^5$, $d).R18_2^7$, $e).R18_4^5$, $e).R14_4^3$ sequences in the $N/2$ mode (red points) at a spinning speed of 10 kHz. For all the experiments, the R element was $180_0$, the mixing time ($\tau_m$) was 100 msec and the z filter was 1 μsec. The $N\tau_r$ dephasing curves obtained using $R10_1^3$, $R18_2^5$ sequences show an upward shift in the dephasing curve, which is very similar to that of the CODEX experiment (black points). The red arrows indicate the first point of the plateau from the $N\tau_r$ dephasing curves which was selected for the $\tau_m$ dependence experiment. The black arrow indicates the $N\tau_r$ value for the CODEX $\tau_m$ dependence experiment.*

The R-CSA CODEX $\tau_m$ dependence experiments were carried out using $N\tau_r$ values obtained from the R-CSA CODEX $N\tau_r$ dependence experiments in the $N/2$ mode. For the R-CSA CODEX $\tau_m$ dependence experiments using the $R10_1^3$, $R10_1^4$, $R18_2^5$, $R18_2^7$, $R18_4^5$, $R14_4^3$ sequences, the $N\tau_r$ values used were 2.08 $msec$, 1.48 $msec$, 2.26 $msec$, 1.73 $msec$, 1.6 $msec$ and 2.05 $msec$ respectively and the dephasing curves obtained are shown in figure 5.16. For the CODEX $\tau_m$ dependence experiment, $N\tau_r$ of 0.8 $msec$ was used. The dephasing curves were fitted with the KWW function (equation 1.44) to extract the correlation time and the values obtained from the CODEX and the R-CSA CODEX experiments are tabulated in table 5.6. The fitted curves show an upward shift in the saturation value for all the R-CSA CODEX experiment compared to CODEX experiments. Correlation times of 1.0 $msec$, 1.3 $msec$, 0.9 $msec$, 1.2 $msec$, 1.3 $msec$, 1.4 $msec$ were obtained for R-CSA CODEX experiments using $R10_1^3$, $R10_1^4$, $R18_2^5$, $R18_2^7$, $R18_4^5$, $R14_4^3$ sequences respectively, while a correlation time of 1.2 $msec$ was obtained from the CODEX experiments, which are tabulated in table 5.6. The correlation times obtained from the R-CSA CODEX except that using $R18_2^5$ and the CODEX experiments are very close (±0.2 $msec$). This indicates that the correlation time is not sensitive to the $N\tau_r$ value or the $S/S_0$ intensity at the plateau, which are different for different sequences.

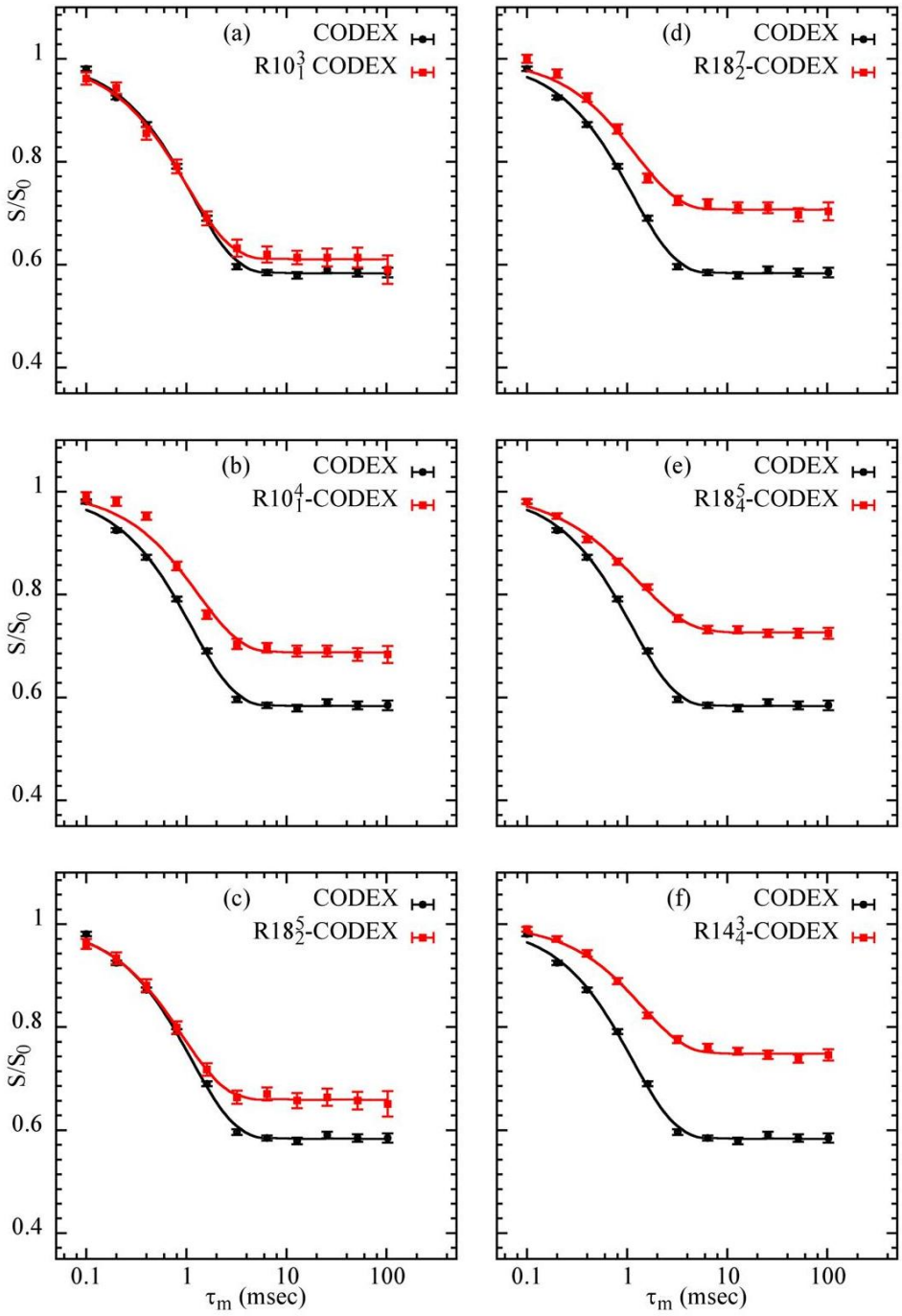


*Figure 5.16: CODEX $\tau_m$ dependence curves along with R-CSA CODEX $\tau_m$ dependence curves obtained using $R10_1^3$, $R10_1^4$, $R18_2^5$, $R18_2^7$, $R18_4^5$, $R14_4^3$ sequences at a spinning speed of 10 kHz. The dephasing curves are fitted with the KWW function to extract the correlation time of motion. The $N\tau_r$ value was taken from the plateau value of the $N\tau_r$ curve obtained in the $N/2$ mode (red arrow of figure 15).*

| R sequence | $N\tau_r\ (msec)$ | $\tau_c\ (msec)$ |
|---|---|---|
| CODEX | 0.8 | 1.2 |
| $R10_1^3$ | 2.08 | 1.0 |
| $R10_1^4$ | 1.48 | 1.3 |
| $R18_2^5$ | 2.26 | 0.9 |
| $R18_2^7$ | 1.73 | 1.2 |
| $R18_4^5$ | 1.6 | 1.3 |
| $R14_4^3$ | 2.05 | 1.4 |

*Table 5.6: The correlation time obtained from the CODEX and the R-CSA CODEX experiments with the $N\tau_r$ value used at 10 kHz spinning speed.*

## 5.8. Conclusion

The CODEX experiment is a well established technique to investigate slow motions of the order of $msec$ to $sec$. CODEX uses two rotor synchronized 180° pulse trains for recoupling chemical shift anisotropy. In R-CSA CODEX experiments the symmetry based CSA recoupling sequences $R10_1^3$, $R10_1^4$, $R18_2^5$, $R18_2^7$, $R18_4^5$ and $R14_4^3$ was used in place of the 180° pulse trains and experiments were carried out at spinning rates of 3 kHz and 10 kHz on a standards sample DMS.

Before using these sequences in the R-CSA CODEX experiments, all the R sequences were tested for its robustness with respect to RF offset and RF power mismatch for three R elements $180_0$, $90_{45}90_{-45}90_{45}$ and $90_0270_{180}$ using SIMPSON simulations and the scaling factor was calculated using SPINDYNAMICA. 2D CSA recoupling experiments were carried out to check the efficiency of the CSA recoupling. The R element $180_0$ which gave better stability to RF power mismatch, offset stability and need less number of pulses for the implementation was used for all further experiments.

Two modes of acquisition are possible in an experiment using symmetry sequences, the $n$ mode and $N/2$ mode. In $n$ mode acquisition, the signal is acquired after full cycle while in the $N/2$ mode the signal is acquired after every $R_{\pi\nu/N}R_{-\pi\nu/N}$ element and therefore the resolution in the $N/2$ mode increases. Simulations of $n$ mode and $N/2$ mode sequence for the 2D CSA recoupling experiment showed that the $N/2$ mode is as good as the $n$ mode acquisition.

Symmetry sequences that recouple CSA can be divided into two categories based on the spatial CSA component which is recoupled. The sequences $R10_1^3$, $R18_2^5$ recouple $\sigma_2$ component of the CSA tensor while $R10_1^4$, $R18_2^7$, $R18_4^5$, $R14_4^3$ recouple $\sigma_1$ component. The results from the 2D experiment shows that the recoupling efficiency of $R10_1^4$, $R18_2^7$ ($\sigma_1$) at 3 kHz are low compared to $R10_1^3$, $R18_2^5$ ($\sigma_2$) sequences. At 10 kHz the recoupling efficiency of all 6 sequences $R10_1^3$, $R10_1^4$, $R18_2^5$, $R18_2^7$, $R18_4^5$, $R14_4^3$ are good. Fitting of the experimental spectra were carried out using SIMPSON OPT package to obtain CSA parameters of the carbonyl environment of alanine. The CSA values obtained from 2D CSA recoupling experiments using selected R sequences are reasonably close to expected values indicating that they are effective for recoupling the CSA and hence used as an alternative for the 180$^o$ pulse trains in the CODEX experiment.

R-CSA CODEX $N\tau_r$ and $\tau_m$ dependence experiments were carried out on the standard sample DMS, at spinning speeds of 3 kHz and 10 kHz and compared with the CODEX experiments. The aim of $N\tau_r$ dependence experiment in this study was to measure the plateau value of $N\tau_r$ for using in the $\tau_m$ dependence experiment, and is not used for motional geometry information. The $N\tau_r$ dephsing curve of $R10_1^4$, $R18_2^7$ in the $n$ mode acquisition is very similar to that of CODEX dephasing curve at 3 kHz, while that of $R10_1^3$, $R18_2^5$ deviate from CODEX dephasing path. Similarly, the $\tau_m$ dependence experiment of $R10_1^4$, $R18_2^7$ show similar dephsing curve as that of CODEX experiment while that of $R10_1^3$, $R18_2^5$ show a deviation. The correlation time is extracted using KWW function and a correlation value of ~3.1 $msec$ is obtained for different symmetry R-CSA CODEX ($\sigma_1$ and $\sigma_2$) and CODEX experiment. The correlation time obtained from the $\tau_m$ dependence experiments using $N/2$ mode acquisition is also similar to both $n$ mode symmetry sequence and CODEX experiment. This indicates the $N/2$ mode acquisition is also a possible option for obtaining the dynamics. Thus the results from the R-CSA CODEX experiments at 3 kHz clearly shows that this approach is as effective as the CODEX experiment in the standard DMS sample, in particular when the $\sigma_1$ sequences are used.

The results from the CODEX $N\tau_r$ dependence experiments at a spinning speed of 10 KHz are not similar to that at 3 kHz. After reaching the minimum value, $N\tau_r$ curve shows an upward shift with increase in $N\tau_r$, indicating that at high

spinning speeds the CODEX may not be effective for the $N\tau_r$ dependence experiments. This is because at this spinning speed, the non ideal nature of the 180$^o$ pulses severely affects the performance of the CODEX $N\tau_r$ dependence experiments. The advantage of symmetry R-CSA CODEX experiments is that, the recoupling efficiency is determined by composite pulses alone and not by ideal pulses. The R-CSA CODEX $N\tau_r$ dependence experiments using $R10_1^3$, $R18_2^5$ sequences in the $n$ mode show a similar upward shift as in the case of the CODEX $N\tau_r$ dependence experiments. The R-CSA CODEX $N\tau_r$ dependence experiments using $R10_1^4$, $R18_2^7$, $R18_4^5$, $R14_4^3$ sequences shows $N\tau_r$ dephasing curves similar to that of the CODEX $N\tau_r$ dependence experiments at 3 kHz. The correlation times obtained from the majority of the R-CSA CODEX $\tau_m$ dependence experiments using the $N\tau_r$ from the $N\tau_r$ dependence experiments using $n$ mode as well as the $N/2$ mode at 10 kHz are very close to that obtained from the CODEX $\tau_m$ dependence experiment.

Therefore it can be concluded that the R-CSA CODEX experiments, in particular the ones using $\sigma_1$ sequences, are effective alternatives to the CODEX experiment with the advantage that it can be implemented at high spinning speeds using reasonable RF powers.

# Appendix

## Simulation of CSA Recoupling using R sequences

In this appendix, the results of the simulations carried out on the R sequences to test their robustness to RF-offset and RF-power mismatch are discussed. The RF-offset of each sequence was varied from -8 kHz to +8 kHz at an interval of 2 kHz, and the RF power of the $^{13}C$ channel was varied from 0.85 to 1.15 relative to the ideal RF power that should be used in the sequence, with an increment of 0.03.

### Simulation Parameters

All the simulations were carried out using the SIMPSON program [24]. Since the R sequences are gamma encoded, a crystal file of with 1 gamma angle with REPULSION 2000 is used for the $\sigma_2$ CSA recoupling and ZCW4180 for the $\sigma_1$ CSA recoupling sequence. 512 points were sufficient for obtaining a good FID in the indirect dimension for the simulations with a spinning speed of 3 kHz and 1024 points for the spinning speed of 10 kHz.

The simulations were performed on the carbonyl environment of Alanine and the methyl environment of DMS. Chemical shift anisotropy of -71 ppm and asymmetry parameter of 0.83 were the parameters used for the simulations of the carbonyl environment in Alanine. A hetero-nuclear dipolar coupling of 6.0 kHz is used between the $^{13}C$ of carbonyl group and the surrounding $^{1}H$ bath. For the $CH_3$ environment of DMS, chemical shift anisotropy of 36 ppm with an asymmetry parameter 0.0 is used. $^{13}C$-$^{1}H$ hetero nuclear dipolar coupling and $^{1}H$-$^{1}H$ homo nuclear dipolar coupling of 8.0 KHz were also used in the simulations. For example, the pulse program used for simulating the CSA recoupling using $R10_1^3$ sequence with R element $180_o$ given below

```
############################################################################
spinsys {
 channels 13C 1H
 nuclei    13C 1H
 shift      1 178p -71p 0.83   0   0    0
 shift      2   2p   3p    0 100 -50 -150
 dipole     1 2 -8000 0 0 0
}
```

```
par {
  variable N                10
  variable n                1
  variable nu               3
  variable off_x            0000
  variable rf_inho          1.00
  spin_rate                 10000
  proton_frequency          300e6
  method                    direct
  gamma_angles              1
  sw                        1.0*spin_rate/n
  rotor_angle               54.74
  np                        128
  crystal_file              rep2000
  start_operator            I1z+I2x
  detect_operator           I1z
  verbose                   111
}

proc pulseq {} {
 global par
 maxdt 1
 set phi1      [expr 1.0*180*$par(nu)/$par(N)]
 set rf        [expr 1.0*$par(spin_rate)*$par(N)/$par(n)/2]
 set rf1H      86000.0
 set tR        [expr 1e6/$rf]
 set pul180 [expr 0.5*$tR]
 set rf        [expr $rf*$par(rf_inho)]
 puts "rf: $rf rf1H: $rf1H"

 reset
  for {set i 1} {$i <= [expr $par(N)/2]} {incr i} {
    # R element
    offset [expr 13350.0+$par(off_x)] 600.0
    pulse $pul180  $rf [expr  $phi1] $rf1H 0
    # R' element
    pulse $pul180  $rf [expr -$phi1] $rf1H 0
   }
 store 1
 reset
 acq $par(np) 1
}

proc main {} {
  global par spinsys
  set f [fsimpson]
  ########################################
  set N [expr round($par(N))]
```

```
 set n [expr round($par(n))]
 set nu [expr round($par(nu))]
 set name1  [format R.$N.$n.{$nu}.CSA.tppm.nseq.pul180_%d_%1.2f_%d \
   $par(off_x) $par(rf_inho) $par(spin_rate)]
 ########################################
 fsave $f $name1.fid
 fzerofill $f 2048
 faddlb $f 50 0
 fft $f
 fsave $f $name1.spe
 fsave $f $name1.txt -xreim
 funload $f
}

#####################################################################
```

The simulations on the $R10_1^3$, $R10_1^4$, $R18_2^5$, $R18_2^7$ sequences at a spinning speed of 3 kHz are discussed first and then the simulation on the $R10_1^3$, $R10_1^4$, $R18_2^5$, $R18_2^7$, $R18_4^5$, $R14_4^3$ sequences at a spinning speed of 10 kHz.

**Simulations of the $R10_1^3$ Sequence at 3 kHz**

The $R10_1^3$ sequence contains ten $R$ elements in one rotor period and the symmetry number $\nu = 3$ determine the phase at which the pulses are applied. This sequence recouples the 2nd order component of the CSA tensor, ie. ($\sigma_2$). When the R element is $180_0$, this sequence has five [$180_{54}180_{306}$] pulse pairs in one rotor period. For the spinning speed of 3 kHz, the RF power is 15 kHz. The simulated spectra show that the sequence is stable with respect to the RF offset from -2 kHz to +2 kHz for both carbonyl environment of alanine and methyl environment of DMS (figure A1a, A2a). Beyond these offset values, there is a significant change in the recoupled CSA pattern. This sequence is stable to RF power mismatch from 0.97 to 1.03 for the carbonyl environment of alanine (figure A3a) and from 0.97 to 1.03 for the methyl environment of DMS (figure A4a). However, the recoupled CSA pattern of both the carbonyl and methyl environments preserve a good line shape for the entire range of RF power mismatch with a continuous decrease in width in the range 0.85 to 1.15. The scaling factor of the sequence is 0.17.

When the R element is $90_{45}90_{-45}90_{45,}$ this sequence contain 5 repeating units of [$90_{99}90_{9}90_{99}90_{261}90_{351}90_{261}$] pulses in one rotor period. For the spinning speed of 3 kHz, the RF power is 22.5 kHz. The simulated spectra show that this sequence is

stable with respect to the RF offset from -2 kHz to +2 kHz (figure A1b, A2b) and stable to RF power mismatch from 0.97 to 1.03 (figure A3b, A4b) for both the carbonyl environment of alanine and the methyl environment of DMS. Beyond these values the recoupled CSA pattern looks distorted. The scaling factor of this sequence is 0.20.

When the R element is $90_0270_{180,}$ this sequence contains 5 repeating units of $[90_{54}270_{234}90_{306}270_{126}]$ pulses in one rotor period. For the spinning speed of 3 kHz, the RF power is 30 kHz. This sequence is stable for a wider range of RF offsets from -6 kHz to +6 kHz for the carbonyl environment of alanine (figure A1c), from -4 kHz to +4 kHz for the methyl environment of DMS (figure A2c) and stable to RF power mismatch from 0.91 to 1.06 for the carbonyl environment of alanine (figure A3c), 0.97 to 1.03 for the methyl environment of DMS (figure A4c). However, the scaling factor of the sequence is very low as 0.06.

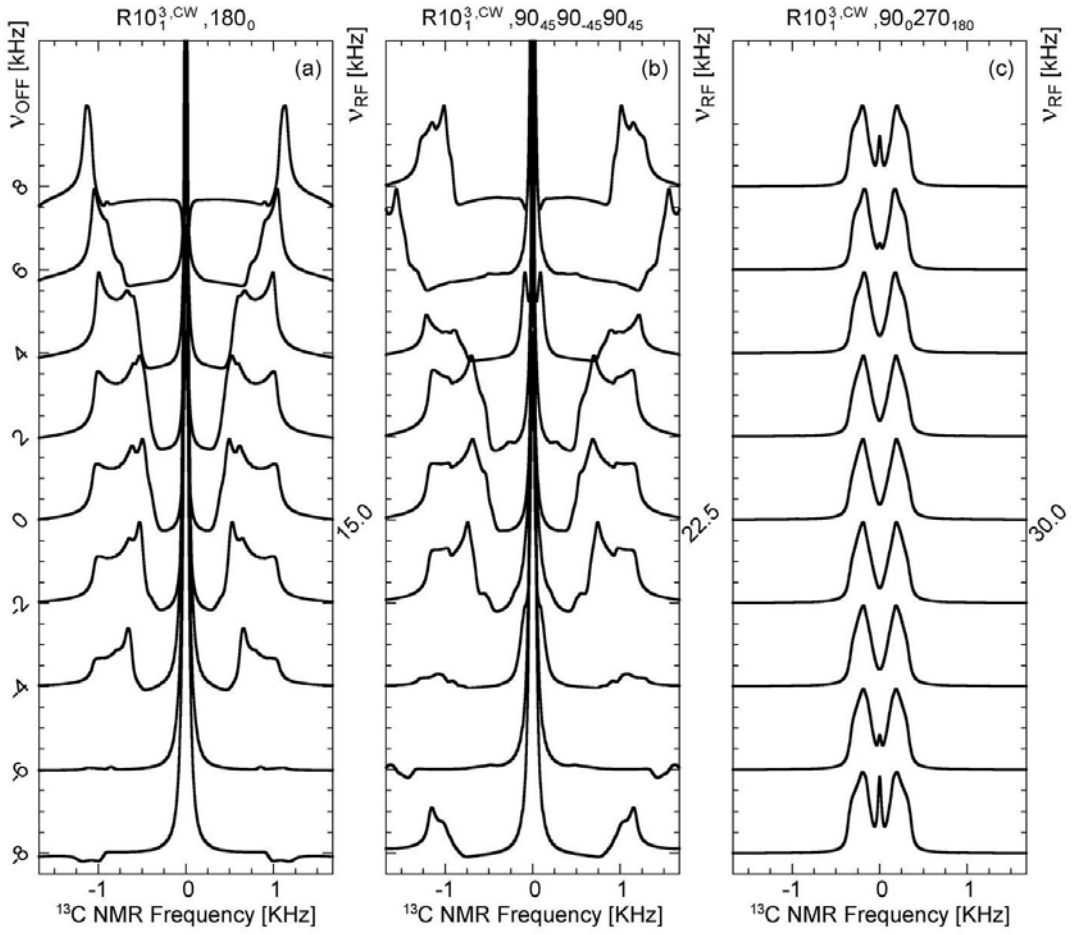


*Figure A1: SIMPSON simulations of the* $R10_1^3$ *sequence to test its robustness to RF -offset using different R elements a).*$[180_{54}180_{306}]$*, b).*$[90_{99}90_990_{99}90_{261}90_{351}90_{261}]$ *and*

*c).[$90_{54}270_{234}90_{306}270_{126}$] at a spinning speed of 3 kHz. Simulations are performed on the carbonyl environment of alanine.*

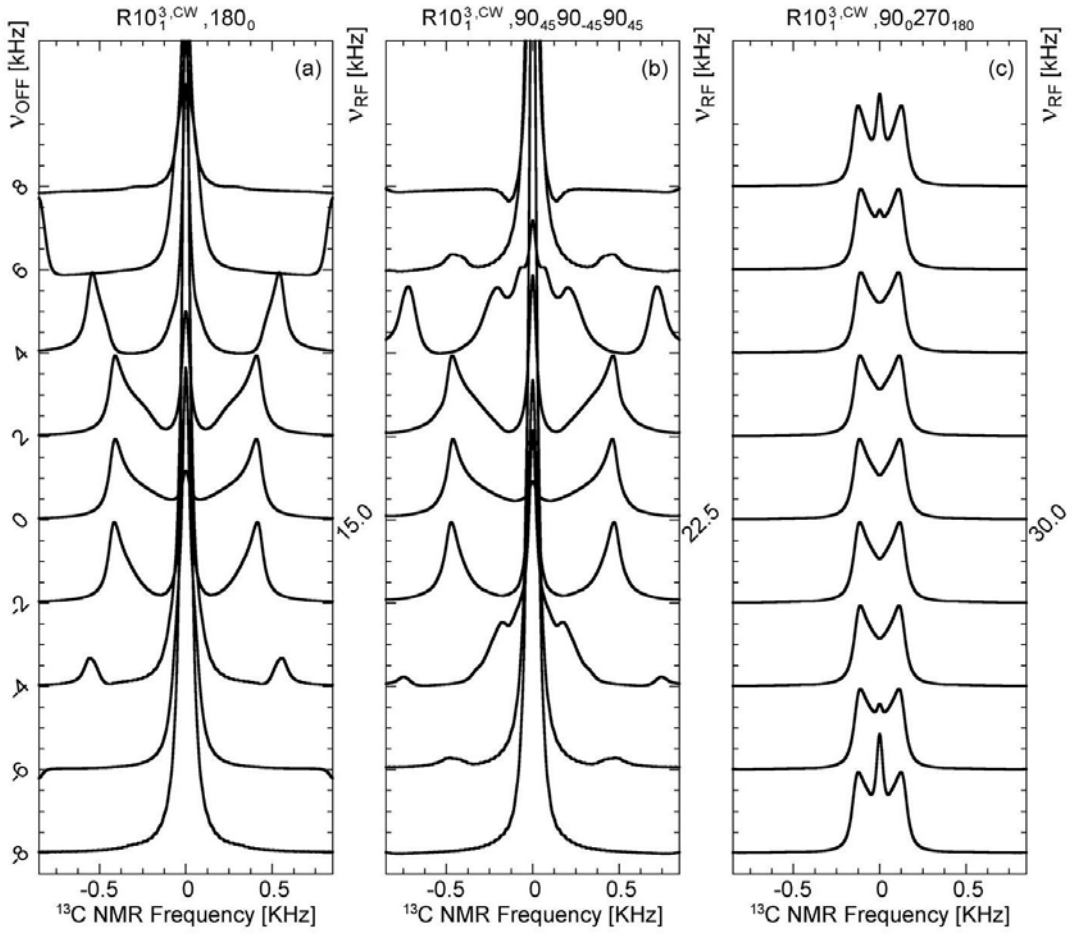


*Figure A2: SIMPSON simulations of the $R10_1^3$ sequence to test its robustness to RF-offset using different R elements a).[$180_{54}180_{306}$], b).[$90_{99}90_{9}90_{99}90_{261}90_{351}90_{261}$] and c).[$90_{54}270_{234}90_{306}270_{126}$] at a spinning rate of 3 kHz. Simulations are performed on the methyl environment of DMS.*

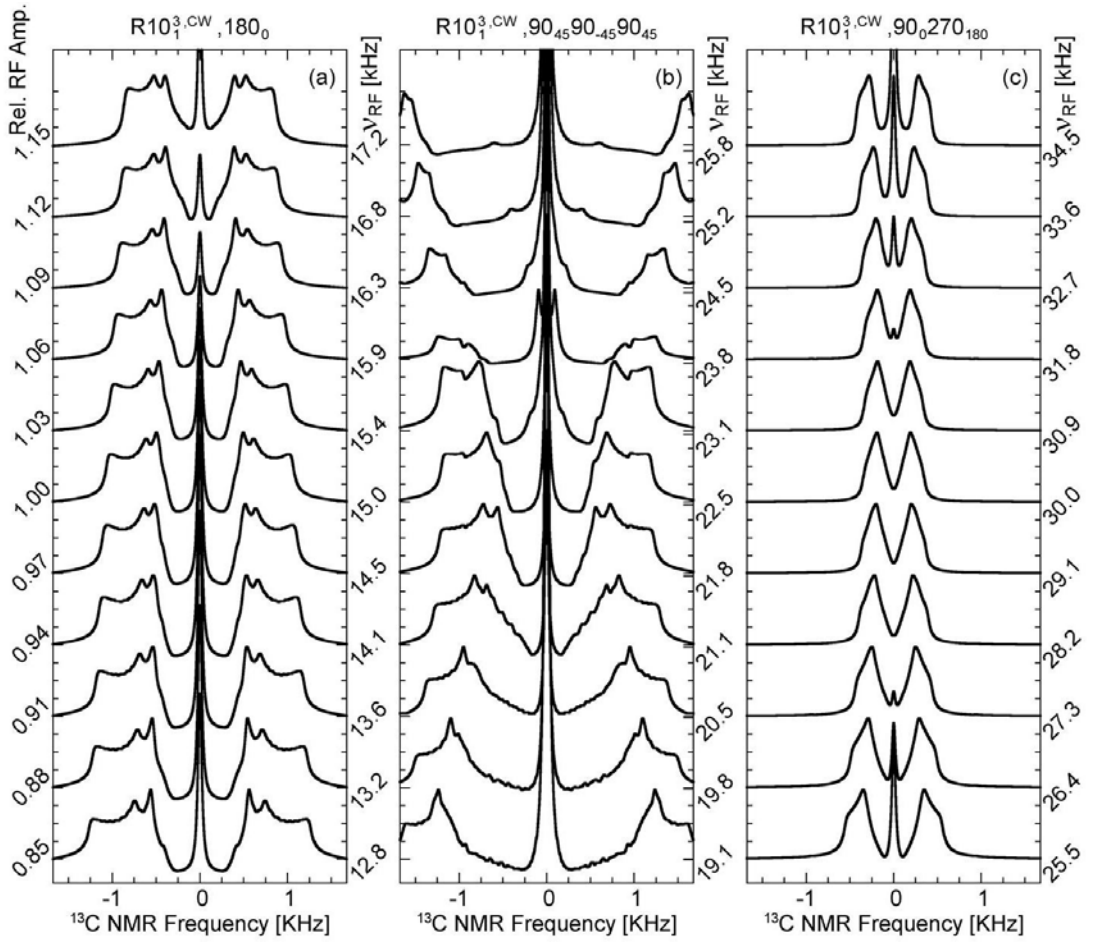


*Figure A3: SIMPSON simulations of the* $R10_1^3$ *sequence to test its robustness to RF- power mismatch using different R elements a).*$[180_{54}180_{306}]$*, b).*$[90_{99}90_{9}90_{99}90_{261}90_{351}90_{261}]$ *and c).*$[90_{54}270_{234}90_{306}270_{126}]$ *at a spinning speed of 3 kHz. Simulations are performed on the carbonyl environment of alanine.*

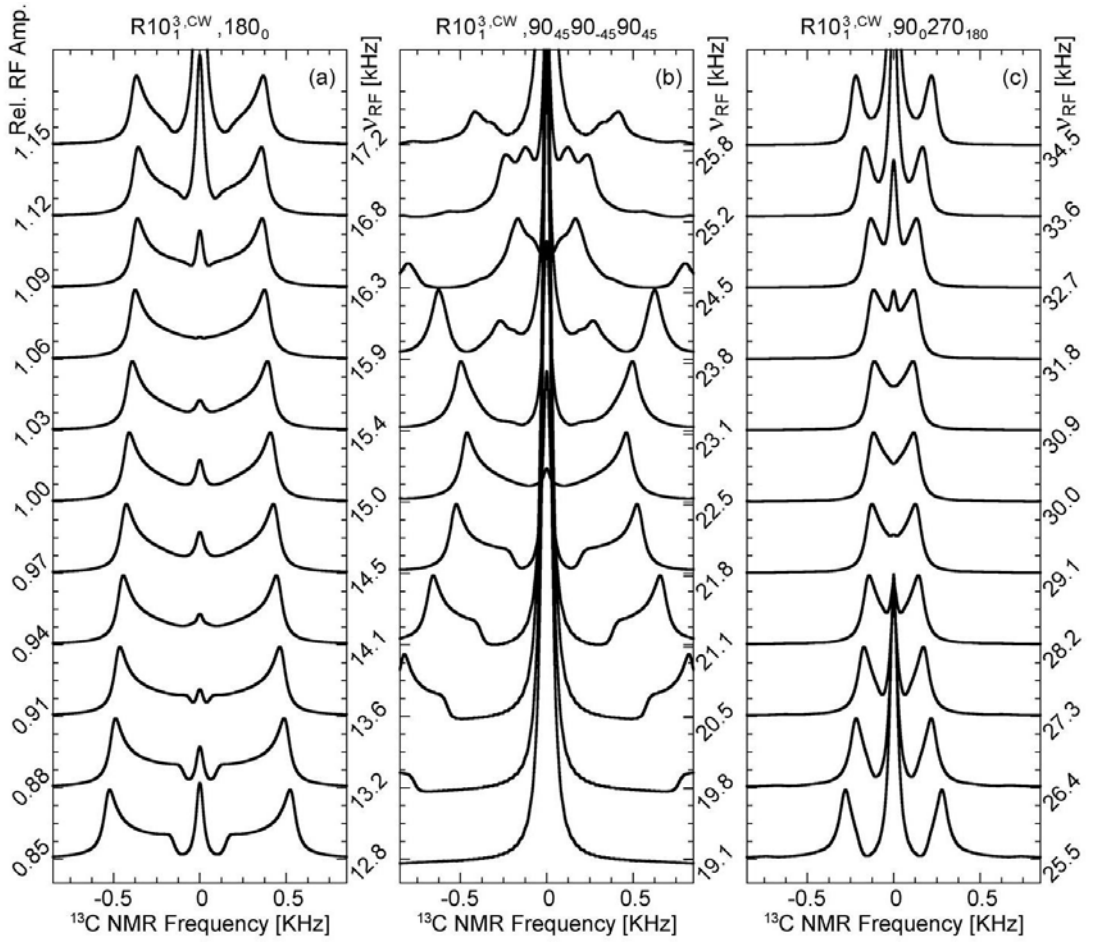


*Figure A4: SIMPSON simulations of the* $R10_1^3$ *sequence to test its robustness to RF- power mismatch using different R elements a).[*$180_{54}180_{306}$*], b).[*$90_{99}90_{9}90_{99}90_{261}90_{351}90_{261}$*] and c).[*$90_{54}270_{234}90_{306}270_{126}$*] at a spinning rate of 3 kHz. Simulations are performed on the methyl environment of DMS.*

### $\mathbf{R10_1^4}$ Sequence @ 3 kHz

The $R10_1^4$ sequence contains ten R elements in one rotor period and the symmetry number $\nu = 4$ determine the phase at which the pulses are applied. This sequence recouples the 1st order component $(\sigma_1)$ of the CSA tensor. When the R element is $180_0$, this sequence has five $[180_{72}180_{288}]$ pulse pairs in one rotor period. For a spinning speed of 3 kHz the RF power is 15 kHz. The simulated spectra show the sequence is stable with respect to the RF offset from -2 kHz to +2 kHz for both the carbonyl environment of alanine and the methyl environment of DMS (figure A5a, A6a). Beyond these offset values, there are significant changes in the recoupled CSA pattern. This sequence is stable to RF power mismatch for the range from 0.97 to 1.03 for the carbonyl environment of alanine (figure A7a) and from 0.97 to 1.03 for the

methyl environment of DMS (figure A8a). But recoupled CSA pattern of both carbonyl and methyl environments preserve a good line shape for the entire range of RF power mismatch with a continuous decrease in width from 0.85 to 1.15. The scaling factor of the sequence was calculated to be 0.26.

When the R element is $90_{45}90_{-45}90_{45,}$ this sequence contains 5 repeating units of $[90_{117}90_{27}90_{117}90_{243}90_{333}90_{243}]$ pulses in one rotor period. For spinning speeds of 3 kHz the RF power is 22.5 kHz. The simulated spectra show the sequence is stable with respect to the RF offset from -2 kHz to +2 kHz (figure A5b, A6b) and stable to RF power mismatch from 0.97 to 1.03 (figure A7b, A8b) for both the carbonyl environment of alanine and the methyl environment of DMS. Beyond these values the recoupled CSA pattern looks distorted. The scaling factor of this sequence is 0.27.

When the R element is $90_{0}270_{180,}$ this sequence contains 5 repeating units of $[90_{72}270_{252}90_{288}270_{108}]$ pulses in one rotor period. For a spinning speed of 3 kHz, the RF power is 30 kHz. This sequence is stable for a wide range of RF offsets from -6 kHz to +6 kHz for the carbonyl environment of alanine (figure A5c), from -6 kHz to +4 kHz for the methyl environment of DMS (figure A6c) and stable to RF power mismatch from 0.94 to 1.09 for the carbonyl environment of alanine (figure A7c), 0.94 to 1.06 for the methyl environment of DMS (figure A8c). However, the scaling factor of the sequence is very low as 0.04.

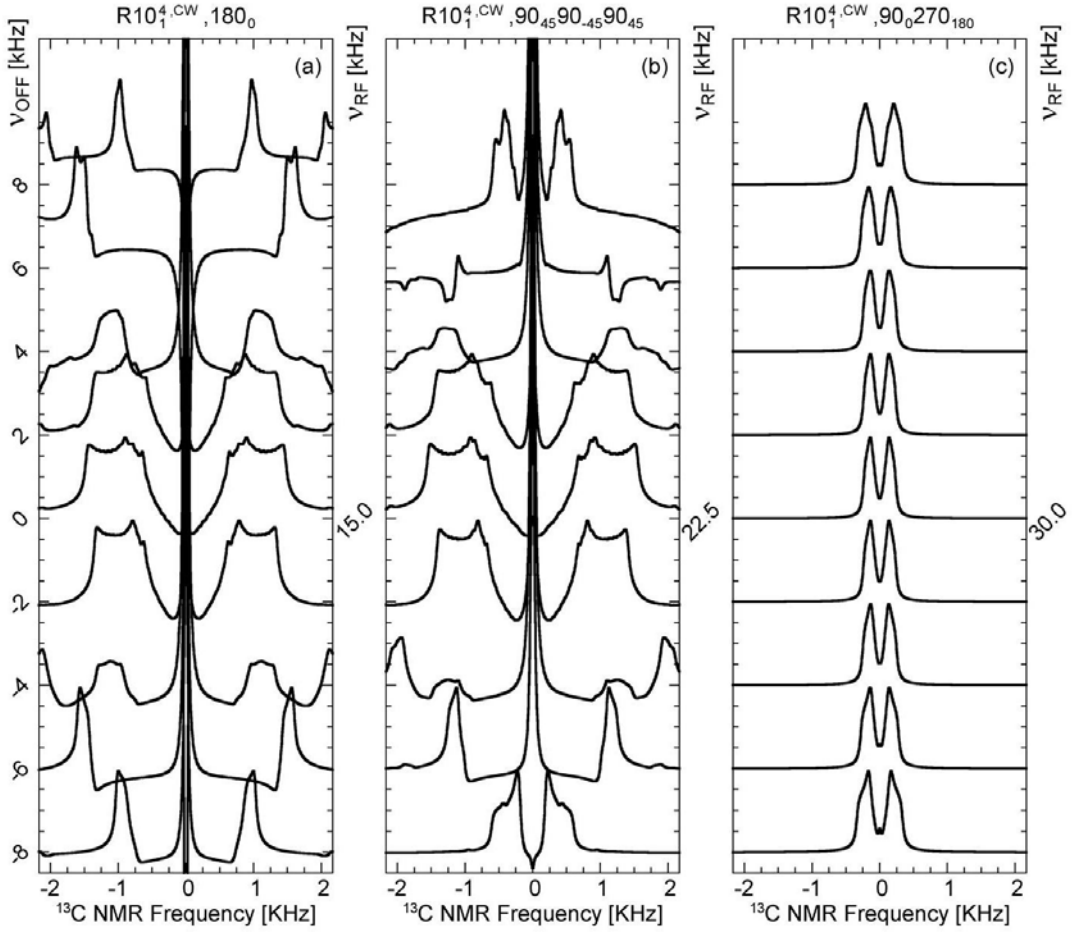


*Figure A5: SIMPSON simulations of the* $R10_1^4$ *sequence to test its robustness to RF-offset using different R elements a).*$[180_{72}180_{288}]$*, b).*$[90_{117}90_{27}90_{117}90_{243}90_{333}90_{243}]$ *and c).*$[90_{72}270_{252}90_{288}270_{108}]$ *at a spinning speed of 3 kHz. Simulations are performed on the carbonyl environment of alanine.*

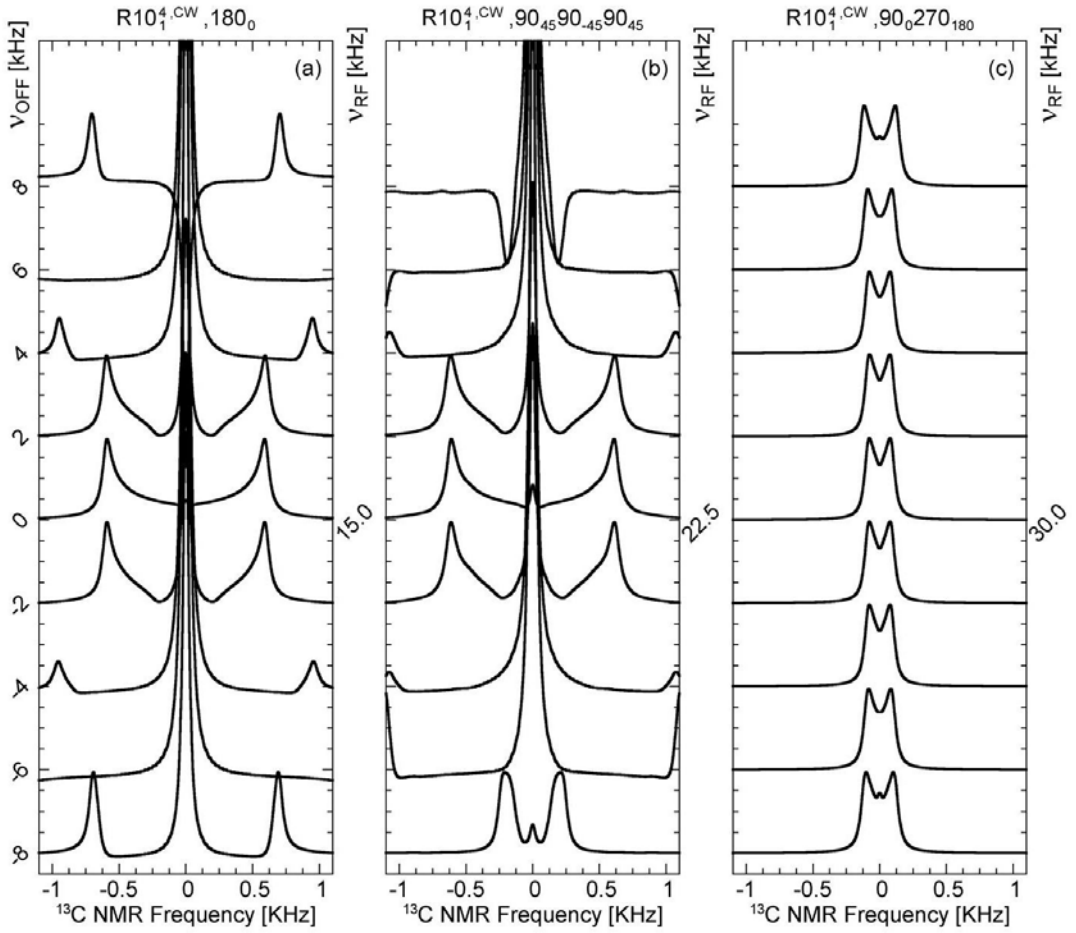


*Figure A6: SIMPSON simulations of the* $R10_1^4$ *sequence to test its robustness to RF-offset using different R elements a).*$[180_{72}180_{288}]$*, b).*$[90_{117}90_{27}90_{117}90_{243}90_{333}90_{243}]$ *and c).*$[90_{72}270_{252}90_{288}270_{108}]$ *at a spinning speed of 3 kHz. Simulations are performed on the methyl environment of DMS.*

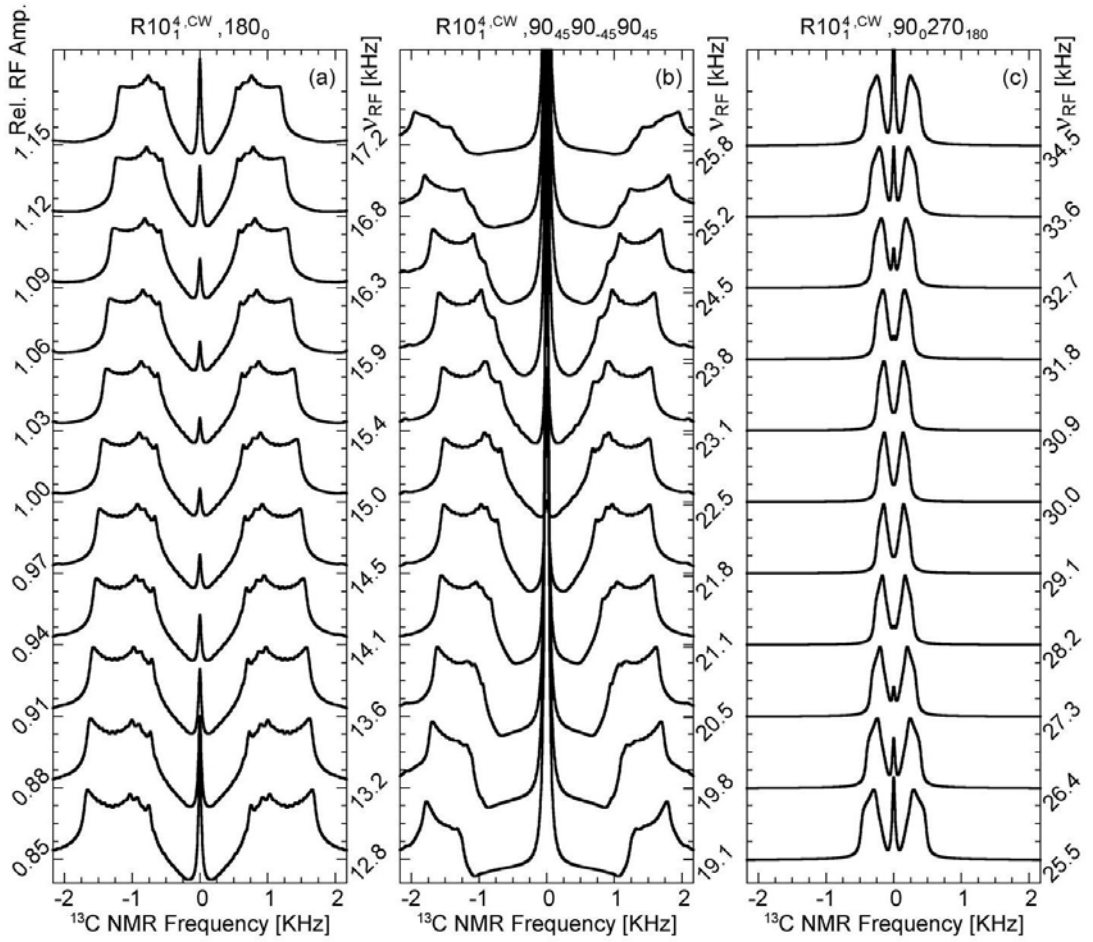


*Figure A7: SIMPSON simulations of the* $R10_1^4$ *sequence to test its robustness to RF- power mismatch using different R elements a).[*$180_{72}180_{288}$*], b).[*$90_{117}90_{27}90_{117}90_{243}90_{333}90_{243}$*] and c).[*$90_{72}270_{252}90_{288}270_{108}$*] at a spinning speed of 3 kHz. Simulations are performed on the carbonyl environment of alanine.*

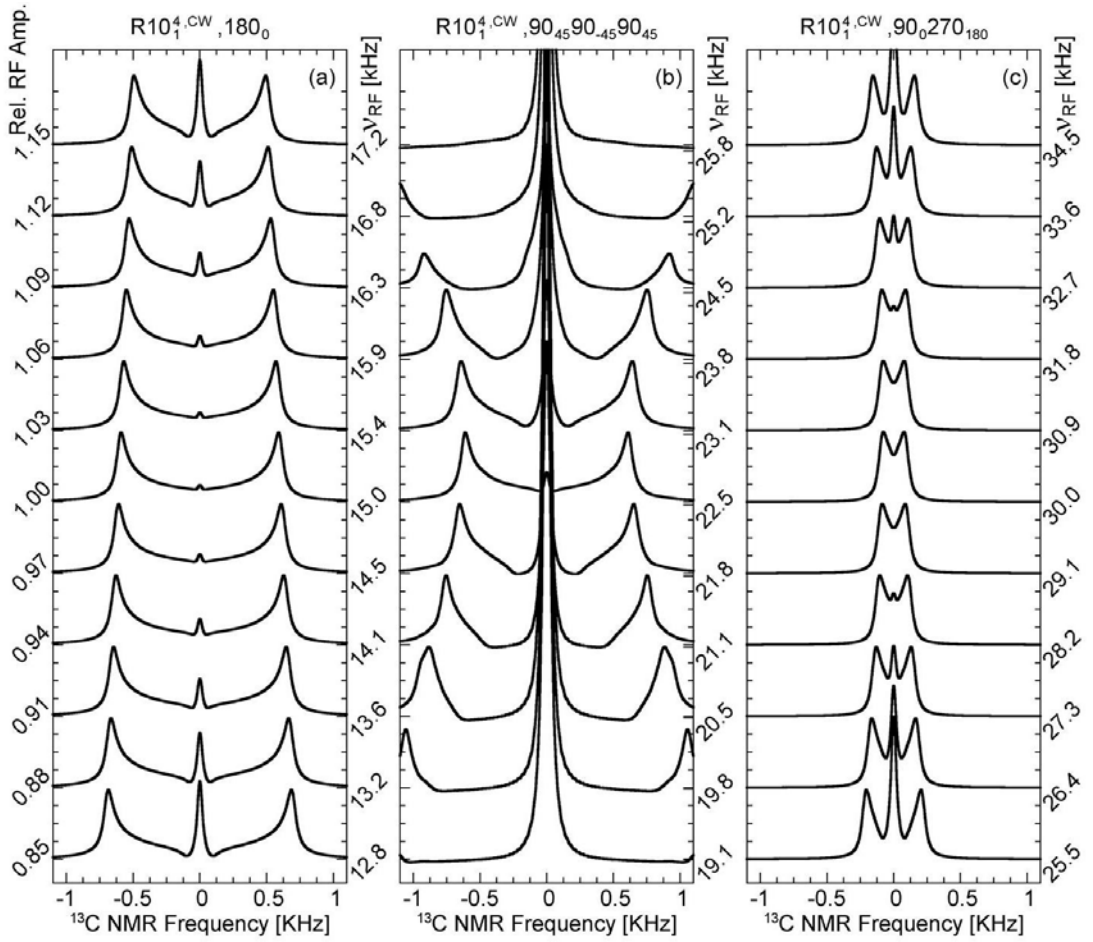


*Figure A8: SIMPSON simulations of the $R10_1^4$ sequence to test its robustness to RF- power mismatch using different R elements a) [$180_{72}180_{288}$], b) [$90_{117}90_{27}90_{117}90_{243}90_{333}90_{243}$] and c) [$90_{72}270_{252}90_{288}270_{108}$] at a spinning rate of 3 kHz. Simulations are performed for methyl environment of DMS.*

### $R18_2^5$ Sequence @ 3 kHz

The $R18_2^5$ sequence contains eighteen R elements in two rotor period and the symmetry number $\nu = 5$ determine the phase at which the pulses are applied. This sequence recouples the 2nd order component ($\sigma_2$) of the spatial CSA tensor. When the R element is $180_0$, this sequence has nine [$180_{50}180_{310}$] pulse pairs in two rotor periods. For spinning speeds of 3 kHz, the RF power is 13.5 kHz. The simulated spectra show the sequence is stable with respect to the RF offset from 0 kHz to +2 kHz (figure A9a, A10a) in the carbonyl environment of alanine and from -2 to +2 kHz (figure A10a) for the methyl environment of DMS. Beyond these offset, there are significant changes in the recoupled CSA pattern. This sequence is stable to RF power mismatch from 0.97 to 1.03 for the carbonyl environment of alanine (figure A11a),

and from 0.97 to 1.03 for the methyl environment of DMS (figure A12a). However, the recoupled CSA patterns of the carbonyl and the methyl environments preserve a good line shape for the entire range of RF power mismatch with a continuous decrease in width from 0.85 to 1.15. The scaling factor of the sequence was calculated to be 0.18.

When the R element is $90_{45}90_{-45}90_{45,}$ this sequence contain nine repeating units of $[90_{95}90_{5}90_{95}90_{265}90_{355}90_{265}]$ pulses in two rotor period. For a spinning speed of 3 kHz, the rf power is 20.25 kHz. The simulated spectra show the sequence is stable with respect to the rf offset from 0 kHz to +2 kHz (figure A9b, A10b) and is highly unstable to rf power mismatch at 3 kHz (figure A11b, A12b) for the carbonyl environment of alanine and the methyl environment of DMS. The scaling factor of this sequence is 0.20.

When the R element is $90_{0}270_{180,}$ this sequence contains nine repeating units of $[90_{50}270_{230}90_{310}270_{130}]$ pulses in two rotor periods. For a spinning speed of 3 kHz, the RF power is 27 kHz. This sequence is stable for a wide range of RF offsets from -6 kHz to +6 kHz for the carbonyl environment of alanine (figure A9c), from -6 kHz to +6 kHz for the methyl environment of DMS (figure A10c) and stable to RF power mismatch from 0.91 to 1.06 for the carbonyl environment of alanine (figure A11c), 0.91 to 1.06 for the methyl environment of DMS (figure A12c). However, the scaling factor of the sequence is very low as 0.06.

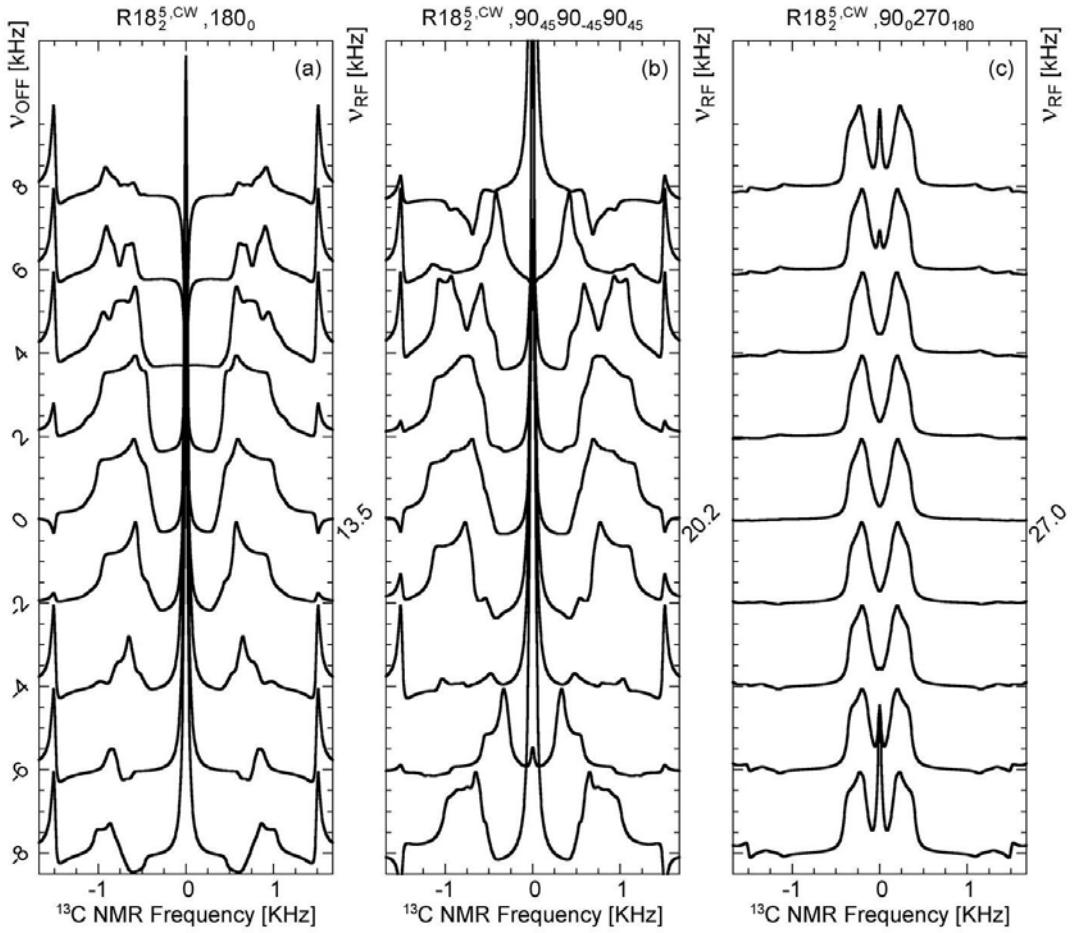


*Figure A9: SIMPSON simulations of the $R18_2^5$ sequence to test its robustness to RF offset using different R elements a).[$180_{50}180_{310}$], b).[$90_{95}90_590_{95}90_{265}90_{355}90_{265}$] and c).[$90_{50}270_{230}90_{310}270_{130}$] at a spinning speed of 3 kHz. Simulations are performed for the carbonyl environment of alanine.*

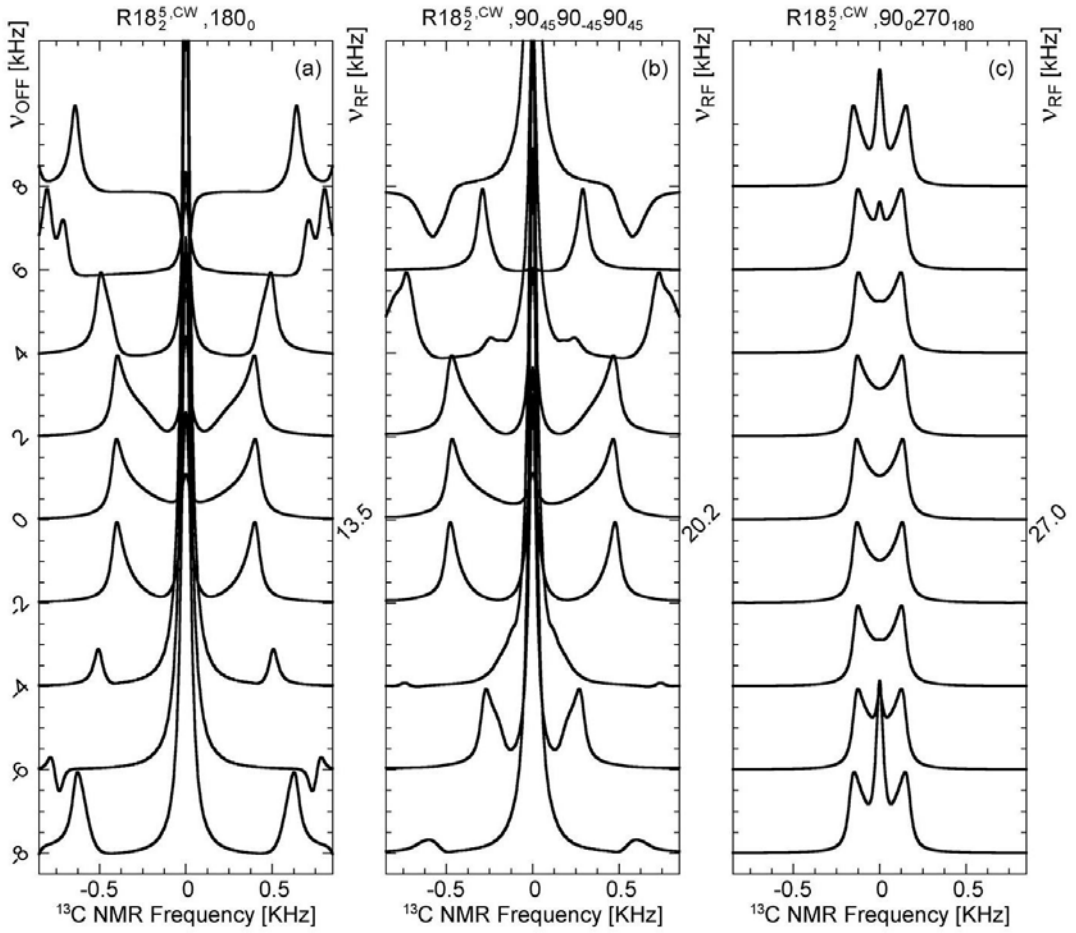


*Figure A10: SIMPSON simulations of the* $R18_2^5$ *sequence to test its robustness to RF-offset using different R elements a).*$[180_{50}180_{310}]$*, b).*$[90_{95}90_590_{95}90_{265}90_{355}90_{265}]$ *and c).*$[90_{50}270_{230}90_{310}270_{130}]$ *at a spinning rate of 3 kHz. Simulations are performed for the methyl environment of DMS.*

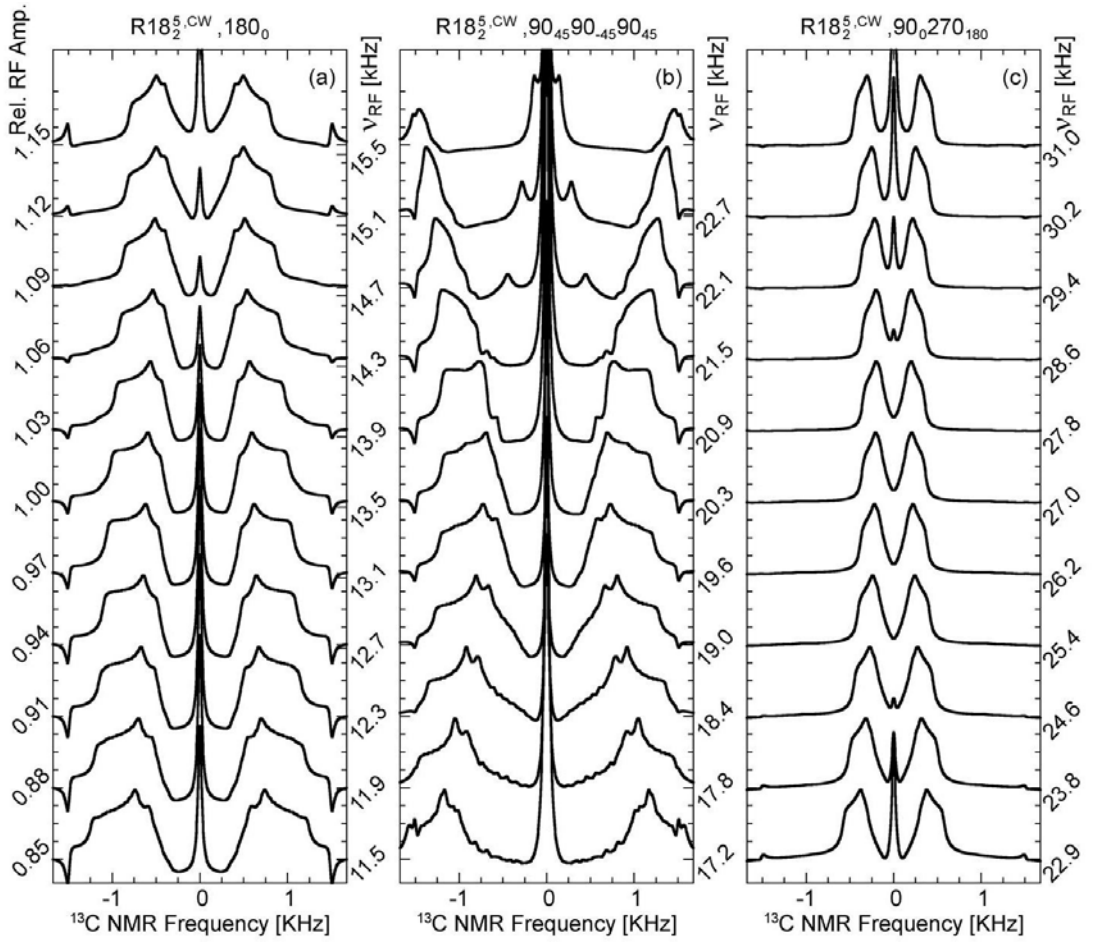


*Figure A11: SIMPSON simulations of the* $R18_2^5$ *sequence to test its robustness to RF-power mismatch using different R elements a).*$[180_{50}180_{310}]$*, b).*$[90_{95}90_590_{95}90_{265}90_{355}90_{265}]$ *and c).*$[90_{50}270_{230}90_{310}270_{130}]$ *at a spinning speed of 3 kHz. Simulations are performed for the carbonyl environment of alanine.*

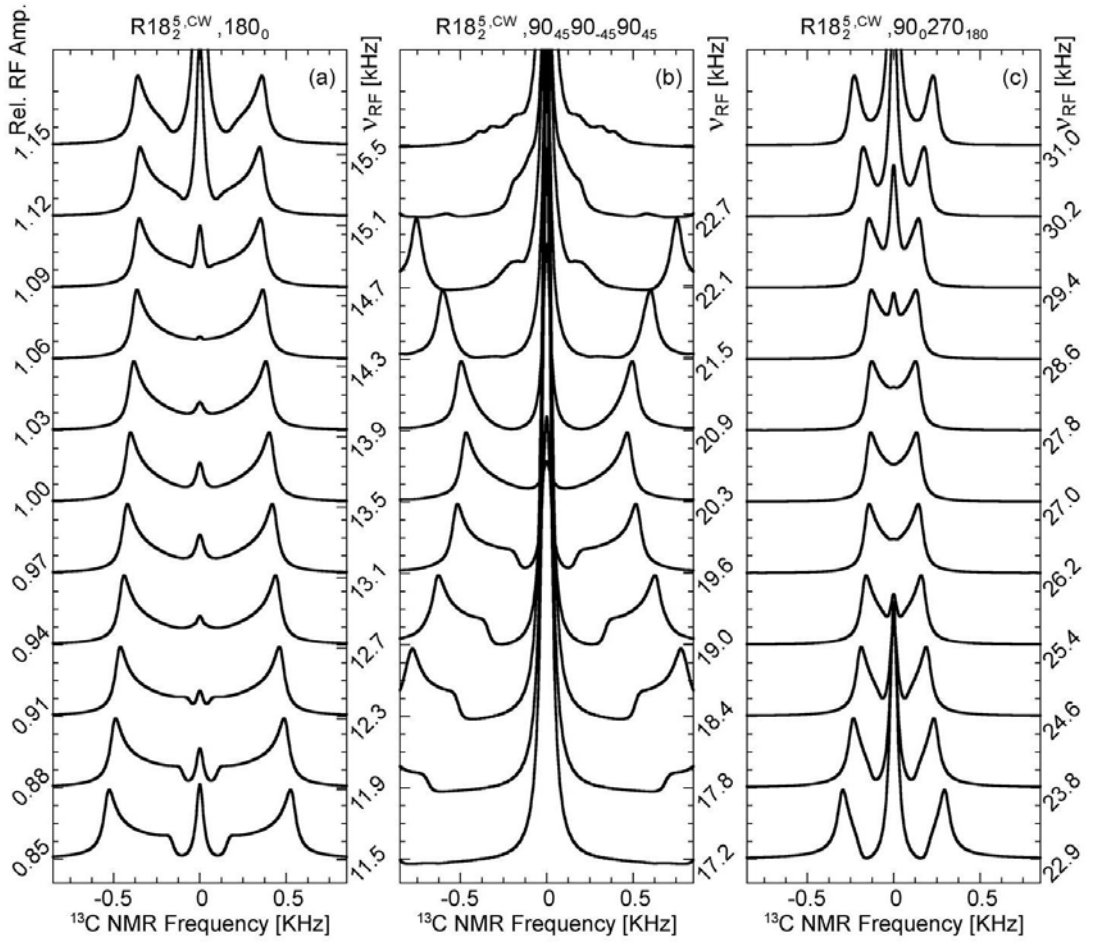


*Figure A12: SIMPSON simulations of the* $R18_2^5$ *sequence to test its robustness to RF- power mismatch using different R elements a).*$[180_{50}180_{310}]$*, b).*$[90_{95}90_590_{95}90_{265}90_{355}90_{265}]$ *and c).*$[90_{50}270_{230}90_{310}270_{130}]$ *at a spinning rate of 3 kHz. Simulations are performed on the methyl environment of DMS.*

### $R18_2^7$ Sequence @ 3 kHz

The $R18_2^7$ sequence contains eighteen R elements in two rotor periods and the symmetry number $\nu = 7$ determine the phase at which the pulses are applied. This sequence recouples the 1st order component of the spatial CSA tensor, ie. $(\sigma_1)$. When the R element is $180_0$, this sequence has nine $[180_{70}180_{290}]$ pulse pairs in two rotor periods. For a spinning speed of 3 kHz, the *RF* power is 13.5 kHz. The simulated spectra show the sequence is stable with respect to the *RF* offset from -2 kHz to +2 kHz (figure A13a, A14a). Beyond these offset values, there is a significant change in the recoupled CSA pattern. The carbonyl environment shows spinning sideband distorts the CSA line shape throughout the spectrum. This sequence is stable to *RF* power mismatch from 0.94 to 1.03 for carbonyl environment of alanine (figure A15a)

and from 0.97 to 1.03 for methyl environment of DMS (figure A16a). Here also the carbonyl environment shows spinning sideband which distorts the CSA pattern throughout the spectrum. But the recoupled CSA pattern of DMS methyl environments preserve a good line shape for the entire range of RF power mismatch with a continuous decrease in width from 0.85 to 1.15. The scaling factor of the sequence was calculated to be 0.26.

When the R element is $90_{45}90_{-45}90_{45,}$ this sequence contain nine repeating units of $[90_{115}90_{25}90_{115}90_{245}90_{335}90_{245}]$ pulses in two rotor period. For spinning speeds of 3 kHz, the RF power is 20.25 kHz. The simulated spectra show that the sequence is unstable with respect to the RF offset for the carbonyl environment of alanine (figure A13b), and stable from -2 kHz to +2 kHz for methyl environment of DMS (figure A14b). This sequence is unstable to *RF* power mismatch for both the carbonyl and methyl environments (figure A15b, A16b). The scaling factor of this sequence is 0.27.

When the R element is $90_{0}270_{180,}$ this sequence contains nine repeating units of $[90_{70}270_{250}90_{290}270_{110}]$ pulses in two rotor period. For a spinning speed of 3 kHz the RF power is 27 kHz. This sequence is stable to a wide range of RF offsets from -6 kHz to +6 kHz for the carbonyl environment of alanine (figure A13c), from -6 kHz to +6 kHz for the methyl environment of DMS (figure A14c) and stable to RF power mismatch from 0.94 to 1.06 for the carbonyl environment of alanine (figure A15c), 0.94 to 1.06 for the methyl environment of DMS (figure A16c). However, the scaling factor of the sequence is very low as 0.05.

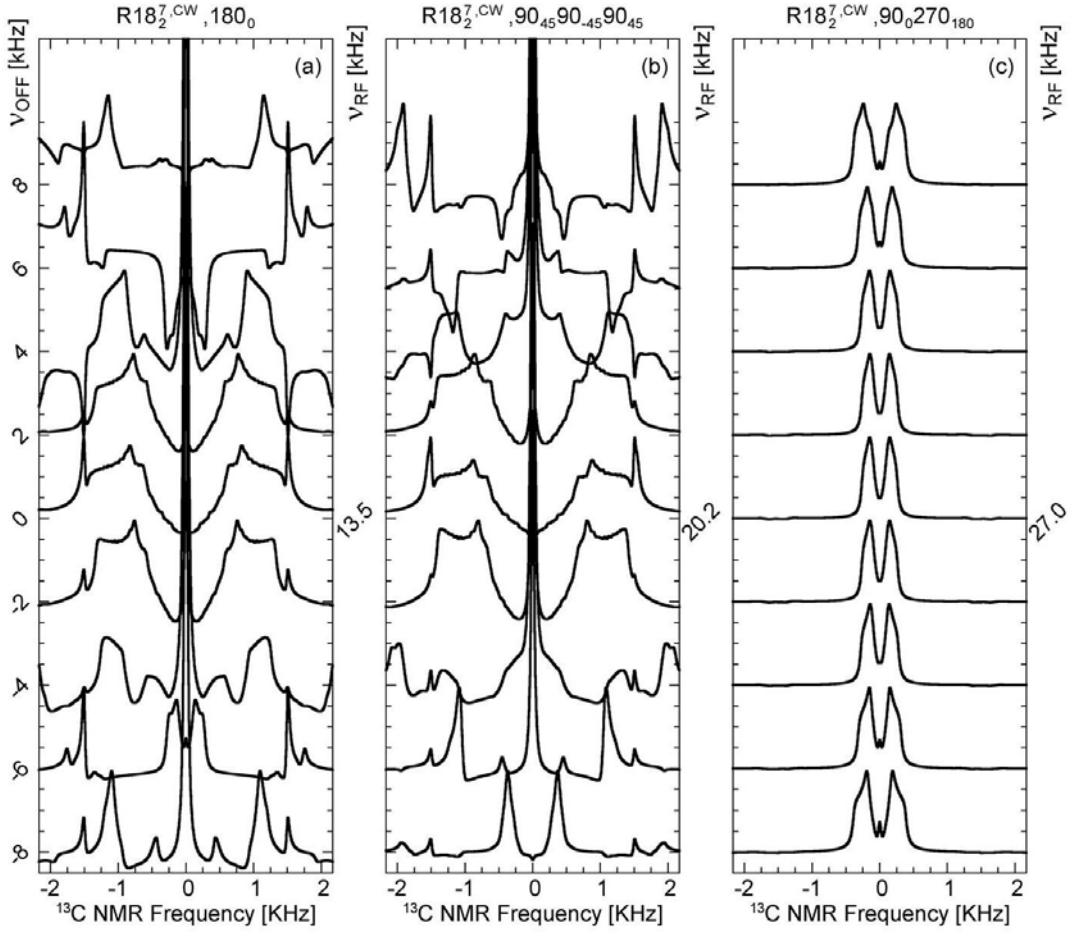


*Figure A13: SIMPSON simulations of the* $R18_2^7$ *sequence to test its robustness to RF -offset using different R elements a).*$[180_{70}180_{290}]$*, b).*$[90_{115}90_{25}90_{115}90_{245}90_{335}90_{245}]$ *and c).*$[90_{70}270_{250}90_{290}270_{110}]$ *at a spinning speed of 3 kHz. Simulations are performed on the carbonyl environment of alanine.*

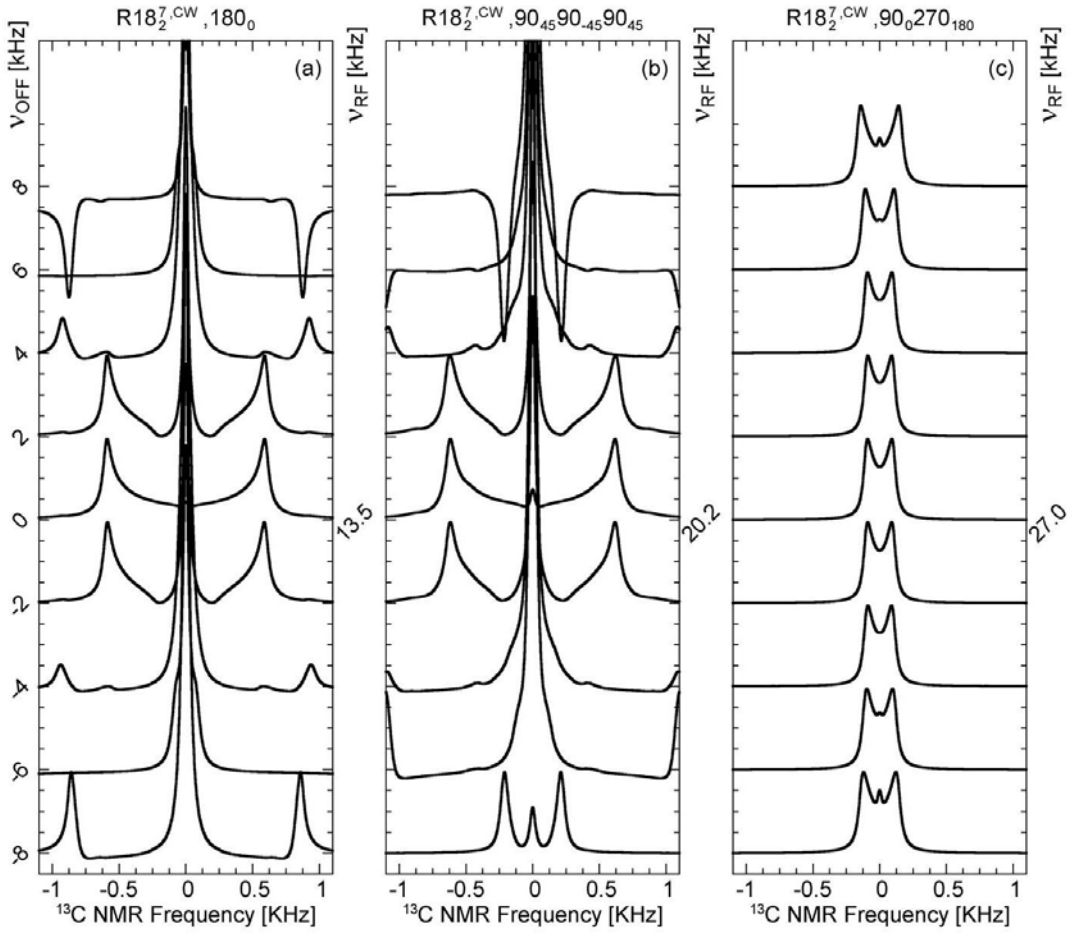


*Figure A14: SIMPSON simulations of the* $R18_2^7$ *sequence to test its robustness towards RF-offset using different R elements a).*$[180_{70}180_{290}]$*, b).*$[90_{115}90_{25}90_{115}90_{245}90_{335}90_{245}]$ *and c).*$[90_{70}270_{250}90_{290}270_{110}]$ *at a spinning rate of 3 kHz. Simulations are performed on the methyl environment of DMS.*

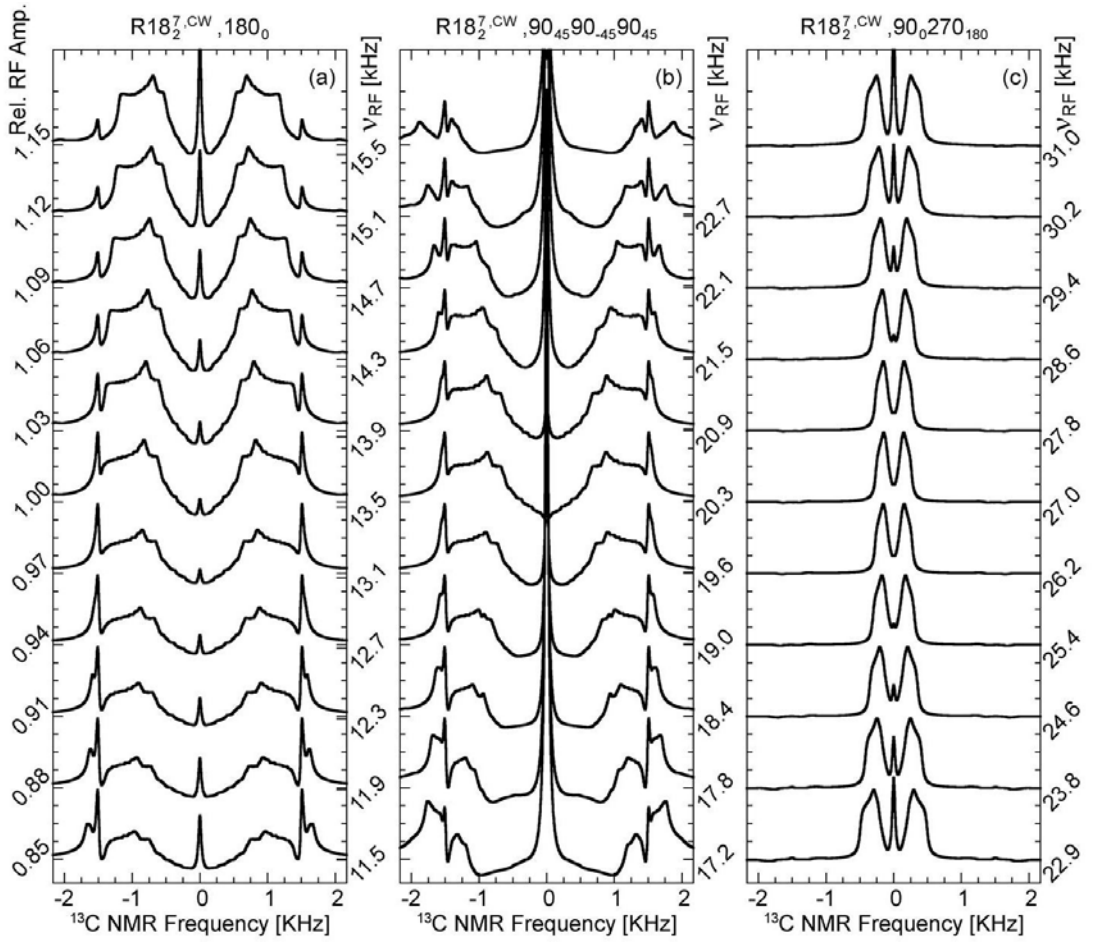


*Figure A15: SIMPSON simulations of the* $R18_2^7$ *sequence to test its robustness to RF-power mismatch using different R elements a).*$[180_{70}180_{290}]$*, b).*$[90_{115}90_{25}90_{115}90_{245}90_{335}90_{245}]$ *and c).*$[90_{70}270_{250}90_{290}270_{110}]$ *at a spinning speed of 3 kHz. Simulations are performed on the carbonyl environment of alanine.*

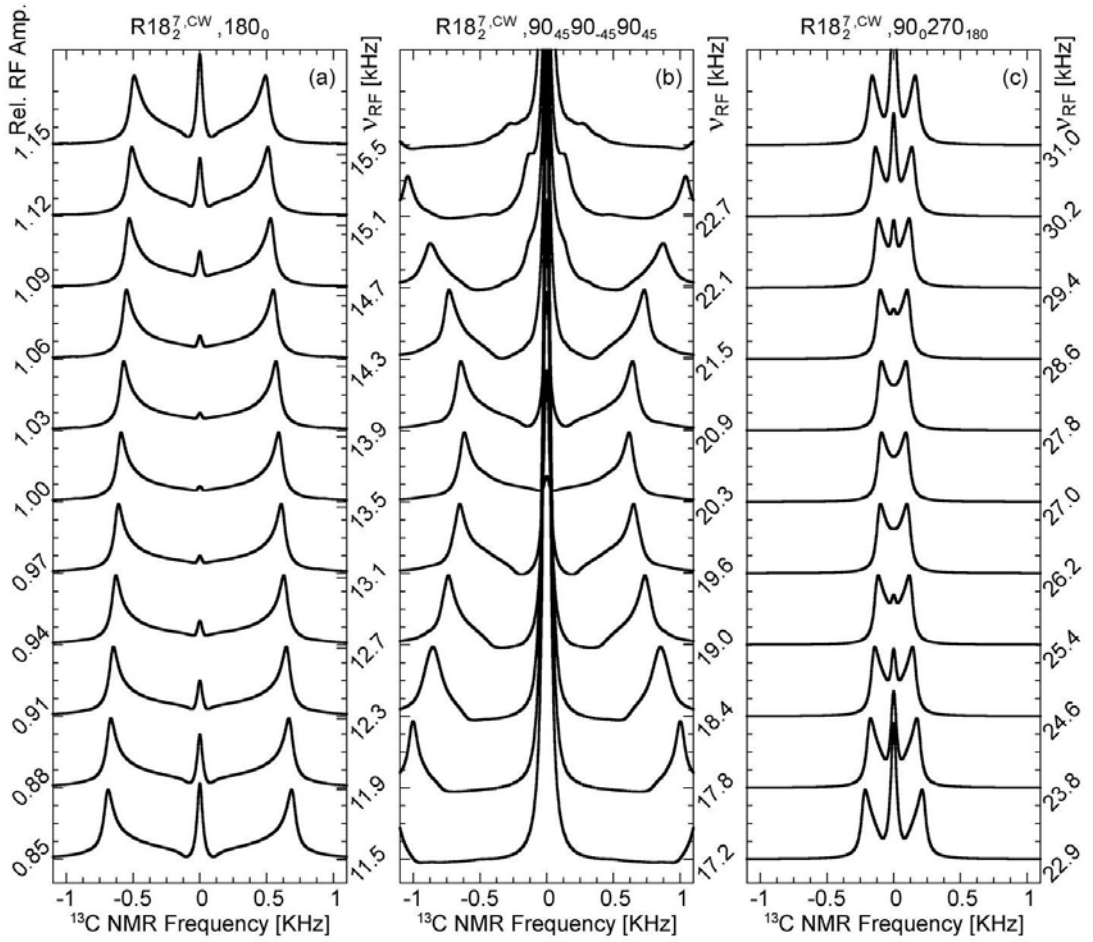


*Figure A16: SIMPSON simulations of the $R18_2^7$ sequence to test its robustness to RF- power mismatch using different R elements a) [$180_{70}180_{290}$], b) [$90_{115}90_{25}90_{115}90_{245}90_{335}90_{245}$] and c) [$90_{70}270_{250}90_{290}270_{110}$] at a spinning rate of 3 kHz. Simulations are performed on the methyl environment of DMS.*

**Simulations at a spinning speed of 10 kHz**

The RF offset and the RF power mismatch dependence of the 6 sequences $R10_1^3, R10_1^4, R18_2^5, R18_2^7, R18_4^5, R14_4^3$ for the carbonyl environment of alanine and the methyl environment of DMS at a spinning speed of 10 kHz is discussed below. As th simulation and experiment. The sequences $R10_1^3, R10_1^4, R18_2^5, R18_2^7$ with $90_{45}90_{-45}90_{45}$ and $90_0270_{180}$ as the R element have RF frequency greater than 50 kHz and there\ avoided them from simulations. These four sequences are discussed first followed by $R18_4^5, R14_4^3$ sequence is carried out.

Figures A17a, and A18a shows the simulations of the RF offset dependence of the $R10_1^3$ sequence with [$180_{54}180_{306}$] as the R element for the carbonyl environment

of alanine and the methyl environment of DMS respectively and is seen that the sequence is stable to RF-offsets from -4 kHz to +4 kHz , for the carbonyl environment of alanine, and from -2 kHz to +2 kHz for the methyl environment of DMS. The scaling factor of the sequence is 0.17. The RF power of the pulses is 50 kHz. Figure A19a, and A20a shows the simulations of the RF power mismatch dependence of the sequence for the carbonyl environment of alanine and the methyl environment of DMS respectively and is seen that it is stable to RF power mismatches from 0.97 to 1.03.

Figure A17b and A18b shows the simulations of the RF offset dependence of the $R10_1^4$ sequence with $[180_{72}180_{288}]$ element for carbonyl environment of alanine and methyl environment of DMS and is seen that the sequence is stable to RF offsets from -4 kHz to +4 kHz for the carbonyl environment of alanine and from -2 kHz to +2 kHz for the methyl environment of DMS. The scaling factor of the sequence is 0.26. The RF power of the pulses is 50 kHz. Figure A19b, and A20b shows the simulations of the RF power mismatch dependence of the sequence for the carbonyl environment of alanine and methyl environment of DMS respectively and is seen that the sequence is stable to RF power mismatches from 0.97 to 1.03.

Figure A17c, and A18c shows the simulations of the RF offset dependence of the $R18_2^5$ sequence with $[180_{50}180_{310}]$ as the R element for carbonyl environment of alanine and methyl environment of DMS respectively and it is seen that the sequence is stable to RF offsets from -4 kHz to +4 kHz for the carbonyl environment of alanine and from -2 kHz to +2 kHz for the methyl environment of DMS. The scaling factor of the sequence is 0.20. Here the pulses are applied with an RF power of 45 kHz. Figure A19c, and A20c shows simulations of the RF power mismatch dependence of the sequence for the carbonyl environment of alanine and methyl environment of DMS respectively and is seen that the seqeunce is stable to RF power mismatches from 0.97 to 1.03. [PTO]

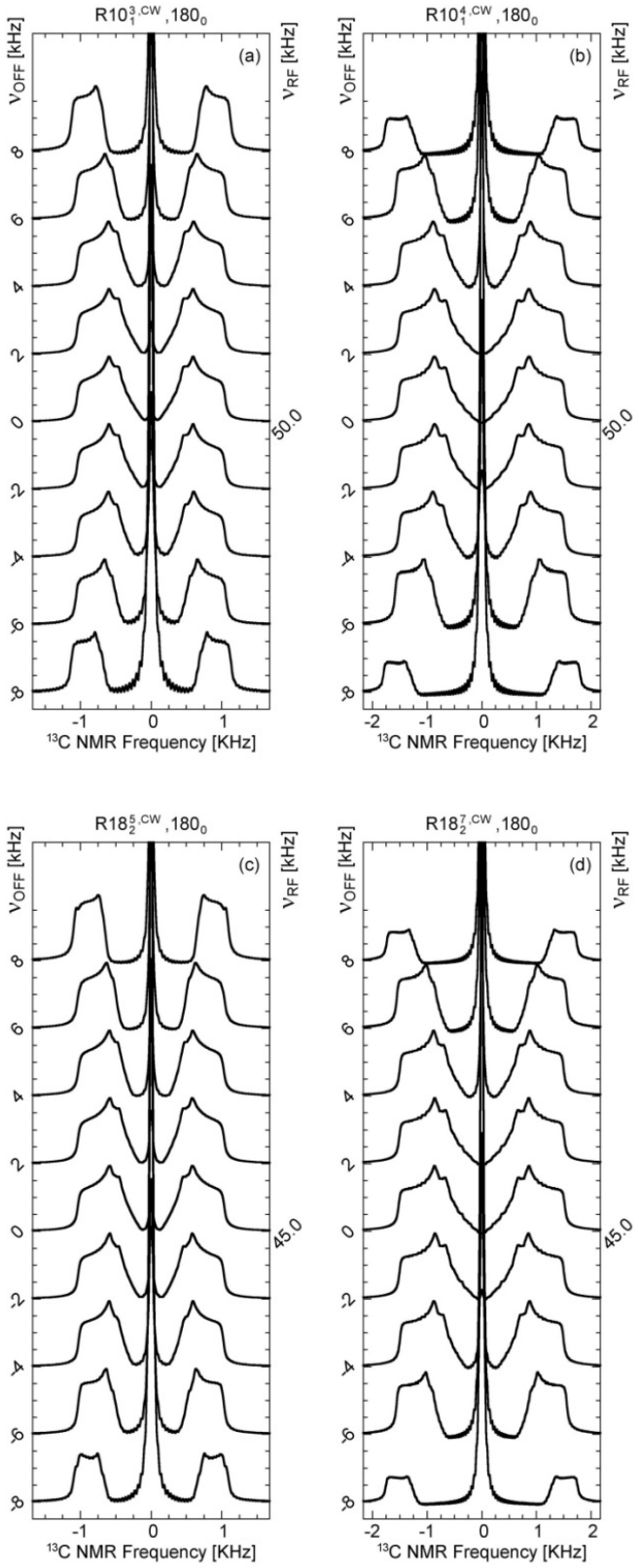


*Figure A17: SIMPSON simulations of the* $a).R10_1^3,\ b).R10_1^4,\ c).R18_2^5,\ d).R18_2^7$ *sequences to test its robustness to RF-offset using different R elements a). [$180_{54}180_{306}$], b).[$180_{72}180_{288}$], c). [$180_{50}180_{310}$], d).[$180_{70}180_{290}$] at a spinning speed of 10 kHz. Simulations are performed on the carbonyl environment of alanine.*

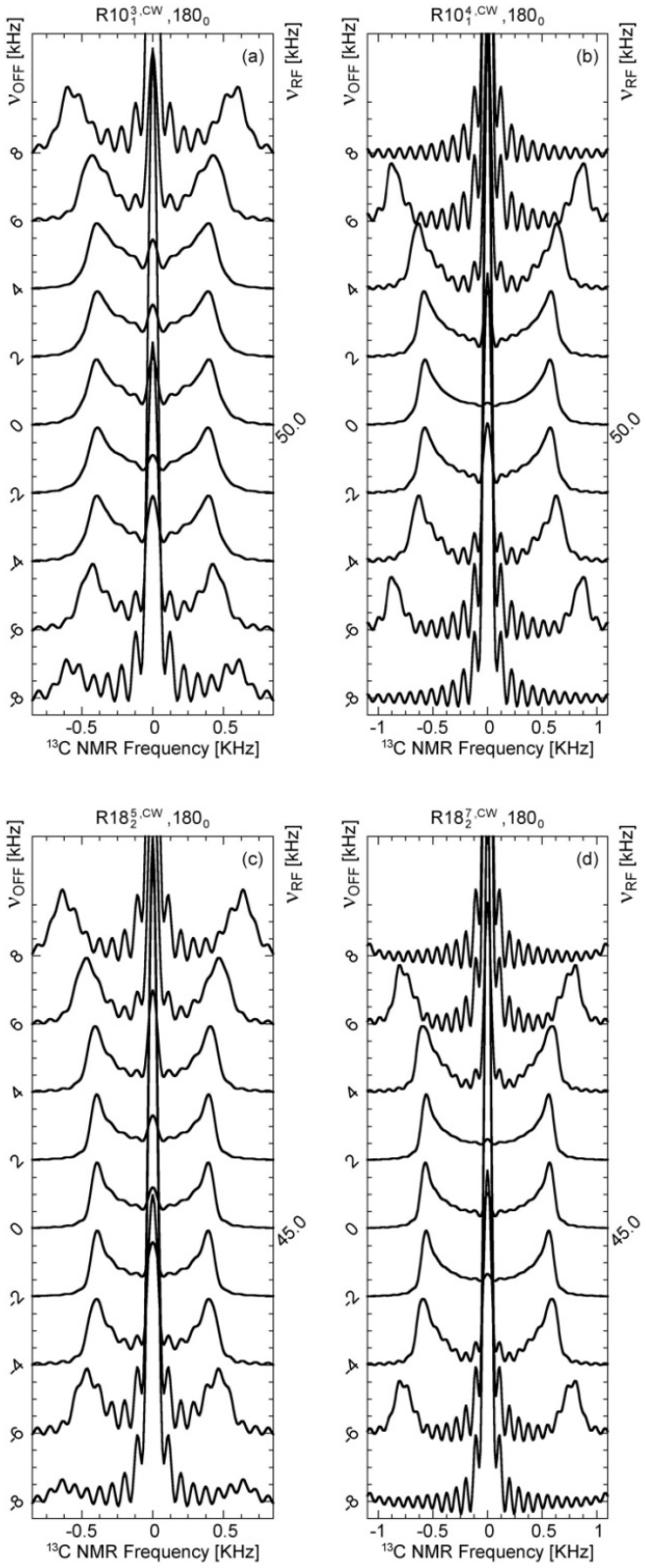


*Figure A18: SIMPSON simulations of the* $a).R10_1^3,\ b).R10_1^4,\ c).R18_2^5,\ d).R18_2^7$ *sequences to test its robustness to RF-offset using different R element a).* $[180_{54}180_{306}]$*, b).*$[180_{72}180_{288}]$*, c).* $[180_{50}180_{310}]$*, d).*$[180_{70}180_{290}]$ *at a spinning speed of 10 kHz. Simulations are performed on the methyl environment of DMS.*

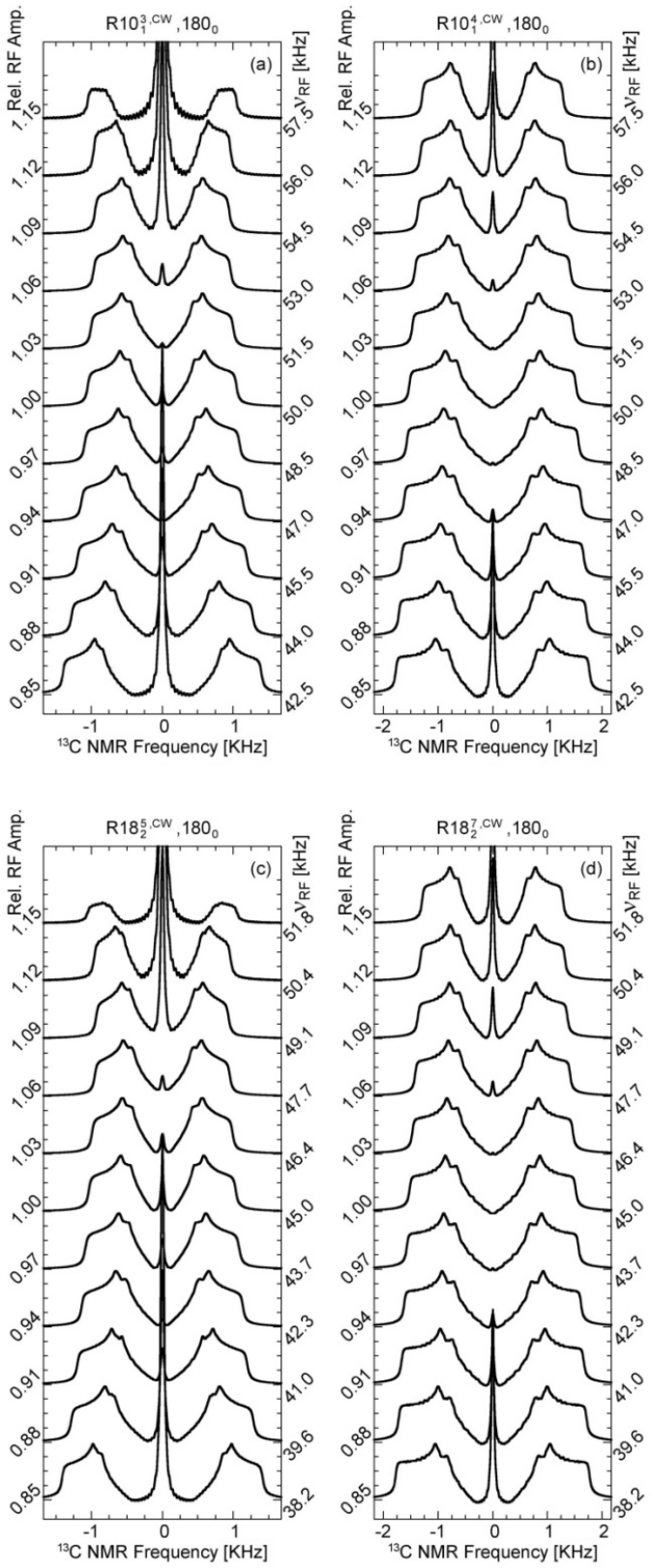


*Figure A19: SIMPSON simulations of the* $a).R10_1^3,\ b).R10_1^4,\ c).R18_2^5,\ d).R18_2^7$ *sequences to test its robustness to RF-power mismatch using different R elements a). [*$180_{54}180_{306}$*], b).[*$180_{72}180_{288}$*], c). [*$180_{50}180_{310}$*], d).[*$180_{70}180_{290}$*] at a spinning speeds of 10 kHz. Simulations are performed on carbonyl environment of alanine.*

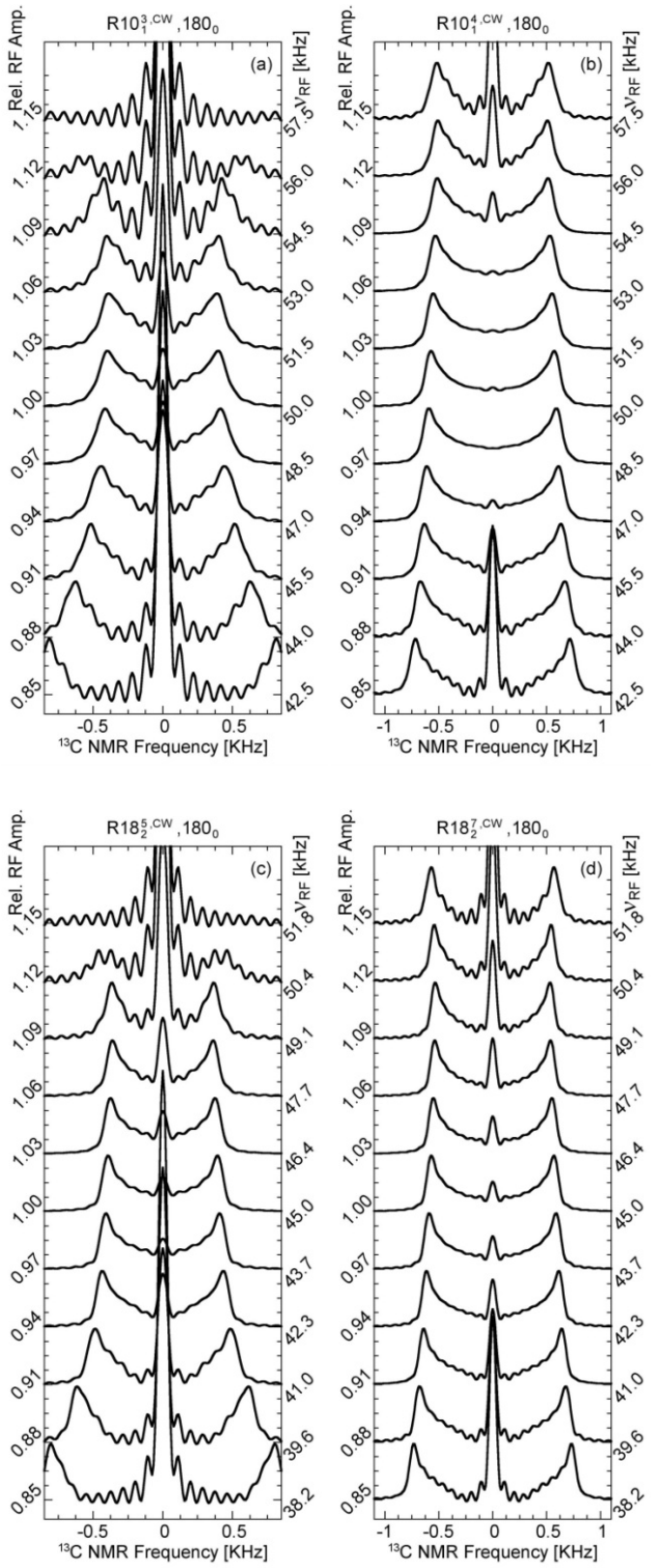


*Figure A20: SIMPSON simulations of the* $a).R10_1^3,\ b).R10_1^4,\ c).R18_2^5,\ d).R18_2^7$ *sequences to test its robustness to RF-inhomogeneity using a). [*$180_{54}180_{306}$*], b).[*$180_{72}180_{288}$*], c). [*$180_{50}180_{310}$*], d).[*$180_{70}180_{290}$*] as the R element at a spinning speed of 10 kHz. Simulations are performed on methyl environment of DMS.*

Figure A17d, 28d shows the offset dependence simulation of $R18_2^7$ sequence with $[180_{70}180_{290}]$ pulse elements for carbonyl environment of alanine and methyl environment of DMS respectively. The simulated spectra show the sequence is offset stable from -4 kHz to +4 kHz for carbonyl environment of alanine and it is stable from -2 kHz to +2 kHz for methyl environment of DMS. The scaling factor of the sequence is calculated as 0.26. The pulses are applied with an RF power of 45 kHz. Figure A19d, A20d shows the RF power mismatch dependent simulation of the sequence for carbonyl environment of alanine and methyl environment of DMS respectively. The spectra show the sequence is offset stable from 0.97 to 1.03.

### $R18_4^5$ Sequence at 10 kHz

The $R18_4^5$ sequence contains eighteen R elements in four rotor periods and the symmetry number $\nu = 5$ determine the phase at which the pulses are applied. This sequence recouples the 1st order component of the spatial CSA tensor ($\sigma_1$). When the R element is $180_0$, this sequence has nine $[180_{50}180_{310}]$ pulse pairs in four rotor periods. For a spinning speed of 10 kHz the RF power is 22.5 kHz. The simulated spectra show that the sequence is stable with respect to the RF offset from -4 kHz to +2 kHz for the carbonyl environment of alanine and the methyl environment of DMS (figure A21a, A22a). Beyond these offset values, there is a significant change in the recoupled CSA pattern. This sequence is stable to RF power mismatch in the range of 0.97 to 1.03 for the carbonyl environment of alanine and the methyl environment of DMS (figure A23a, A24a). The recoupled CSA pattern of both carbonyl and methyl environments preserve a good line shape for the entire range of RF power mismatch that was monitored with a continuous decrease in width from 0.85 to 1.15. The scaling factor of the sequence is 0.25.

When the R element is $90_{45}90_{-45}90_{45,}$ this sequence contain nine repeating units of $[90_{95}90_{5}90_{95}90_{265}90_{355}90_{265}]$ pulses elements in four rotor periods. For a spinning speed of 10 kHz, the RF power is 33.7 kHz. The simulated spectra show that the sequence is stable with respect to the RF offset from -2 kHz to +2 kHz (figure A21b, A22b) and is highly unstable to RF power mismatch (figure A22b, A23b). The scaling factor of this sequence is 0.29.

When the R element is $90_0270_{180,}$ this sequence contains nine repeating units of $[90_{50}270_{230}90_{310}270_{130}]$ pulses in four rotor periods. For a spinning speed of 10 kHz, the RF power is 45 kHz. This sequence is stable for a wide range of RF offsets from -8 kHz to +8 kHz for the carbonyl environment of alanine (figure A21c), from -8 kHz to +8 kHz for the methyl environment of DMS (figure A22c) and stable to RF power mismatch from 0.94 to 1.06 for the carbonyl environment of alanine (figure A23c), from 1.00 to 1.03 for the methyl environment of DMS (figure A24c). However, the scaling factor of the sequence is low as 0.09.

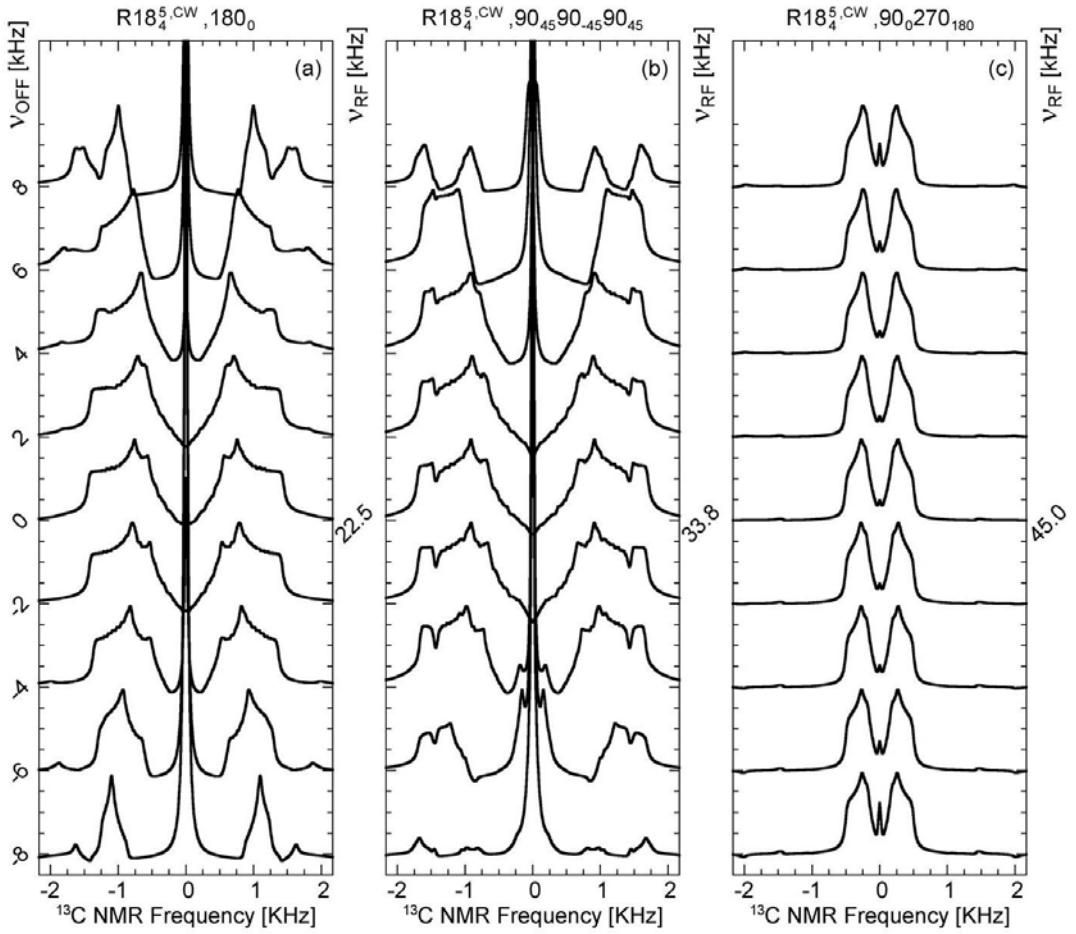


*Figure A21: SIMPSON simulations of the $R18_4^5$ sequence to test its robustness to RF-offset using different R elements a).[$180_{50}180_{310}$] b).[$90_{95}90_590_{95}90_{265}90_{355}90_{265}$] and c).[$90_{50}270_{230}90_{310}270_{130}$]at a spinning speed of 10 kHz. Simulations are performed on the carbonyl environment of alanine.*

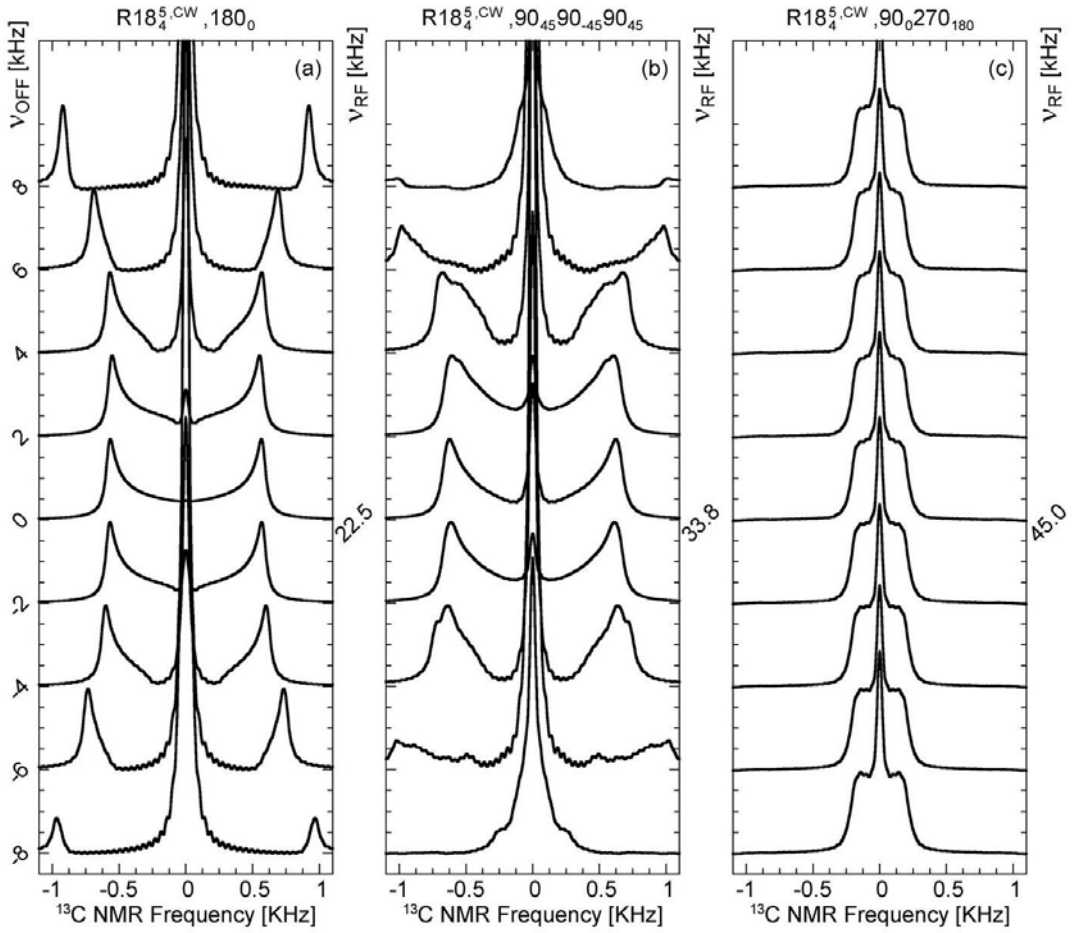


*Figure A22: SIMPSON simulations of the* $R18_4^5$ *sequence to test its robustness to RF-offset using different R elements a).*$[180_{50}180_{310}]$ *b).*$[90_{95}90_590_{95}90_{265}90_{355}90_{265}]$ *and c).*$[90_{50}270_{230}90_{310}270_{130}]$*at a spinning speed of 10 kHz. Simulations are performed on the methyl environment of DMS.*

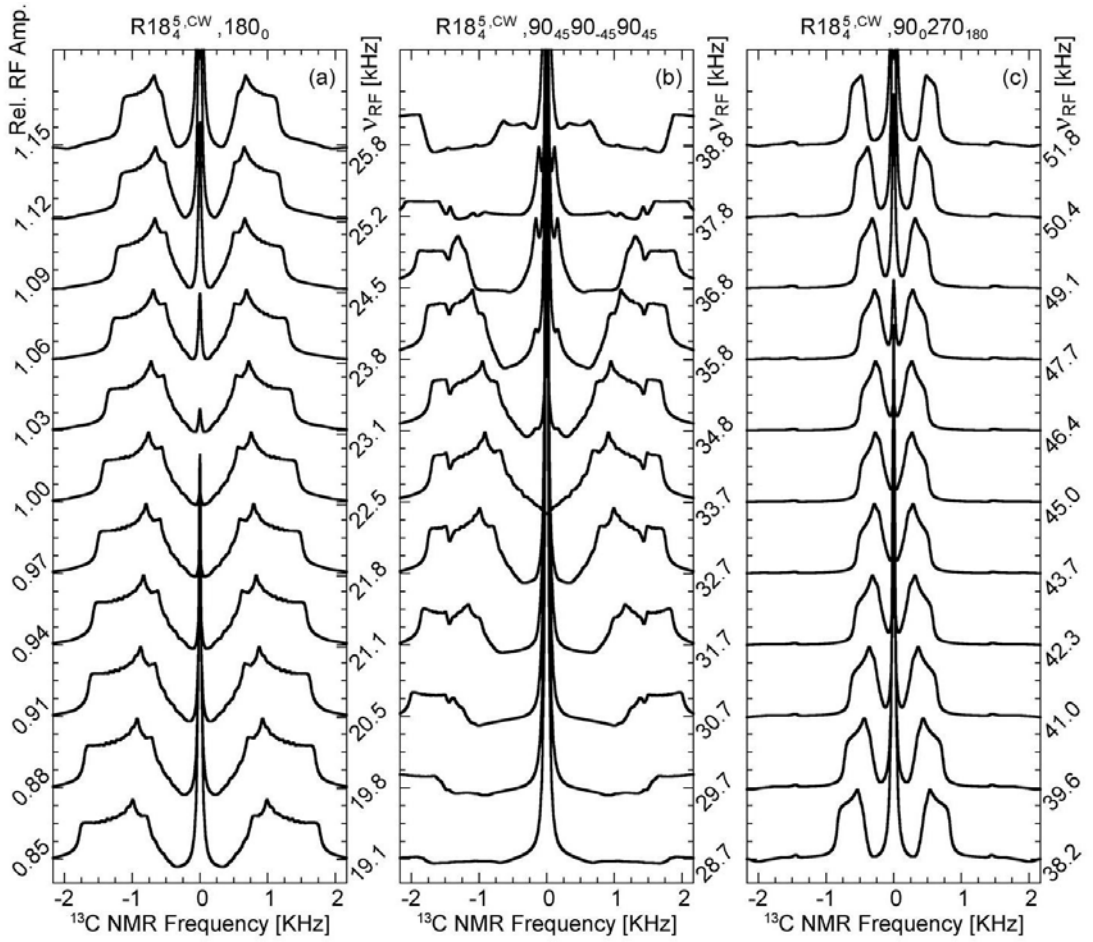


*Figure A23: SIMPSON simulations of the $R18_4^5$ sequences to test its robustness to RF-power mismatch using different R elements a). $[180_{50}180_{310}]$, b).$[90_{95}90_590_{95}90_{265}90_{355}90_{265}]$ and c).$[90_{50}270_{230}90_{310}270_{130}]$ at a spinning speed of 10 kHz. Simulations are performed on the carbonyl environment of alanine.*

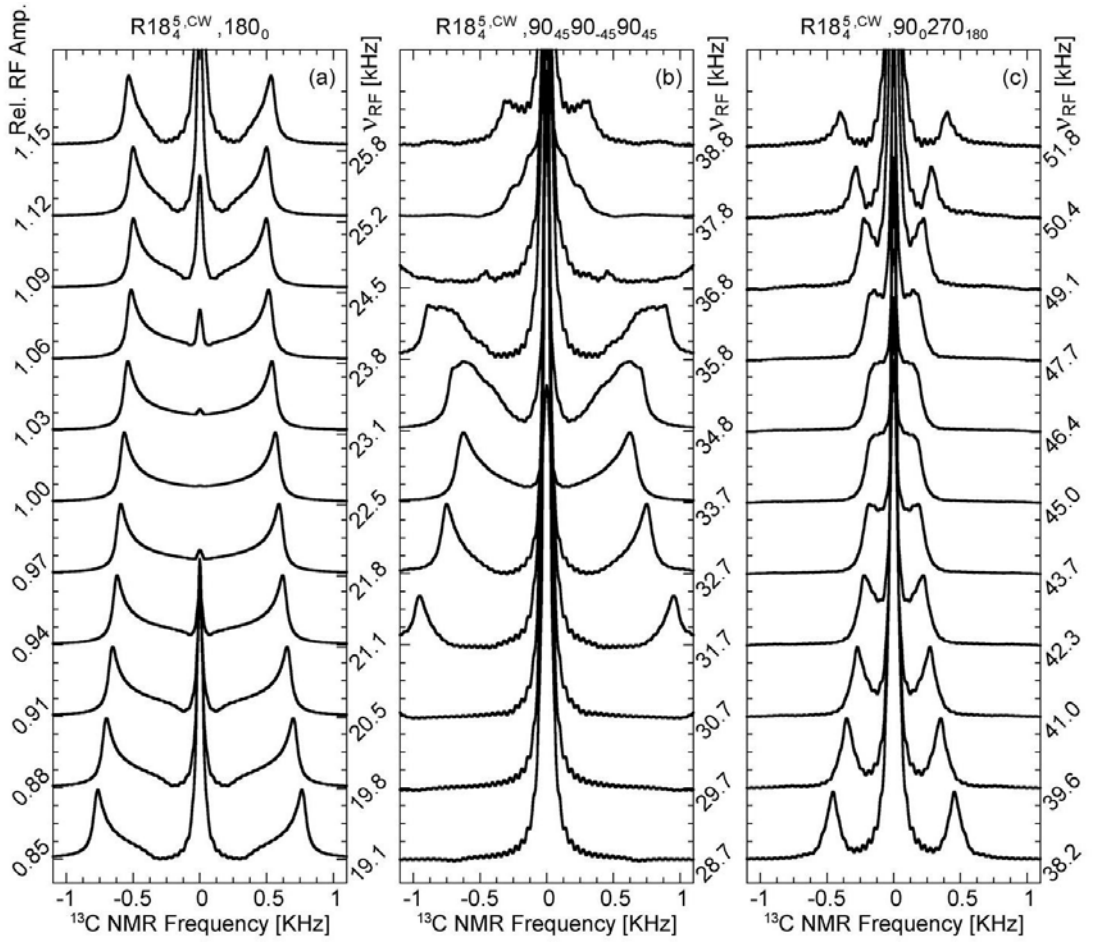


*Figure A24: SIMPSON simulations of the* $R18_4^5$ *sequence to test its robustness to RF-power mismatch using different R elements a).* $[180_{50}180_{310}]$*, b).*$[90_{95}90_590_{95}90_{265}90_{355}90_{265}]$ *and c).*$[90_{50}270_{230}90_{310}270_{130}]$ *at a spinning speed of 10 kHz. Simulations are performed on the methyl environment of DMS.*

### $\mathbf{R14_4^3}$ Sequence at 10 kHz

The $R14_4^3$ sequence contains fourteen R elements in four rotor periods and the symmetry number $\nu = 3$ determine the phase at which the pulses are applied. This sequence recouples the 1st order component of the spatial CSA tensor ($\sigma_1$). When the R element is $180_0$, this sequence has seven $[180_{38.57}180_{321.42}]$ pulse pairs in four rotor periods. For a spinning speed of 10 kHz the RF power is 17.5 kHz. The simulated spectra show that the sequence is stable with respect to the RF offset from -2 kHz to +2 kHz for both the carbonyl environment of alanine and methyl environment of DMS (figure A25a, A26a). Beyond these offset values, there are significant changes in the recoupled CSA pattern. This sequence is stable to RF power mismatches in the range 0.94 to 1.03 for the carbonyl environment of alanine (figure A27a), and from

0.97 to 1.03 for the methyl environment of DMS (figure A28a). The recoupled CSA pattern of both the carbonyl and the methyl environments preserve a good line shape for the entire range of RF power mismatch conditions with a continuous decrease in width from 0.85 to 1.15. The scaling factor of the sequence is 0.24.

When the R element is $90_{45}90_{-45}90_{45,}$ this sequence contains seven repeating units of $[90_{83.57}90_{353.57}90_{83.57}90_{276.43}90_{173.57}90_{276.43}]$ pulses in four rotor periods. For spinning speeds of 10 kHz, the RF power is 26.3 kHz. The simulated spectra show the sequence is stable with respect to the RF offset from -2 kHz to +2 kHz (figure A25b, A26b) and to RF power mismatch from 0.97 to 1.03 at 10 kHz (figure A27b, A28b). The scaling factor of this sequence is 0.3.

When the R element is $90_0270_{180,}$ this sequence contains seven repeating units of $[90_{38.57}270_{218.57}90_{321.42}270_{141.42}]$ pulses in four rotor periods. For a spinning speed of 10 kHz, the RF power is 35 kHz. This sequence is stable for a wider range of RF offsets from -8 kHz to 6 kHz for the carbonyl environment of alanine (figure A25c), from -8 kHz to +8 kHz for the methyl environment of DMS (figure A26c) and stable to RF power mismatch from 0.94 to 1.06 for the carbonyl environment of alanine (figure A27c) and from 0.97 to 1.06 for the methyl environment of DMS (figure A28c). However, the scaling factor of the sequence is low as 0.11.

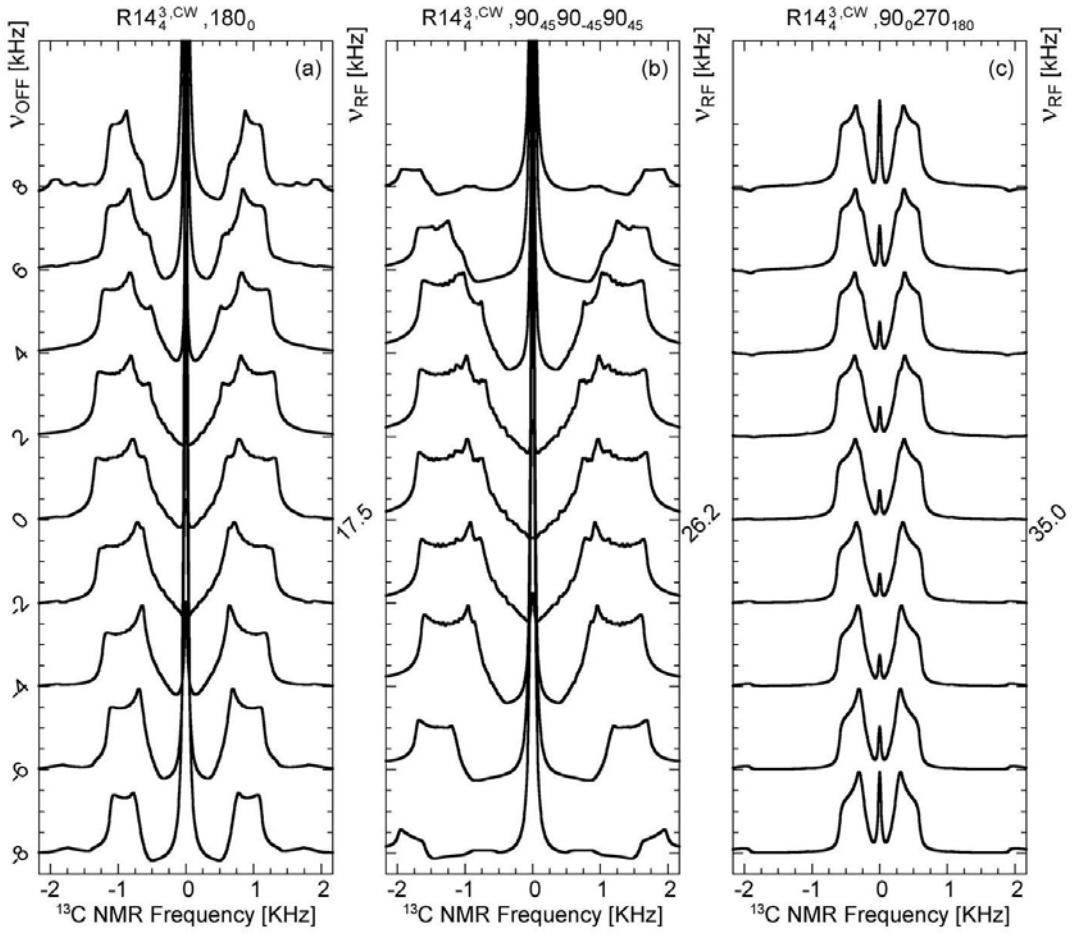


*Figure A25: SIMPSON simulations of the* $R14_4^3$ *sequences to test its robustness to RF-offset using different R elements a).*$[180_{38.57}180_{321.42}]$*, b).*$[90_{83.57}90_{353.57}90_{83.57}90_{276.43}90_{173.57}90_{276.43}]$ *and c).*$[90_{38.57}270_{218.57}90_{321.42}270_{141.42}]$ *at a spinning speed of 10 kHz. Simulations are performed on the carbonyl environment of alanine.*

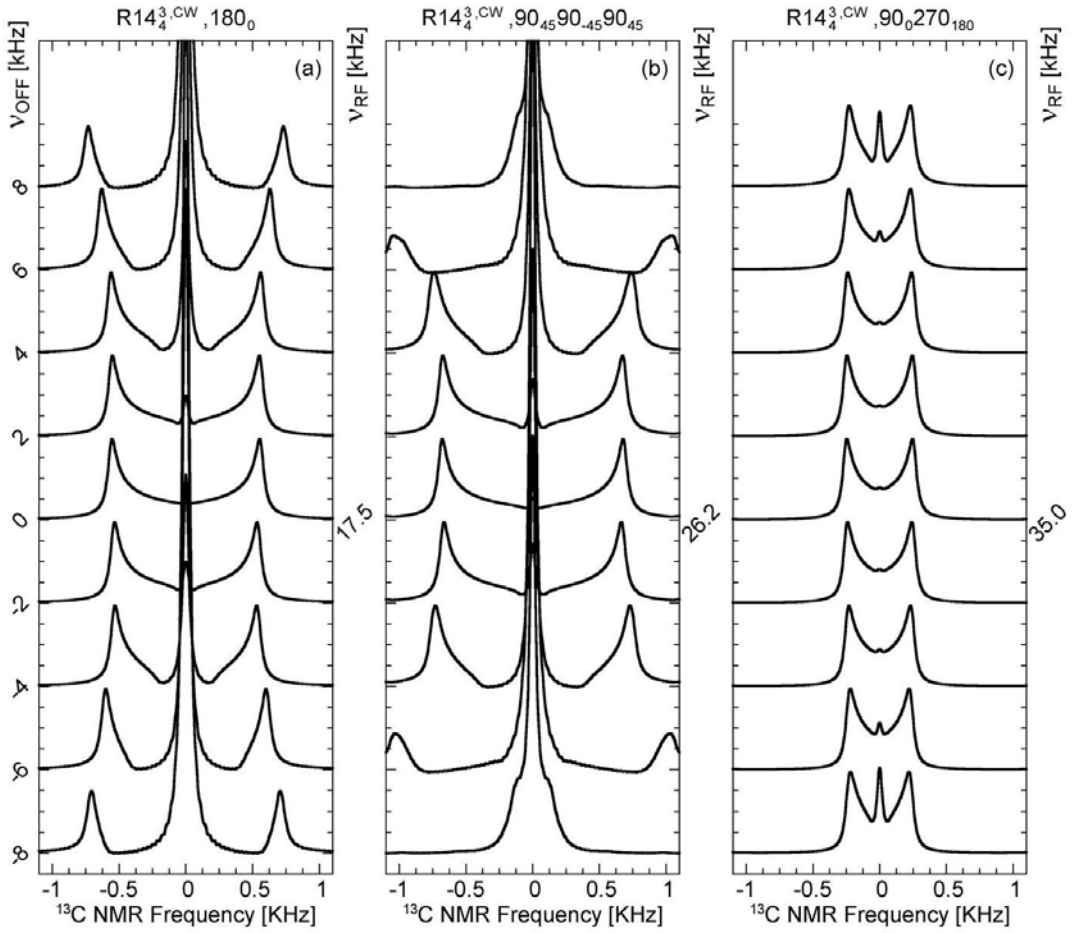


*Figure A26: SIMPSON simulations of the $R14_4^3$ sequences to test its robustness to RF-offset using different R elements a).[$180_{38.57}180_{321.42}$], b).[$90_{83.57}90_{353.57}90_{83.57}90_{276.43}90_{173.57}90_{276.43}$] and c).[$90_{38.57}270_{218.57}90_{321.42}270_{141.42}$] at a spinning speed of 10 kHz. Simulations are performed on the methyl environment of DMS.*

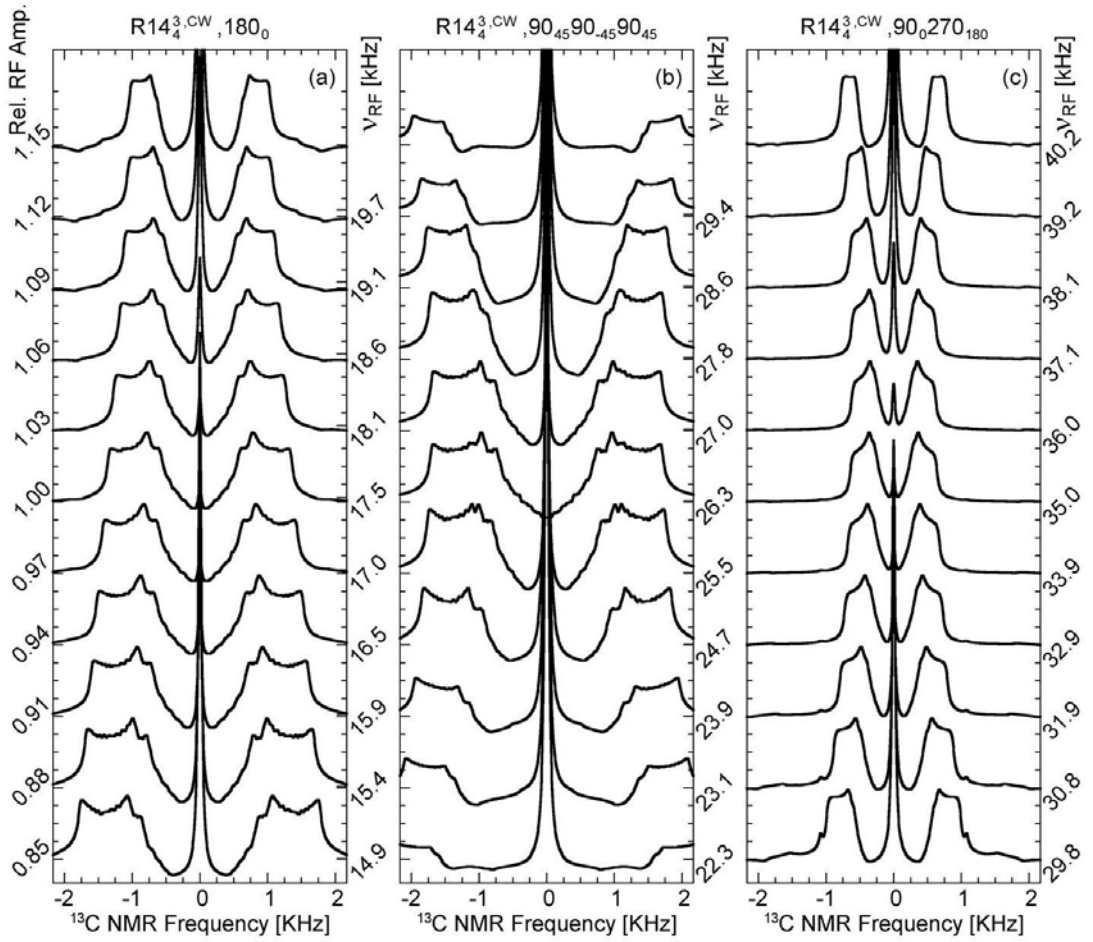


*Figure A27: SIMPSON simulations of the $R14_4^3$ sequences to test its robustness to RF-power mismatch using different R elements a).[$180_{38.57}180_{321.42}$], b).[$90_{83.57}90_{353.57}90_{83.57}90_{276.43}90_{173.57}90_{276.43}$] and c).[$90_{38.57}270_{218.57}90_{321.42}270_{141.42}$] at a spinning speed of 10 kHz. Simulations are performed on the carbonyl environment of alanine.*

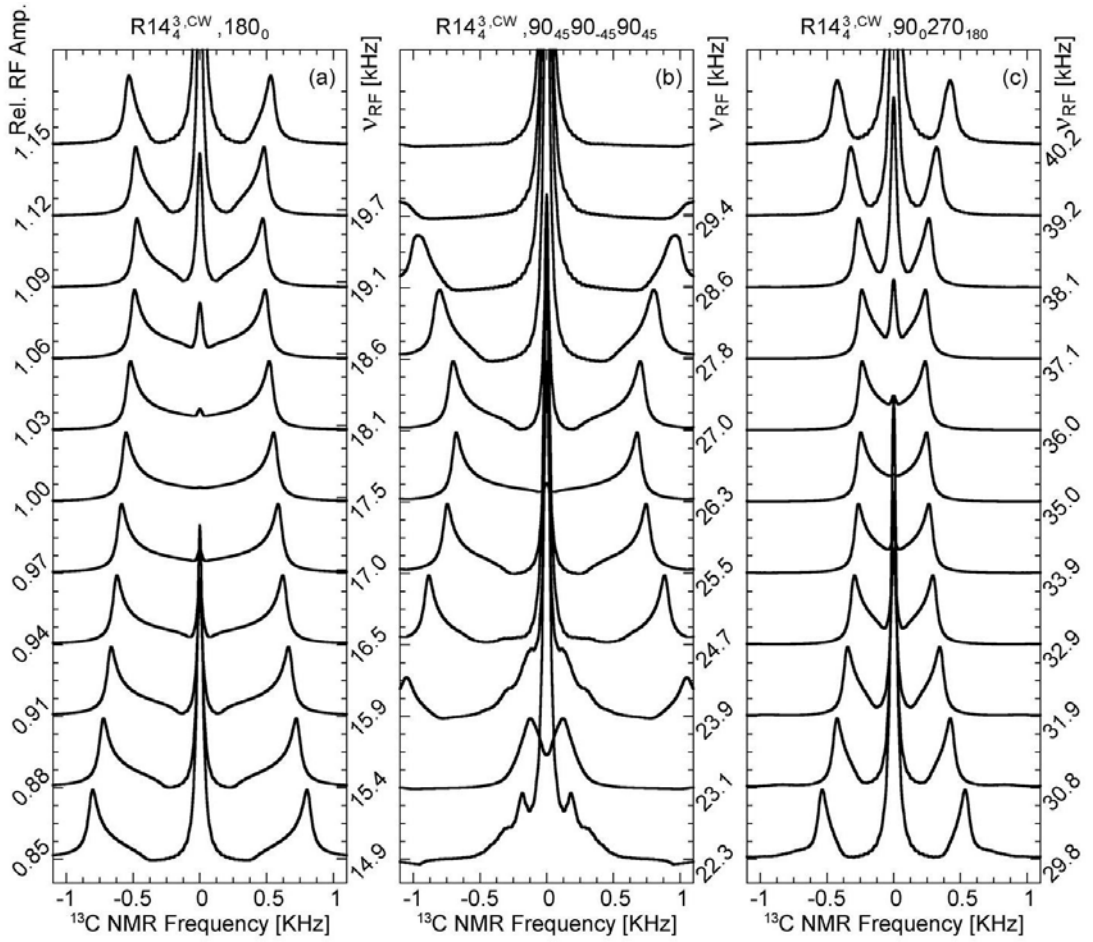


*Figure A28: SIMPSON simulations of the $R14_4^3$ sequences to test its robustness to RF-power mismatch using different R elements a).[$180_{38.57}180_{321.42}$], b).[$90_{83.57}90_{353.57}90_{83.57}90_{276.43}90_{173.57}90_{276.43}$] and c).[$90_{38.57}270_{218.57}90_{321.42}270_{141.42}$] at a spinning speed of 10 kHz. Simulations are performed on the methyl environment of DMS.*

# References


[1] M.H. Levitt, Spin Dynamics, John Wiley & Sons Ltd, Chichester, **2008**

[2] A.P.M. Kentgens, E.d. Boer and W.S. Veeman, *J. Chem. Phys.,* 87, 6859-6866, **1987**

[3] A. Hagemeyer, K. Schmidt-rohr and H.W. Spiess, *Advances in mangetic Resonance,* 13, 85-130, **1989**

[4] G. Kumaraswamy, N.S. Surve, R. Mathew, A. Rana, S.K. Jha, N.N. Bulakh, A.A. Nisal, T.G. Ajithkumar, P.R. Rajamohanan and R. Ratnagiri, *Macromolecules,* 45, 5967-5978, **2012**

[5] F. Bloch, *Phys. Rev.,* 70, 460-474, **1946**

[6] E.M. Purcell, H.C. Torrey and R.V. Pound, *Phys. Rev.,* 69, 37-38, **1946**

[7] W.D. Knight, *Phys. Rev.,* 76, 1259-1260, **1949**

[8] W.G. Proctor and F.C. Yu, *Phys. Rev.,* 77, 717-717, **1950**

[9] H.S. Gutowsky and D.W. McCall, *Phys. Rev.,* 82, 748-749, **1951**

[10] R.R. Ernst and W.A. Anderson, *Rev. Sci. Instrum.,* 37, 93-102, **1966**

[11] W.P. Aue, E. Bartholdi and R.R. Ernst, *J. Chem. Phys.,* 64, 2229-2246, **1976**

[12] W.P. Aue, D.J. Ruben and R.G. Griffin, *J. Magn. Reson.,* 43, 472-477, **1981**

[13] K. Nagayama, A. Kumar, K. Wüthrich and R.R. Ernst, *J. Magn. Reson.,* 40, 321-334, **1980**

[14] A. Wokaun and R.R. Ernst, *Chem. Phys. Lett.,* 52, 407-412, **1977**

[15] U. Piantini, O.W. Sorensen and R.R. Ernst, *J. Am. Chem. Soc.,* 104, 6800-6801, **1982**

[16] L. Braunschweiler and R.R. Ernst, *J. Magn. Reson.,* 53, 521-528, **1983**

[17] J. Jeener, B.H. Meier, P. Bachmann and R.R. Ernst, *J. Chem. Phys.,* 71, 4546-4553, **1979**

[18] A.A. Bothner-By, R.L. Stephens, J. Lee, C.D. Warren and R.W. Jeanloz, *J. Am. Chem. Soc.,* 106, 811-813, **1984**

[19] G. Bodenhausen and D.J. Ruben, *Chem. Phys. Lett.,* 69, 185-189, **1980**

[20] A. Bax, R.H. Griffey and B.L. Hawkins, *J. Magn. Reson.,* 55, 301-315, **1983**

[21] A. Bax and M.F. Summers, *J. Am. Chem. Soc.,* 108, 2093-2094, **1986**

[22] R.R. Ernst, G. Bodenhausen and A. Wokaun, Principles of Nuclear Magnetic Resonance in One and Two Dimensions, Oxford University Press, Oxford, **1987**

[23] S.A. Smith, T.O. Levante, B.H. Meier and R.R. Ernst, *J. Magn. Reson., Ser A,* 106, 75-105, **1994**

[24] M. Bak, J.T. Rasmussen and N.C. Nielsen, *J. Magn. Reson.,* 147, 296-330, **2000**

[25] E.R. Andrew, A. Bradbury and R.G. Eades, *Nature,* 183, 1802-1803, **1959**

[26] I.J. Lowe and R.E. Norberg, *Phys. Rev.,* 107, 46-61, **1957**

[27] I.J. Lowe, *Phys. Rev. Lett.,* 2, 285-287, **1959**

[28] A. Pines, M.G. Gibby and J.S. Waugh, *J. Chem. Phys.,* 59, 569-590, **1973**

[29] J. Schaefer and E.O. Stejskal, *J. Am. Chem. Soc.,* 98, 1031-1032, **1976**

[30] T.G. Oas, R.G. Griffin and M.H. Levitt, *J. Chem. Phys.,* 89, 692-695, **1988**

[31] T. Gullion and J. Schaefer, *J. Magn. Reson.,* 81, 196-200*,* **1989**
[32] R. Tycko, G. Dabbagh and P.A. Mirau, *J. Magn. Reson.,* 85, 265-274*,* **1989**
[33] H.W. Spiess, *J. Chem. Phys.,* 72, 6755-6762*,* **1980**
[34] H.W. Spiess, *Adv. Polym. Sci.,* 66, 23-58*,* **1985**
[35] H.W. Spiess, *Colloid and Polymer Science,* 261, 193-209*,* **1983**
[36] Y. Yang, M. Schuster, B. Blümich and H.W. Spiess, *Chem. Phys. Lett.,* 139, 239-243*,* **1987**
[37] V. Gérardy-Montouillout, C. Malveau, P. Tekely, Z. Olender and Z. Luz, *J. Magn. Reson., Ser A,* 123, 7-15*,* **1996**
[38] D. Reichert, H. Zimmermann, P. Tekely, R. Poupko and Z. Luz, *J. Magn. Reson.,* 125, 245-258*,* **1997**
[39] P. Tekely, J. Brondeau, K. Elbayed, A. Retournard and D. Canet, *J. Magn. Reson.,* 80, 509-516*,* **1988**
[40] D. Reichert, G. Hempel, Z. Luz, P. Tekely and H. Schneider, *J. Magn. Reson.,* 146, 311-320*,* **2000**
[41] E.R. deAzevedo, W.G. Hu, T.J. Bonagamba and K. Schmidt-Rohr, *J. Chem. Phys.,* 112, 8988-9001*,* **2000**
[42] J. Schaefer, R.A. McKay, E.O. Stejskal and W.T. Dixon, *J. Magn. Reson.,* 52, 123-129*,* **1983**
[43] J. Schaefer, E.O. Stejskal, R.A. McKay and W.T. Dixon, *Macromolecules,* 17, 1479-1489*,* **1984**
[44] M. Hong, X. Yao, K. Jakes and D. Huster, *J. Phys. Chem. B,* 106, 7355-7364*,* **2002**
[45] C.H. Wu, A. Ramamoorthy and S.J. Opella, *J. Magn. Reson., Ser A,* 109, 270-272*,* **1994**
[46] S.V. Dvinskikh, H. Zimmermann, A. Maliniak and D. Sandström, *J. Magn. Reson.,* 164, 165-170*,* **2003**
[47] M.H. Levitt, Symmetry-Based Pulse Sequences in Magic-Angle Spinning Solid-State NMR, Encyclopedia of Nuclear Magnetic Resonance, John Wiley & Sons, Chicester, **2002**
[48] A. Brinkmann, M. Eden and M.H. Levitt, *J. Chem. Phys.,* 112, 8539-8554*,* **2000**
[49] A. Brinkmann and M.H. Levitt, *J. Chem. Phys.,* 115, 357-384*,* **2001**
[50] A. Abragam, Principles of Nuclear Magnetism, Oxford University Press, Oxford, Oxford, **1961**
[51] M.J. Duer, Introduction to Solid-State NMR Spectroscopy: Principles and application, Blackwell, Cambridge, **2004**
[52] C.A. Fyfe, K.C. Wong-Moon, Y. Huang and H. Grondey, *J. Am. Chem. Soc.,* 117, 10397-10398*,* **1995**
[53] H. Miura, T. Terao and A. Saika, *J. Magn. Reson.,* 68, 593-596*,* **1986**
[54] A. Lesage, D. Sakellariou, S. Steuernagel and L. Emsley, *J. Am. Chem. Soc.,* 120, 13194-13201*,* **1998**
[55] T.A. Early, B.K. John and L.F. Johnson, *J. Magn. Reson.,* 75, 134-138*,* **1987**
[56] M. Baldus and B.H. Meier, *J. Magn. Reson., Ser A,* 121, 65-69*,* **1996**
[57] P.P. Man, Quadrupolar Interactions, Encyclopedia of Magnetic Resonance, **2011**

[58] A.J. Shaka, J. Keeler, T. Frenkiel and R. Freeman, *J. Magn. Reson.,* 52, 335-338, **1983**

[59] A.E. Bennett, C.M. Rienstra, M. Auger, K.V. Lakshmi and R.G. Griffin, *J. Chem. Phys.,* 103, 6951-6958, **1995**

[60] A. Detken, E.H. Hardy, M. Ernst and B.H. Meier, *Chem. Phys. Lett.,* 356, 298-304, **2002**

[61] B.M. Fung, A.K. Khitrin and K. Ermolaev, *J. Magn. Reson.,* 142, 97-101, **2000**

[62] U. Haeberlen and J.S. Waugh, *Phys. Rev.,* 175, 453-467, **1968**

[63] W.K. Rhim, D.D. Elleman and R.W. Vaughan, *J. Chem. Phys.,* 59, 3740-3749, **1973**

[64] B.C. Gerstein, R.G. Pembleton, R.C. Wilson and L.M. Ryan, *J. Chem. Phys.,* 66, 361-362, **1977**

[65] A. Bielecki, A.C. Kolbert and M.H. Levitt, *Chem. Phys. Lett.,* 155, 341-346, **1989**

[66] E. Vinogradov, P.K. Madhu and S. Vega, *Chem. Phys. Lett.,* 314, 443-450, **1999**

[67] S.R. Hartmann and E.L. Hahn, *Phys. Rev.,* 128, 2042-2053, **1962**

[68] G. Metz, X.L. Wu and S.O. Smith, *J. Magn. Reson., Ser A,* 110, 219-227, **1994**

[69] M. Maricq and J.S. Waugh, *Chem. Phys. Lett.,* 47, 327-329, **1977**

[70] M.M. Maricq and J.S. Waugh, *J. Chem. Phys.,* 70, 3300-3316, **1979**

[71] J. Herzfeld and A.E. Berger, *J. Chem. Phys.,* 73, 6021-6030, **1980**

[72] A. Bax, N.M. Szeverenyi and G.E. Maciel, *J. Magn. Reson.,* 52, 147-152, **1983**

[73] A. Bax, N.M. Szeverenyi and G.E. Maciel, *J. Magn. Reson.,* 55, 494-497, **1983**

[74] Y. Yarim-Agaev, P.N. Tutunjian and J.S. Waugh, *J. Magn. Reson.,* 47, 51-60, **1982**

[75] A. Bax, N.M. Szeverenyi and G.E. Maciel, *J. Magn. Reson.,* 51, 400-408, **1983**

[76] I. Yoshitaka and T. Takehiko, *J. Chem. Phys.,* 109, 1366-1374, **1998**

[77] Z. Gan, D.M. Grant and R.R. Ernst, *Chem. Phys. Lett.,* 254, 349-357, **1996**

[78] J.D. Gross, P.R. Costa and R.G. Griffin, *J. Chem. Phys.,* 108, 7286-7293, **1998**

[79] S.F. Liu, J.D. Mao and K. Schmidt-Rohr, *J. Magn. Reson.,* 155, 15-28, **2002**

[80] J.C.C. Chan and R. Tycko, *J. Chem. Phys.,* 118, 8378-8389, **2003**

[81] Y. Nishiyama, T. Yamazaki and T. Terao, *J. Chem. Phys.,* 124, 064304-064311, **2006**

[82] L. Müller, A. Kumar, T. Baumann and R.R. Ernst, *Phys. Rev. Lett.,* 32, 1402-1406, **1974**

[83] J.S. Waugh, *Proc. Natl. Acad. Sci.,* 73, 1394-1397, **1976**

[84] R.K. Hester, J.L. Ackerman, B.L. Neff and J.S. Waugh, *Phys. Rev. Lett.,* 36, 1081-1083, **1976**

[85] S.J. Opella and J.S. Waugh, *J. Chem. Phys.,* 66, 4919-4924, **1977**

[86] J.E. Roberts, G.S. Harbison, M.G. Munowitz, J. Herzfeld and R.G. Griffin, *J. Am. Chem. Soc.,* 109, 4163-4169, **1987**

[87] A. Ramamoorthy, F.M. Marassi, M. Zasloff and S.J. Opella, *J. Biomol. NMR,* 6, 329-334, **1995**

[88] T.A. Cross and S.J. Opella, *Curr. Opin. Struct. Biol.,* 4, 574-581, **1994**

[89] F.M. Marassi and S.J. Opella, *Curr. Opin. Struct. Biol.,* 8, 640-648, **1998**

[90] B.-J. van Rossum, C.P. de Groot, V. Ladizhansky, S. Vega and H.J.M. de Groot, *J. Am. Chem. Soc.,* 122, 3465-3472*,* **2000**

[91] Y.K. Lee, N.D. Kurur, M. Helmle, O.G. Johannessen, N.C. Nielsen and M.H. Levitt, *Chem. Phys. Lett.,* 242, 304-309*,* **1995**

[92] M. Hohwy, H.J. Jakobsen, M. Eden, M.H. Levitt and N.C. Nielsen, *J. Chem. Phys.,* 108, 2686-2694*,* **1998**

[93] X. Zhao, M. Edén and M.H. Levitt, *Chem. Phys. Lett.,* 342, 353-361*,* **2001**

[94] Q. Wang, X. Lu, O. Lafon, J. Trebosc, F. Deng, B. Hu, Q. Chen and J.-P. Amoureux, *Phys. Chem. Chem. Phys.,* 13, 5967-5973*,* **2011**

[95] M.G. Munowitz, R.G. Griffin, G. Bodenhausen and T.H. Huang, *J. Am. Chem. Soc.,* 103, 2529-2533*,* **1981**

[96] M. Munowitz, W.P. Aue and R.G. Griffin, *J. Chem. Phys.,* 77, 1686-1689*,* **1982**

[97] D. Reichert and K. Saalwachter, Dipolar Coupling : Molecular-Level Mobility, encyclopedia, **2002**

[98] D. Reichert, O. Pascui, E.R. deAzevedo, T.J. Bonagamba, K. Arnold and D. Huster, *Magn. Reson. Chem.,* 42, 276-284*,* **2004**

[99] E.R. deAzevedo, K. Saalwachter, O. Pascui, A.A. de Souza, T.J. Bonagamba and D. Reichert, *J. Chem. Phys.,* 128, 104505-104512*,* **2008**

[100] K. Schmidt-Rohr and H.W. Spiess, Multidimensional Solid-State NMR and Polymers, Academic Press, London, **1994**

[101] R. Hentschel, J. Schlitter, H. Sillescu and H.W. Spiess, *J. Chem. Phys.,* 68, 56-66*,* **1978**

[102] H.W. Spiess and H. Sillescu, *J. Magn. Reson.,* 42, 381-389*,* **1981**

[103] D. Hentschel, H. Sillescu and H.W. Spiess, *Polymer,* 25, 1078-1086*,* **1984**

[104] E. Rössler, H. Sillescu and H.W. Spiess, *Polymer,* 26, 203-207*,* **1985**

[105] M. Wehrle, G.P. Hellmann and H.W. Spiess, *Colloid. Polym. Sci,* 265, 815-822*,* **1987**

[106] J.J. Dumais, L.W. Jelinski, M.E. Galvin, C. Dybowski, C.E. Brown and P. Kovacic, *Macromolecules,* 22, 612-617*,* **1989**

[107] A.L. Cholli, J.J. Dumais, A.K. Engel and L.W. Jelinski, *Macromolecules,* 17, 2399-2404*,* **1984**

[108] J.J. Dumais, A.L. Cholli, L.W. Jelinski, J.L. Hedrick and J.E. McGrath, *Macromolecules,* 19, 1884-1889*,* **1986**

[109] J. Hirschinger, D. Schaefer, H.W. Spiess and A.J. Lovinger, *Macromolecules,* 24, 2428-2433*,* **1991**

[110] H.T. Edzes and J.P.C. Bernards, *J. Am. Chem. Soc.,* 106, 1515-1517*,* **1984**

[111] A.F. de Jong, A.P.M. Kentgens and W.S. Veeman, *Chem. Phys. Lett.,* 109, 337-342*,* **1984**

[112] D. Schaefer, H.W. Spiess, U.W. Suter and W.W. Fleming, *Macromolecules,* 23, 3431-3439*,* **1990**

[113] C. Schmidt, S. Wefing, B. Blümich and H.W. Spiess, *Chem. Phys. Lett.,* 130, 84-90*,* **1986**

[114] Z. Luz, P. Tekely and D. Reichert, *Prog. Nucl. Magn. Reson. Spectrosc.,* 41, 83-113*,* **2002**

[115] E.R. deAzevedo, W.G. Hu, T.J. Bonagamba and K. Schmidt-Rohr, *J. Am. Chem. Soc.,* 121, 8411-8412*,* **1999**
[116] K. Saalwachter and I. Fischbach, *J. Magn. Reson.,* 157, 17-30*,* **2002**
[117] O. Pascui, M. Beiner and D. Reichert, *Macromolecules,* 36, 3992-4003*,* **2003**
[118] T.J. Bonagamba, F. Becker-Guedes, E.R. DeAzevedo and K. Schmidt-Rohr, *J. Polym. Sci., Part B: Polym. Phys.,* 39, 2444-2453*,* **2001**
[119] T. Miyoshi, O. Pascui and D. Reichert, *Macromolecules,* 35, 7178-7181*,* **2002**
[120] A. Krushelnitsky, E. deAzevedo, R. Linser, B. Reif, K. Saalwachter and D. Reichert, *J. Am. Chem. Soc.,* 131, 12097-12099*,* **2009**
[121] M.H. Levitt, D. Suter and R.R. Ernst, *J. Chem. Phys.,* 84, 4243-4255*,* **1986**
[122] A.E. Bennett, C.M. Rienstra, J.M. Griffiths, W. Zhen, J.P.T. Lansbury and R.G. Griffin, *J. Chem. Phys.,* 108, 9463-9479*,* **1998**
[123] V. Ladizhansky and S. Vega, *J. Chem. Phys.,* 112, 7158-7168*,* **2000**
[124] R. Zhang, Y. Chen, T. Chen, P. Sun, B. Li and D. Ding, *J. Phys. Chem. A,* 116, 979-984*,* **2012**
[125] D.A. Torchia, *J. Magn. Reson.,* 30, 613-616*,* **1978**
[126] F. Becker-Guedes, E. deAzevedo, T. Bonagamba and K. Schmidt-Rohr, *Appl. Magn. Reson.,* 27, 383-400*,* **2004**
[127] Spindynamica : a packages for spin dynamical calculations in Mathematica, http://www.spindynamica.soton.ac.uk/about/
[128] D.H. Brouwer and J.A. Ripmeester, *J. Magn. Reson.,* 185, 173-178*,* **2007**
[129] G. Hou, I.-J.L. Byeon, J. Ahn, A.M. Gronenborn and T. Polenova, *J. Chem. Phys.,* 137, 134201-134210*,* **2012**
[130] M. Veshtort and R.G. Griffin, *J. Magn. Reson.,* 178, 248-282*,* **2006**
[131] G. Sextro, *Ullmann's Encyclopedia of Industrial Chemistry,* 367-379*,* **2000**
[132] M.Y. Keating, B.B. Sauer and E.A. Flexman, *Journal of Macromolecular Science, Part B,* 36, 717-732*,* **1997**
[133] H. Suzuki, J. Grebowicz and B. Wunderlich, *Die Makromolekulare Chemie,* 186, 1109-1119*,* **1985**
[134] B.E. Read and G. Williams, *Polymer,* 2, 239-255*,* **1961**
[135] H. Hama and K. Tashiro, *Polymer,* 44, 2159-2168*,* **2003**
[136] H. Hama and K. Tashiro, *Polymer,* 44, 3107-3116*,* **2003**
[137] H. Hama and K. Tashiro, *Polymer,* 44, 6973-6988*,* **2003**
[138] W.S. Veeman, E.M. Menger, W. Ritchey and E. de Boer, *Macromolecules,* 12, 924-927*,* **1979**
[139] A.L. Cholli, W.M. Ritchey and J.L. Koenig, *Spectrosc. Lett.,* 16, 21-28*,* **1983**
[140] P. Tekely, D. Canet and J.-J. Delpuech, *Mol. Phys.,* 67, 81-96*,* **1989**
[141] A.P.M. Kentgens, A.F. De Jong, E. De Boer and W.S. Veeman, *Macromolecules,* 18, 1045-1048*,* **1985**
[142] (a) Delrin Design Guide, Module III, E.I. DuPont deNemours and Company (http://www2.dupont.com/Plastics/en_US/assets/downloads/design/DELDGe.pdf). (b) The deflection temperature is defined as the temperature when an arbitrary deformation occurs when subjecting a defined standard sample to an arbitrary set of testing conditions (see:

http://www.astm.org/Standards/D648.htm). Therefore, the deflection temperature is an engineering measure of the modulus and does not necessarily correspond to a sudden structural transition at that temperature.,

[143] A.L.V. Geet, *Anal. Chem.,* 40, 2227-2229*,* **1968**

[144] A. Bielecki and D.P. Burum, *J. Magn. Reson., Ser A,* 116, 215-220*,* **1995**

[145] D.J. States, R.A. Haberkorn and D.J. Ruben, *J. Magn. Reson.,* 48, 286-292*,* **1982**

[146] H. Uehara, T. Yamanobe and T. Komoto, *Macromolecules,* 33, 4861-4870*,* **2000**

[147] R. Sanjay, R.L. Dirk, W.H.H. Günther, M. Brahim and C.M.M.M. Pieter, *J. Phys.: Condens. Matter,* 19, 205122-205143*,* **2007**

[148] R. Sanjay and A.E. Terry, *Adv Polym Sci,* 180, 161-194*,* **2005**

[149] Solvay Design Guide - Radel - PPSU, Veradel - PESU, Acudel - modified PPSU, http://www.solvaysites.com/sites/solvayplastics/EN/specialty_polymers/SulfonePolymers/Pages/Overview.aspx

[150] C.L. Aitken, J.S. McHattie and D.R. Paul, *Macromolecules,* 25, 2910-2922*,* **1992**

[151] A.F. Yee and S.A. Smith, *Macromolecules,* 14, 54-64*,* **1981**

[152] J.Y. Jho and A.F. Yee, *Macromolecules,* 24, 1905-1913*,* **1991**

[153] M.D. Poliks, T. Gullion and J. Schaefer, *Macromolecules,* 23, 2678-2681*,* **1990**

[154] A.S. Merenga, C.M. Papadakis, F. Kremer, J. Liu and A.F. Yee, *Macromolecules,* 34, 76-81*,* **2000**

[155] J. Schaefer, E.O. Stejskal, D. Perchak, J. Skolnick and R. Yaris, *Macromolecules,* 18, 368-373*,* **1985**

[156] A.K. Roy, A.A. Jones and P.T. Inglefield, *Macromolecules,* 19, 1356-1362*,* **1986**

[157] C. Xiao and A.F. Yee, *Macromolecules,* 25, 6800-6809*,* **1992**

[158] S. Arrese-Igor, A. Arbe, A. Alegria, J. Colmenero and B. Frick, *The Journal of Chemical Physics,* 120, 423-436*,* **2004**

[159] S. Arrese-Igor, A. Arbe, A. AlegrÃ-a, J. Colmenero and B. Frick, *Appl. Phys. A,* 74, s454-s456*,* **2002**

[160] C.F. Fan and S.L. Hsu, *Macromolecules,* 25, 266-270*,* **1992**

[161] S. Arrese-Igor, A. Arbe, A. AlegrÃa, J. Colmenero and B. Frick, *The Journal of Chemical Physics,* 123, 14907*,* **2005**

[162] S. Arrese-Igor, O. Mitxelena, A. Arbe, A. Alegría, J. Colmenero and B. Frick, *J. Non-Cryst. Solids,* 352, 5072-5075*,* **2006**

[163] S. Arrese-Igor, A. Arbe, A. Alegría, J. Colmenero and B. Frick, *Appl. Phys. A,* 74, s454-s456*,* **2002**

[164] S. Arrese-Igor, A. Arbe, A. Alegría, J. Colmenero and B. Frick, *Chem. Phys.,* 292, 363-370*,* **2003**

[165] S. Arrese-Igor, A. Arbe, A. Alegría, J. Colmenero and B. Frick, *J. Chem. Phys.,* 120, 423-436*,* **2004**

[166] D. Garlotta, *J. Polym. Environ.,* 9, 63-84*,* **2001**

[167] A. Sodergard and M. Stolt, *Prog. Polym. Sci.,* 27, 1123-1163, **2002**
[168] P. van de Witte, H. Esselbrugge, A.M.P. Peters, P.J. Dijkstra, J. Feijen, R.J.J. Groenewegen, J. Smid, J. Olijslager, J.M. Schakenraad, M.J.D. Eenink and A.P. Sam, *J. Controlled Release,* 24, 61-78, **1993**
[169] J.M. Schakenraad, J.A. Oosterbaan, P. Nieuwenhuis, I. Molenaar, J. Olijslager, W. Potman, M.J.D. Eenink and J. Feijen, *Biomaterials,* 9, 116-120, **1988**
[170] J.C. Middleton and A.J. Tipton, *Biomaterials,* 21, 2335-2346, **2000**
[171] D.W. Grijpma and A.J. Pennings, *Macromol. Chem. Phys.,* 195, 1649-1663, **1994**
[172] H. Maeda, T. Kasuga, M. Nogami and M. Ueda, *Science and Technology of Advanced Materials,* 6, 48-53, **2005**
[173] S.D. Park, M. Todo, K. Arakawa and M. Koganemaru, *Polymer,* 47, 1357-1363, **2006**
[174] J. Mijovic and J.-W. Sy, *Macromolecules,* 35, 6370-6376, **2002**
[175] M. Kanchanasopa and J. Runt, *Macromolecules,* 37, 863-871, **2004**
[176] J.F. Mano, *Macromolecular Bioscience,* 5, 337-343, **2005**
[177] W.G. Hu and K. Schmidt-Rohr, *Acta Polym.,* 50, 271-285, **1999**
[178] A. Krushelnitsky and D. Reichert, *Prog. Nucl. Magn. Reson. Spectrosc.,* 47, 1-25, **2005**
[179] A. Nogales, T.A. Ezquerra, F. Batallán, B. Frick, E. López-Cabarcos and F.J. Baltá-Calleja, *Macromolecules,* 32, 2301-2308, **1999**
[180] S. Arrese-Igor, A. Arbe, A. Alegría, J. Colmenero and B. Frick, *J. Chem. Phys.,* 123, 014907-014910, **2005**
[181] M.R. Hansen, R. Graf and H.W. Spiess, *Acc. Chem. Res.,* 46, 1996-2007, **2013**
[182] E.R. deAzevedo, T.J. Bonagamba and D. Reichert, *Prog. Nucl. Magn. Reson. Spectrosc.,* 47, 137-164, **2005**
[183] L.M. McDowell and J. Schaefer, *Curr. Opin. Struct. Biol.,* 6, 624-629, **1996**
[184] K. Saalwachter, *Prog. Nucl. Magn. Reson. Spectrosc.,* 51, 1-35, **2007**
[185] D. Reichert, O. Pascui, T.J. Bonagamba, E.R. deAzevedo and A. Schmidt, *Chem. Phys. Lett.,* 380, 583-588, **2003**
[186] D. Reichert, O. Pascui, T.J. Bonagamba, P. Belton, A. Schmidt and E.R. deAzevedo, *J. Magn. Reson.,* 191, 141-147, **2008**
[187] W. Li and A. McDermott, *J. Biomol. NMR,* 45, 227-232, **2009**
[188] W. Li and A. McDermott, *J. Magn. Reson.,* 222, 74-80, **2012**
[189] S.B. Elavarasi, A. Kumari and K. Dorai, *J. Phys. Chem. A,* 114, 5830-5837, **2010**
[190] G. Hou, S. Paramasivam, I.-J.L. Byeon, A.M. Gronenborn and T. Polenova, *Phys. Chem. Chem. Phys.,* 12, 14873-14883, **2010**
[191] M.H. Levitt, *J. Chem. Phys.,* 128, 052205-052225, **2008**